# DEVELOPMENT OF A HIGH-SPEED HIGH-PRECISION MICRO-GROOVE CUTTING PROCESS

BY

KEITH ALLEN BOURNE

DISSERTATION

Submitted in partial fulfillment of the requirements
for the degree of Doctor of Philosophy in Mechanical Engineering
in the Graduate College of the
University of Illinois at Urbana-Champaign, 2010

Urbana, Illinois

Doctoral Committee:

Professor Shiv G. Kapoor, Chair
Professor Richard E. DeVor, Co-Director of Research
Professor Placid M. Ferreira
Professor Brian T. Cunningham

# Abstract

A high-speed, high-precision chip formation-based micro-groove cutting process has been developed for cutting grooves in metals with nearly arbitrarily shaped cross-sections, which have widths and depths of a few hundred nanometers to a few microns, and lengths of tens of millimeters. A flexible tool, consisting of a single-point cutting geometry mounted on the end of a small cantilever, is moved along a workpiece surface while a constant cantilever deflection is maintained to apply a cutting load. Depth of cut for a given tool shape is determined by cutting load and workpiece material properties. A major advantage of the flexible tool concept is increased depth of cut precision. Furthermore, the use of a flexible tool enables the process to be robust against machine tool registration error, guide misalignment, and component inertial deflections. The process was implemented by fitting a 5-axis micro-scale machine tool with a specially constructed micro-groove cutting assembly.

Early, experiments using diamond-coated AFM probes as tools demonstrated process viability up to cutting speeds of 25 mm/min and chip formation at the sub-micron scale. However, AFM probe geometries proved too fragile for this demanding application. High quality tools with improved cutting geometries were designed and fabricated via focused ion beam machining of single-crystal diamond tool blanks, and tool edge radii of 50 - 64 nm were achieved. The improved tools enabled well-formed rectangular grooves to be cut in aluminum at up to 400 mm/min with widths of 300 nm to 1.05 μm and depths up to 2 μm. Complex compound v-shaped grooves were also produced. Virtually no tool wear (less than 20 nm) was observed over a cutting distance

of 122.4 mm. Small amounts of side burr formation occurred during steady-state cutting, and exit burr formation occurred when a tool exited from a workpiece. Parallel 1.05 μm wide grooves were controllably cut as close as 1.0 μm apart, and machining of intersecting grooves was successfully demonstrated.

To better understand process mechanics including chip formation, side burr formation, and exit burr formation at the small size scale involved, a 3D finite element model of the process was developed. Validation with experimental results showed that on average the model predicted side burr height to within 2.8%, chip curl to within 4.1%, and chip thickness to within 25.4%. An important finding is that side burr formation is primarily caused ahead of a tool by expansion of material compressed after starting to flow around a tool rather than becoming part of a chip. Also, three exit burrs, two on the sides of a groove and one on the bottom of a groove, are formed when a thin membrane of material forms ahead of a tool and then ruptures as the tool exits a workpiece. Finally, conclusions about the process are drawn and recommendations for future work are presented.

# Acknowledgements

I'd like to express my gratitude towards my co-advisors, Professor Richard E. DeVor and Professor Shiv G. Kapoor. This work would not have been possible without their financial support, advice, and encouragement. I am particularly grateful for their insightful comments and questions about my work, their meticulous assistance during writing, and for many enjoyable conversations we've had on a wide variety of subjects. I'd also like to thank the members of my dissertation committee, Professor Placid M. Ferreira and Professor Brian T. Cunningham, for their time and their helpful suggestions.

I gratefully acknowledge the financial support of the Center for Nanoscale Chemical-Electrical-Mechanical Manufacturing Systems at the University of Illinois at Urbana-Champaign, which is funded by the National Science Foundation under grants #DMI-032-8162 and #CMMI-07-49028. I also gratefully acknowledge the financial support of the Grace Wicall Gauthier Chair in Mechanical Science and Engineering at the University of Illinois at Urbana-Champaign.

I gratefully acknowledge use of the Frederick Seitz Materials Research Laboratory Central Facilities at the University of Illinois, which is partially supported by the U.S. Department of Energy under grants DE-FG02-07ER46453 and DE-FG02-07ER46471. My appreciation also goes to the helpful staff of this laboratory including Tony Banks, Jim Mabon, Scott MacLaren, and Mike Marshall.

I wish to state my appreciation for all the administrative help provided by many of the Department of Mechanical Science and Engineering staff including Marian L.

Brinkerhoff, Robert, E. Coverdill, Polly A. Kroha, Ruthie J. Lattina, Vance I. McCall, Elaine J. Nicholas, and Bob Nichols.

I want to thank all of my former and current research colleagues for their friendship, advice, and assistance. I especially want to thank Kurt Adair, Ashwin Balasubramanian, Onik Bhattacharyya, Peter Bittorf, Kevin Calzada, Ken Heinz, Andrew Honegger, Dr. Martin Jun, Alex Krejcie, George Lanstaff, Dr. Xinyu Liu, Dr. Sunghyuk Park, Andy Phillip, Tim VanRevenswaay, Dr. Johnson Samuel, Kyle Stacy, Dr. John Wentz, Bingyi Yu, and James Zhu

Finally, I want to thank my family for their encouragement, advice, and support throughout this work and throughout my life. They have made it possible for me to reach this point in my life and complete this work.

# Contents

# List of Figures

# List of Tables

# Chapter 1

# Introduction

## 1.1 Background and Motivation

There is an increasing demand for miniature devices with micro-scale features and macro-scale devices with surface textures that include micro-scale features. Micro-grooves are one such feature that appears in many devices. Micro-grooves have typically been fabricated using various processes in which material is deposited, patterned using photolithography, and etched. Such processes have enabled cost-effective production of large batches of devices and are responsible for many of the currently successfully micro-electromechanical system (MEMS) devices on the market. However, deposition, pattern, and etch-based processes have disadvantages that include limits on the materials that devices can be fabricated from, limits on feature geometries, the need for expensive equipment for some processes, the use of hazardous chemicals, and the need to fabricate a potentially expensive series of masks for each new type of device. The later limitation can render prototyping, or the production of small batches of custom devices, more time-intensive and expensive than would be desirable in some cases. Therefore, it is desirable to develop additional micro-groove fabrication technologies that avoid these problems.

Micro-grooves can, for example, be part of hot embossing molds, micro-forming dies, optical lithography masks, micro-fluidic devices, micro-optics, micro-heat exchangers, and engineered surface textures. A few more specific applications are as follows:

1. A micro-optics application with demanding requirements is the fabrication of molds for next generation ultrathin LED backlight light guides, which involves cutting long grooves with complex cross-sections and depths of a about a micron in metals.
2. The fabrication of high-density micro-heat exchangers may involve cutting many tightly packed, long, high aspect ratio micro-grooves with widths that may be as small as a few hundred nanometers and with pitches less than a micron.
3. The fabrication of a series of intersecting curvilinear grooves with widths and depths of a few microns may be used to build up complex surface patterns on metallic surfaces, such as the recently developed anti-microbial texture developed by Sharklet Technologies [40]. Other patterns may be use to modify the wetting characteristics of a surface [41] or to achieve various optical diffraction effects.

These applications impose the following process requirements: (1) the ability to cut grooves in metals that are between a few hundred nanometers wide and a few microns wide, (2) the ability to cut patterns of many grooves that are each several millimeters long, (3) the ability to cut patterns of curvilinear grooves, (4) the ability to cut grooves with nearly arbitrary cross-sections, and (5) the ability to cut grooves with minimal burr formation / material distortion. Additionally, economic considerations impose the additional requirements of having (6) a good material removal rate, (7) the ability to cut fully programmable patterns of grooves, and (8) the ability to fabricate micro-grooves using relatively inexpensive equipment. It is also highly desirable in general that a micro-groove process should be able to (9) achieve relative tolerances of approximately $10^{-2}$ or better. Lastly, it is desirable for a micro-groove cutting process to (10) be capable

of cutting grooves in flat or curved workpiece surfaces, which is of particular importance if a surface pattern is to be cut into a complex die or mold.

Several processes exist, in addition to more conventional deposition, pattern, and etch-based processes, which are suitable for producing micro-grooves with various process-dependent characteristics. Material removal processes based on the application of thermal energy are laser scribing and micro-electrical discharge machining (μ-EDM). A processes based on electrochemical dissolution is micro-electrochemical machining (μ-ECM). Mechanical material removal processes include micro-endmilling, micro-fly cutting, micro-scale shaping / planing, and atomic force microscope (AFM) scribing.

However, none of these processes meet all of the requirements previously listed. In particular, only solid-state ECM, micro-fly cutting, micro-scale shaping / planing, and AFM scribing are capable of achieving the target widths. Furthermore, of these processes, solid-state ECM [33, 42] requires physical contact between a superionic stamp and a workpiece, which renders it difficult to cut features into large curved surfaces. Also, the stamp must still be fabricated using some other process. Micro-fly cutting can only cut straight grooves, has been limited to v-shaped grooves when grooves widths were less than about 20 μm [14, 15], and requires a very rigid and expensive machine tool. Micro-scale shaping / planing suffers from burr formation issues, and requires a stiff and expensive machine tool to perform well. Also, very narrow grooves cut with this process have been limited to v-shaped cross-sections [31, 43]. Lastly, while AFM scribing can be used to cut extremely narrow grooves or can build up grooves as wide as the range of travel of the AFM by moving an AFM probe in a raster pattern during cutting, this process is extremely slow, is limited to grooves with very short lengths [24,

32, 44, 45], and requires expensive equipment. Therefore, since no process meets all of the requirements previously listed, and there is a gap in current manufacturing capabilities that motivates the development of a new micro-groove cutting process

## 1.2 Research Objectives, Scope, and Tasks

### 1.2.1 Research Objectives and Scope

The ultimate objective of this research is to develop a cost-effective micro-groove cutting process capable of meeting the ten process requirements listed in the previous section. That is, the ability to cut programmable patterns of curvilinear grooves with nearly arbitrary cross-sections in metals that are between a few hundred nanometers and a few microns wide, up to a few microns deep, and between tens of microns to several millimeters long. This process should have a good material removal rate, avoid significant burr formation / material distortion, and achieve relative tolerances of approximately $10^{-2}$ or better. Also, this process should be capable of cutting grooves into curved surfaces.

To achieve this objective, it is necessary to both design a new process and build a machine tool that can implement it. Then, a thorough understanding of the process must be developed through both experimental and analytical studies in order to achieve good performance and enable process planing. Lastly, it is necessary to demonstrate the viability of the process by fabricating parts with test features representative of types of features required in applications.

Experimental work will be limited to cutting grooves that are between a few hundred nanometers and a few microns wide in smooth planar workpieces. These workpieces will consist of a metal film evaporated onto a flat substrate. In order to limit

the number of experiments conducted, only one homogenous workpiece material will be considered. Simulations of the cutting process will similarly be limited in terms of the workpiece. Lastly, any test parts intended to demonstrate process capabilities will be limited to small sizes sufficient to demonstrate the fabrication of features of interest.

### 1.2.2 Research Tasks

**Task 1: Process Development**

A micro-machining process capable of meeting the research objectives will be developed. This process will make use of a flexible single-point cutting tool consisting of a cutting geometry, similar to the geometry of a micro-planing tool, attached to the end of a cantilever. During cutting, this tool will be moved across the surface of a workpiece while the cantilever is bent in order to apply a cutting load. Therefore, a test-bed on which the process can be implemented will be developed by retrofitting an existing 5-axis machine tool. Tool geometries for use with the process will also be developed.

**Task 2: Experimental Study of the Cutting Process**

The machine tool will be used to experimentally explore process characteristics. Initial experiential studies will be conducted, in which commercial AFM probes are used as flexible cutting tools, in order to gain a general understanding of the process. Based on this understanding, the process will be improved until reasonably good results are achieved. This will include selection of better machining conditions and selection of better tool geometries.

**Task 3: Process Modeling**

While experimental studies of the cutting process can provide useful insights, limitations inherent in experimentation, especially at the micro-scale, mean that a full

understanding of the process cannot be achieved through experimentation alone. Therefore, the third task will be to model the cutting processes. This model will be used to gain an improved understanding of the cutting process in order to enable improved performance and process planing.

**Task 4: Fabrication Capabilities Demonstration**

The forth task of this research is to demonstrate the fabrication of the types of features that are required in order to fabricate parts representative of the applications that drove the process requirements listed in this chapter. This includes demonstration of the ability to cut grooves of varying geometries, to cut very narrow grooves, to cut closely spaced grooves, and to cut surface patterns composed of multiple grooves.

## 1.3 Thesis Outline

This thesis is organized as follows. Chapter 2 presents a review of literature on micro-groove formation processes, other than conventional deposition, pattern, and etch-based processes, which can be used to form micro-grooves with widths of 50 μm or less. The processes covered are laser scribing, micro-electrical discharge machining (μ-EDM), micro-electrochemical machining (μ-ECM), micro-endmilling, micro-fly cutting, micro-scale shaping / planing, and atomic force microscope (AFM) scribing. A summary of these processes, in which they are evaluated in terms of process requirements, follows and shows that there is a subset of useful micro-groove features that cannot be readily fabricated using currently available processes. Hence, there is a need for a new process to fill this gap, which is the focus of this thesis. This is followed by a more fundamental discussion of micro-scale chip formation-based material removal that focuses on features unique to the micro-scale. Lastly, methods that can be used to model chip formation-

based material removal process are discussed with emphasis given to finite element methods.

Chapter 3 describes the micro-groove cutting process and the machine tool developed to implement the processes. In the chapter, the obstacles associated with meeting process requirements are first described. Then, the design of a micro-groove cutting process intended to not be hampered by the presented obstacles is described. Next, requirements imposed upon a machine tool that is used to implement the developed process are given. The machine tool used to implement the process is then described in detail. The last part of the chapter describes the operation of the machine tool during process setup and during micro-groove cutting.

Chapter 4 discusses three early experiments where commercial AFM probes were used as flexible single-point micro-cutting tools. The setup of the experiments is first discussed. Then the results of the first experiment, where long cuts were made using multiple tool passes, are discussed. Emphasis is placed on tool wear and the formation of grooves via multiple tool passes. Next, a second experiment is discussed where process conditions are varied in a factorial design during short cuts using only one tool pass each. Due to the experimental setup, tool wear, groove geometry, effective rake angle, and chip morphology are more exactly related to process conditions during the second experiment. A third experiment is then discussed that demonstrates the ability to cut grooves that have curved trajectories. Over the courses of the chapter, it is shown that the largest restriction on groove quality is the use of commercial AFM probes as tools, which are shown to not be suitable for micro-groove cutting.

Chapter 5 concerns the development of improved cutting tools that offer superior performance to the AFM probes used in Chapter 4. The chapter first proposes several micro-groove cutting tool design principles. A tool fabrication process is then described that involves making four through cuts into a suitable tool blank using focused ion beam (FIB) machining in order to fabricate tool designs based on the proposed principles. The tool fabrication procedure used to make several tools, which includes a description of the equipment used, follows.

Chapter 6 describes six experiments conducted using the improved tools introduced in Chapter 5 in order to evaluate their capabilities. First, the tools used in the experiments and the experimental procedure are described. The first four experiments are then described in order. These experiments collectively evaluate the effects of varying cutting load, cutting speed, and tool geometry. Emphasis is placed on tool wear, resultant groove cross-sectional geometry, burr height, variations in groove depth over the course of a cut, and chip morphology. Next, a fifth experiment is described, which is used to evaluate how close together parallel rectangular grooves can be cut while maintaining control of the dimensions of the resultant features. Lastly, a sixth experiment is described where grooves are cut that intersect each other in order to evaluate the ability to cutting complex surface patterns.

Chapter 7 discusses the development of a finite element model of the micro-groove cutting process that was experimentally evaluated in Chapter 6. The chapter starts by describing the capabilities that the model must posses in order to properly represent the process. Then the overall modeling approach is discussed. Next, acquisition of workpiece material properties is described. This is followed by a discussion of how to

model the contact between the tool and workpiece, how to model tool and workpiece geometry, and what boundary conditions to use during simulations. A study in which simulation parameters are varied in order to calibrate the model using experimental data follows. Model results are also compared to experiments for validation purposes.

In chapter 8, the model described in Chapter 7 is used to examine micro-groove cutting in detail. First, the design of simulation experiments is discussed. Next, cutting forces, chip flow, and stress-strain states present during steady-state cutting at the symmetry plane of a cut are evaluated when cutting using three different depths of cut and two different rake angles. Out-of-cutting plane effects present during steady-state cutting are then evaluated. This includes a discussion of out-of-cutting plane workpiece material flow, side burr formation, and separation of a chip from a workpiece. Next, the potential for the delamination of a thin film being cut is examined. Exit burr formation is then discussed in detail and methods of potentially reducing exit burr size are presented.

Chapter 9 provides a brief summary of the work described in this thesis and gives several conclusions that are based on the completed work. Recommended areas of future work are then outlined, which should be addressed in order to render the developed micro-groove cutting process commercially viable.

# Chapter 2

# Literature Review

The previous chapter outlined the importance of micro-manufacturing processes capable of producing long micro-grooves, other than conventional deposition, pattern and etch-based processes. Additionally, several criteria that such processes should satisfy were established.

This chapter reviews research into the development of such non-photolithography-based processes that can be used to form micro-grooves with widths of 50 μm or less. These processes can be based on application of thermal energy to a workpiece, induced electrochemical dissolution of a workpiece, or mechanical material removal. Material removal processes based on the application of thermal energy include laser scribing and micro-electrical discharge machining (μ-EDM). A material removal processes based on electrochemical dissolution of a workpiece is micro-electrochemical machining (μ-ECM). Lastly, mechanical material removal processes suitable from micro-groove cutting include micro-endmilling, micro-fly cutting, micro-scale shaping / planing, and atomic force microscope (AFM) scribing.

In this chapter, each of these processes is described and both advantages and disadvantages associated with these processes are presented. Afterwards, via a summary and comparison of current processes capabilities, it is shown that there is currently an important subset of micro-groove features that cannot be readily fabricated using the currently available processes and that there is a need for a new process to fill this gap.

## 2.1 Laser Scribing-Based Micro-Groove Cutting

### 2.1.1 Process Description

Laser scribing can be used to cut grooves in a wide range of materials at fairly high speeds. In laser scribing, material is removed via the interaction between focused laser light and a workpiece surface. Material removal can be accomplished either through a pyrolithic process involving a rapid thermal cycle of localized heating, melting, and vaporization or through a photolithic process involving localized breaking of chemical bonds in the workpiece material [46]. A photolithic process usually occurs when cutting polymers with ultraviolet wavelength lasers, and a pyrolithic process occurs when laser cutting most other materials [46].

Lasers can be grouped into two types: continuous and pulsed. Continuous lasers generate a beam with time-invariant power and are unsuitable for micro-scale machining because thermal damage will occur around laser processed regions and prohibit the formation of sharp structures [2]. Pulsed lasers rapidly generate a series of brief laser pulses that tend to have a higher peak power that the constant power of a comparable continuous laser. When pulsed lasers are used for cutting, the length and power of the laser pulses has a significant effect on the cutting action.

When the laser pulse length is on the order of nanoseconds, the electrons associated with the atoms that make up the workpiece surface absorb the laser energy, the absorbed energy is transferred to the crystal lattice of the workpiece material, and heat conducts into the workpiece. As a result, a small portion of the workpiece will first heat to its melting point and then vaporize somewhat, which results in droplets of resolidified material and craters around the machining area [46]. With picosecond pulse times,

however, there is not enough time for the heat to conduct very far into the workpiece before it is carried away via ejected material. As a result, melting of the workpiece only occurs up to an extremely shallow depth, which results in higher precision [46]. Lastly, with femtosecond pulse times, there is not enough time for heat to transfer from the electrons to the lattice and hence all energy is stored in a thin surface layer that directly evaporates without any melting occurring, which results in very high-precision ablation [46]. However, outside of a laboratory setting, femtosecond lasers are not readily used [46], and hence both a melt pool and ridges formed around the melt zone due to resolidification of debris are often present.

In addition to laser pulse time, factors that affect final groove geometry and quality include workpiece material properties, workpiece surface conditions, laser wavelength, laser power, timing of the laser pulses, speed the laser is scanned along the workpiece, how the beam is focused, and the pressure of any assist-gas. All of these parameters must be selected correctly in order to cut grooves of acceptable quality that have a desired geometry, which can complicate the use of laser scribing as a general purpose groove cutting process.

In particular, factors such as the timing of the laser pulses and material properties determine how heat flows through a workpiece during cutting. The amount of energy that a given spot on a workpiece is exposed to depends on the how much energy is contained in each pulse, how focused the beam is, how frequent the pulses are, and how fast the laser is scanned along the workpiece. Ideally the other parameters are adjusted to allow the speed parameter to be as high as possible while achieving a desired groove geometry. However, if the cutting speed is too high for a given pulse frequency, ridges

can be formed at the bottom of the resultant groove, which can increase surface roughness [2]. Hence, cutting speeds reported in the literature have varied greatly, between 24 mm/min for glass in one reported case [47] and 18,000 mm/min for silicon in another case [1].

### 2.1.2 Laser Scribed Groove Characteristics

One of the major advantages of laser scribing is the ability to quickly cut grooves in a wide range of materials, with different mechanical properties, that do not need to be electrically conductive. Materials reported to have been cut in the literature include polymers, glasses, metals, ceramics, crystals, and amorphous materials. Polymers that have been cut include polycarbonate, polyester, polyethylene, Plexiglas [46], and benzo-cycle-butene resin [48]. Glasses that have been cut include Corning microscope slide material [47], commercial Vitrocom S-105 [47], doped silica [47], and fused silica capillary fibers [47]. Metals that have been cut include stainless steel [2, 49], tungsten [2, 49], nickel-base alloys [49], copper [49], platinum [50], aluminum [50, 51], nickel [2], molybdenum [51], and gold [51]. Ceramics that have been cut include aluminum oxide [49], aluminum nitride ceramic [49], sapphire [2, 49], zirconium dioxide [50, 51], and aluminum titanate ceramic [52]. Lastly, some other materials cut include silicon [2], silicon dioxide [1], lithium-niobate [2], diamond-like carbon [2], and tin dioxide [51].

Laser scribing also allows micro-grooves with a few different cross-sectional shapes to be created. The cross-sections that have been achieved in the literature are v-shaped, trapezoidal, and round bottomed with sloped sidewalls. V-shaped grooves can be cut using a single pass of a laser beam focused down to a small spot under certain cutting conditions and can be very well defined, as shown in Fig. 2.1A. Trapezoidal grooves can

be achieved by using either a larger spot size and a single pass of a laser [52, 53] or by repeatedly passing a laser with a small spot size over a groove in a raster pattern that results in a wider flat bottomed groove like the one shown in Fig. 2.1B [1]. Round bottomed grooves can result from using a small spot size but different machining conditions than those used to produce v-shaped grooves [47].

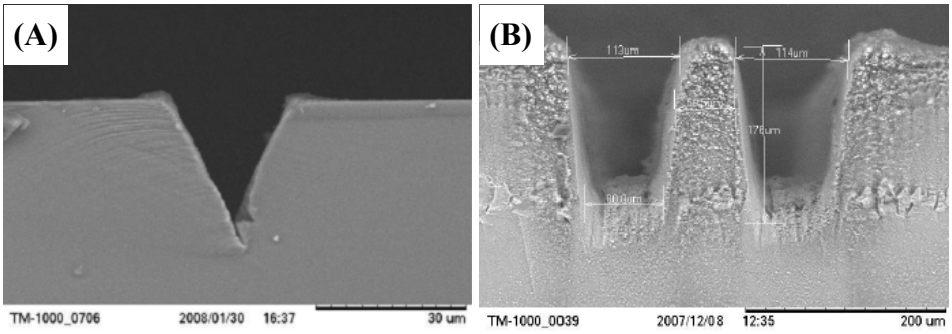


Figure 2.1: V-shaped (A) and trapezoidal (B) grooves cut in silicon [1]

In the literature, laser scribing has not been used to cut grooves smaller than several microns wide. This may well be because the smallest laser spot sizes available have been limited to no less than a couple microns and ultimate groove width tends to be a few microns larger than the spot size. As an example, some of the narrow grooves reported to have been cut in various materials are as follows: The groove in Fig. 2.2A is 21 μm wide and was cut in stainless steel using a 10 kW peak power laser that was focused down to a 11 μm diameter spot, that delivered 2 nanosecond pulses at a rate of 10 kHz, and that was scanned at 600 mm/min. Also, as shown in Fig. 2.2B, grooves as narrow as 18.5 μm wide have been cut in nickel use similar machining conditions [2]. Even narrower grooves 7-8 μm wide and a 12 μm wide have been reported to have been cut in lithium niobate and sapphire, respectively, using a 10 kW peak power laser that delivered 2 nanosecond pulses at a rate of 3 kHz while scanning at 180 mm/min and

while focused to spot 4 μm in diameter [2]. Lastly, grooves as narrow as 6.3 μm have been laser scribed in glass [47]. Therefore, the limitations on groove shape and minimum groove width limit the usefulness of laser scribing for micro-groove cutting.

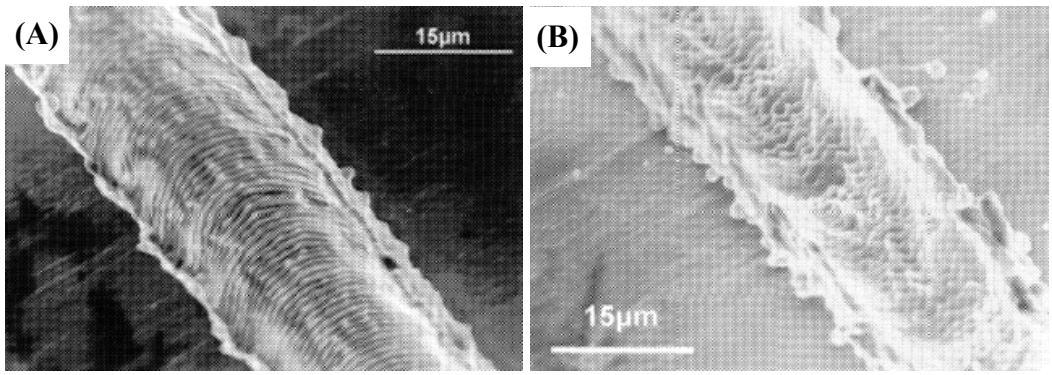


Figure 2.2: Grooves cut in stainless steel (A) and nickel (B) [2]

## 2.2 Micro-Electrical Discharge Machining (μ-EDM)

### 2.2.1 Process Description

Micro-electrical discharge machining (μ-EDM) is a machining process that enables precise amounts of material to be removed from an electrically-conductive workpiece regardless of the strength or hardness of the material. During μ-EDM the forces applied to the workpiece are negligible and hence extremely delicate parts can be machined. Also, burr formation does not occur like with many mechanical material removal processes. However, some of the removed material can redeposit around machined features under some cutting conditions. Also, non-conductive workpieces generally cannot be cut with μ-EDM with the exception of thin non-conductive films on top of a conductive substrate.

In both macro-scale EDM and μ-EDM, the tool and workpiece act as electrodes that are submerged in a suitably chosen dielectric fluid. When the tool and workpiece are

close enough to each other, they are oppositely charged with sufficient voltage to achieve dielectric breakdown of the fluid in the gap between them. When the resultant current arcs between the electrodes, melting and vaporization of material on both the tool and workpiece surface occurs [54]. Following the electrical discharge, the plasma column formed between the tool and workpiece collapses. It is generally believed that shockwaves, electromagnetic forces, and electrostatic forces generated from the plasma column collapse cause the ejection of molten material from the tool and workpiece [55]. This process is repeated many times over the course of machining and the resultant debris is generally evacuated from the gap between the tool and workpiece via circulation of the dielectric fluid.

In μ-EDM, the shape of the tool electrode has a large effect on the shape of the features produced. In order to produce micro-grooves, there are four basic types of tool electrode shapes that have been investigated by several researchers: pin electrodes [3, 56, 57], disk electrodes [4, 58], foil electrodes [5, 55, 59], and die electrodes [6].

### 2.2.2 μ-EDM Pin Electrode

The simplest μ-EDM tool electrode that can be used for groove cutting is a pin with a diameter slightly smaller than the desired groove width. To create a groove, the electrode is moved through the workpiece, along a trajectory that describes the groove shape, at a rate that maintains a constant gap between the tool and material to be removed. This technique has the advantage of allowing the creation of a wide range of groove geometries but can be very slow [4]. For instance, sinking a pin electrode with a diameter of 55 μm into a 304 stainless steel, which does not even fully form a groove, has been done at a rate of only 1.302 mm/min when a deionized water dielectric fluid was

used [54]. Also, a similar sinking operation with a 33 μm diameter electrode and kerosene as the dielectric fluid could only be performed at 0.0264 mm/min when a 17-7PH stainless steel workpiece was used [54].

However, despite its limitations, groove cutting using a pin electrode has been investigated as a means of manufacturing masks for photolithography. For instance, photomasks have been fabricated that consist of a 120 nm thick chromium film deposited on borosilicate glass, which include grooves in the chromium that are 200 μm long, 22 μm wide, and 120 nm deep that were cut using a 20 μm diameter pin electrode [3]. Such a groove is shown in Fig. 2.3. Additionally, features such intercepting 40 μm wide, 100 μm deep, and 300 μm long slots have been machined using a pin electrode [54].

Material removal rate can also be increased by rotating the pin electrode during machining, but this also increases tool wear and surface roughness. For example, in one study the use of a rotating electrode increased the material removal rate by about 50% while also increasing tool wear by about 60% and increasing surface roughness by about 45% [57]. However, even this increase in cutting speed is not enough to render cutting with a pin electrode time efficient.

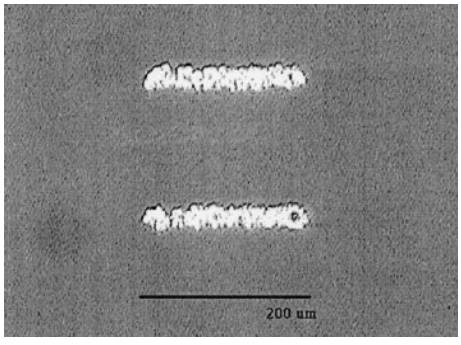


Figure 2.3: μ-EDM grooves cut with a pin electrode as part of a photomask [3]

## 2.2.3 μ-EDM Disk Electrode

Material removal rates can be increased by using a rotating disk-shaped electrode, which is suitable for cutting straight grooves only, and the use of this type of electrode has been referred to as both rotating disk EDM [58] and electrical discharge grinding (EDG) [54]. The principle of operation is that a rotating disk, which may only be tens of microns thick and tens of millimeters in diameter, cuts via electrical discharges between the edge of the disk and a workpiece, as shown in Fig. 2.4A. Since the rotating disk electrode has a greater area of near contact with a workpiece, more material can be removed per electrical discharge. Also, the disk rotation can help remove debris from the gap. Debris removal can be further enhanced by mounting the workpiece upside-down and cutting from beneath it so that gravity helps remove debris [58].

For example, using a rotating electrode with a thickness of 25 μm, the channels shown in Fig. 2.4B where cut, which are about 50 μm wide. It has also been reported that EDG has been used to cut 60 mm long, 60 μm wide, and 900 μm deep channels in stainless steel [54].

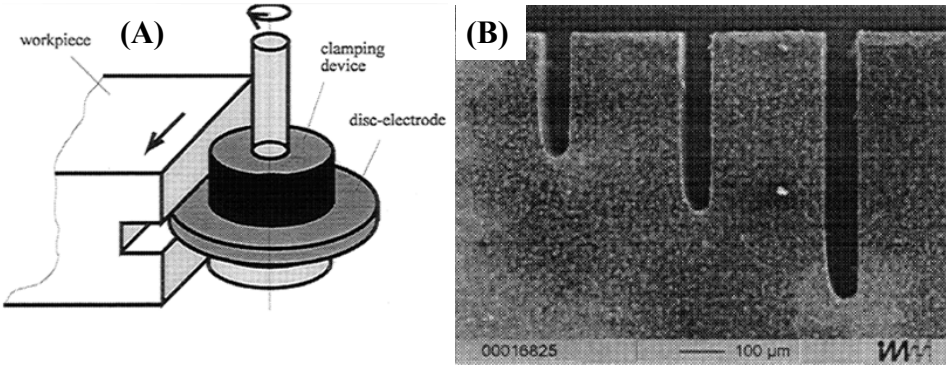


Figure 2.4: EDG (A) and channels cut via EDG (B) [4]

### 2.2.4 μ-EDM Foil Electrode

A foil tool electrode can be used to achieve even higher material removal rates, and consists of a piece of foil made of a material like as stainless steel as thin a 10 μm. The edge of the foil electrode is sunk into a workpiece, while μ-EDM is occurring in order to cut a groove, as shown in Fig. 2.5A [5], and hence an entire groove can be cut via a single operation, although the material removal rate is still fairly slow. The grooves can be either straight, if a flat piece of foil is used, or curved if a bent piece of foil is used [59]. Also, removal of debris from the gap can be facilitated by mounting the workpiece upside-down and cutting from below, which allows debris removal to be aided by gravity [55]. This in turn permits grooves as narrow as twice the foil thickness to be cut [55].

Stainless steel foil electrodes that are 10 μm thick have been used to successfully cut 50 μm wide, 7 mm long, and 7 – 69 μm deep grooves in brass, although variations in depth over successive grooves due to tool wear were significant [5]. An image of some of these grooves is shown in Fig. 2.5B. Under different machining conditions, grooves with widths a small as 34 μm with a depth of 53 μm have been machined [59], and groove widths as small as 25 μm can be achieved [55]. The surface roughness of such grooves tends to be 1 – 3 μm Ra and the rate at which the grooves can be cut is about 4.1 microns of groove depth per minute for a 20 mm long and 200 μm wide groove [55].

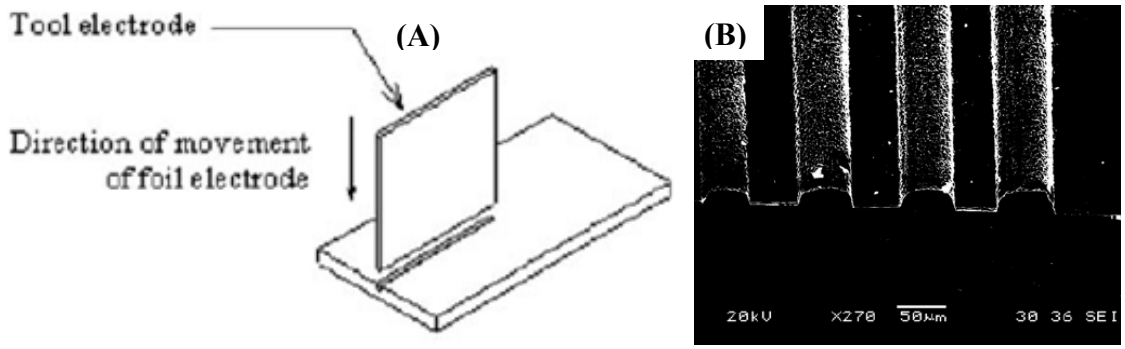


Figure 2.5: μ-EDM with foil electrode (A) and resultant grooves (B) [5]

## 2.2.5 μ-EDM Groove Cutting Die Electrode

The most efficient, but also complex, μ-EDM tool is a die consisting of a series of raised sections that correspond to desired grooves to be cut into a workpiece via one μ-EDM tool sinking operation. Hence, the use of such an electrode can greatly increase the material removal rate. However, the cost is that complicated tools must be fabricated, which must be carried out via some process that is inexpensive and repeatable since the tool electrode will wear out.

One way to make such a complicated tool is to use the LIGA (Lithographie Galvanoformung Abformung) processes. LIGA is a microfabrication process where a thick layer of radiation sensitive polymer, which has been coated onto a substrate, is selectively exposed to x-rays that break down the polymer in the irradiated areas so that the irradiated polymer can be removed to form deep trenches. Nickel is electroplated onto the coated substrate and forms a negative of the pattern present in the polymer. High-aspect ratio features, feature sizes of about a micron, form accuracies of less than a micron, and surface roughness of about 30 nm are achievable using LIGA [4].

LIGA fabricated electrodes can be used to machine structures as small as 10 μm with form accuracies of 1 μm [4]. Depending on the machining conditions and EDM-

technology used it is sometimes possible to get Ra values smaller than 0.1 μm and aspect ratios between 5 and 20 [4]. However, the LIGA process requires expensive specialized equipment to implement and is fairly slow.

For example, Figure 2.6A shows an electrode fabricated by UV-LIGA, a less expensive process similar to LIGA that makes use of ultraviolet radiation instead of x-rays but that has lower resolution. The raised portions of the electrode are 250 μm high, the electrode is μm 1340 thick, and the electrode took 72 hours to fabricate [6]. Figure 2.6B shows a series of 9.99 μm deep grooves cut in stainless steel using the electrode that have a surface roughness of 0.78 μm Ra, and Fig. 2.6C shows a magnified view of one of the grooves [6].

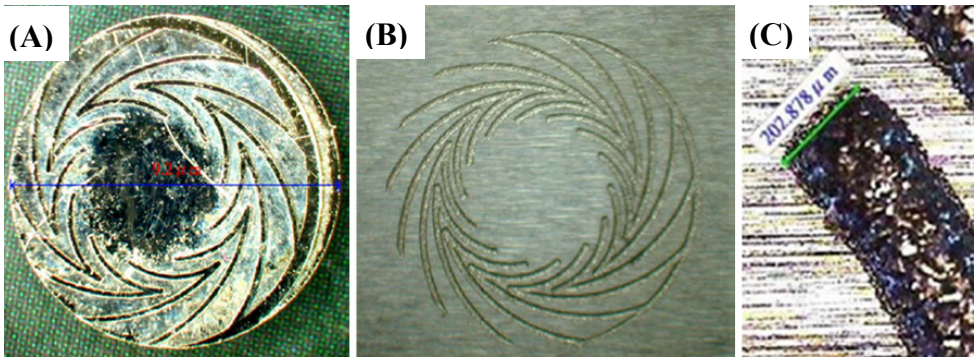


Figure 2.6: μ-EDM groove cutting electrode produced by UV-LIGA (A), features cut with the electrode (B), and a magnified view of a groove cut with the electrode (C) [6]

# 2.3 Micro-Electrochemical Machining (μ-ECM)

## 2.3.1 Overview

Electrochemical machining (ECM) is a process capable of cutting micro-scale features in electrically conductive materials regardless of the mechanical properties of the materials. This process also has the advantages of negligible tool wear, negligible cutting forces,

and smooth burr-free surface finish. However, dimensional control in commonly used wet ECM processes is very complicated, and the fabrication of extremely tiny features on the order of a few microns in size does not currently appear possible. More recently developed solid-state superionic stamping ECM processes mitigate these issues, but introduce additional process requirements [33, 42].

### 2.3.2 Wet (μ-ECM) Processes

Conventional wet ECM is the controlled dissolution of portions of a workpiece surface via an electrochemical reaction. In this reaction, either continuous or pulsed voltage is applied across a tool and workpiece where the tool is a positively changed anode and the workpiece is a negatively charged cathode. The tool and workpiece are separated by a small gap through which an electrolyte flows. The voltage induces a reaction in which the workpiece dissolves in some region around the tool while the tool does not dissolve, and reaction byproducts are carried away by the electrolyte. The amount and shape of the material removed depends on the tool position, the tool shape, the amount of voltage applied, the timing of the voltage if it is pulsed, and the electrolyte.

In micro-electrochemical machining (μ-ECM), the major challenge is insuring that material removal is localized, i.e., attempts to machine a narrow groove on one part of the workpiece do not cause changes to other parts of the workpiece. One means of limiting the machined region is to cover the areas that are not to be machined with a protective mask that can be applied using conventional photolithography techniques [60]. Due to the focus of this chapter, mask-based techniques are not further elaborated on. Other means of achieving localized workpiece dissolution involve control of process parameters and careful selection of tool shapes.

To achieve localized workpiece dissolution in μ-ECM, it is desirable to use a much smaller gap between the tool and workpiece than would be suitable in macro-scale ECM [61]. However, if a constant voltage is applied across the tool and workpiece, as is done at the macro-scale, a small gap will result in unwanted electrical discharges between the tool and workpiece. This can be avoided by using a series of short voltage pulses that are each 5 – 5000 nanoseconds long [61]. In such a case, the gap between the tool and workpiece can be reduced to about 5 μm, which is a good value for micromachining [62]. When using pulsed voltage, dissolution of the workpiece only occurs during the voltage pulse and dissolution products such as sludge, gas bubbles, and heat can be flushed from the gap when no voltage is applied. The use of pulsed voltage results in improvements in dimensional controllability, shaping accuracy, process stability, and allows for simplification of tool design [61].

There are several tool configurations that can be used to cut micro-grooves. One method for cutting long grooves that extend from one end of a flat surface to the other end is to use a wire tool, as shown in Fig. 2.7A [7]. For example, as shown in Fig. 2.7B, a 10 μm diameter tungsten wire can be used to cut long grooves in 304 stainless steel as narrow as about 35 μm, when using 6.5 volt pulses with a pulse time between 200 and 300 nanoseconds, a period of 7 microseconds, and through use of a 0.1 M sulfuric acid solution electrolyte [7].

Alternatively, custom electrodes can be fabricated that can be sunk into a workpiece in order to create a set of grooves. For example, Fig. 2.8 shows a groove cut in stainless steel using a 40 μm wide electrode that was shaped via electrical discharge machining [8]. It is also possible to use tool electrodes with a complicated shape that

allows a series of grooves to be cut in one electrode sinking operation, similar to how the LIGA fabricated electrodes described in the previous section were used. In such operations, the introduction of low frequency and amplitude tool vibrations along the direction of tool travel can improve flushing conditions and increase shape accuracy [63].

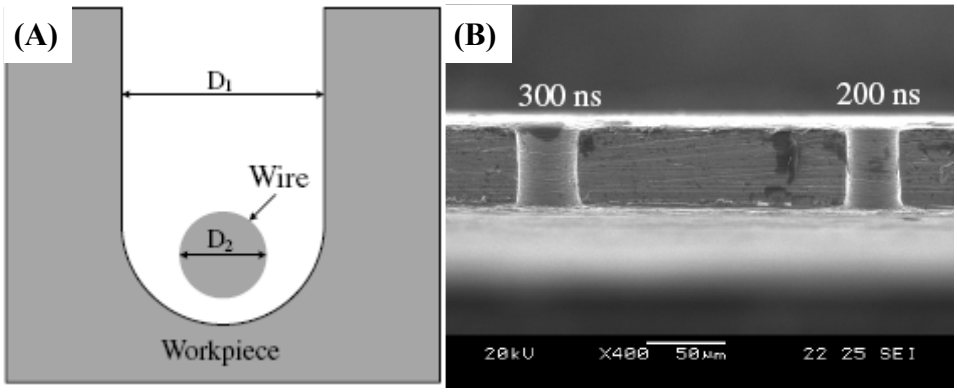


Figure 2.7: Wire μ-ECM tool electrode (A) and features cut using a 10 μm wire while using two different voltage pulse lengths [7]

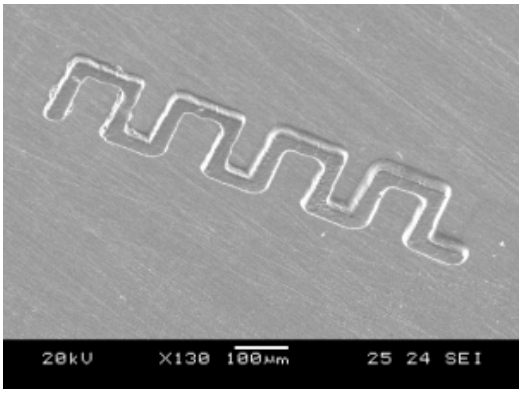


Figure 2.8: Grooves cut in stainless steel via repeated μ-ECM sinking operations with a specially shaped electrode [8]

However, issues associated with wet μ-ECM limit its usefulness in cutting microgrooves. Specifically, a groove will be wider than the tool used to cut it, and a groove will not have exactly the same shape as the corresponding tool. For example, based off features machined in the literature [7, 8, 62] using tools as small as 10 μm, it

appears that the resultant grooves will usually be no less than about 6 μm wider than the electrode, which prevents arbitrary narrow grooves from being cut. It has also been shown that tools with sharp corners will cut features that are larger than the tool and have rounded corners [61]. Hence, arbitrary groove cross-sections are very difficult to achieve.

### 2.3.3 Solid-State Superionic Stamping μ-ECM Process

Solid-state superionic stamping μ-ECM uses a patterned solid electrolyte or superionic conductor as a stamp and etches a metallic film via an electrochemical reaction [42]. That is, the electrolyte, e.g. silver sulfide, is solid instead of the liquid used with conventional wet ECM processes. During etching, the stamp, which must contain the pattern to be etched, is placed into physical contact with a workpiece. Etching occurs on application of an electrical bias with the workpiece substrate as the anode and a metallic electrode at the back of the stamp as a cathode [42].

This process has been used to produce features down to 50 nm on silver films of thicknesses ranging from 50 nm to 500 nm [42]. Etching of copper with a resolution of 80 nm has also been demonstrated [33]. Therefore, unlike conventional wet μ-ECM, groove widths narrow enough to meet the groove width process requirement described Chapter 1 are possible with this process. However, since direct physical contact between the stamp and workpiece is required, the shape of the stamp and workpiece must be very well matched. This renders it difficult to cut into rough or curved workpiece surfaces. Also, as currently implemented, the stamp must itself be patterned and hence direct CNC control of the patterns cut cannot be accomplished like with processes where the pattern of grooves cut is dependent on the trajectory of a tool.

## 2.4 Micro-Endmilling

### 2.4.1 Process Description

Micro-endmilling is a versatile mechanical material removal process capable of cutting a wide range of structures in a wide range of materials. Using this process, grooves with nearly vertical sidewalls can be cut at speeds up to several hundred millimeters per minute and at depths between a few microns and a few tens of microns. However, viable micro-endmills capable of cutting grooves with widths of 50 μm or less are relatively new. Up until 2004 the smallest commercially available micro-endmills had a diameter of 50 μm [12], and today the smallest viable commercially available micro-endmills are 25 μm in diameter [9].

Currently, development of micro-endmill designs with diameters of 50 μm or less, development of processes to produce these tools, and examination of the micro-endmilling process at the micro-scale are areas of active research [11, 12, 13, 30, 64, 65, 66]. Additionally, suitable machine tools must be employed in order to effectively perform micro-endmilling, and the development of such machine tools has also been of interest to several researchers [38, 67, 68].

### 2.4.2 Machine Tools Suitable for Micro-Endmilling

Micro-endmilling has traditionally been performed on large, stiff, and expensive high-precision machine tools. More recently, there has been considerable research aimed at developing small relatively inexpensive micro-scale machine tools (mMTs) suitable for micro-machining operations such as micro-endmilling [38, 67, 68]. This research has resulted in the development in lower cost commercially available machine tools [69].

The main requirements for mMTs are that they must be stiff, they must be highly repeatable and hence able to achieve high accuracies via calibration, and they must be capable of achieving accelerations one to two orders of magnitude higher than are necessary during macro-scale machining. The last requirement exists because of cutting mechanisms unique to micro-endmilling [68].

### 2.4.3 Micro-Endmill Design

A significant challenge when micro-endmilling features with sizes of 50 μm or less is the design and fabrication of suitable micro-endmills. One commercially available micro-endmill geometry, shown in Fig. 2.9A, is the scaled down geometry of a conventional macro-scale endmill, with two helical flutes, which is fabricated using precision diamond grinding of tungsten carbide. Viable endmills with this geometry are commercially available at sizes as small as 25 μm in diameter [9]. However, subsurface damage, which can result from grinding, lowers the strength of ground endmills [11], and the grinding processes applies forces to a micro-endmill that can break it during fabrication unless great care taken [64]. Also, the helical grooves cut in the tungsten carbide blank, in order to form conventionally shaped endmills, reduce tool strength and stiffness [12], which are already very small due to unfavorable scaling laws.

Therefore, much of the research into micro-endmills with a diameter of 50 μm of less has focused on the use of straight fluted endmills. Figures 2.9B – 2.9H show several straight flute designs that have been fabricated and tested by various researchers [10 - 13] that are representative of what has been examined in the broader literature. Figure 2.9B and Fig. 2.9G show single-flute endmills, where the former is fabricated using fewer cuts but the latter affords a greater relief angle on the cutting edge. Figures 2.9C, 2.9D, 2.9F,

and 2.9H show several two-flute designs where Fig. 2.9C shows the simplest two-flute design and Fig. 2.9D shows the second simplest design, which is more suitable for plunging due to the end relief on the tool. The design shown in Fig. 2.9F affords the most cutting edge relief out of the two-flute designs shown, and the design in Fig. 2.9H affords a zero degree rake angle, which is more positive than in the other designs. Lastly, Fig. 2.9I shows an endmill cut out of sintered polycrystalline diamond that cuts not through the use of a well defined cutting edge but rather through the action of the many micro-asperities.

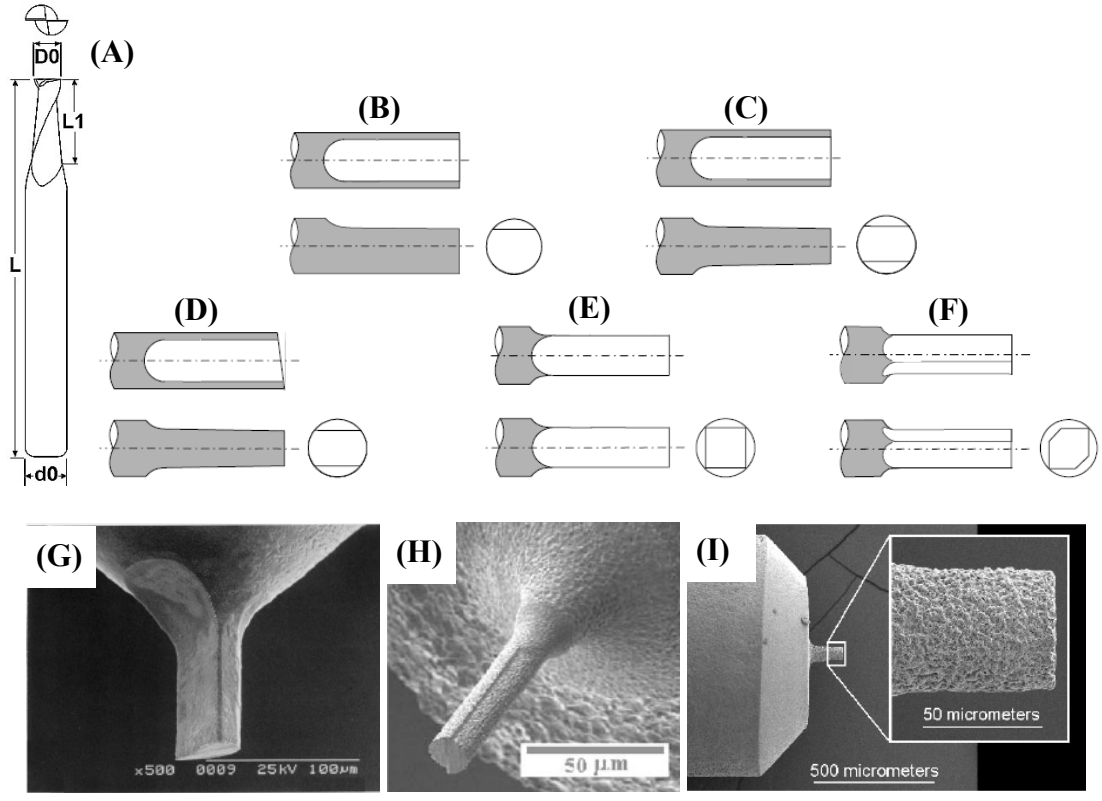


Figure 2.9: Various types of micro-scale endmills (A) [9], (B-F) [10], (G) [11], (H) [12], and (I) [13]

A comparative study involving all of the designs explored in the literature is not available. However, it has been reported that out of the five designs shown in Figs. 2.9B

– 2.9F, the best cutting performance with achieved using the design in Fig. 2.9F when cutting duralumin, an age-hardening aluminum alloy [10]. Nearly burr-free precision machining of electroless nickel plating was achieved using the tool shown in Fig. 2.9G [11]. The tool shown in Fig. 2.9H achieved good results when cutting PMMA when the aspect ratio of the tool was low, but tended to deflect significantly when the tool was fabricated with a high aspect ratio, which limited the potential depth of cut [12]. Lastly, the fluteless design in Fig. 2.9G did a good job of cutting smooth channels in ultra low expansion glass [13].

### 2.4.4 Micro-Endmill Fabrication

Fabrication of micro-endmills has been accomplished via diamond grinding [10, 64], focused ion beam machining [30, 70 - 73], wire electrical discharge grinding [11, 13, 66], and a combination of both electrical discharge grinding and focused ion beam machining [12]. Diamond grinding affords fast material removal rates and can be performed using relatively inexpensive equipment. However, there are disadvantages associated with diamond grinding, which include subsurface damage [11], potential for tool breakage [64], and limitations on the smallest feature sizes that can be readily fabricated.

Focused ion beam (FIB) machining permits tools to be cut out of any material regardless of hardness and can be used to achieve cutting edge radii as small as at least 100 nm [3], and it applies no forces to the tool that might break it during fabrication. However, FIB fabrication of micro-endmills is also very slow. For instance, a 25 μm diameter tool blank, produced via grinding and polishing, may require between one and three hours of FIB machining time in order to produce to useable tool [30, 73].

Alternatively, μ-EDM can be used to fabricate tools made of tungsten carbide [66] and polycrystalline diamond that consists of sintered diamond grains in a cobalt matrix [13]. This fabrication method can be considerably faster than FIB machining while still minimizing the forces that the tool is subjected. However, the surface finish and cutting edge quality that results is not very good [66]. However, a secondary FIB machining operation can be used to sharpen such a tool [64].

### 2.4.5 Micro-Endmilling Process Characteristics

A variety of materials have been reported to have been successfully machined using micro-endmills with diameters of 50 μm or less. Metals including brass [64], 4340 steel [30], aluminum 6061-T6 [66], aluminum 6061-T4 [30], duralumin [10], and electroless nickel phosphorous plating [11] have been cut with tungsten carbide tools. Aluminum 6061-T4 and Brass have also been cut with high-speed steel tools [30]. Plastics such as polymethyl methacrylate (PMMA) have been cut with both high-speed steel and tungsten carbide tools [12, 30, 70 - 73]. Lastly, tungsten carbide, silicon [65], and soda lime glass [13] have been cut with sintered polycrystalline diamond tools.

The smallest diameter functional endmill reported in the literature had a diameter of 20 μm and was used to cut PMMA [12]. The widths of grooves cut with micro-endmills tend to be between the tool diameter and 3 μm more than the tool diameter [12, 71]. Grooves with nearly vertical sidewalls and depths of tens of microns have been achieved using multiple tool passes. Also, reported surface finishes tended to be better than 200 nm Ra [10, 12, 13, 30, 66, 70, 71]. Claims about tool life in the literature included 6 hours of continuous machining in Al 6061-T6 with a 21.7 μm diameter tool

without tool fracture [30], and cutting a distance of 1000 mm in electroless nickel phosphorus platting without appreciable tool wear [11].

It should be noted, however, that there are several issues associated with micro-endmilling that complicate the process. These issues include: deflection and breakage of the endmills, runout, and burr formation. Deflection and breakage of the endmills is problematic because stiffness reduces rapidly with a reduction in endmill diameter. As a result, noticeable bending can occur with cutting with smaller diameter endmills, which can result in significant dimensional errors [12] and limit the smallest possible tool diameter. Runout due to both spindle runout and tool geometrical errors can cause uneven chiploads to be taken by different flutes of the tool, which can induce vibrations in the tool that degrade surface finish [74]. Runout can also cause rubbing between non-cutting portions of a tool and workpiece, which can generate enough forces on the tool to cause tool breakage [12]. Lastly, burr formation can greatly reduce the quality of grooves cut in some materials, and burr reduction strategies have been an area of active research [10, 64].

## 2.5 Micro-Fly Cutting

### 2.5.1 Process Description

Micro-fly cutting is a mechanical material removal process capable of producing patterns of long straight grooves. In micro-fly cutting, a single-point diamond tool is fixed to a rotating spindle so that the tool engages a workpiece, produces a chip, and exits the workpiece once per spindle revolution while the workpieces is traversed underneath the tool to produce a groove. As shown in Fig. 2.10A, the axis of rotation of the spindle can be oriented such that it lies in a plane parallel to a workpiece surface so that the

profile of the diamond tool will be reproduced in the workpiece. Alternatively, the spindle can be mounted at a 45° angle relative to the workpiece, as shown in Fig. 2.10B, so that only the corner of a diamond tool does any cutting, which allows for the production of v-shaped grooves without the need for a tool with a complicated geometry [14].

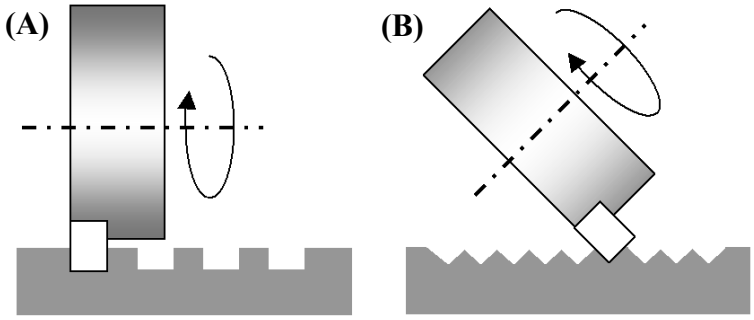


Figure 2.10: Micro-fly cutting of vertical sidewall channels (A), and v-grooves (B)

## 2.5.2 Micro-Fly Cut Features

Several different types of grooves can be produced via micro-fly cutting. For instance, grooves with trapezoidal cross-sections can be cut in brass using a FANUC ROBOnanoUi machine [14]. These grooves, which are shown in Fig. 2.11A, have an opening angle of 3 degrees, a width of 20 μm, a pitch of 35 μm, and a depth of 100 μm. Grooves with v-shaped cross-sections have also been reported [14, 15, 17]. For example, Fig. 2.11B shows v-grooves with a 1 μm pitch and 0.5 μm depth that were cut in a oxygen free copper workpiece using the micro-fly cutting configuration shown in Fig. 2.10B, a cutting speed of 20,000 rpm, a workpiece feed rate of 20 mm/min, and a depth of cut between 2 – 10 μm over the course of the workpiece [15].

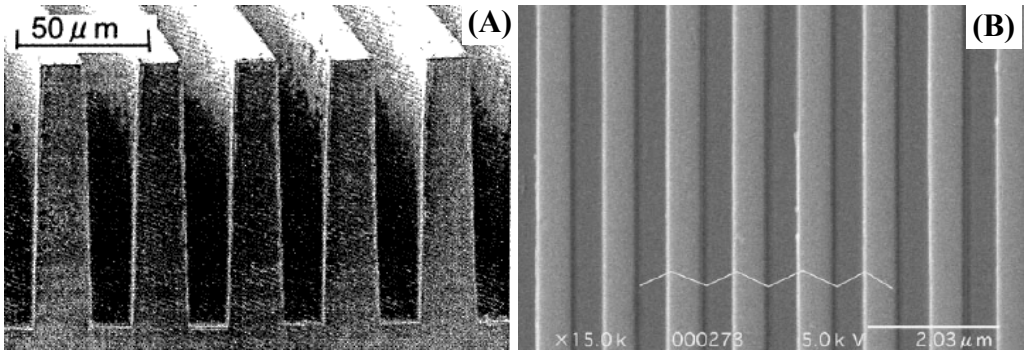


Figure 2.11: Trapezoidal grooves [14] (A), and v-grooves [15] (B) formed by micro-fly cutting

Micro-fly cutting has the limitation that all cuts must be in straight. However, by rotating and indexing a workpiece when the tool is retracted it is possible to combine many grooves in order to produce fairly complex repeating features. For instance, Fig. 2.12A shows part of an injection-molding die where 50 μm wide posts were formed via a series of perpendicular cuts [16], and Figs. 2.12B and 2.12C show arrays of micro-pyramids formed via series of non-perpendicular v-groove cuts.

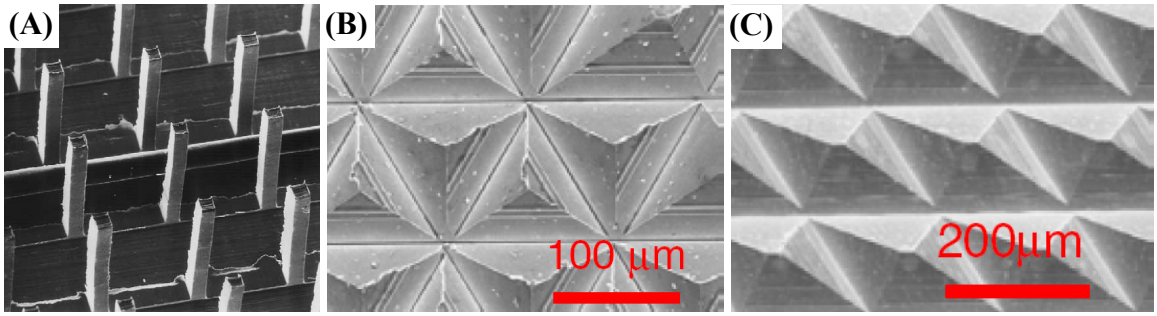


Figure 2.12: Posts [16] (A), 3-sided pyramids [17] (B), and 4-side pyramids [17] (C) formed by micro-fly cutting

## 2.5.3 Micro-Fly Cutting Process Characteristics

Workpiece materials that have been cut using micro-fly cutting include brass, copper, and nickel phosphorous electroless plating. Feedrates between 20 mm/min [15]

and 100 mm/min [17] have been reported, and devices such as a 12 mm diameter rotary encoder disk containing 32768 v-grooves have been fabricated in about 12 hours [15]. Groove widths as small as 1 μm for v-grooves [15] and 20 μm for trapezoidal grooves have also been reported [14]. Lastly, Surface finishes as good as 1 nm Ra has also been reported in some cases when machining copper [15].

Micro-fly cutting does, however, have several issues that reduce the usefulness of the process. One limitation imposed by the process is that, although v-grooves as narrow as 1 μm can be fabricated, grooves cannot follow a curvilinear path. Also, a highly rigid machine with high precision positioning capability is required in order to make consistent high quality cuts, which significantly drives up equipment costs. Wear over the course of many cuts, 32768 cuts in one study [15], can also be significant enough to require resharpening of the tool to avoid variations in groove geometry and temperature variations can affect groove depths over many cuts. Lastly, burr formation can be a significant issue in some cases.

Burr formation in micro-fly cutting has been a subject of some study [17, 80]. In micro-fly cutting, the single-point tool enters and then exists the workpiece once during each tool revolution, and hence exit burr formation is the predominant burr formation mode. These burrs tend to be larger when the workpiece material is more ductile due to chips not being as easily separated from the workpiece. Hence a better surface finish is achieved, for example, when cutting brass than when cutting copper [18]. Also, more significant burr formation occurs when the cutting tool has a large edge radius. For instance, when cutting v-grooves in brass with a cutter surface speed of 350 m/min, and a depth of 10 μm, and a tool with edge radius of 80 nm burr formation occurs. However,

when a tool edge with a 200 nm edge radius is used under the same conditions, significant burr formation occurs [18].

Another factor that has been found to have a significant effect on burr formation is the direction that the spindle is rotated relative to the direction of cut. As shown in Fig. 2.13 use of a down-cut, where the cutter moves in same direction as the workpiece feed when engaged with the workpiece, results in less burr formation than when cutting in the opposite direction [18].

Cutting speed has been found to have very little effect on burr formation [17]. However, uncut chip thickness has been found to have a significant effect on burr formation and should generally be minimized. For instance, for a test cut in brass at a cutter surface speed of 180 m/min, the height of the resultant burr is plotted in Fig. 2.14 for several uncut chip thicknesses [17]. As can been seen from the figure, burr formation is minimized when the undeformed chip thickness is minimized. Hence selection of an undeformed chip thickness during process planing has to be dependent on the acceptable amount of burr formation since reduction in uncut chip thickness also reduces material removal rate.

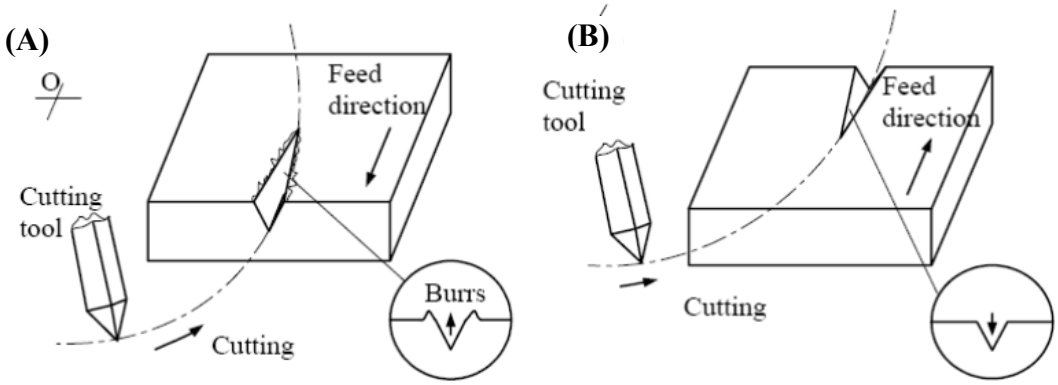


Figure 2.13: Effect of up-cut (A) and down-cut (B) on burr formation [18]

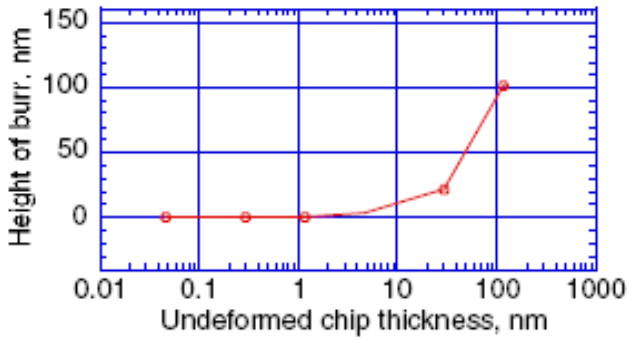


Figure 2.14: Effect of undeformed chip thickness on exit burr height [17]

# 2.6 Micro-Scale Shaping / Planing

## 2.6.1 Process Description

Micro-scale shaping is a mechanical material removal process suitable for producing arbitrary patterns of grooves that can have a wide variety of cross-sectional geometries. In micro-scale shaping a workpiece is held stationary, and a single point cutting tool attached to a xyz motion platform is moved into and through the workpiece in order to remove material in the form of chips. A similar process is micro-scale planing where the workpiece is moved and the cutting tool is held stationary. From a chip formation standpoint these two processes are sufficiently similar that they are treated together in this section.

Materials that have been cut include soft materials such as copper [14], electroless nickel phosphorous plating [21], and polycarbonate [19]. Also included are harder brittle materials that can be cut in a ductile mode at sufficiently small depths of cut such as gallium arsenide [43] and Pyrex glass [31].

Using micro-scale shaping, grooves can be formed that have a similar cross-section as the shaping tool, or larger features can be formed via multiple adjacent tool

passes. Tools are typically made of single crystal diamond [14, 21 - 23], but researchers have also investigated high-speed steel and micrograin tungsten carbide tools [20]. These tools can generally be categorized as either having a v-shaped rake face or arbitrarily shaped rake face. Tools with a v-shaped rake face are suitable for cutting v-shaped grooves and often have either a pyramidal or a flattened triangular geometry, where an example of the latter is shown in Fig. 2.15A. These tools can be fabricated via lapping [14]. Fabrication of tools with arbitrary rake face geometries requires a more involved process such as focused ion beam (FIB) machining. [20]. An example of a representative FIB machined micro-scale shaping tool is shown in Fig. 2.15B.

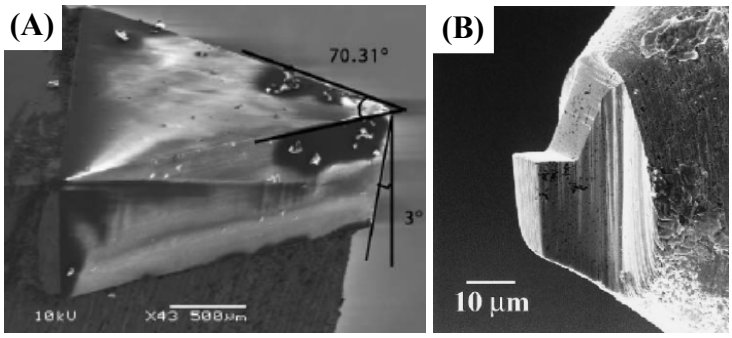


Figure 2.15: A micro-scale shaping tool with a v-shaped rake face (A) [19] and a rectangular shaped rake face (B) [20]

## 2.6.2 Cutting with Tools with a V-Shaped Rake Face

Several researchers have conducted micro-scale shaping experiments using single-crystal diamond tools with v-shaped rake faces [14, 19, 21]. For example, curvilinear v-shaped grooves with a pitch of 35 μm have been cut in oxygen free copper at a speed of 20 mm/min without significant burr formation in order to make a mold for a double-focused lens [14]. Other researches have cut microgroove and micropyramid arrays in electroless nickel phosphorus plating [21]. Additionally, one hundred micron

deep v-shaped grooves have been cut in polycarbonate and silicon for use as fiber optic positioning guides while using depths of cut per tool pass of 2 – 6 microns and cutting speeds between 15 and 85.8 mm/min [19]. During such tests it has been found that the combination of workpiece material, cutting speed, and rake angle has an important effect on performance in micro-scale shaping [19].

One of the issues involved with cutting v-shaped grooves is the nature of the chip flow resulting from the tool shape. That is, shearing occurs of both side edges of the rake face so material flows towards the center of the rake face. As shown in Fig. 2.16A, this results in the formation of a material stagnation region, which has been attributed to the formation of significant side burrs, as shown in Figure 2.16B [21]. One method to alleviate this problem is to first take a relatively deep rough cut in which significant burr formation occurs and then perform a second tool pass in which the depth of cut is only about one micron [21]. During this second cut, chip flow is as shown in Fig. 2.16C, and neither the material stagnation region nor the resulting side burr are present, as shown in Fig. 2.16D.

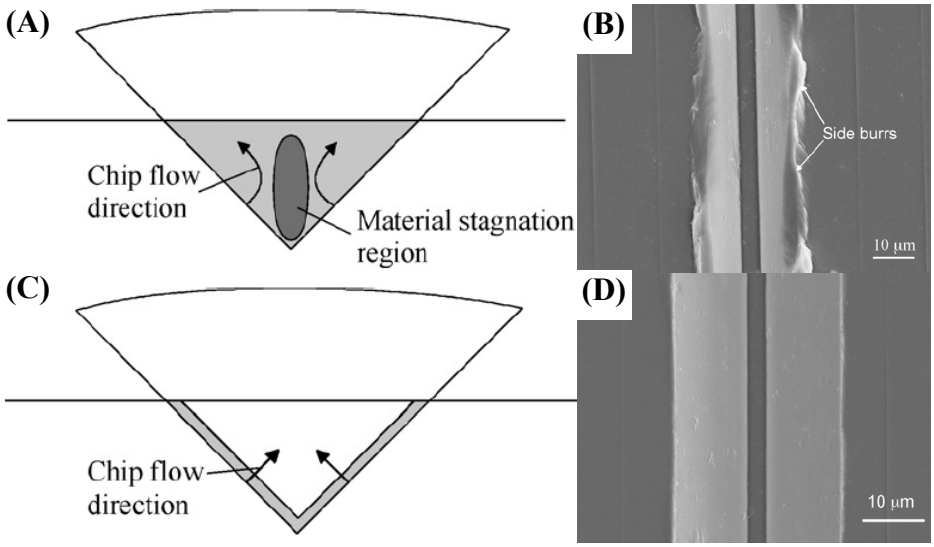


Figure 2.16: Chip flow using one tool pass (A-B) or two tool passes (C-D) [21]

## 2.6.3 Fabricating Tools with an Arbitrarily Shaped Rake Face

Micro-scale shaping tools with arbitrarily shaped rake faces can be fabricated using FIB machining. In this machining process, a stream of ions, often gallium ions, are accelerated towards a workpiece and remove material from the workpiece atom by atom via sputtering. This technique has been used to fabricate micro-scale shaping tools with widths as small as 10 μm [22] out of materials including C2 micrograin tungsten carbide, M42 high-speed steel [20], and single crystal diamond [23]. Furthermore, most other materials can be cut with this method.

Like macro-scale shaping tools, the tools reported to have been fabricated by FIB machining have a well defined rake face, side clearance faces, and an end clearance face [20, 22, 23]. The shapes of the rake face have varied from simple rectangular shapes, as seen in Fig. 2.17A, to more complicated shapes such as the split rectangular rake face shown in Fig. 2.17B or the double v-shaped rake face in Fig. 2.17C.

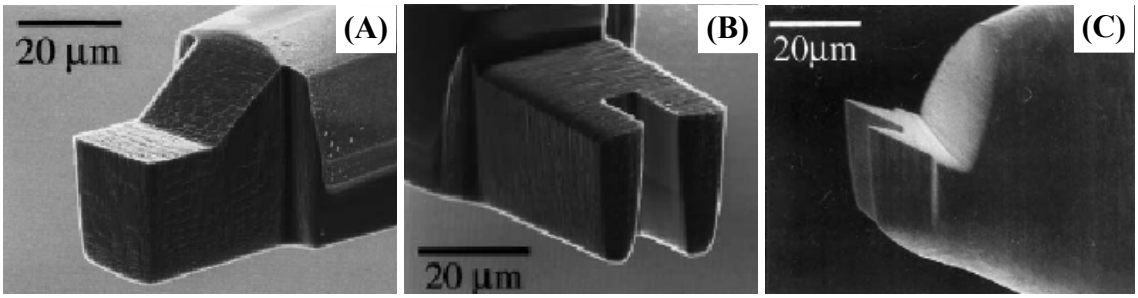


Figure 2.17: FIB machined micro-scale shaping tools with rectangular rake face (A) a split rectangular rake face (B), and a double v-shaped rake face (C) [22]

Adams et al. described a procedure for fabricating micro-scale shaping tools via FIB machining and describe some of the issues that arise [20]. In the described procedure, the tools are first ground to achieve as close to the net shape as possible without using FIB machining because grinding is a much faster material removal process.

Next, the resultant cylindrical blank is held in a rotary spindle inside a FIB machine, which is used to change the orientation of the tool blank relative to the ion beam. A series thru cuts are then performed with the tool blank, at different orientations in order to fabricate the tool, as shown in Fig. 2.18 [20].

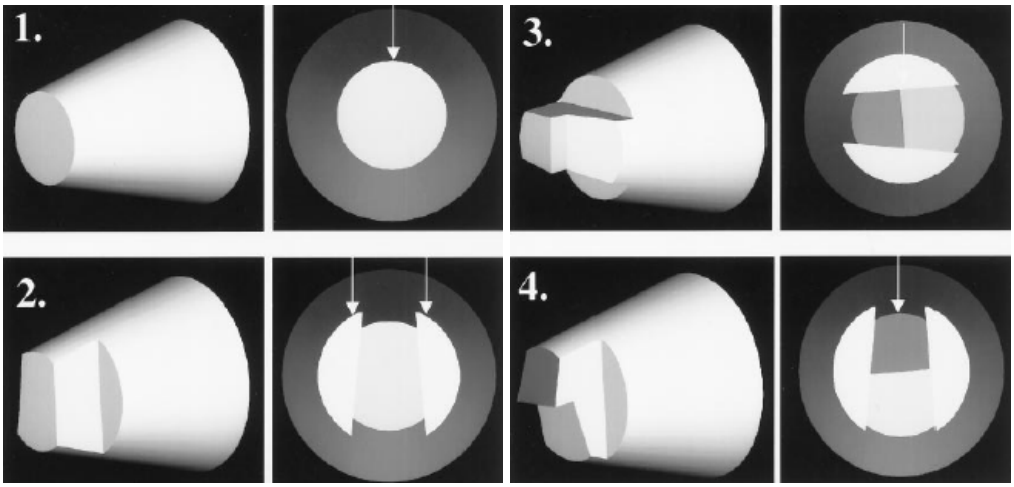


Figure 2.18: Micro-scale shaping tool formation procedure [20]

In order to produce a good tool via FIB machining it is necessary to take into account some characteristics of the FIB machining process. One noteworthy characteristic is that the ion beam is not an infinitely narrow line of ions but rather a spread of ions with a Gaussian distribution. This means that the edges of machined surfaces that face the beam tend to become rounded. Hence, some researchers have chosen to fabricate the cutting edge of their tools by cutting the rake face first and then cutting the intersecting end clearance face from behind so that the cutting edge is partially shielded from the ion distribution by the bulk of the tool, as shown in Fig. 2.18 [20, 22]. In this way the effect of the ion distribution on the quality of the cutting edge is reduced, and as a result edge radii between 0.4 and 0.04 μm have been achieved [20, 22].

Another characteristic of FIB machining is that the amount of material sputtered off a surface is a function of the angle of incidence between the beam and the surface. As a result, a taper is introduced when cutting features, i.e., when cutting a trench the top of the trench will be wider than the bottom. The angle of the taper is typically 2 – 4 degrees with respect to the ion beam [22]. Also, as shown in Fig. 2.18, it is possible to take advantage of this to achieve various relief angles [20].

### 2.6.4 Cutting with Tools with an Arbitrarily Shaped Rake Face

Using FIB fabricated micro-scale shaping tools, grooves have been cut in several workpiece materials. These materials have mostly been relatively soft and have included PMMA, Al 6061, brass [20], oxygen free copper, nickel phosphorous plating, and a micrograin aluminum alloy RSA-905 [23]. Groove depths between 4 and 10 μm have been investigated [20, 23]. Also, surface finishes between 0.11 and 0.25 μm Ra have been reported for aluminum and surface finishes between 0.17 and 0.29 μm Ra have been reported for brass at a cutting speed of 6.4 mm/min [20].

It has been found that there is a closer match between tool width and groove width when smaller depths of cut per tool pass, such as 2 μm, are used rather than larger depths of cut per tool pass, such as 5 μm [20]. It has also been found that large grained materials tend to have a larger variation in cutting forces over the course of a cut, compared to micrograin or amorphous materials, due to variations in crystallographic orientation [23]. Lastly, cutting tests performed using several workpiece materials have shown that the cutting mechanism in micro-scale shaping is very similar to macro-scale cutting, as shown in Fig. 2.19 [23].

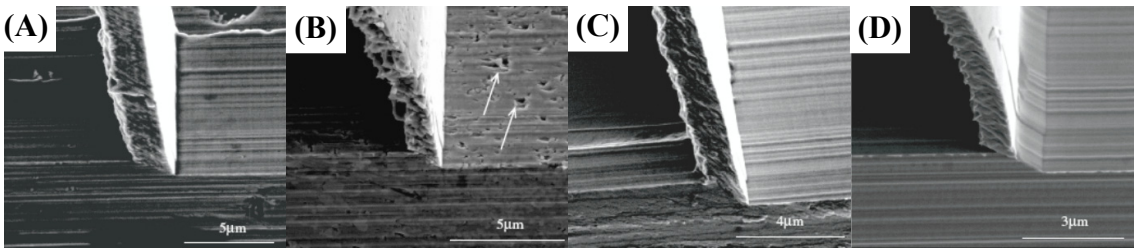


Figure 2.19: Chips generated during orthogonal machining of Al-6061 (A), RSA-905 (B), oxygen free copper (C), and nickel phosphorus plating (D) [23]

## 2.6.5 Load-Based Methods to Achieve Very Low Depths of Cut

V-grooves with fairly large depths of cut can be achieved by using a conventional rigid machine tool that moves a micro-scale shaping tool along a set trajectory. However, when extremely small depths of cut where desired some researchers chose to control the load on the tool rather than its position [31,43]. This is because extremely precise control of tiny loads can be easier than extremely precise control of tool position. In such as case, the depth of cut is a result of tool geometry, workpiece material properties, applied load, and cutting conditions.

Using such a load-based cutting method Goss, S.H., et al. [43] cut groves up to 10 nm deep in gallium arsenide wafers using loads between 0 and 20 μN, which were applied via a nanoindenter while the workpiece was moved by stepper motors. The cutting speed used was 25 μm / sec and the area of the patterns cut was 30 μm x 30 μm. Such a low load, and hence low depth of cut, allowed the material to be cut in a ductile mode [43]. In a similar manner, 300 μm long v-grooves between 10 and 120 nm in depth were cut in Pyrex glass at speeds of 10 μm / sec by using a nanoindenter with a Berkovich diamond tip to apply cutting loads between 0.1 and 10 mN [31].

## 2.7 Atomic Force Microscope (AFM) Scribing

The material removal methods listed in the previous sections are mostly used for creating grooves with widths on the order of 10 μm or wider. For the creation of much narrower grooves, many researchers have considered the use of an atomic force microscope (AFM) as a machine tool. This is because in atomic force microscopy, an extremely sharp AFM probe lightly contacts a surface in order to measure surface features via physical contact, and hence this probe can be used as a cutting tool.

In the following subsections an overview of atomic force microscopy is provided in order to render both the capabilities and limitations of AFMs apparent. Research into conventional scribing with an AFM is reviewed, and then research into ultrasonic AFM cutting is reviewed. Finally, work aimed at overcoming some of the limitations inherent in cutting with an AFM is reviewed.

### 2.7.1 General Overview of Atomic Force Microscopy

An AFM is a device for measuring the 3d topography and surface characteristics of a small section of a sample with nanometer level lateral resolution and sub-nanometer elevation resolution. An AFM can be used to measure several characteristics of a sample surface using various techniques. However, in the context of this chapter, only contact mode measurement of surface topology is discussed.

A schematic of a typical AFM is shown in Fig. 2.20. In a contact-mode AFM, an extremely sharp AFM tip is brought into contact with a sample surface. This AFM tip is mounted on the end of a flexible cantilever, and the assembly of the AFM tip and cantilever is called an AFM probe. The forces on the AFM tip due to contact with the sample cause a slight deflection of the cantilever. This deflection is measured by shining

a laser beam onto the back of the cantilever and measuring the angle it is reflected at via four photodetectors positioned in the path of the reflected beam. The sample typically sits on a piezoelectric scanning stage capable of adjusting the lateral x-y position of the sample and sometimes the z height of the sample. Alternatively, the scanning stage may only adjust the x-y position of the sample and a separate z-stage may adjust the height of the AFM probe.

During metrology, the scanning stage is used to move the sample underneath the AFM probe in a raster pattern. Any cantilever deflection due to the presence of surface topology is measured and input into a feedback loop that adjusts the distance between probe and sample surface in order to maintain a constant and extremely small cantilever deflection. The trajectory of the z-stage can then be used to calculate the height of the sample surface at each point that the AFM tip contacts. In effect, this allows the AFM to act like an extremely sensitive micro/nano-scale contact profilometer.

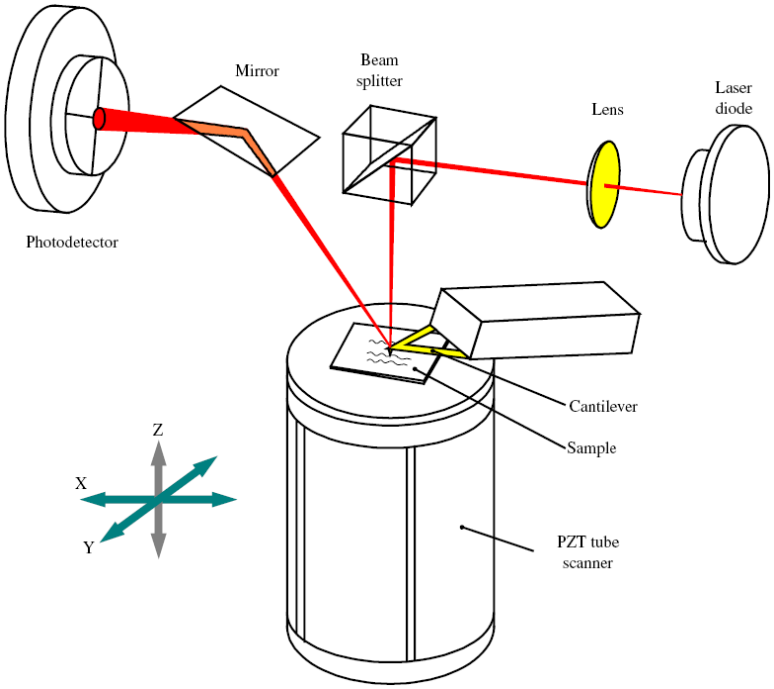


Figure 2.20: Schematic of a typical AFM system [24]

The scanning stage used to move the sample is typically a piezoelectric scanner with extremely high resolution. The piezoelectric material typically used in these scanners is lead zirconate titante (PZT), and two types of scanners are used commercially: a tripod scanner and a tube scanner [75]. The tripod scanner was developed first and consists of three independent piezoelectric actuators arranged orthogonal to each other such that they support the sample stage like a tripod. Hence, by extending some combination of the actuators, precisely controlled 3D motion is possible. However, the most popular scanner today is the simpler tube scanner [75]. This scanner consists of a tube made of piezoelectric material. One end of the tube sits on some highly stable surface, and the sample sits on top of the other end of the tube. Four electrodes are attached to the outside surface of the tube, one in each quadrant. By applying opposing voltages to the electrodes on opposite sides of the tube, the tube can be made to bend slightly, which laterally translates a sample placed upon the top of the tube. All four electrodes can be employed to achieve lateral x-y motion and to extend or contract the tube for z-direction motion.

These two scanner designs work well for metrology but have a few disadvantages. Specfically, there will usually be some coupling between the axes of motion [75], there can be significant hysteresis introduced by the piezoelectric material, maximum lateral motions tend not be very large, and in the case of tube scanners lateral motion introduce sample tilt [28]. However, some of these issues, such as hysteresis can be mitigated through the use of feedback control.

## 2.7.2 Conventional AFM Scribing Process Overview

The force applied to a sample by an AFM tip, during AFM metrology, is on the order of nanonewtons, which ideally results in no modification of the scanned surface, i.e., only extremely small elastic deformations of the surface occur. However, the force resulting from deformation of an AFM cantilever can be set to be considerably greater, which enables the AFM tip to scribe a surface. Modification of a sample surface in this manner offers the advantage of being able to produce extremely small features and then being able to examine the features insitu using the same AFM probe, provided that the probe is not significantly worn during scribing.

Micro-scale AFM scribing can be used to produce grooves, or pockets comprised of many grooves [76], that have depths between a few nanometers and few hundred nanometers and that have lengths between a few hundred nanometers and tens of microns. Freeform patterns can also be cut using some more advanced AFMs that have a scanner that allows precise and repeatable positioning via feedback and, which provides software support for such operations [77]. The footprints of such patterns tend to be limited to about 100 μm x 100 μm due to limitations in the range of typical piezoelectric scanners, which is why most research into AFM cutting has been focused on production of very small features that easily fit in the working area of a AFM.

A wide range of materials have been reported to have been cut. These materials include metals such as aluminum [24, 44], gold [78], gold-palladium [79], and nickel [32]. Polymers including polymethylmethacrylate (PMMA) [80], polyimide [76], polystyrene, and polycarbonate [27] have been cut. Lastly, semi conductor materials such as single crystal silicon [25, 45, 81] have been cut via AFM scribing.

The AFM probes used as cutting tools have included silicon probes [44, 78, 80], silicon nitride probes [76, 79], diamond tipped probes [24, 25, 32], and diamond coated silicon probes [45]. It has been reported that probes coated with hard materials such as diamond or carbon have a longer life during scribing [79]. However, the tip radius of coated probes can be up to a few hundred nanometers larger than the uncoated tip radius, which changes the nature of contact between the AFM tip and workpiece. Additionally, probes used for cutting in the literature have included cantilevers made of silicon [44, 45, 78, 80], silicon nitride [76, 79], steel [24, 25], and stainless steel [81]. Diamond tipped AFM probes with sapphire cantilevers are also commercially available [82].

In the literature, a wide range of experiments has been conducted using different cutting loads, cutting speeds, cut lengths, and number of AFM tip passes. Experiments have used loads that range from 100 nN, when cutting 2 nm deep and 20 nm wide trenches in polyimide [76], to 100 μN when cutting 88.7 nm deep pockets in single crystal silicon [81]. However, the more typically employed loads are in the range of a few tens of micronewtons [24, 32, 45]. Reported cutting speeds tend to vary between 0.006 mm/min [24] and 3 mm/min [44]. Also, the typical length of the cuts reported is between a few microns [24, 32, 45] and tens of microns [45]. However, cuts as long as the full range of motion of an AFM scanner are possible, which tends to be about 100 μm. Finally, the number of AFM tip passes can be as low a one, but has been reported to be as high as 1600 in some cases [44].

### 2.7.3 Conventional AFM Scribing Process Characteristics

Due to its importance as a material in microfabrication, several researchers have investigated AFM scribing of single crystal silicon [25, 45, 81]. These researchers have

observed three material removal regimes during experiments. It has been found that when using a sharp diamond tip, plastic deformation of a silicon workpiece requires at least 14 μN of load [45]. At loads barely high enough to plastically deform the material, such as about 20 μN, very fine workpiece wear debris are generated, as shown in Fig. 2.21A, but there is no evidence of residual stresses in the resultant surface or dislocation arrays that would indicate shearing [25]. This indicates a ploughing dominated cutting regime. At higher loads, such as 40 μN, courser chip-like debris has been observed and there is evidence of residual stresses in the workpiece surface [25]. Even higher loads, such as 80 μN, have been shown to result in chip-like debris, as shown in Fig. 2.21B, and the presence of dislocation arrays [25]. This suggests a shearing dominated material removal mode. Lastly, increasing the load to about 190 μN results in a transition to brittle material behavior, which results in poorer surface finish [81]. Hence, an AFM can be used to machine a silicon workpiece in a ductile ploughing mode, a ductile shearing mode, and a brittle fracture mode. This is not unlike machining of brittle materials of larger size scale via processes like diamond turning. Also, the transition from ploughing to shearing dominated modes can be seen in Fig. 2.21 as a transition in the shape of the load – depth curve and in chip morphology.

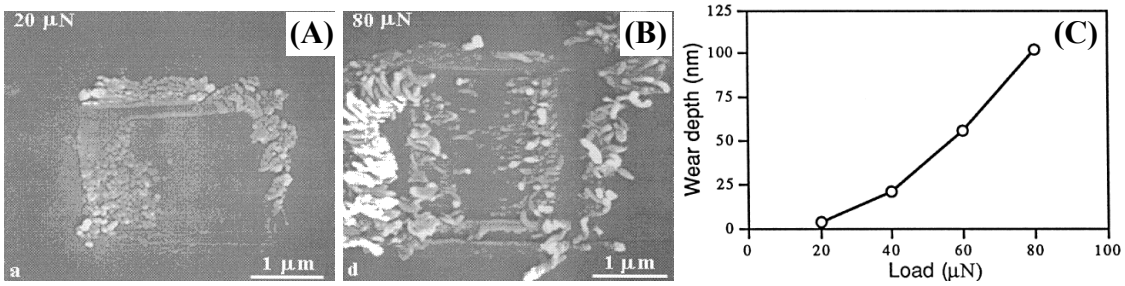


Figure 2.21: Depth and chip morphology as a function of load when cutting (100) single crystal silicon with an AFM [25]

Several researchers have also investigated the cutting of metals with AFMs [24, 32, 44, 78]. Very thin gold films have been cut with loads of a few micronewtons and it has been found that grooves have a cleaner shape when multiple AFM tip passes are used, that tip shape plays a important role in the cutting process, and that the thickness and morphology of the film have a strong effect on the resultant structures [78]. It has also been found that, when cutting grooves in aluminum with a sharp diamond AFM that has a tip radius of 15 nm, there is a nonlinear increase in both depth and surface roughness with an increase in applied load, as shown in Fig. 2.22A [24]. Depth also increases with the number of tool passes used, while the surface roughness decreases, as shown in Fig. 2.22B [24]. The depth and roughness of grooves cut in aluminum have been found to not be affected by cutting speed, except at very low speeds of 1 μm/sec or less where the surface roughness increases [24]. Similarly, when pockets were cut nickel with an AFM, it was found that depth of cut increased nonlinearly with load, increased with the number of tool passes, and was not strongly affected by cutting speed [32].

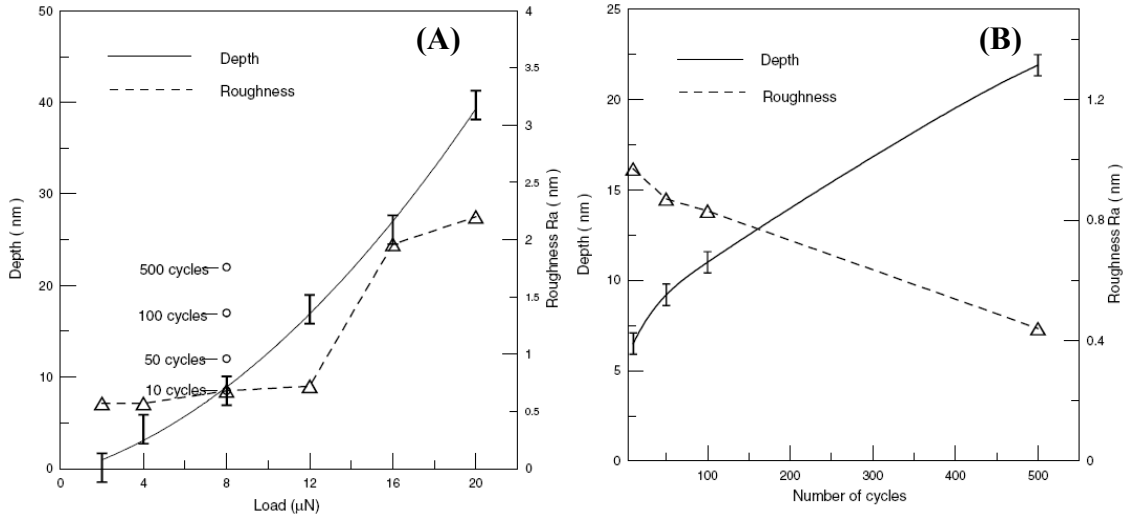


Figure 2.22: Depth of cut and surface roughness when cutting grooves in aluminum as a function of load (A) and the number of AFM tip passes when the load is 8 μN (B) [24]

## 2.7.4 Ultrasonic AFM Scribing

The majority of research into AFM scribing is as described previously, i.e., an AFM tip is smoothly moved over a surface under some load, and can be referred to as conventional AFM scribing. However, there are some advantages to introducing low-amplitude ultrasonic movements between the AFM tip and the workpiece [26, 27]. In the literature, one way in which such movements have been achieved is by depositing a film of a desired workpiece material onto a quartz crystal resonator [26, 27, 83]. Once the quartz crystal is mounted on a AFM scanner, as shown in Fig. 2.23, high frequency lateral oscillations can be introduced by applying alternating voltages of a suitable frequency to the quartz crystal resonator, also as shown in Fig. 2.23. Alternatively, the AFM scanner can be redesigned to permit ultrasonic oscillations to be introduced directly without the need for a secondary ultrasonic stage [28].

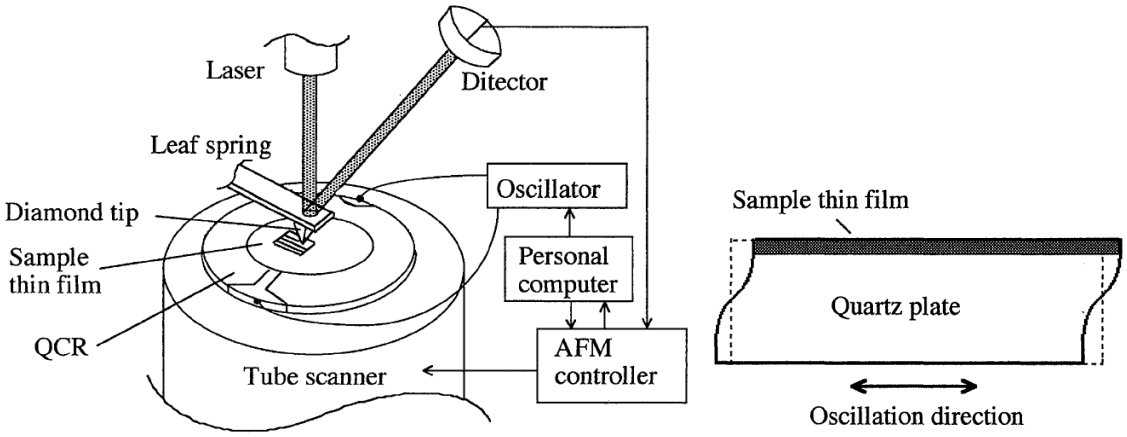


Figure 2.23: Method of ultrasonically vibrating a sample during AFM scribing [26]

There are two major advantages to ultrasonic excitation: increase in depth of cut when cutting both metals and polymers, and improvement in surface finish when cutting polymers. [27]. For instance, when cutting aluminum using four AFM tip passes, an AFM tip load of 18.9 μN, and a speed of 0.18 mm/min, the use of 5 MHz ultrasonic

excitation can cause an increase in depth of cut from about 20 nm to 110 nm [26]. Furthermore, the amount of increased depth rises with increasing load, rises with increasing numbers of tool passes, and decreases with increasing cutting speed [26].

Improvements in surface finish due to ultrasonic excitation can be seen when cutting some polymers such as polystyrene, polycarbonate, and PMMA that display poor cutting behavior during conventional AFM scribing. That is, during conventional AFM scribing of a pocket, if the load on the tip is not sufficiently high a distorted raised surface will result instead of a groove or pocket. When cutting with a sufficiently high load, a raised surface will still result during the first tool pass, and by about the third tool pass this raised surface will distort and form ridges. After about twenty tool passes, a pocket will be formed with a very bumpy bottom surface and poorly controlled depth, as shown in Fig. 2.24A [27]. By contrast, if ultrasonic excitation is used, a groove or pocket can be formed during even the first AFM tip pass, and the resultant surface will be much smoother as shown in Fig. 2.24B [27].

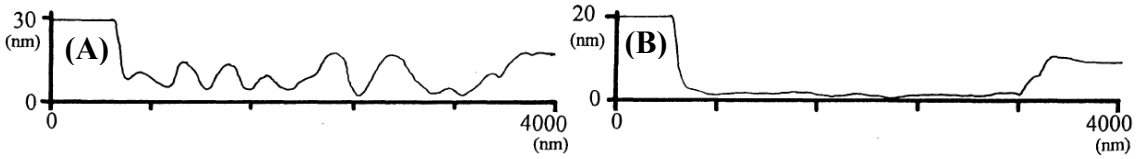


Figure 2.24: Polystyrene surface after 20 conventional scratches at 0.18 mm/min and 5 μN (A) and after 2 ultrasonic scratches at 0.18 mm/min and 3.6 μN (B) [27]

## 2.7.5 Advanced AFM Platforms for Machining

The piezoelectric scanners used to move the sample in a conventional AFM have several limitations. The range of motion of these scanners used tends to be fairly limited. Also, interference between the three axes of motion exists and becomes significant during relatively large displacements [28]. Large displacements can also result in tilting of the

sample when tube type scanners are used [28]. Furthermore, the considerable hysteresis and axis coupling / crosstalk that can occur renders complicated scan trajectories, covering an area greater than a few tens of microns, difficult to perform accurately and repeatedly unless position sensing and feedback is employed.

Much research has been concentrated on AFM cutting while moving the sample in a repeating lateral raster pattern, in order cut a pocket, or while moving the sample back and forth along one axis of motion in order to cut a line [24, 25, 32, 81]. This is possibly because many commercial AFMs are set up such that these patterns are very easy to create. However, in order to efficiently cut freeform curvilinear grooves it is necessary to be able to move the sample scanner in such as way as to achieve arbitrary trajectories like those that can be achieved with a CNC machine tool.

One way of accomplishing such trajectory control is to equip a conventional tube scanner with position measurement sensors, such as optical levers, and use these sensors as the basis for standard CNC control of the sample stage and/or AFM probe position [84]. In fact, High-end AFMs that include closed-loop controlled scanners and software for AFM-based lithography are commercially available [77], but such machine are very expensive.

There have also been proposals to build AFMs with altogether different motion platforms. For instance, a nanometric AFM cutting machine has been constructed in which the sample scanner of a conventional AFM is replaced with a small and ultra high precision Stewart platform, as shown in Fig. 2.25A [28]. This motion platform has a movable range of 20 μm in the x-y lateral directions, a range of 100 μm in the z-direction, and a motion accuracy of 100 nm. It can also be used to induce ultrasonic

vibrations with frequencies up to at least 10 kHz and with amplitudes up to at least 59 nm [28]. Additionally, in order to achieve greater ranges of motion, other researchers have proposed constructing a modular AFM / nanometric cutting machine with both linear motors and piezoelectric actuators for motion control, as shown in Fig. 2.25B [29].

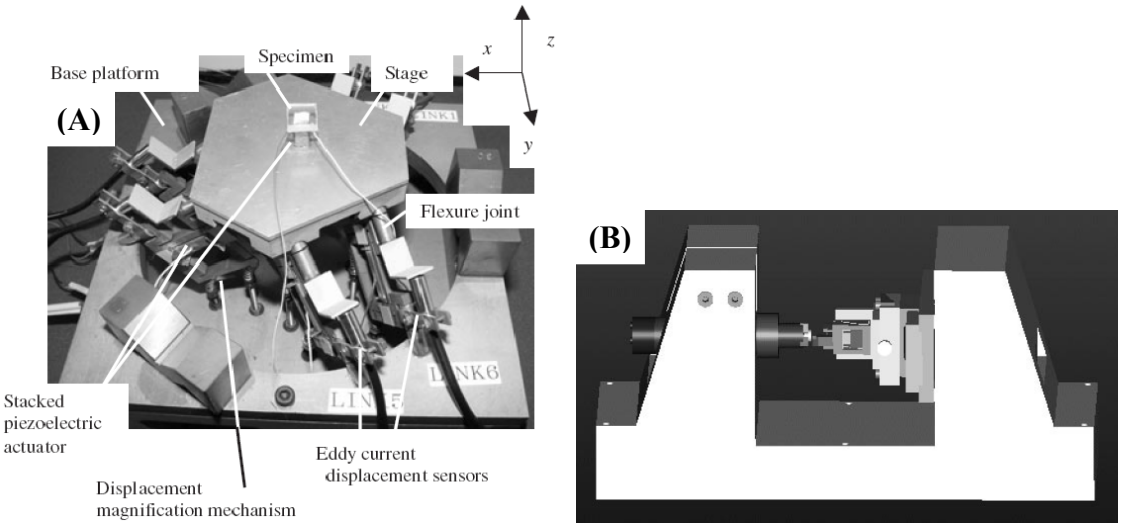


Figure 2.25: Stewart platform for use with an AFM (A) [28] and layout of bench-type nanometer machining platform (B) [29]

## 2.8 Summary of Processes and Gap in Capabilities

Several existing groove cut processes have been reviewed that are capable of cutting grooves less than 50 μm wide, and each of these processes has been shown to have advantages and disadvantages. The advantages of disadvantages of non-mechanical groove cutting process are summarized in Table 2.1, and a similar summary for mechanical groove cutting processes is provided in Table 2.2. Additionally, each of these processes meets some of the micro-groove cutting process requirements listed in Chapter 1, but none of the processes meet all of the requirements, as shown later in this section.

Table 2.1: Summary of each existing non-mechanical micro-groove cutting process

| Process | Advantages | Disadvantages |
|---|---|---|
| Laser Scribing | • Very fast<br>• Cuts most materials<br>• No tool to wear out | • Limit on smallest groove width<br>• Ridges formed around cut due to resolidification molten material<br>• Many process parameters that must be set experimentally |
| μ-EDM | • Cuts all electrically conductive material<br>• Negligible cutting forces | • Limits on smallest groove width<br>• Finite tool life<br>• Complicated tooling required for good material removal rates<br>• Can't cut non-conductive materials except thin films on a conductive substrate |
| μ-ECM (Wet) | • Cuts any electrically conductive material<br>• Negligible cutting forces<br>• Smooth burr free surface finish<br>• No tool wear | • Limits on smallest groove width<br>• Difficult to design a tool that produces a specific geometry<br>• Can't cut non-conductive materials |
| μ-ECM (Solid-State Superionic Stamping) | • Can cut very high resolution features in metallic workpieces<br>• Can cut a entire pattern of features in one operation<br>• Good surface finish | • Need to fabricate a new stamp for each new pattern of grooves<br>• Requirement of physical contact between stamp and workpiece renders the use of rough or curved workpiece surface difficult |

As shown in Tables 2.1 and 2.2, a major disadvantage of several of the processes is a limit on the narrowest possible grooves. This is particularly problematic because the first process requirement established in Chapter 1 is the ability to cut grooves with widths between a few hundred nanometers and a few microns. Figure 2.26 shows the widths that can be achieved using each process previously described. The only processes that at least partially meet the requirement are solid-state superionic stamping μ-ECM, micro-fly

cutting, micro-scale shaping / planing, and AFM scribing. Also, only AFM scribing and solid-state superionic stamping μ-ECM can achieve the full range of target widths.

Table 2.2: Summary of each existing mechanical micro-groove cutting process

| Process | Advantages | Disadvantages |
|---|---|---|
| Micro-Endmilling | • Cuts many materials<br>• Fast material removal rates<br>• Very vertical groove sidewalls<br>• High-aspect ratio grooves | • Smallest tool diameter and largest aspect ratio limited by tool stiffness<br>• Tool fabrication can be difficult<br>• Burr formation<br>• Finite tool life |
| Micro-Fly Cutting | • Very narrow and shallow grooves<br>• Relatively fast cutting speed<br>• Low surface roughness | • Burr formation<br>• Finite tool life<br>• Extremely rigid machine tool required<br>• Only straight grooves can be cut |
| Micro-Scale Shaping / Planing | • Can cut narrow channels<br>• Arbitrary cross-sections<br>• Can cut curvilinear grooves | • Burr formation<br>• Finite tool life<br>• Requires high precision machine |
| AFM Scribing | • Can cut extremely narrow and shallow grooves<br>• Insitu metrology cut features | • Very low material removal rates<br>• Cannot produce long grooves<br>• Cannot produce deep grooves |

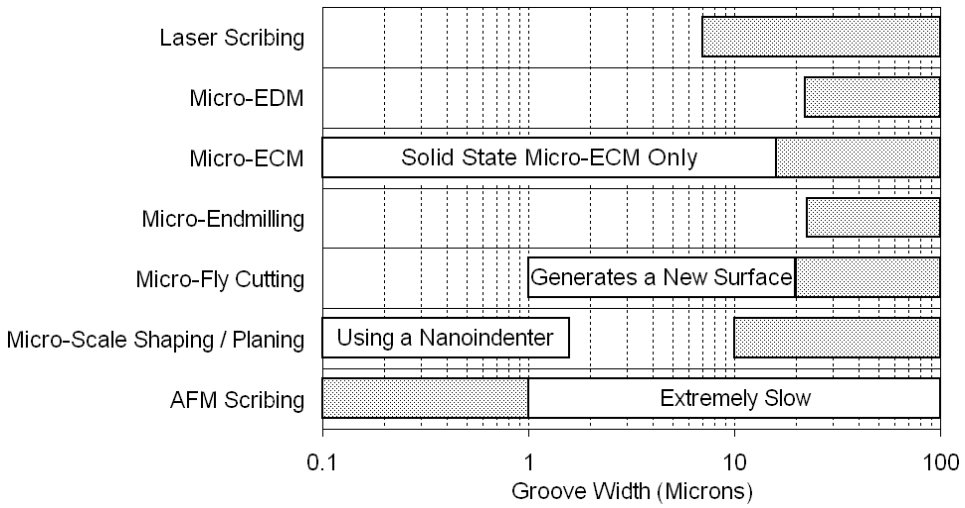


Figure 2.26: Groove width capabilities [2, 3, 7, 14, 21, 30 - 33]

Table 2.3 shows how well each process meets the other process requirements listed in Chapter 1. As can be seen in the table, none of the processes meet all of the requirements. Of the processes capable of achieving the target groove widths, solid state superionic stamping μ-EDM, is limited to groove patterns already present on a stamp, requires the production of stamp prior to machining, and imposes that requirement that the stamp and workpiece must perfectly match up so that good physical contact is achieve, which renders it difficult to cut into rough or curved surface. Micro-fly cutting can only cut straight grooves, has been limited to v-shaped grooves when grooves widths were less than about 12 μm, and requires a very rigid and expensive machine tool. Micro-scale shaping / planing suffers from burr formation issues, and requires a stiff and expensive machine tool to perform well. Also, very narrow grooves cut with this process are limited to v-shaped cross-sections. Lastly, AFM scribing can be used to cut extremely narrow grooves or can build up grooves as wide as the range of travel of the AFM by moving an AFM probe in a raster pattern during cutting. However, this process is extremely slow, is limited to grooves with very short lengths, and requires expensive equipment.

In conclusion, none off the micro-groove cutting processes in the existing literature meet all of the application-driven process requirements discussed in Chapter 1. This means that there is a gap in current manufacturing capabilities that motivates the development of a new micro-groove cutting process that is capable of meeting the statement requirements. The following chapters of this work are aimed at the development of such a process, which will provide a useful micro-fabrication tool that does not currently exist.

Table 2.3: Satisfaction of groove cutting requirements by existing processes

| **Key**<br>Fully Meets Requirement ●<br>Partially Meets Requirement ◖<br>Does Not Meet Requirement ○<br>**Requirements** | Laser Scribing | µ-EDM | Wet µ-ECM | Solid-State Superionic Stamping | Micro-Endmilling | Micro-Fly Cutting | Micro-Scale Shaping/ Planing | AFM Scribing |
|---|---|---|---|---|---|---|---|---|
| Grooves with Lengths of Millimeters | ● | ● | ● | ◖ | ● | ● | ● | ○ |
| Curvilinear Grooves Patterns | ● | ◖ | ● | ● | ● | ○ | ● | ● |
| Arbitrary Cross-sectional Shapes | ○ | ◖ | ◖ | ◖ | ○ | ◖ | ◖ | ◖ |
| Minimal Burrs / Redeposited Material | ◖ | ◖ | ● | ● | ○ | ◖ | ○ | ◖ |
| Good Material Removal Rate | ● | ◖ | ◖ | ◖ | ● | ● | ● | ○ |
| Programmable Groove Patterns | ● | ◖ | ◖ | ○ | ● | ◖ | ● | ● |
| Costs Less than $100,000 | ● | ○ | ○ | ● | ● | ○ | ◖ | ○ |
| Can Cut Grooves into Curved Surfaces | ● | ● | ● | ○ | ● | ◖ | ● | ○ |

## 2.9 Chip-Based Micro-Scale Cutting Mechanics

As described in the previous sections, exiting micro-groove cutting processes are unable to meet the process requirements outlined in Chapter 1. This thesis concerns the development of a new micro-groove cutting process that is capable of meeting these requirements. The new process, which is described in detail in the next chapter, makes use of chip removal-based metal cutting. Micro-scale metal cutting shares several similarities with macro-scale metal cutting, which is a well established field, and numerous textbooks are available on the subject [85 - 87]. Hence macro-scale metal cutting is not reviewed here for brevity.

However, these are also aspects of metal cutting that are unique to the micro-scale. These aspects of the process are introduced by the size of the edge radius of the tool relative to the uncut chip thickness and by the size of the uncut chip thickness

relative to the workpiece microstructure. This subsection provides a brief review of the aspects of the chip removal-based cutting process that are unique to the micro-scale.

## 2.9.1 Effective Rake Angle

At the macro-scale, cutting tools can often be treated as being sharp enough for edge radius effects to be negligible. However, when cutting at the micro-scale, the assumption of a sharp tool can be invalid if the edge radius is on the same size-scale as the uncut chip thickness. An example of such a situation is shown in Fig. 2.27 where the cutting edge of a tool has a radius, $r_e$, and the uncut chip thickness is given as $t_c$.

As a result of the edge radius being on a similar size scale as the uncut chip thickness, the effective rake angle can be much more negative than the rake angle would be based on rake face orientation alone [88]. This effect can be estimated by drawing a line between the lowest point on the tool and the point on the rake face where the chip separates from the tool, as shown in Fig. 2.27 [89]. The point of tool-chip separation can in turn be estimated as some multiple, $\xi$, of the uncut chip thickness [89]. When lacking actual cutting data for a particular cutting operation, $\xi$ can be roughly estimated to be 1.5 [89] because this value is in the middle of the range of physically realistic values reasoned by Manjunathaiah et al. [90].

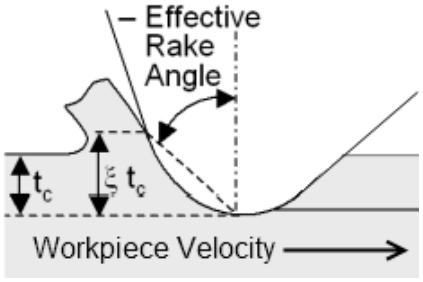


Figure 2.27: Effective rake angle at the micro-scale

Using the effective rake angle estimation method, it can be seen that effective rake angle is rendered significantly more negative when the edge radius is large relative to the uncut chip thickness. This in turn increase the amount of ploughing expected, which can result in poorer surface finish. Conversely, when the edge radius is small relative to the uncut chip thickness, the effective rake angle is very close to the value found based on rake face orientation alone, and the tool can considered sharp.

### 2.9.2 Minimum Chip Thickness

As mentioned in the previous subsection, in micro-scale cutting the uncut chip thickness can be on the order of the edge radius of the tool. As a result, the minimum chip thickness effect becomes significant. The concept is that when the uncut chip thickness is less than the minimum chip thickness no chip is formed and no material is removed from the workpiece surface. Ploughing of workpiece material via plastic deformation can still occur. When the uncut chip thickness is greater than the uncut chip thickness a chip is formed, which removes material from the workpiece [91]. This was shown via molecular dynamics simulations used to study the ultimate accuracy that is achievable using edge-radiused tooling [92].

The minimum chip thickness effect can be seen in Fig. 2.28, which shows finite element simulation results from the cutting of ferrite [34]. Figure 2.28A shows the cutting action when the uncut chip thickness does not exceed the minimum chip thickness. Note that the material behind the cutting edge is at the same height as the material ahead of the cutting edge. By contrast, Fig. 2.28B shows chip formation when the uncut chip thickness does exceed the minimum chip thickness.

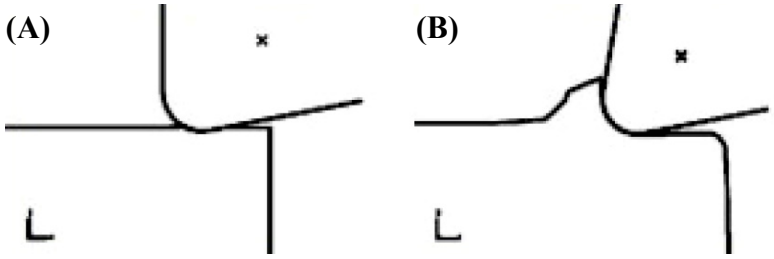


Figure 2.28: Finite element simulation when cutting ferrite with an uncut chip thickness below (A) and above (B) the minimum chip thickness [34]

The minimum chip thickness can be expressed as a material dependent fraction of the cutting edge radius of a tool [93]. For example, using finite element analysis, the minimum chip thickness has been estimated as 14% - 25% and 29% - 43% of the edge radius for pearlite and ferrite, respectively [34]. Hence, if material removal is to occur effectively during very shallow cuts, it is important for the tool to be sharp enough to insure chip formation occurs. The minimum chip thickness can be estimated for various materials using an analytical model [93].

## 2.9.3 Heterogeneous Workpiece Microstructure

Many commonly machined workpiece materials with useful properties have a heterogeneous microstructure. For example, many brass alloys are composed of grains of alpha-brass and beta-brass. Cast iron is composed of ferrite, pearlite, and nodules of graphite. Also, depending of the heat treatment used, steel alloys can be composed of grains with various phase structures. Furthermore, each of the constituent materials that make up a microstructure can have different material properties, e.g., flow stress, modulus of elasticity, and thermal conductivity.

It should also be noted that the microstructure of pure materials can also behave as if it were heterogeneous in some cases. For example, a high purity aluminum

workpiece is composed of many grains that are each a single aluminum crystal and the crystalline orientation of each grain can vary. This causes a heterogeneous behavior because the material properties of each crystal are anisotropic, which has been shown to experimentally result in changes in cutting forces [94].

In macro-scale machining, it is possible for the uncut thickness to be sufficiently large relative to the size of the grains that make up a workpiece for many grains to be present throughout the thickness of a chip. Hence, models of the cutting process that ignore the microstructure may be effective in such a case. However, at the micro-scale, uncut chip thickness can be so small that only a few grains are included throughout the thickness of a chip. In extreme cases, the uncut chip thickness may even be less than the size of a single grain. In such a case, the behavior of the material around the cutting zone can change significantly depending on the grains present in the cutting zone at a given time.

An approach used to investigate the effects of cutting through a heterogeneous microstructure is to create a finite element model where the mesh captures of the shape of the microstructure and material properties are specified for each region of the same material. This approach has been successfully used to study orthogonal machining of cast iron [95 - 97]. Alternatively, a mechanistic model can be constructed where the microstructure is modeled and the specific cutting energy for a given constituent is used as the tool passes through that constituent. This approach has been successfully used to model micro-endmilling through a cast iron workpiece [98].

## 2.10 Modeling of Micro-Scale Cutting

Later in this thesis it will be necessary to model the chip formation-based micro-groove cutting process described in the next chapter. Therefore, this section provides a brief overview of modeling techniques suitable for use at the micro-scale. Particular attention is played to the finite element modeling technique, which is capable of providing the most information about the cutting process at the micro-scale without requiring excessive amounts of computational resources.

### 2.10.1 Model Types

The types of machining models available are analytical models, mechanistic models, molecular dynamics (MD) models, and finite element models. Analytical models seek to describe the flow of material during cutting and the cutting forces generated using a series of specialized analytical expressions. These models can vary significantly in complexity. One type of analytical model particularly suitable for use at the micro-scale, where tool edge radius effects are prevalent, is the slip-line field model [99]. Using a slip-line field model as a basis, the effects of the minimum chip thickness and elastic recovery can also be handled [93] in order to get good force predictions and surface roughness information. However, in the orthogonal cutting case, such models are generally limited to predicting surface generation under the cutting edge, and cannot predict what happens at the side of a orthogonal cut or predict burr formation. Such models also fail to provide information about the stress and strains throughout a workpiece during cutting.

Mechanistic models allow for easy computation of cutting forces by means of a relationship between the cross-sectional area of a cut and the specific cutting energy of

the material being cut. These models can also be adapted to handle heterogeneous micro-structures [98]. However, these models do not provide detailed information about chip flow or the workpiece surface generated during cutting.

Molecular dynamics models explicitly model the interactions between molecules making up both the tool and workpiece during cutting. This provides a very accurate representation of the cutting process and the resultant workpiece surface. Such models have been used to explore processes such a nanometric orthogonal cutting [100] and nanometric cutting with an AFM tip [101]. However, simulations involving volumes of workpiece material larger than a few thousand cubic nanometers are computationally prohibitive and hence even with recent increases in computer power, workpiece sizes have been limited to rectangular volumes less than 20 nm on a side [100 - 102]. Therefore, while these models are suitable for gaining insights into micro-scale effects they are not suitable for simulating of the formation micro-scale features.

Finite element models can represent the cutting processes in a way that is computationally feasible when cutting features with sizes of less than a micron and larger. This type of model can also provide detailed information about the cutting process, which includes stresses, strains, temperatures, cutting forces, and the shape of the finished workpiece. Both 2D and 3D representation of the cutting process are possible even through 2D models are more common in the literature. Therefore, finite element models are deemed most suitable for detailed study of a micro-groove cutting process of the type described later in this work.

## 2.10.2 Finite Element Model Uses

Finite element models have been used to study many aspects of machining both at the micro-scale and at the macro-scale. Orthogonal cutting models have been used to, for example, investigate the effects of changing process parameters such as cutting speed, rake angle, and coefficient of friction on process characteristics including shear angle, chip thickness, strain, strain rate, stress, temperature, chip curl, tool-chip contact length, and cutting force [103 - 105]. Models capable of evaluating the effects of tool wear have also been instigated [106].

Other researchers have used finite element modeling to investigate fundamental aspects of the cutting process. For instance, the effect of using tools with large edge radii relative to the depth of cut, which is relevant to micro-scale cutting, has been investigated [107, 108]. Another set of studies investigated size effect at the micro-scale by addressing the contributions of the decrease in cutting temperature in the secondary shear zone seen at the micro-scale and the presence of strain gradient hardening [107, 109]. The effect of cutting through a workpiece with a heterogeneous micro-structure has been addressed via finite element modeling [95 - 97]. Finite element modeling has also been used to gain insights into the actual method of separation between a chip and workpiece during machining, which lead to the conclusion that there is ductile fracture ahead of the cutting edge of a tool [35, 108].

Finite element models have been used to examine characteristics of chip formation and chip flow. For instance, both 2D [110] and 3D [111] studies have investigated segmented chip formation. Studies of chip breaking have also been performed [112].

Finite element models have been used to examine finished workpiece characteristics and how those characteristic can be adjusted by modifying the cutting process. For example, residual stresses in the workpiece following cutting, which affect part quality and deformation, have been investigated [104, 113]. Exit burr formation has been investigated during orthogonal metal cutting [114, 115], during drilling [116, 117], and during face milling [118]. The geometry formed around the entry of a drilled hole has also been considered [119].

Lastly, it should be noted that while the previously listed work was more academic in nature, finite element modeling of machining is now an industrially used tool for process improvement. One software tool used for this purpose is AdvantEdge FEM™, which is produced by Third Wave Systems, Inc, and can handle both 2D and 3D machining simulations. [120] Another industrial software package is DEFORM™, which is produced by Scientific Forming Technologies Corporation and can also handle 2D and 3D machining simulations, even through it is optimized for forming operations [121]. Software packages like these are used for purposes including calculation of cutting forces and torques, determining ways of increasing material removal rates, improving tool life, predicting chip shape, shortening product design cycles, and reducing trial and error during manufacturing process setup [120]. Using such tools process such as milling, turning, broaching, sawing, drilling, boring, tapping, and groove cutting can be evaluated [120].

### 2.10.3 Finite Element Model Characteristics

Researchers have used finite elements to model orthogonal cutting. Many of these models have treated the process as 2D via the plane strain approximation, which

allows for observations of chip formation and subsurface stresses provided that the wide of the cut is much greater than the depth of cut. An example of a typical 2D finite element model is shown in Fig. 2.29.

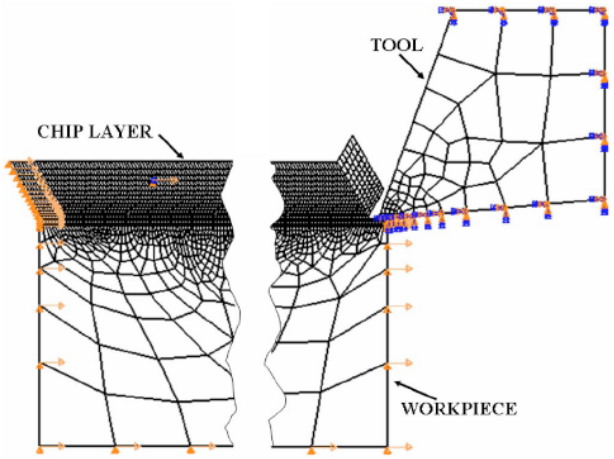


Figure 2.29: Example of a typical 2D finite element model of orthogonal cutting [35]

Models broadly differ based on (1) the integration scheme used to acquire the solution, (2) the formulation of the model, (3) how chip formation is modeled, (4) how thermal effects are modeled, and (5) whether the model is 2D or 3D.

**Integration Scheme**

Metal cutting is an inherently nonlinear dynamic process, and hence finite element solution methods suitable for such systems must be employed. Two solution methods are implicit dynamic analysis and explicit dynamic analysis. The former method solves for dynamic quantities during a current time increment based on values from a previous time increment and at the current time increment. Hence implicit, nonlinear equations must be solved at each time step, typically via some iterative solution method [122]. This method has been used by several researchers to simulate orthogonal cutting [103, 109, 123]. However, implicit dynamic analyses generally have problems

handing complex contact conditions, complex boundary conditions, and material failure, which can render it difficult to achieve solution convergence and limit modeling options.

Many other researchers have created machining models based on the use of explicit dynamic analysis [35, 110, 114, 116, 117, 119, 120, 124, - 127]. The explicit dynamics procedure calculates dynamic quantities during a current time step using only quantities that were already calculated in a previous time step via the use of a central-difference time integration rule [122]. This method can accommodate complex contact conditions, complex boundary conditions, very large deformations, and material failure. However, use of this method does introduce the need to use many very small time increments in order to insure a stable solution. The implications of this are discussed in much more detail in Chapter 7.

**Formulation of the Model**

One of three finite element formulations is used when modeling machining processes: the Lagrangian formulation, the Eulerian formulation, or the adaptive Lagrangian-Eulerian (ALE) formulation. When using the Lagrangian formulation, elements that make up the finite element mesh each corresponding to a piece of material that never leaves the element. That is, deformation of the workpiece mesh corresponds to deformation of the underlying material. This formulation can be used to simulate transient dynamic events such as the entrance of a tool into a workpiece, chip formation, and exit of a tool from a workpiece. However, care has to be taken to avoid excessively distorted elements. Many researchers have used this formulation when modeling metal cutting [35, 103, 104, 109, 114, 124, 123].

The Eulerian finite element formulation has also been used to model metal cutting [128]. Using this formulation, the configuration of the finite element mesh never changes. Rather, material flows into and out of the elements. This formulation is particularly suitable for modeling steady-state machining using a small number of elements. However, prior knowledge about the shape of the chip must be acquired from some other source in order to properly select the mesh shape. Transient events such as exit burr formation also cannot be handled by this method.

The ALE formulation is a hybrid of the Lagrangian and Eulerian formulations. During calculation of dynamic quantities for a time increment, the workpiece material moves with the mesh as with the Lagrangian formulation. However, between selected increments the mesh is allowed to shift independent of the material, like with the Eulerian formulation. The ALE formulation can be used to model transient events while avoiding highly distorted elements, or it can be used to model steady-state cutting in a similar manner to the Eulerian formulation. The ALE formulation has been used to model machining processes by several researchers [125 - 127]. However, it should be noted that the parameters used to control the movement of the mesh independent of the underlying material must be carefully fine tuned for machining [125].

**How Chip Formation is Modeled**

Lagrangian and some ALE formulation cutting models must be able to handle chip formation and separation from a workpiece. Several approaches have been used that can be broadly categorized as indentation-based, nodal separation-based, or element failure-based. In the first approach, chip formation is treated as an indentation process where the tool is the indenter, and the chip forms solely due to plastic flow of workpiece

material around the tool. Since the mesh has to flow around the tool, distortion of elements in the mesh becomes a significant concern. Researchers modeling machining processes have relied on remeshing and solution mapping algorithms [95, 109, 110, 118 – 120] or the ALE formation for this purpose [127]. Such an approach by itself, however, cannot simulate discontinuous chip formation.

Another approach used by several researchers is to is to model the chip and workpiece as two separate meshes that are joined by constraints initially applied at corresponding nodes [103, 104, 123]. Each of the nodal constrains are removed in sequence to allow a chip to separate from the uncut workpiece. The separation criterion can vary significantly and be based on quantities such as effective plastic strain at a node [123], stress at a node [103], or distance between the cutting edge of the tool and a node [104].

Yet another approach is to enable chip separation via failure and deletion of elements within a workpiece based on some damage law. This allows the workpiece mesh to essentially be cut. Experiments and simulations have suggested that this approach is physically realistic when a ductile fracture criterion is used [35]. The region in which elements can fail can be limited to a sacrificial layer between the chip and uncut workpiece [35, 114, 125] or can consist of the entire workpiece [116, 117, 124, 126].

**How Thermal Effects are Modeled**

During machining, heat is generated due to plastic work and due to rubbing between the tool and workpiece. This heat conducts through the workpiece material and the tool material. Heated workpiece material experiences thermal expansion and thermal

softening, which lowers its flow stress. Finite element modeling of heat generation and heat transfer during machining has been treated with varying levels of detail.

Heat generation in the workpiece can be modeled as some fraction of the plastic work in the deformed workpiece material [122]. Many researchers that have chosen to address heat generation have made the assumption that heat generation occurs so quickly during machining that there is not enough time for the heat to conduct through the workpiece before a section of material gets hot enough to experience significant thermal softening. Hence adiabatic heating is assumed where all thermal energy within an element remains in that element [114, 116, 123, 124]. This approach simplifies computation and reduces required computer time.

More advanced models have included also included heat generation at the interface between the tool and workpiece, which can be modeled as some fraction of the dissipated energy at the interface [103]. Other researchers have chose to coupled thermo-mechanical models where heat conduction is model as well mechanical deformation [35, 110, 125, 127]. However, as discussed in Chapter 7, such models can be computationally expensive at the micro-scale.

**Model Dimensionality**

Many of finite element models of the cut in the literature examine the case of orthogonal cutting. This allows for the use of a relatively simple model that still provides useful information about the cutting process. One particularly common simplification is to treat orthogonal cutting using a 2D finite element model [35, 95, 103, 104, 109, 110, 114, 123, 124, 125, 128]. This is generally accomplished via the use of the plane strain assumption, which is valid when all strain tensor components orientated out of the cutting

plane are small enough to be treated as zero. This can be the case when the width of a cut is much greater than the depth of cut, and hence this is an implicit assumption built into in most 2D finite element models in the literature.

Full 3D finite element model-based studies of cutting have also been performed. For example, 3D finite element models have been used to simulate orthogonal [111, 126] and oblique [111, 127] cutting of a tab of material narrower than the tool used to cut it. Full 3D modeling of a portion of a cut during face milling [118] has also been performed. Drilling [119] and exit burr formation during drilling has been examined using 3D finite element models [116. 117]. Lastly, industrially used FEA packages are capable of simulating operations such as milling, turning, broaching, sawing, drilling, boring, tapping, and groove cutting [120]. However, it should be noted that 3D finite element-based analysis of orthogonal groove cutting where the depth of cut is similar to or greater than the width of cut does not appear to have received much attention, which is of interest since such conditions can occur during chip formation-based micro-groove cutting.

## 2.11 Chapter Summary

In this chapter several different micro-groove cutting processes were presented that have been previously reported in the literature. Each of these processes was described in detail, and the capabilities of each process were compared to the process requirements established in Chapter 1. Based on this comparison it was concluded that no existing process meets all of the requirements, and hence there is a gap in current manufacturing capabilities that needs to be filled by a new micro-groove cutting process.

Following discussion of exiting micro-groove cutting process, a brief discussion of orthogonal metal cutting was provided that emphasized the difference between cutting

at the macro-scale and at the micro-scale. This was intended to provide background for later chapters in this work where micro-groove cutting, via a chip formation-based material removal process, is discussed.

A discussion of methods of modeling a chip formation-based material removal process followed, which is intended to provide background for Chapter 7 where the micro-groove cutting process developed in the next chapter is also modeled. Particular focus was given to finite element models, since such models provide the most information about the cutting process at the micro-scale while remaining computationally feasible. Additional details about finite element modeling that are relevant to the development of a new cutting model are provided Chapter 7.

In conclusion, a new micro-groove cutting process needs to be developed to fill a gap in current micro-manufacturing capabilities, which is the subject of this work. The development of such a process is described in the next chapter. In Chapter 4 and Chapter 6, extensive experimentation is described that thoroughly demonstrates the viability of the process and its current capabilities. Finite element modeling of the process is then performed in order to gain a better understanding of the process. This is necessary because some process outputs cannot be readily observed experimentally.

# Chapter 3

# Micro-Groove Cutting Process and Machine Tool

## 3.1 Introduction

Chapter 2 established the need for a new micro-groove cutting process to meet the requirements established in Chapter 1. This chapter describes a newly developed process intended to meet this need. This process enables the formation of extremely narrow and shallow curvilinear features normally associated with AFM scribing while overcoming the limitations of AFM scribing such as low cutting speeds, limited cut lengths, limited groove cross-sections, and limited depth of cut. Rather, the cut lengths, achievable cross-sections, cutting speeds, and potential depths of cut are more in line with those possible using micro-scale shaping / planing. However, in comparison to micro-scale shaping / planing, the new process enables much smaller features and the use of inexpensive machine tools with relaxed accuracy and stiffness requirements.

In the first part of this chapter, process requirements are reiterated and obstacles to meeting these requirements are described. In the second part of this chapter, the design of a micro-groove cutting process intended to not be hampered by the presented obstacles is described. In the third part of this chapter, requirements imposed upon a machine to that is used to implement the developed process are given. In the forth part of the chapter, the machine tool used to implement the process is described in detail. The

last part of the chapter describes the operation of the machine tool during process setup and during micro-groove cutting.

## 3.2 Requirements / Motivating Statements

### 3.2.1 Process Requirements

In the first chapter, several requirements for a micro-groove cutting process were established based on the need to produce specific classes of parts with micro-scale features in an economically viable manner. These requirements are repeated here for convenience.

1. The ability to cut grooves in metals that are between a few hundred nanometers wide and a few microns wide.
2. The ability to cut patterns of many grooves that are each several millimeters long.
3. The ability to cut patterns of curvilinear grooves.
4. The ability to cut grooves with nearly arbitrary cross-sections
5. The ability to cut grooves with minimal burr formation / material distortion.
6. Good material removal rate.
7. The ability to cut fully programmable patterns of grooves
8. The ability to fabricate micro-grooves using relatively inexpensive equipment.
9. The ability to achieve relative tolerances of approximately 1% or better.
10. The ability to cut grooves in flat or curved workpiece surfaces.

There are three challenges in regards to meeting these requirements. The first challenge is being able to cut desired patterns of grooves. The second challenge is being able to achieve various groove shapes. The third change is being able to cut long, shallow grooves that meet a specified tolerance.

### 3.2.2 Example Process Specifications

The process requirement involving the achievement of a given tolerance at a given size scale is best explored through the use of example groove specifications. Therefore, consider a straight groove that has a rectangular cross-section. Let the groove be 10 mm long, 1 μm deep, 1 μm wide, and have a 1% relative tolerance on groove depth. I.e. uncertainty in groove depth should be no more than 10 nm. Also, consider cutting this groove into a flat workpiece and alternatively into a workpiece with a sinusoidally varying height. Such a specification is representative of features that are challenging to produce.

### 3.2.3 Micro-Scale Shaping / Planing as a Candidate Process

Of the existing processes described in Chapter 2, micro-scale shaping / planing meets several of the process requirements. Specifically, curvilinear patterns of grooves with various cross-sections can be readily cut. Long grooves, meeting of exceeding the 10 mm length specification in the example, can be readily cut. Cutting speeds upwards of 85.8 mm/min with depths of cut per tool pass upwards of 6 μm can be achieved [19], which results in a good material removal rate. Fully programmable patterns of grooves can be readily cut. Lastly, although grooves cut in the literature have been wider than about 10 μm in most cases, there is no fundamental physical limitation that states that a micro-scale shaping / planing tool capable of cutting narrower grooves can not be fabricated

However, micro-scale shaping / planing does have problems with achieving the tolerance specified in the example. Therefore, the micro-scale shaping / planing process only provides a good staring point for the development of a new process with improved

capabilities. Determining a means of overcoming this issue is accomplished by examining why conventional micro-scale shaping / planing has this deficiency. This involves a discussion of issues regarding encoder resolution, linear guide alignment, tool-workpiece registration uncertainty, and machine tool stiffness.

**Encoder Resolution Issues**

Conventional high-precision machine tools require some means of determining the positions of the machine stages in order to control the trajectory of a tool relative to a workpiece. This is typically accomplished via linear or rotary encoders that have some set resolution. Also, in such machines, linear and rotary encoders are typically set to directly measure stage position without the use of mechanical amplification such a gearing, and hence there is ideally a one-to-one correlation between tool or workpiece motion and encoder output. Therefore, encoder resolution has a direct impact on the accuracy of the machine tool and the tolerances that it can reliably achieve.

Encoder outputs serves as inputs to feedback loops that are used to actuate the motors in such a way as to achieve target stage positions. Since feedback algorithms are ultimately based on the measurement of position error, the actual position of the stages, and hence the tool relative to a workpiece, will dither by at least ± 1 encoder count. In practice, depending factors such as friction of machine bearings, stage loadings, motor capabilities, and control electrics, stage dither can be significantly larger. Hence an estimable of ± 2 encoder counts is more realistic.

This means that if a machine tool has linear encoders with a resolution of 20 nm, such as the 5-axis micro-scale machine tool constructed at the University of Illinois [38], stage position will have an uncertainty of 80 nm imposed by encoder resolution alone.

Hence, when cutting a micro-groove where a relative tolerance of 10% is required, the shallowest groove that could be cut is 800 nm. If a relative tolerance of 1% is required the shallowest groove that could be cut is 8 μm. Alternatively, encoders with a 5 nm resolution, such as those sold by MicroE Systems [129] would enable grooves as shallow as 200 nm to be cut with 10% relative tolerance and grooves as shallow a 2 μm to be cut with 1% relative tolerance. Therefore, in order to cut grooves with 1 μm or depth, such as the groove provided in the example specification, even higher resolution encoders with 2.5 nm increments are need. This increases machine tool cost and prohibits the use of many existing machine tools that do not generally have such high-resolution encoders.

**Linear Guide Alignment Issues**

When constructing a machine tool, it is very difficult to perfectly align the stages of the machine. Rather there is some misalignment that ensures that there will be error between the expected and actual position of a tool if the stages are assumed to be perfectly aligned. With modern micro-scale machine tools, the solution to this problem is to construct a highly repeatable machine tool and then calibrate it so that any stage misalignments can be compensated for with software following calibration.

Many of the methods of machine tool calibration suitable for macro-scale machine tools are not suitable for smaller micro-scale machine tools [68]. An inexpensive calibration technique suitable for such machine tools has recently been developed [68]. Using this method, a three axis micro-scale machine tool (mMT) with 100 nm resolution encoders was calibrated so that when endmilling slots, error in the depth of cut was only 0.8 μm per every 10 mm of travel [68], which is sufficient for micro-endmilling of slots that are tens of microns deep. However, when cutting a 1 μm

deep groove this still causes an error of up to 80% of the groove depth. Hence, an involved and expensive calibration technique would be required in order for most machine tools to be accurate enough to cut the groove given in the example specification.

**Issues Due to Tool / Workpiece Registration Uncertainty**

In a conventional cutting process, the cutting edge of a tool travels along a precisely controlled trajectory that insures that it passes through a workpiece at a desired depth. A difficulty that arises with this approach is that the location of the cutting edge must be known relative to the workpiece surface at all times during a cut with a level of accuracy at least as high as the tolerance on groove depth, assuming that all other factors contributing to uncertainty in the depth of cut are negligible. I.e., extremely accurate tool / workpiece registration is required. For example, if a one micron deep groove is to be cut with 10% relative depth tolerance, the registration accuracy must be at least 100 nm or better and if 1% relative tolerance is required the registration accuracy must be at least 10 nm or better, provided that other sources of error are negligible.

Three factors complicate acquiring and maintaining registration: (1) uncertainty in the cutting edge position, (2) uncertainty in the workpiece shape, and (3) uncertainty in the workpiece position. Uncertainty in the cutting edge position during registration can be caused by limitations in tool setting accuracy. Following registration, tool wear can cause additional uncertainty in the cutting edge position. For instance, if 15 nm of material wears off the edge of a tool, a value taken from experiments that will be discussed in Chapter 6, then the cutting edge is actually 15 nm further from the workpiece than indicated during registration, which would result in 1.5% additional error when cutting a 1 μm deep groove.

Uncertainty in the workpiece shape is a major problem when cutting grooves into a workpiece because it becomes necessary to know the exact shape of the workpiece to better than the groove depth tolerance. Hence, the tolerance than can be achieved either becomes dependent on the tolerances that can be achieved during production of the overall workpiece shape or a detailed high-accuracy metrology step must be added.

Uncertainty in workpiece shape can be particularly problematic with cutting patterns of grooves into the curved surface of a mold or die. This is because tolerances of approximately 100 μm may be acceptable on the overall part shape from a molding standpoint, but the inclusion of the micro-grooves increase the required tolerance to a fraction of a micron, which greatly increases cost. This is particularly true since in macro-scale die making a tolerance of about 25 μm is generally considered tight. Furthermore, even when parts have a much simpler planar geometry, tolerances of 1 μm or better can be difficult to achieve. This can be seen in Fig. 3.1, which shows a profile of a carefully ground and polished nickel workpiece prepared for used in micro-groove cutting experiments via several grinding and polishing operations. Hence, if extremely tight tolerances are not practical in operations that precede micro-groove cutting, detailed metrology of a workpiece is necessary, which increases manufacturing time and cost.

However, even if the exact shape of the workpiece is known, problems still arise if the orientation of the workpiece relative to the tool is not known with accuracy better than the groove depth tolerance. In order to achieve such accuracy, there must either be the ability to transfer a workpiece from any previous steps in a manner repeatable to at least than required tolerance or there must be a metrology apparatus integrated into the groove cutting machine tool. The former option can be achieved through the use of a

calibrated kinematically repeatable pallet [68], but great care must be taken for small positioning errors to not compound themselves such that the overall error is beyond the allowable tolerance. The latter option increases machine tool cost by the cost of the metrology system and detailed scanning of every workpiece can increase setup time by anywhere from minutes to hours depending on the system used.

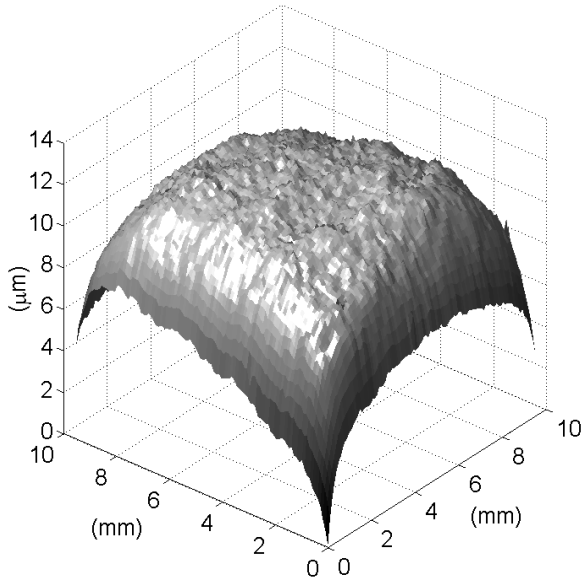


Figure 3.1: Polished nickel workpiece surface

**Machine tool Stiffness Issues**

In conventional machining, in order for a cutting tool to pass through a workpiece along a precisely controlled trajectory, it is necessary for the machine tool to be highly rigid. This is because the components of the kinematic linkage connecting the cutting edge and workpiece are subjected to various forces that that can cause them to deflect in unexpected ways. This introduces positioning uncertainty that is influenced by the machine structure, inertial forces from stage movements, and cutting forces.

At the micro-scale inertial forces can be particularly significant. This can be seen by mounting an extremely flat artifact to a machine tool in place of a workpiece and

mounting a laser displacement sensor in place of a tool. Ideally, in such a setup, the laser sensor would output a straight line profile if a single machine tool stage is traversed such that the laser scans along the test artifact. In practice, due to inertia, a deviation from this profile in excess of the roughness of the artifact can appear if the machine tool is insufficiently stiff. For example, Fig 3.2 shows the output of a laser displacement sensor fitted to a high-precision machine tool constructed by Phillip et al. [38] where one of the machines stages was moved back and fourth. It can be seen that inertia caused workpiece wobble that could introduce groove depth uncertainty as high as 300 nm, which indicates that this machine tool, costing about $50,000, would not be stiff enough micro-groove cutting using conventional micro-scale shaping / planing and a more expensive machine tool would be required.

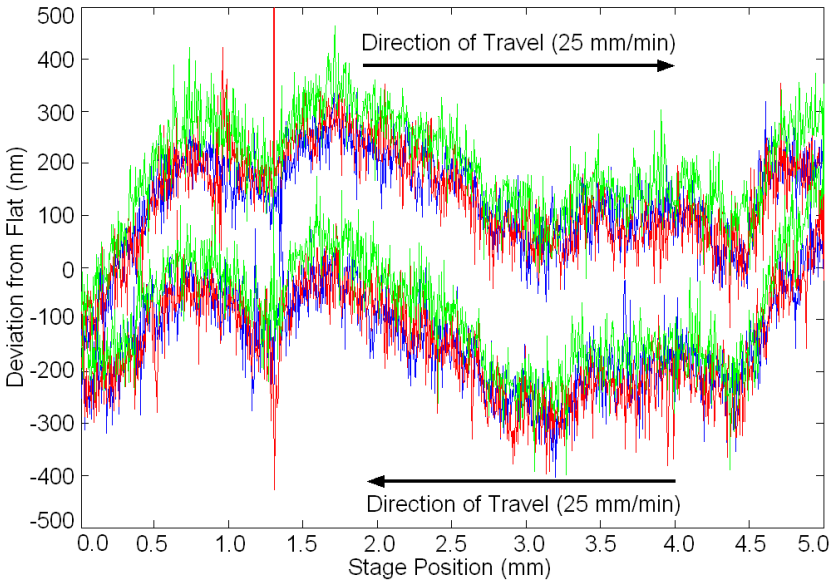


Figure 3.2: Apparent deviation from workpiece flatness due to inertia when translating a stage of an example 5-axis machine tool at 25 mm/min

## 3.3 Micro-Groove Cutting Process Design

### 3.3.1 Process Concept

In the previous subsection it was shown that there are several difficulties associated with conventional micro-scale shaping / planing processes that render micro-groove cutting at the desired size scale highly expensive. For example, The FANUC ROBOnanoUi machine [14] would likely enable the process requirements to be meet, but this machine costs over $1,000,000. Therefore, if chip formation-based metal cutting is to be used, some means of circumventing issues with encoder resolution, linear guide alignment, tool-workpiece registration, and machine tool stiffness must be developed.

In order to alleviate encoder resolution issues, some means of mechanically amplifying measured resolution instead of simply switching to increasing higher resolution encoders is desirable. Also, in order to deal with uncertainties in tool and workpiece position due to linear guide misalignments, insufficiently accurate registration, and inertial effects, a means of having the cutting edge of a tool follow a workpiece surface via some intrinsic process mechanic is desirable as well. Both of these features can be achieved through the use of a load-based cutting process.

Such a micro-groove cutting process, which is developed in this work, makes use a flexible cutting tool that can cut while applying selected loads via careful control of tool deflection. Such a tool can be configured much like an AFM probe, i.e., a flexible cantilever that is held on one end and with a protrusion on the other end that is intended to contact a surface. However, unlike an AFM probe, the geometry of the protrusion does not need to be suitable for metrology, but rather is optimized for cutting and will have a cutting edge. Such a tool is shown schematically in Fig. 3.3 and is essentially a

flexible micro-scale planing tool. This is the overall tool configuration use throughout this work.

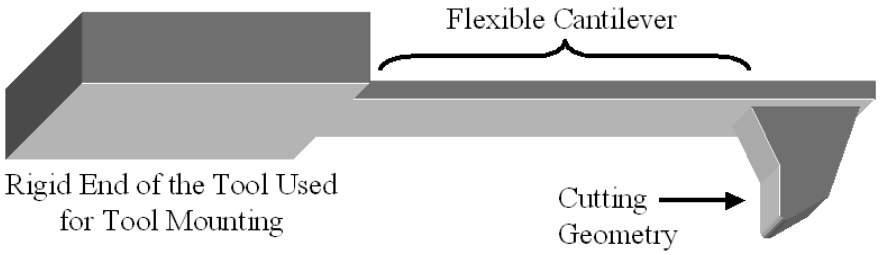


Figure 3.3: Example schematic of a flexible cutting tool

The cutting geometry of the tool, i.e., the geometry of the protrusion on the free end the cantilever, may very significantly depending on the application. A simple pyramidal geometry, which is already present on may AFM probes, might be used in some cases. In other cases, geometry like that found on a macro-scale shaping, planing, or parting tool might be used. Development of effective cutting geometries is the subject of later chapters in this work.

In order to cut a micro-groove, the held end of the flexible tool is first advanced towards a workpiece until the cutting edge of the tool contacts the workpiece. Advancing the held end of the tool even closer to the workpiece causes the cantilever to bend and applies a load onto the cutting edge, which causes it to sink into the workpiece. The amount of cantilever deflection, and hence the amount of applied load, is maintained at some target value via feedback, which can be time varying, in order to control the load on the cutting edge. While this occurs, the workpiece is traversed underneath the tool along a desired cutting path and a chip is formed from the action of the cutting geometry passing through the workpiece, as shown in Fig. 3.4. The resultant depth of cut is determined by the workpiece material, tool geometry, and cutting conditions.

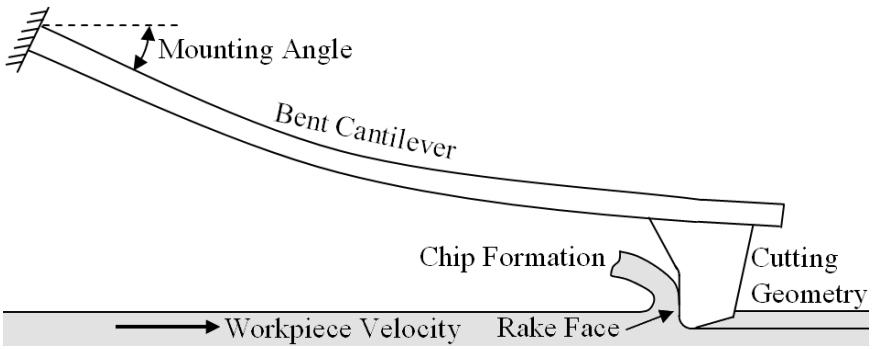


Figure 3.4: Micro-groove cutting

There are two major advantages to this concept that alleviate the four issues previously discussed. The first advantage is that use of a flexible cantilever to derive loads results in depth of cut resolution amplification. This is because the cantilever deflections required to develop a load that results in a depth of cut can be several times larger than the depth of cut. For example, it will be shown in Chapter 6 that a tool can be constructed with a 100 N/m stiffness that can cut a 1 μm deep groove in pure aluminum when a 1.4 mN load is used. To derive such a load a cantilever deflection of 14 μm is required. This is 14 times the resultant depth of cut. Hence, if two position sensors of equivalent resolution were used to measure stage position and cantilever deflection, it would be possible to know the load applied at the cutting edge with 14 times more resolution than stage position. This alleviates the issue associated with having a high enough encoder resolution.

The second major advantage is that the cutting edge is spring loaded against the workpiece. Hence, as long as constant cutting conditions are maintained, the cutting edge of the tool will pass through the workpiece at a constant depth. I.e., the cutting edge will follow a trajectory that adjusts itself based of the contours of the workpiece surface in order to maintain a set depth of cut. Hence, it is no longer necessary to eliminate

uncertainties in tool position relative to the workpiece surface due to linear guide misalignments, insufficiently accurate tool-workpiece registration, or undesired motions due to inertial effects on insufficiently stiff components. The reduction in required machine tool capability results in a significant reduction in cost. For example, using conventional micro-scale shaping / planing, a machine tool like the FANUC ROBOnano, which costs over $1,000,000, would be required. However, using the developed process, a machine tool costing less than a $100,000 can be employed instead.

### 3.3.2 Process Parameters

Several process parameters are associated with the new micro-groove cutting process. Some of these are familiar from micro and macro-scale shaping / planing and others are introduced by the use of a flexible tool. Parameters 1-6 make up the former set and parameters 7-11 make up the latter set.

1. Cutting speed
2. Cutting edge radius, $r_e$
3. Rake angle
4. Rake face shape: E.g. a rake face with a rectangular shape will cut a groove with a rectangular cross-section and a rake face with a v-shape will cut a groove with a v-shaped cross-section.
5. End clearance angle
6. Side clearance angles
7. Mounting angle: the angle the non-bending end of the tool is held at relative to the workpiece surface, as defined in Fig. 3.4.

8. Applied cutting load: the load applied at the cutting edge along a direction coincident with the direction of approach of the tool towards the workpiece (typically normal to the workpiece surface). This load is set by setting amount of cutting edge displacement, cantilever stiffness, and the mounting angle.
9. Cutting edge displacement: displacement of the cutting edge of the tool along the same direction that the cutting load is applied.
10. Overall tool cantilever stiffness: the amount of applied load at the cutting edge that results from a unit cutting edge displacement.
11. The maximum applied load that does not result in cantilever breakage.

### 3.3.3 Issues that Arise Due to the Use of a Flexible Tool

There a three issues introduced by the use of a flexible cutting tool that must be addressed. These are indirect control of depth of cut, cantilever bending behavior, and the increased complexity of setting the rake angle.

The first issue arises from the fact that the trajectory of the tool cutting edge is not directly controlled, and hence the depth of cut is not directly controlled. Rather, a cantilever deflection is controlled, which results in a load being applied at the cutting edge. The depth of cut that results from this load is determined by cutting conditions, tool geometry, and workpiece material. The relationship between these factors must be either determined experimentally or via simulations based on cutting mechanics.

The second issue that arises from the use of flexible tool is the need to account for the behavior of the tool cantilever. Specifically, there is a need to select cantilevers with suitable stiffnesses, to be able to calculate the deflection required to generate a given load, and to insure that cantilever plastic deformation or breakage does not occur.

Mathematical models of varying complexity exist that enable these tasks to be performed. For the cantilevers used in this work, Euler-Bernoulli cantilever beam theory is adequate.

Figure 3.5 shows a cantilever beam, of length L, which is fixed on one end and free on the other end. If a load of magnitude P and / or a moment of magnitude M is applied to the free end, it the resultant deflection, d, is given by Equation (3.1) where E is the modulus of elasticity and I is the area moment of inertia of the cantilever. The cantilever stiffness can be found by dividing the applied load by resultant deflection. Equation (3.2) provides the end angle, ω, of the beam in radians. Equation (3.3) can be used to calculate the maximum tensile stress in the cantilever, $\sigma_{max}$, which in the figure, occurs on the bottom of the fixed end of the cantilever. In the equation, c is the distance between the neutral axis of the cantilever and the bottom of the cantilever.

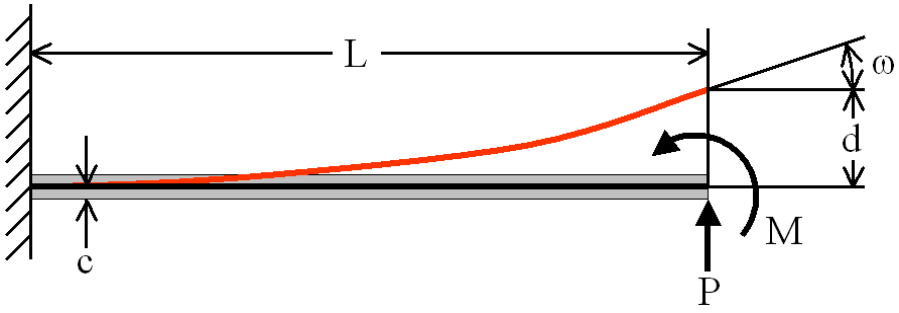


Figure 3.5: Cantilever beam

(3.1) $$d = d_{Load} + d_{Moment} = \frac{P L^3}{3 E I} + \frac{M L^2}{2 E I}$$

(3.2) $$\omega = \omega_{Load} + \omega_{Moment} = \frac{P L^2}{2 E I} + \frac{M L}{E I}$$

(3.3) $$\sigma_{Max} = \frac{M_{Base}\, c}{I} = \frac{(L P + M)}{I}$$

Using Equations (3.1) and (3.2) bending characteristics of cantilever can be predicted, and by using Equation (3.3) in conjunction with cantilever material properties, the amount of applied load required for cantilever breakage due to material plastic deformation or fracture can be found. Using these equations, a tool cantilever shape and material must be selected so that enough flexibility is achieved to insure sufficient resolution amplification, as described earlier. Conversely, the tool must be stiff enough and strong enough to insure that loads can be developed that are sufficient to achieve a desired depth of cut.

The third issue that arises from the use of flexible tools is increased complexity involved in setting the rake angle during cutting. This is because the orientation of the rake face of a flexible tool changes whenever the cantilever portion of the tool bends, as shown in Fig. 3.6. Hence, the rake angle is not set by geometry alone. Rather, the rake angle is dependent on cutting forces that bend the tool cantilever as well as tool geometry and tool orientation.

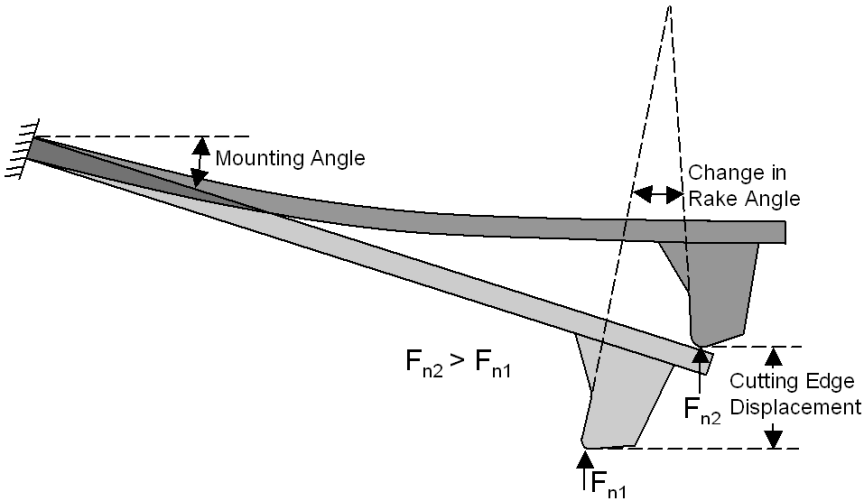


Figure 3.6: Change in rake angle due to applied load

As can be seen in Fig. 3.6 increased bending of the tool due to increased cutting forces normal to the workpiece surface will result in a more negative effective rake angle. Also, a greater mounting angle will result in a more positive effective rake angle. Both these effect must be accounted for in order to set the rake angle during cutting.

Additionally, it should be noted that when cutting micro-scale grooves, the assumption of a sharp tool might be invalid in some cases, which further affects the rake angle. As described in Chapter 2, this occurs when the finite edge radius of the tool is similar in magnitude to the uncut chip thickness. This edge radius effect has been addressed by many researchers and causes the effective rake angle to be more negative than it would be otherwise.

### 3.3.4 Required Process Planning / Setup

During micro-groove cutting, the ultimate goal is to cut a high quality micro-groove of some desired depth that might vary over the course of the cut. This involves having the cutting edge of the tool pass through the workpiece at controlled depths while the rake face of the tool maintains a constant orientation suitable for achieving good performance, i.e., the depth of cut is controlled and the rake angle does not change. However the depth of cut in turn depends on cutting conditions such a speed and applied load, cutting geometry, and workpiece material. Therefore, it is necessary to be able to accurately control the load applied to the tool during cutting, which is empirically related the depth of cut, and to control rake angle.

The applied cutting load is generated by bending of the tool cantilever, and hence in order to control the magnitude of the applied load the amount of cantilever deflection must be controlled. As a load is applied to the cutting edge, the cantilever portion of the

tool will bend by an amount corresponding to the magnitude of the load, which in turn sets the orientation of the cutting geometry. As described in the previous section, this is problematic because the rake and clearance angles of the tool then become a function of cutting load, and hence could end up varying between cuts or even over the course of a cut if several different depths of cut are desired. This issue is avoided by taking advantage of the fact that both the load on the cutting edge and the orientation of the end of the tool cantilever are set by the amount of cantilever displacement at some point (the cutting edge is used in this work) and the angle the tool mounting angle. Hence, a desired cutting load and cutting geometry orientation can be achieved by correctly setting these two values.

The required cutting edge displacement and mounting angle must be calculated at the start of each cut and at every point where there is a change in the desired depth of cut, and hence a change in the required cutting load. The calculation of these values can be achieved by using a cantilever beam model of the tool, or alternatively a finite element model of the tool. In this work, a cantilever beam model is used where the cantilever portion of the tool is treated as an Euler-Bernoulli beam, and the cutting geometry is assumed to be rigid. A diagram of this model is shown in Fig. 3.7.

In the model, cutting forces are assumed to be applied only at the cutting edge. It is also assumed that the applied force is oriented normal to the workpiece surface and equals $F_n$. Force in the cutting direction, $F_c$, is neglected because it is unknown and because it is not expected to contribute much to cantilever deflection. This is because $F_c$ acts on the cantilever via a moment developed by pushing on the cutting geometry, and due to the shape of the tool the corresponding moment arm is small. All angles are

specified such that rotations in the counterclockwise direction are positive. Hence, the tool mounting angle defined previously is denoted as –θ, and the tool end angle is denoted as ϕ.

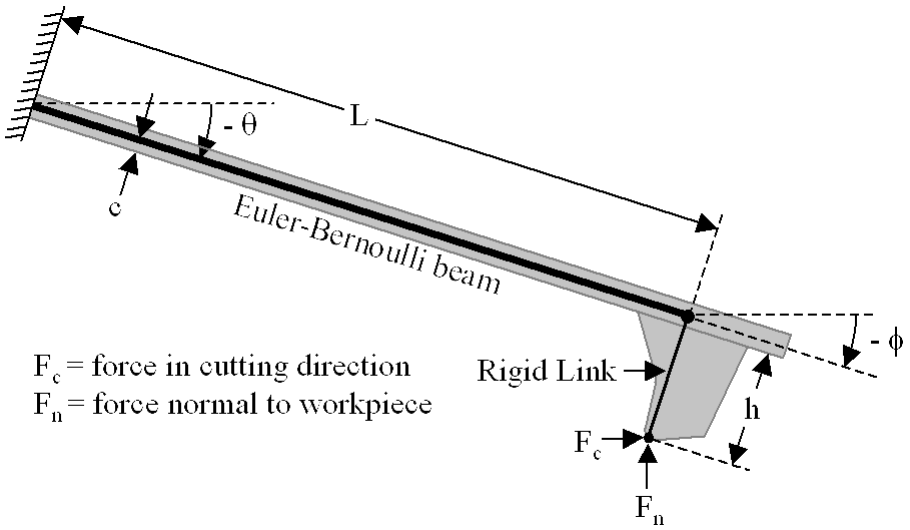


Figure 3.7: Cantilever beam model of flexible tool

The end angle of the tool can be calculated via Equation (3.4) where the other term in the equation, ω, is given by Equation (3.2). The end angle is used calculate the loads applied to the Euler-Bernoulli beam as shown in Equations (3.5) and (3.6) where h is the distance the cutting edge extends from the cantilever. Note that Equations (3.1) – (3.6) are coupled and may be solved iteratively. The displacement at the cutting edge, δ, can be found from geometry and is given by Equation (3.7).

(3.4) $$\phi = \theta + \omega$$

(3.5) $$P = F_n \cos(\theta)$$

(3.6) $$M = Fn\left(h + c\right)\sin(\phi)$$

(3.7) $$\delta = d\cos\theta - \left(c + h\right)\cos\phi + \left(c + h\right)\cos\theta$$

This model is used during planning of the start of each cut and of every point where there is a change in the desired cutting load. At these points, the desired load and a candidate mounting angle is fed into the model, which outputs the required cutting edge displacement and the resultant end angle of the tool, and hence the orientation of the cutting geometry as a result of cantilever bending. The mounting angle is varied iteratively until the cutting geometry orientation is as desired, i.e., it is some constant value dictated by the tool design. The pairs of cutting edge displacement and tool orientation values form two trajectories that are followed during the actual cutting operation.

## 3.4 Machine Tool Requirements

A machine tool used to implement the described micro-scale groove cutting process must have several capabilities. These include (1) the ability to measure tool deflection at a sufficient speed and with a sufficient amount of accuracy, (2) the ability to control the mounting angle, (3) the ability to control the orientation of the tool relative to the direction of cut, and (4) adequate tool / workpiece positioning. Each of these requirements and the reasoning behind them are described in this section.

### 3.4.1 Deflection Measurement Requirement

Any machine tool intended to make use of the described micro-groove cutting process must incorporate a sensor capable of measuring tool cantilever deflection. Several types of sensors can be used for this purpose. For instance, the optical lever-based laser displacement sensor commonly used in atomic force microscopes could be used. This inexpensive yet highly sensitive sensor works by shining a laser beam onto

the back of a cantilever and positioning photosensors in the path of the beam such that more light will hit some sensors and less light will high others depending on the angle of the reflected beam, which is in turn dictated by the amount of cantilever deflection. Other sensors can include confocal laser displacement sensors, capacitive sensors, and strain gage-based sensors. However, in the latter case the sensor would have to be incorporated into the flexible tool rather than being part of the machine tool.

The tool deflection measurement sensor must have sufficient measurement range, sufficient bandwidth, and sufficient resolution. The required measurement range is dictated by the maximum amount of tool deflection desired during a cut. Depending the tool design this value can varying arbitrary since an increasingly long cantilever can bend by increasing large amounts prior to permanent breakage. For example, in this work, a minimum measurement range of 20 μm is required since all of the tools used, and discussed in later chapters, would fracture at or prior to this deflection. Such a small measurement range is well within the capabilities of most sensors.

Required sensor bandwidth is determined by the maximum desired cutting speed, and the required distance between measurements in the direction of cut. This distance, in turn, is selected such that a cutting load can be maintained in the presence of changes in the workpiece surface height or material properties. If cutting speed, S, is given in mm/min, sample frequency, f, is given in Hz, and the required distance between measurements, $d_{meas}$, is given in microns, then the required bandwidth is given by Equation (3.8).

$$f = \frac{1000\,S}{60\,d_{meas}} \tag{3.8}$$

Hence, a homogeneous workpiece with a simple surface profile that does not change in height much can be cut using a low bandwidth sensor. Alternatively a low cutting speed can be used to enable the use of a low bandwidth sensor. On the other hand, higher bandwidth sensors enable more complex workpieces to be used and higher cutting speeds to be employed. For example, say that a workpiece is homogeneous and the surface height varies sinusoidally in the direction of cut such that there is a distance of 100 μm between peaks. Also let it be assumed that 20 adjustments in cantilever deflection are sufficient to follow the feature and that the cutting speed is 400 mm/min. Then distance $d_{meas}$ = 5 μm and the required sensor sample rate = 1333 Hz. This is close to the 1562 Hz bandwidth of the sensor chosen for this work, which is discussed in more detail later in this chapter.

Required sensor resolution is determined by the specified groove depth tolerance and the ratio of tool deflection to resultant groove depth, which in turn depends on tool stiffness and the amount of cutting load required to achieve a given depth of cut. If the tool stiffness, k, is given in N/m, the required load to cut a feature, $F_n$, is given in mN, and the required relative tolerance, $t_{rel}$, is given in percent, then the required resolution, r, given in nm, can be estimated by equation (3.9)

$$r = \frac{10{,}000\, F_n\, t_{rel}}{k} \tag{3.9}$$

For example, it will be shown in a later chapter that it is possible to construct a tool that will cut a 1 μm deep groove into a pure aluminum workpiece when a cutting load of 1.4 mN is used. Hence, if this tool has a 100 N/m stiffness, a deflection of 14 μm is required to achieve this depth of cut. Therefore, in order to avoid load, and hence depth of cut, variations of greater than 1% a sensor resolution of 140 nm would be

required, which is readily achievable. The required resolutions would increase if the depth of cut was decreased and the same relative tolerance was required and would decrease if a less stiff cantilever was used.

### 3.4.2 Tool Mounting Angle Control Requirement

As described previously in this chapter, it is necessary to adjust the angle a flexible tool is held at relative to a workpiece surface, the mounting angle, in order to apply a desired cutting load while maintaining a desired rake angle. Furthermore, since the required load may vary over the course of a cut it is necessary to be able to vary the mounting angle simultaneously. Therefore, a suitable machine tool must include a rotary stage that allows the tool mounting angle to be varied. The total amount of allowable variation need not be more than about 10° to accommodate all the flexible tools used in this work.

### 3.4.3 Tool Orientation Control Requirement

Cutting geometries suitable for use in cutting micro-grooves will generally consist of a rake face, cutting edge, and non-cutting clearance faces. During cutting, the tool must be orientated such that chips separate from the workpiece at the cutting edge and flow up the rake face. The tool must also be oriented such that there is little to no rubbing between the workpiece and non-cutting faces of the tool. This means that the direction of cut dictates how the tool must be oriented or vise versa. This is shown in Fig. 3.8 where three example cuts are shown from a top down perspective where only the cutting geometry, and not the rest of the tool, is drawn. Additionally, since the cutting geometry of a flexible tool is mounted onto the end of a cantilever, it is desirable for the

tool to cut through the workpiece in a direction coincident with the central axis of the cantilever in order to prevent cantilever twisting due to cutting forces.

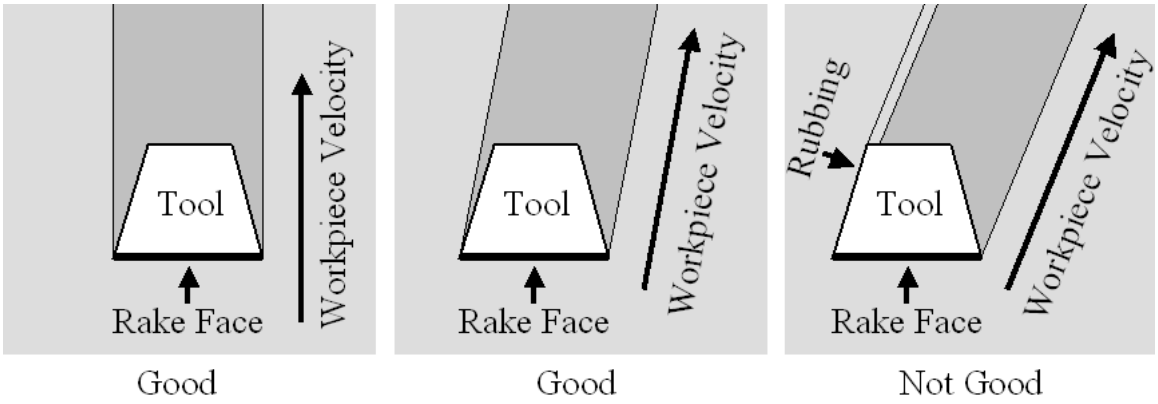


Figure 3.8: Example cutting tool orientations relative to direction of cut

Both the need to avoid rubbing between the workpiece and non-cutting faces of the tool and the need to avoid cantilever twisting impose restrictions on allowable cutting trajectories. To overcome this limitation it is necessary to be able to rotate either the tool or workpiece relative to the direction of cut. Therefore, the machine tool must incorporate a rotary stage that enables either the workpiece or flexible cutting tool to be rotated.

## 3.4.4 Machine Tool Stage Requirements

As mentioned when discussing the previous two requirements, two rotary stages are required in order to be able to control the tool mounting angle and in order to be able to change the orientation of the tool relative to the direction of cut. The former stage must have a range of travel of at least 10° to accommodate the various tool mounting angles that may be necessary. The latter stage must be able to rotate freely without limit in order to be able to perform the kinds of movements required to insure correct tool orientation relative to the direction of cut at all times.

In addition to the rotary stages, at three linear stages are also required: two stages to traverse the workpiece underneath the flexible cutting tool and one stage to control the distance between the workpiece and the held end of the flexible tool. The required resolutions of the first two linear stages and the rotary stage that controls the orientation of the tool relative to the direction of cut is dictated by the required tolerance on groove path shape. Specifically the resolution must be set high enough that no location on the workpiece dithers more than the allowable tolerance on groove path shape where stage dither will inevitably be at least ± 1 count. The resolution on the stage controlling the distance between where the tool is held and the workpiece can be set lower since tool deflection is what is regulated during cutting as opposed to stage position.

## 3.5 Developed Micro-Groove Cutting Machine Tool

A machine tool has been constructed in order to implement the micro-groove cutting process previously described in this chapter and to satisfy the requirements described in the previous section. This machine tool consists of two parts: a groove cutting assembly and a 5-axis motion platform onto which the assembly is mounted. The groove cutting assembly includes all the hardware required to make use of a flexible tool that would not tend to be included on a conventional machine tool. The motion platform is an existing 5-axis micro-scale machine tool (mMT) that was previously developed at the University of Illinois at Urbana-Champaign (UIUC) [38] and used to study micro-endmilling. The spindle of the mMT has been removed to make room for the groove cutting assembly.

## 3.5.1 Groove Cutting Assembly Description

A groove cutting assembly has been constructed for holding a flexible cutting tool and measuring deflection of the tool due to applied forces during cutting and workpiece registration. The assembly is shown schematically in Fig. 3.9 mounted into the rotary b-stage of the motion platform that is described in the next subsection. As shown in the figure, the assembly consists of five parts: (1) a tool holder bar, (2) a 3-axis manual positioning stage, (3) a base plate, (4) an upright sensor mounting block, and (5) a confocal laser displacement sensor.

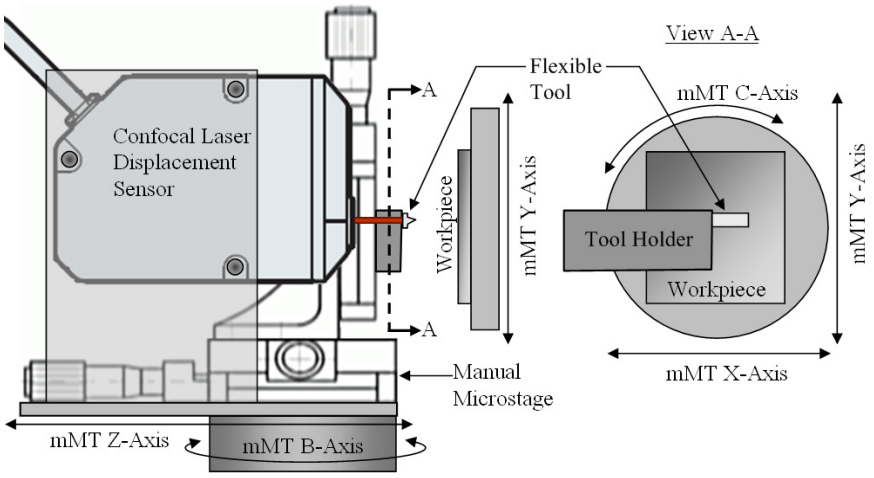


Figure 3.9: Schematic of the micro-groove cutting assembly

Prior to use, a flexible cutting tool is mounted to the tool holder bar via Aquabond™ thermal adhesive as shown in Fig. 3.10. This is accomplished by heating the tool holder bar on a hot plate to a about 110° C, melting some of the adhesive onto the mounting site, gently setting the rigid end of the tool into the adhesive, and then allowing the tool holder bar to cool back to room temperature. Note that the contact site is set at an angle relative to the rest of the tool holder, which insures that the tool cutting geometry is always closer to the workpiece than any other point on the tool. This insures

that rubbing between other parts of the tool and the workpiece does not occur and cause undesirable gouging of the workpiece during groove cutting.

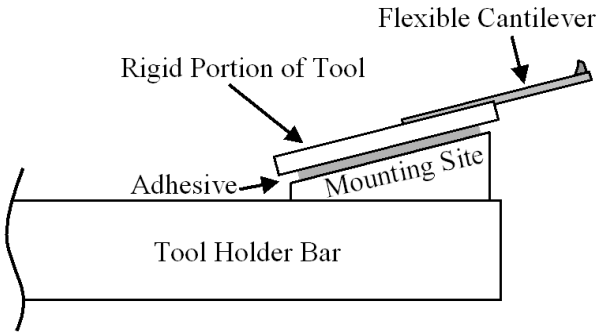


Figure 3.10: Mounting of a flexible tool to the tool holder bar

The tool holder bar is shown in Fig. 3.11. After gluing on a tool, the tool holder bar is attached to a 3-axis manual micro-positioning stage via three M4 bolts. Additionally, there are two 0.125" diameter hardened steel dowel pins press fit into the tool holder bar, which correspond to two high precision alignment holes drilled in the micro-positioning stage. These pins constrain the tool holder bar's placement much more effectively than bolts alone would, which in turn cuts down on drift in tool holder bar position than occurs as the bolts settle slightly in the hours following tightening.

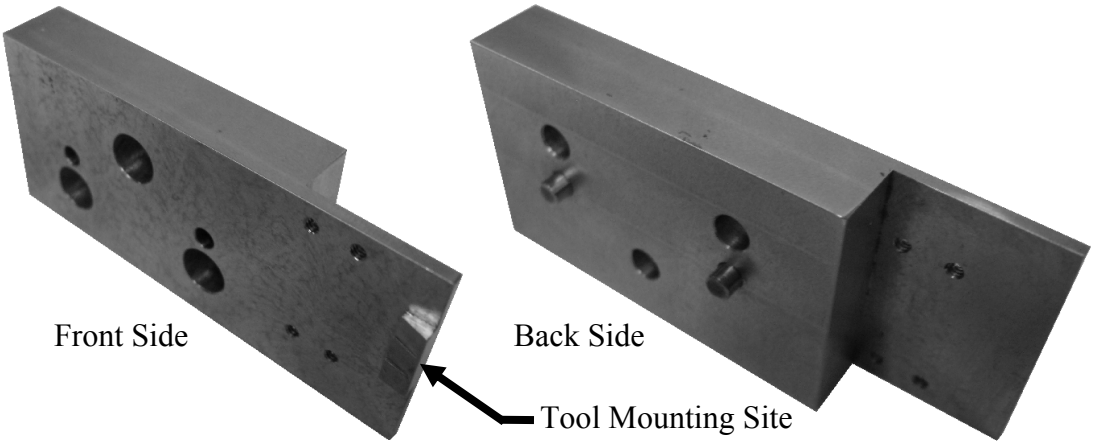


Figure 3.11: Tool holder bar

The 3-axis manual micro-positioning stage is used to adjust tool position in order to align the end of the cantilever portion of a flexible tool with the beam from a confocal laser displacement sensor, which is used to measure tool deflection. The manual micro-stage, shown in Fig. 3.12, consists of a Standa 7T264-10SS ultra low profile two-axis micro-stage connected to a Standa 7T164-10 single-axis micro-stage via a 90-degree angle bracket. Each axis of the manual micro-stage has 10 mm of travel and an adjustment sensitivity of 1 μm.

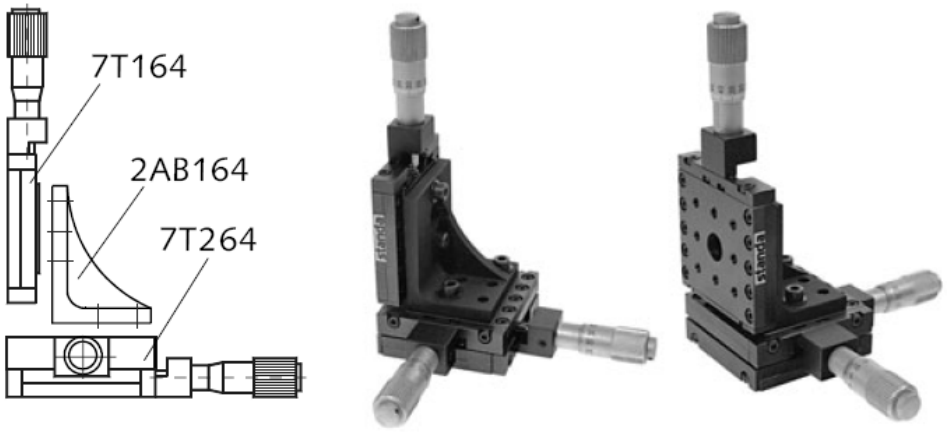


Figure 3.12: Standa manual micro-positioning stage [36]

The manual micro-stage is bolted to a base plate that is into turn bolted onto the b-stage of the 5-axis motion platform. Also bolted to the base plate is an upright sensor mounting block, and bolted to this block is a Keyence LT-9010M confocal laser displacement sensor.

The Keyence LT-9010M confocal laser displacement sensor, shown in Fig. 3.13A, is used to measure tool deflection during cutting and workpiece registration. The sensor can measure displacements with a resolution of 10 nm and has a measurement range of ± 0.3 mm. The spot size of the laser is 2 μm in diameter, which is small enough to focus onto the 15 μm - 60 μm wide cantilevers used in this work. The sensor can be

set to continuously measure the displacement of a single spot on a tool (displacement mode) or to continuously sweep back and forth (scanning mode). The former option allows displacement of a single point to be measured at a rate of 1562 Hz, while the latter option allows the bent shape of the tool to be measured at a rate of 27 Hz via 13 points located at 10 μm lateral increments. The sensor also has a built-in optical microscope, and an example of the output from the microscope during cutting is shown in Fig. 3.13B.

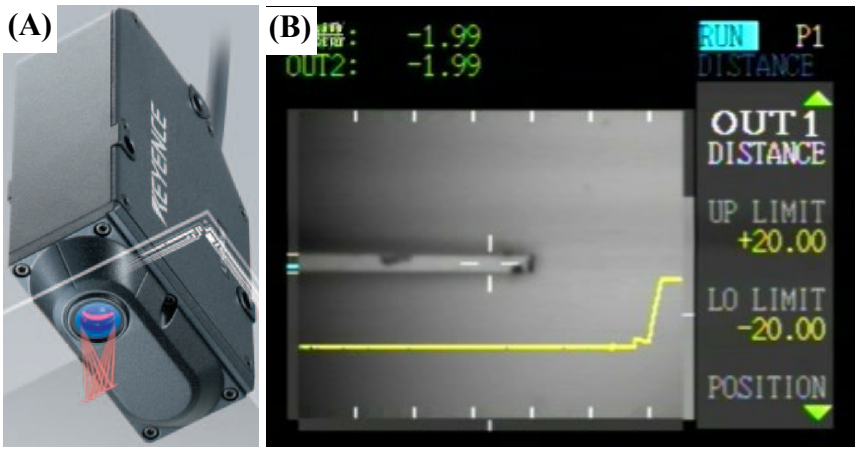


Figure 3.13: Keyence LT-9010M confocal laser displacement sensor (A) [37] and video output from sensor (B)

The outputs from the sensor of interest consist of a the video signal transmitted via USB, a voltage proportional to the measured displacement, a voltage flag indicating when a new measurement is being output, and a second voltage flag indicating the start of a scan when the unit is in scanning mode. The voltage indicating the measured displacement value can vary between +10 and –10 volts. In this work, the sensor is configured such that +10 volts indicates a measured value of +20 μm, 0 volts indicates a measured value of 0 μm, and –10 volts indicates a measured value if –20 μm.

The fully assembled micro-groove cutting assembly is shown from several different angles in Fig. 3.14. In the figure, the base plate is sitting directly on a tabletop

surface. A bolt circle consisting of 5 holes, and visible in Fig. 3.14A and Fig. 3.14B, is cut into the base plate and used for mounting of the base plate onto the rotary b-stage of the 5-axis motion platform.

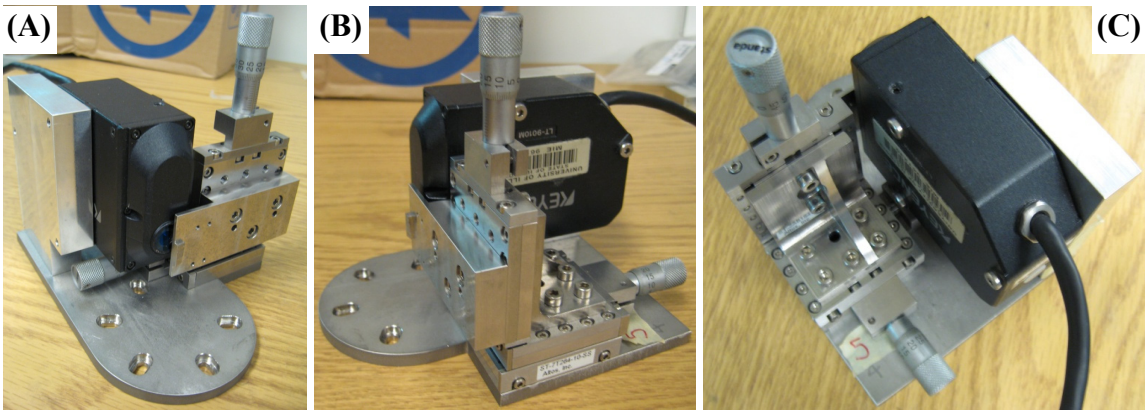


Figure 3.14: Micro-groove cutting assembly

It was found that during some groove cutting assembly movements that occur during cutting, the inertia of the upright axis of the manual micro-positioning stage and the tool mounting bar was sufficient to overcome the restraining forces imposed by springs inside the other two axis of the manual micro-positioning stage. As a result the tool holder would sometimes vibrate in an undesired manner. The amplitude of this vibration was only a few microns, but at the size scale involved such vibration is unacceptable, and is avoided by adding the ability to lock the position of the manual micro-positioning stage. This is accomplished via the addition of a c-clamp that is tightened once the stage is in position as shown in Fig. 3.15.

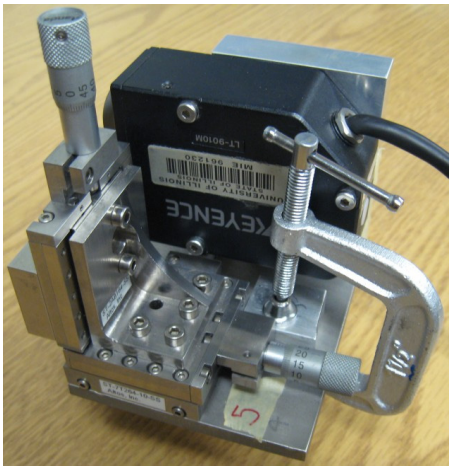

Figure 3.15: Clamping of manual micro-position stage to lock its position

## 3.5.2 Description of the 5-Axis mMT Motion Platform

The groove cutting assembly was mounted onto the rotary b-stage of an existing 5-axis mMT that was previously developed at the University of Illinois and Urbana-Champaign (UIUC) [38]. The mMT served as a motion platform for linearly translating and rotating the micro-groove cutting assembly, and is shown in Fig. 3.16. This machine was selected because of the high positional accuracy of its stages and because of the ability of the workpiece to be rotated 360 degrees. Note that in the figure the spindle that would normally be attached to the machine has been removed to make room for the micro-groove cutting assembly, which mounts to the bolt circle on the b-stage of the machine.

The stages of the mMT are driven by linear and rotary brushless AC motors. The travel of the linear x, y, and z stages is 35 mm and each stage is equipped with an optical linear encoder with 20 nm resolution. The machine also has a rotary b-stage that allows the micro-groove cutting assembly to rotate up to 180 degrees and a c-stage that allows

the workpiece to be rotated 360 degrees. Each rotary stage is equipped with an optical rotary encoder with a resolution of 0.316 arcsec [38].

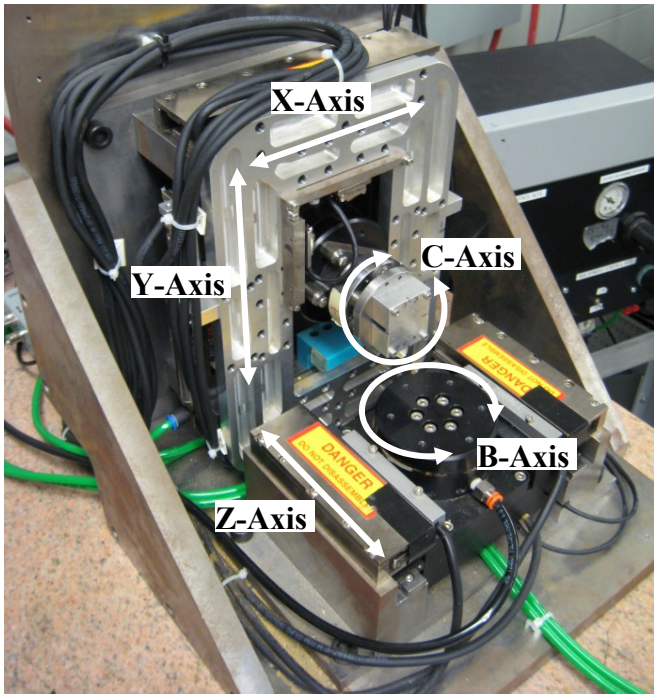


Figure: 3.16: 5-axis mMT [38] without spindle attached

Workpieces are mounted to detachable pallets, like the one shown in Fig. 3.17, that join the to rotary c-stage of the mMT via a repeatable kinematic coupling. The coupling consisting of 3 balls and mating v-grooves and is held together via magnets. The use of these pallets allows workpieces to be removed and then replaced with approximately 1 μm repeatability.

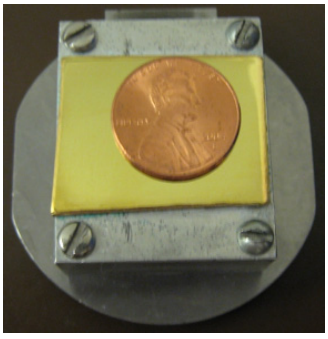

Figure: 3.17: Workpiece kinematic pallet

### 3.5.3 Groove Cutting Assembly / mMT Hardware Integration

The groove cutting assembly was bolted to the b-stage of the 5-axis mMT as shown in Fig. 3.18, which was taken from the same angle as the image of the mMT without the groove cutting assembly in Fig. 3.16. This configuration enables the groove cutting assembly to be brought towards or retracted from the workpiece via the z-stage and rotated via the b-stage. The workpiece can also be traversed in an x-y plane perpendicular to the direction of approach of the groove cutting assembly (the z-axis) and can be rotated about an axis parallel to the z-axis.

Figure 3.18: 5-axis mMT with groove cutting assembly attached

As stated earlier in this chapter, the tools used in the micro-groove cutting process only cut effectively in a narrow range of directions. For the tools used in this work, these directions are nearly coincident with the axis of the tool cantilever. Also, the tools were always mounted to the tool holder bar such that the axis of the cantilever nearly aligned with the x-axis of the mMT. Hence, all cuts must be made such that the vector component of the instantaneous workpiece material velocity, near the cutting zone, in the

y-direction is very small. This constraint would limit the types of groove patterns that could be cut if the machine only had 3 linear axes and the tool was limited to a fixed orientation. However, since the workpiece can rotate via the mMT c-stage, it is possible to change the rotary orientation of the tool relative to the workpiece. This renders it possible to produce curvilinear grooves without violating the velocity constant, as shown in Fig. 3.19.

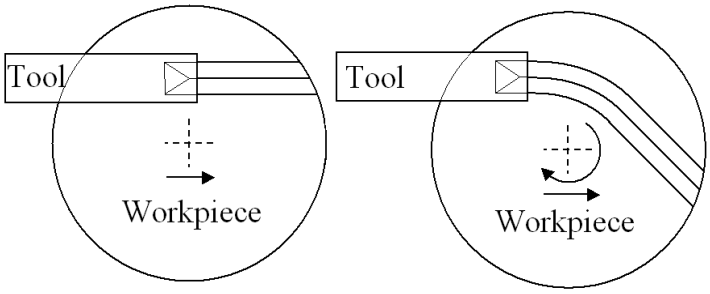


Figure 3.19: Ability of workpiece rotary stage to enable curvilinear cuts

## 3.5.4 Groove Cutting Assembly / mMT Electronics Integration

The 5-axis mMT is controlled by a fully programmable open architecture Delta Tau Turbo UMAC CNC controller [130]. This controller can be configured to control various numbers of machine axes, to provide various numbers of channels of digital I/O, and to provide various numbers of channels of analog I/O by adding or removing expansion cards and setting software flags. Implementation of PID control with feedforward for each machine axes and coordinated trajectory control for multiple axes is implemented on the controller in its factory provided state. Additionally, user programs can be run on the controller that directly read from input channels, perform various calculations, and affect the actions of any of the controlled stages.

In addition to being configured to control the 5-axis mMT, the controller is also configured to accept inputs from the Keyence LT-9010M confocal laser displacement

sensor. Specifically, the controller reads three analog outputs from the laser sensor using three 16-bit analog to digital (A2D) converter channels: an output voltage proportional the measured displacement, an output voltage flag indicating a new reading, and an output voltage flag indicating the start of a new scan with the laser is set in scanning mode. The sample rate is 5000 Hz, which is the servo cycle update frequency of the controller.

## 3.6 Groove Cutting Machine Tool Operation

In order to cut a set of micro-grooves using the developed process, five operations must be performed. First, process planing must be carried out. This involves calculating the orientation that the tool must be held at and the necessary amount of tool deflection for each cut to be performed as described previously in this chapter. Second, the tool must be mounted to the tool holder bar and the position of the bar must be adjusted to allow the laser displacement sensor to reliably measure tool deflection. Third, the workpiece must be registered such that the location of the cutting edge to the tool is known relative to the workpiece surface. Fourth, the tool / laser displacement sensor must be calibrated in order to relate displacement at the cutting edge of the tool to laser displacement sensor output. Fifth the grooves are cutting into the workpiece. Each of these operations is described in the remainder of this chapter.

### 3.6.1 Tool Setting

The tool to be used is mounted onto the tool holder bar using Aquabond™ thermal adhesive such that it is oriented as shown in Fig. 3.20A. Next the tool holder bar is bolted to the 3-axis manual micro-stage included in the groove cutting assembly. The manual micro-stage is then adjusted to get the end of the cantilever portion of the tool to

appear in the crosshairs of the Keyence LT-9010M confocal laser displacement sensor microscope output as shown in Fig. 3.20B. Note that the cantilever will appear horizontal in the image if it is properly mounted to the tool holder bar. Additionally, the manual micro-stage is used to adjust the distance between the cantilever and laser displacement sensor such that the sensor output reads between -10 and 0 μm. Lastly, the manual micro-stage is locked in place via a clamp, as shown in Fig. 3.15, in order to minimize undesired movement during cutting.

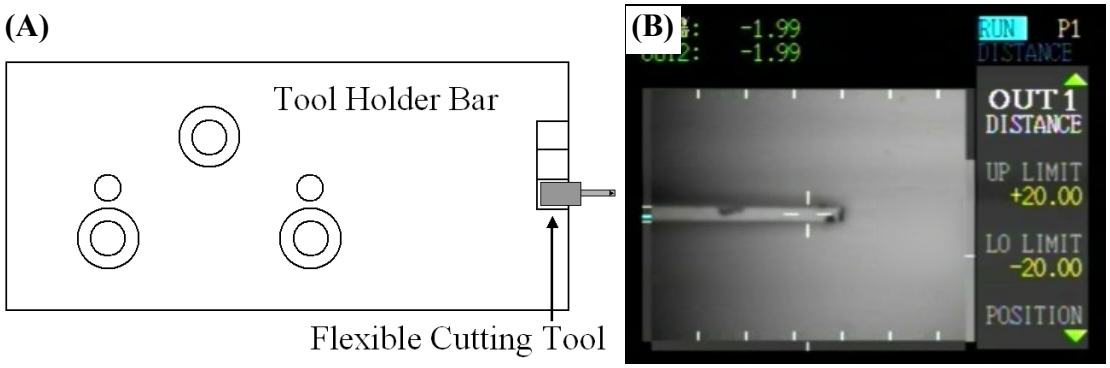


Figure 3.20: Mounted tool orientation (A) and aligned tool seen in the microscope (B)

Following tool setting, there may be a period where the output from the laser displacement sensor will drift with time. One cause is thermal effects within the laser sensor itself, which can be minimized by turning on the sensor at least an hour prior to use so that it can reach a steady state temperature. Another cause of drift is slight shifting in the bolts used to mount the tool holder bar and slight shifting of the clamp used to lock the manual micro-stage. This drift typically reduces to an acceptable level of about 5 nm per minute or less within one hour. The time required for the drift to reach acceptable levels can also sometimes be decreased by gently tapping the manual micro-stage.

## 3.6.2 Workpiece Registration

The workpiece must be registered such that the location of the cutting edge of the tool is known relative to the workpiece surface. This can be done via a series of tool / workpiece touch-off operations because the cutting tool is sufficiently flexible for even light contact between the tool and workpiece to cause a detectable tool deflection. Hence, the location of a point on the workpiece surface relative to the cutting edge of a loaded tool is found by advancing the z-stage of the mMT, and hence the groove cutting assembly, towards the workpiece until a readily detectable deflection occurs. In this work, such a deflection was considered to occur when the signal from the laser sensor, filtered via a digital 4$^{th}$ order Butterworth low pass filter with a cutoff frequency of 50 Hz, exceeded a 80 nm threshold. The full touch-off procedure is shown via a flow chart in Fig. 3.21.

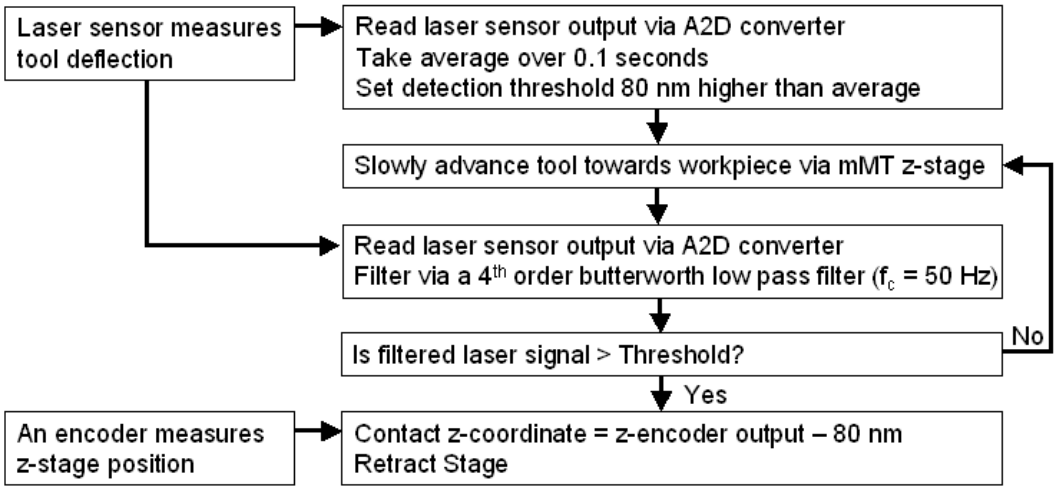


Figure 3.21: Tool / workpiece touch-off procedure

All of the workpieces used in this work could be idealized as planes. Hence, registration consisted of touch-off operations against three points on a workpiece that were not co-linear and then fitting the coordinates of these points to a plane. This method

can also be extended to registration of non-planar workpieces provided that the workpiece geometry is well known and a sufficient number of touch-off operations are performed in order to enable a linear regression of the contact coordinates to the known geometry.

### 3.6.3 Tool Calibration

Prior to cutting, a calibration operation must be carried out in order to relate laser displacement sensor output to actual displacement of the cutting edge of the tool. This is necessary because variations in tool mounting position, and hence the portion of the tool seen by the sensor, would otherwise render it difficult to correlate measured displacement to displacement at a known point on the tool, as shown in Fig. 3.22. Furthermore, only deflection of a known point on the tool can be mathematically related to applied cutting load, which in turn controls the depth of cut.

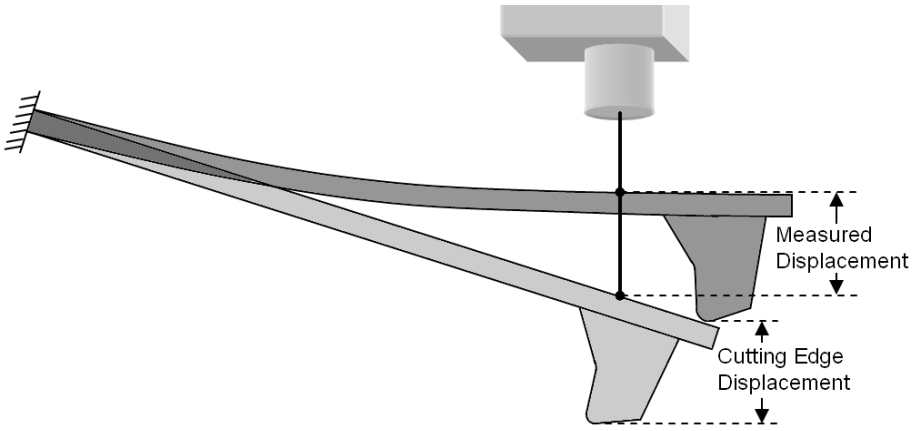


Figure 3.22: Cutting edge displacement and measured displacement

A calibration curve is generated by moving the cutting edge of the tool into contact with a flat alumina artifact and then continuing to move the groove cutting assembly some additional distance toward the artifact. Laser sensor output is related to the additional distance traveled to generate a calibration curve. Also, in cases where a

tool is to be held at significantly different angles when cutting at different loads, a calibration curve may be generated for each angle in order to enable more precise control of the applied load. The full calibration procedure is shown via a flow chart in Fig. 3.23 and an example calibration curve, produced when calibrating with a 965 μm long tool, is shown in Fig. 3.24.

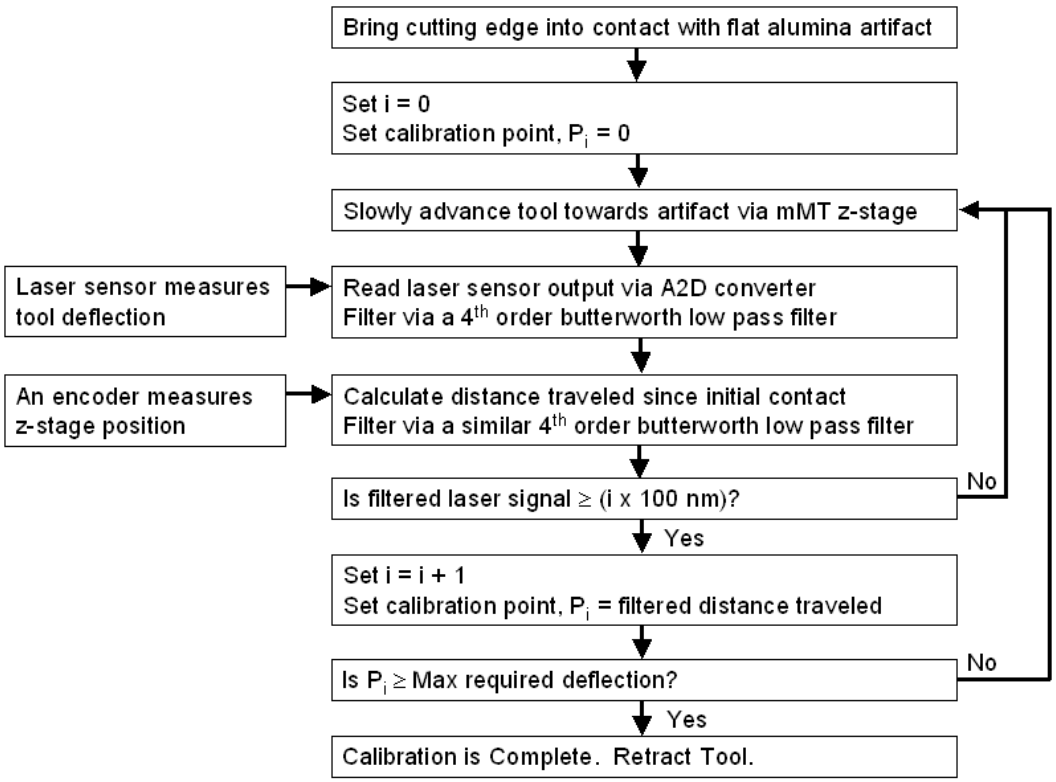


Figure 3.23: Calibration procedure

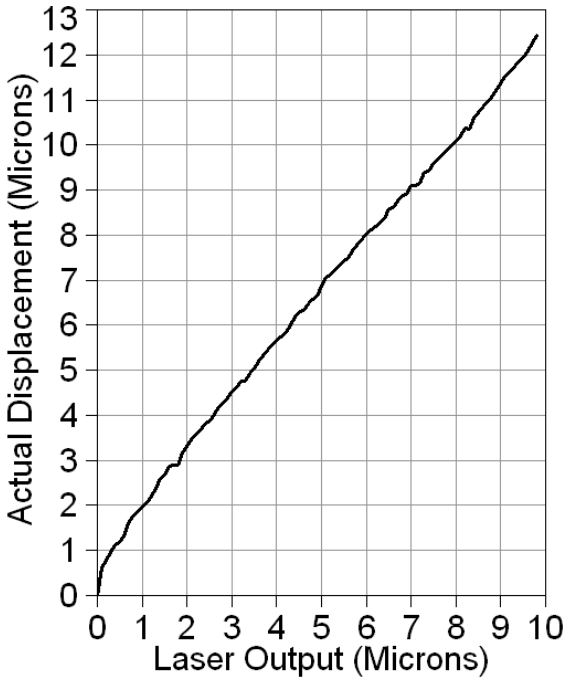


Figure 3.24: Example calibration curve

## 3.6.4 Micro-Groove Cutting

Following tool setting, workpiece registration, tool / laser calibration, and process planning, micro-grooves can be cut. In order to cut a micro-groove, the groove cutting assembly is first rotated via the mMT b-stage so that the tool is held at the correct mounting angle for the start of the cut. The calculation of this angle was described previously. Then, the cutting assembly is advanced towards the workpiece until the cutting edge of the tool contacts the workpiece where the cut is to start.

In a standard CNC machine tool, where there is no tool flexibility, a tool trajectory would be specified that would have the tool pass through the workpiece at some specified depth. The cut would be broken up into many time steps, e.g., 5000 steps per second in the case of the controller used in this work. At each time step, the controller would calculate target positions for each machine stage based of the specified trajectory. Also at each time step, the target positions, along with the actual stage

positions provided by the encoders, would be fed into the feedback algorithms regulating the position of each stage in order to execute the cut. However, since tool deflection feedback is also used, this approach is slightly modified in work.

Specifically, the xyzc-trajectory initially specified, if followed exactly, would only result in the cutting edge of the tool skimming over the surface of the workpiece. That is, a nominal trajectory is specified that tells the controller approximately where the stages need to be to perform the cut. During the cut itself, in addition to stage positions, tool cantilever displacement is also read by the controller and converted to cutting edge displacement via the calibration curve. The measured cutting edge displacement is used to adjust the z-component of the specified nominal trajectory in real time in order to insure that the corresponding cutting edge displacement, calculated during process planing, is achieved, as shown in the block diagram in Fig. 3.25. This adjusted xyzc-trajectory is used to calculate the target positions for the machine stages, which are fed into the feedback algorithms regulating the position of each stage, also as shown in Fig. 3.25. In this way the desired cutting edge displacement trajectory is followed and hence the desired cutting load trajectory is achieved. After the move is complete, the tool is retracted and the process can be repeated for as many cuts as desired.

Note that during cutting, the laser sensor can be set in either displacement mode or scanning mode. The use of displacement mode results in the highest possible sensor bandwidth, which is ideal for reliably cutting a groove at speeds up to about 400 mm/min. However, the use of scanning mode enables the exact shape of the bent cantilever to be found, which can be useful from an experimental standpoint. From a control algorithm standpoint, the difference is that the two zero order holds in the block

diagram in Fig. 3.25 update at 5000 Hz when the laser is set to displacement mode and only update at about 27 Hz when the laser is set in scanning mode. Additionally, in the latter case, each update coincides with the time when the scanning laser passes over the same point on the tool cantilever.

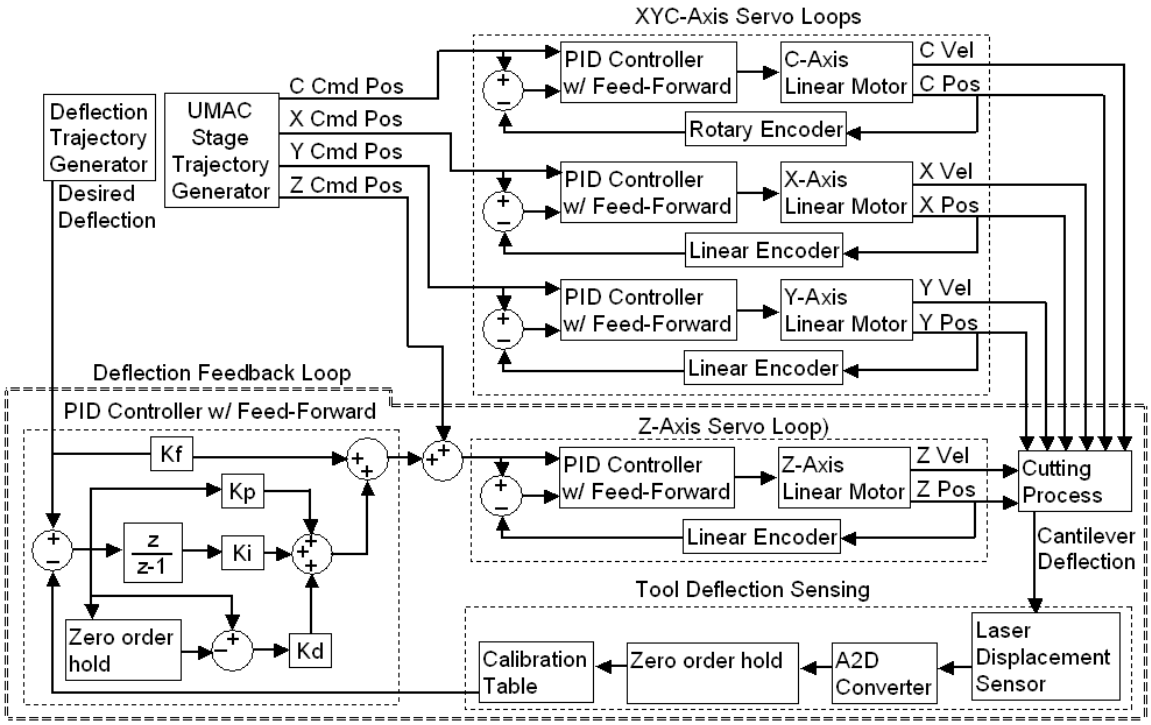


Figure 3.25: Block diagram of control algorithm used during micro-groove cutting

# 3.7 Chapter Summary

In this chapter, a micro-groove cutting process was described that makes use of a flexible cutting tool and is intended to meet the process requirements established in Chapter 1. A process based on a flexible cutting tool is used in order to mitigate issues associated with encoder resolution, linear guide alignment, tool-workpiece registration uncertainty, and machine tool stiffness that are present in conventional groove cutting with rigid tools. This enables machine tools to be used for high precision micro-groove cutting that cost about a tenth of what they would otherwise.

A machine tool was also described that is used to implement the micro-groove cutting process. This machine tool consists of a groove-cutting module that can be mounting onto a suitable 5-axis motion platform and an existing micro-scale machine, which serves as the motion platform. Also described is the set of steps required in order to cut a set of grooves using the machine tool. This machine tool and the described groove cutting procedure are used in experiments described in the next chapter where commercial AFM probes are used as flexible cutting tools in order to evaluate the viability of the developed process.

# Chapter 4

# Micro-Groove Cutting Experiments Using AFM Probes as Flexible Cutting Tools

## 4.1 Chapter Introduction

### 4.1.1 Overview

In the previous chapter, a new micro-groove cutting process was described that has several unique characteristics. Therefore, in order to render the new process practical, a though understanding of the process must be acquired. In particular, the mechanics of the process and the effects of machining parameters such as cutting speed, tool geometry, and tool load on groove geometry, chip morphology, and tool wear need to be understood. The purpose of this chapter is to gain such an understanding.

In this chapter, the results are experiments are presented that explore the effects of varying cutting speed, varying cutting load, and varying the orientation of cutting geometry during micro-groove cutting. The cutting geometry orientation is controlled through the combination of the load applied to a flexible tool and the angle that the tool is held at (mounting angle) relative to the workpiece during cutting. In the experiments described in this chapter, diamond-coated AFM probes were used as flexible cutting tools due to their low cost and the ease with which they could be obtained.

Three experiments are described in which grooves are cut in aluminum workpieces. The first experiment demonstrates groove formation, groove shape, and tool wear resulting from cutting long grooves via successive tool passes. The second more

systematic experiment explores the effects of cutting speed, cutting load, and AFM probe mounting angle on groove geometry, tool wear, and chip formation when short grooves are cut using only one tool pass each. Lastly, a third experiment is described in which the cutting of long curvilinear grooves is explored. The results of these experiments clearly show the promise of the newly developed process, but also demonstrate the limitations imposed by using commercial AFM probes as tools, which are addressed in the next chapter.

### 4.1.2 Acknowledgement of Previous Publication

The contents of this chapter have been previously published by the author of this dissertation as a technical paper in the ASME Journal of Manufacturing Science and Engineering [131]. ASME holds the copyright for the published content. Text, tables, and figures in this chapter are reproduced with the permission of ASME.

## 4.2 Description of Experiments

### 4.2.1 AFM Probes Used as Flexible Cutting Tools

In all three experiments described in this chapter, NanoWorld Probepoint® DT-NCHR AFM probes were used as flexible cutting tools. An example of such an AFM probe is shown in Fig. 4.1. Each probe consists of a monolithic silicon cantilever and AFM tip, with a nominal stiffness of 42 N/m, coated with a 100 – 200 nm thick layer of polycrystalline diamond. The probes have a three-sided pyramidal geometry near the apex of the AFM tip and there are two clearance faces on the trailing side of the tip. There are also two faces on the leading side of the tip, but they are oriented such that only one face, the rake face, meets with the two clearance faces to form the cutting edge, as

shown in Fig. 4.1. Both the cutting edge and tip apex have radii of 100 – 200 nm due to the conformal diamond coating.

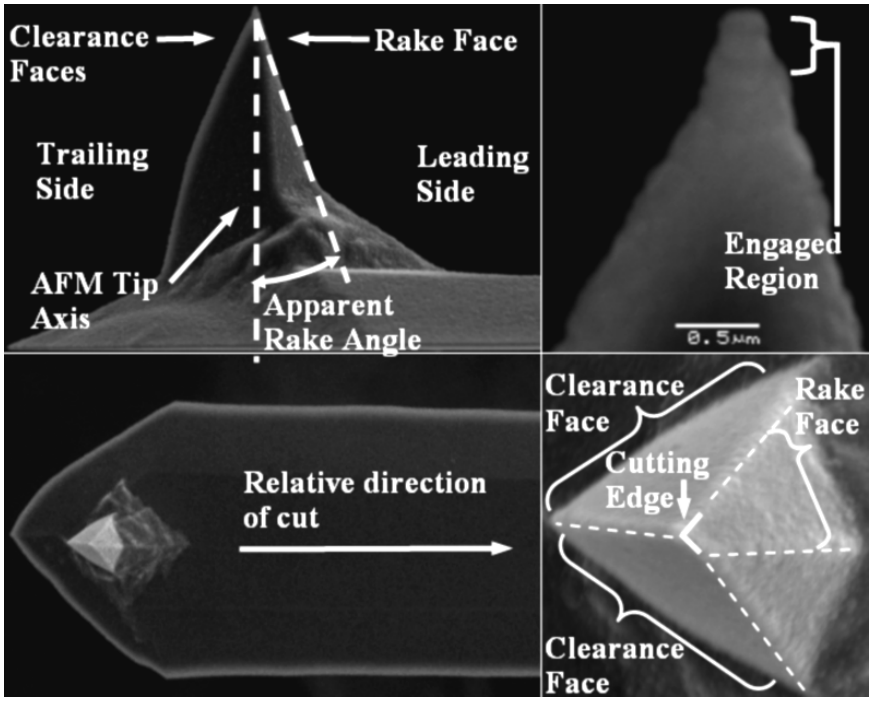


Figure 4.1: DT-NCHR diamond coated AFM tip

## 4.2.2 Experimental Procedure

Three different micro-groove cutting experiments were conducted. The purpose of the first experiment was to examine the feasibility of cutting long grooves using multiple tool passes and to examine the formation of these grooves. The second experiment was conducted in order to examine the effects of cutting speed, cutting load, and tool mounting angle during short cuts. Lastly, the third experiment was conducted in order to examine the viability of cutting long continuous curvilinear grooves. Process outputs of interest included effective rake angle during cutting, resultant groove geometry, tool wear, and chip morphology.

The workpiece used for Experiment 1 consisted of a 1.6 μm thick thermally evaporated aluminum film deposited on a polished silicon substrate. During Experiments 2 and 3 the workpiece consisted of a 1.2 μm thick aluminum film thermally evaporated onto a 10 nm thick chromium adhesion layer that was thermally evaporated onto a polished silicon substrate. For both workpieces the depth of cut was less than 25% of the film thickness and the film Ra was less than 5 nm as measured with a Veeco NT1000 Optical Profilometer.

The test procedure was very similar to the general-purpose groove cutting procedure described in Chapter 3. The only difference is during the process planning stage. That is, the previous chapter described a process planning procedure where both the angle the tool is to be held at during cutting (the mounting angle) and the amount of deflection the tool should experience are calculated in order to achieve a desired cutting load and rake angle. However, in the experiments described in this chapter only, the mounting angle is manually set and a deflection is calculated to achieve a desired tool load. Hence, the rake angle of the tool is allowed to vary due to changing cutting conditions and mounting angle in order to see the effect of cutting when using different rake angles.

All grooves were cut in ambient air without the use of any lubricants or coolants. During these cuts, the applied cutting load was ramped up from zero to a desired steady state load over the first portion of each cut, which caused the depth of cut to ramp up from zero to some steady state value. This was done to minimize tool breakage due to sudden loading.

Following each experimental trial the worn AFM tip was examined with an SEM. The SEM images were used to determine the amount of tool wear and to examine chips stuck to each tip. The SEM images were also used to get the worn shape of each tip. During the second experiment the shapes of each tip were also used in combination with the bent shapes of each AFM cantilever to calculate the effective rake angle at the beginning and end of each test. A commercial AFM was used to image sections of each cut groove. These images were examined and used to calculate parameters describing groove geometry: groove depth, groove width, groove skewness, groove kurtosis, and burr height.

## 4.3 Experiment 1: Long, Multiple Tool Pass Cuts

In the first experiment, seven tests were conducted at the conditions listed Table 4.1. In each test, 10 parallel grooves spaced 20 μm apart were cut using five tool passes per groove. The first tool pass for each groove was 4 mm long, the second 3.9 mm long, the third 3.8 mm long and so on. This meant that the groove shape following each tool pass could be later measured.

Table 4.1: Experiment 1 Conditions

| Test | 1A | 1B | 1C | 1D | 1E | 1F | 1G |
|---|---|---|---|---|---|---|---|
| Speed (mm /min) | 25 | 25 | 25 | 15 | 1.2 | 25 | 25 |
| Mounting Angle (deg) | 5.0 | 6.2 | 5.1 | 5.2 | 5.2 | 18.4 | 29.8 |
| Nom. Load (mN) | 0.26 | 0.4 | 0.68 | 0.4 | 0.4 | 0.4 | 0.4 |

All grooves in Experiment 1 had the same general features. This can be seen in Fig. 4.2, which shows SEM images of grooves from each test in the experiment. It can be seen that groove depth and width appear fairly consistent over the few microns shown. The grooves are bordered with attached burrs and partially broken-off burrs.

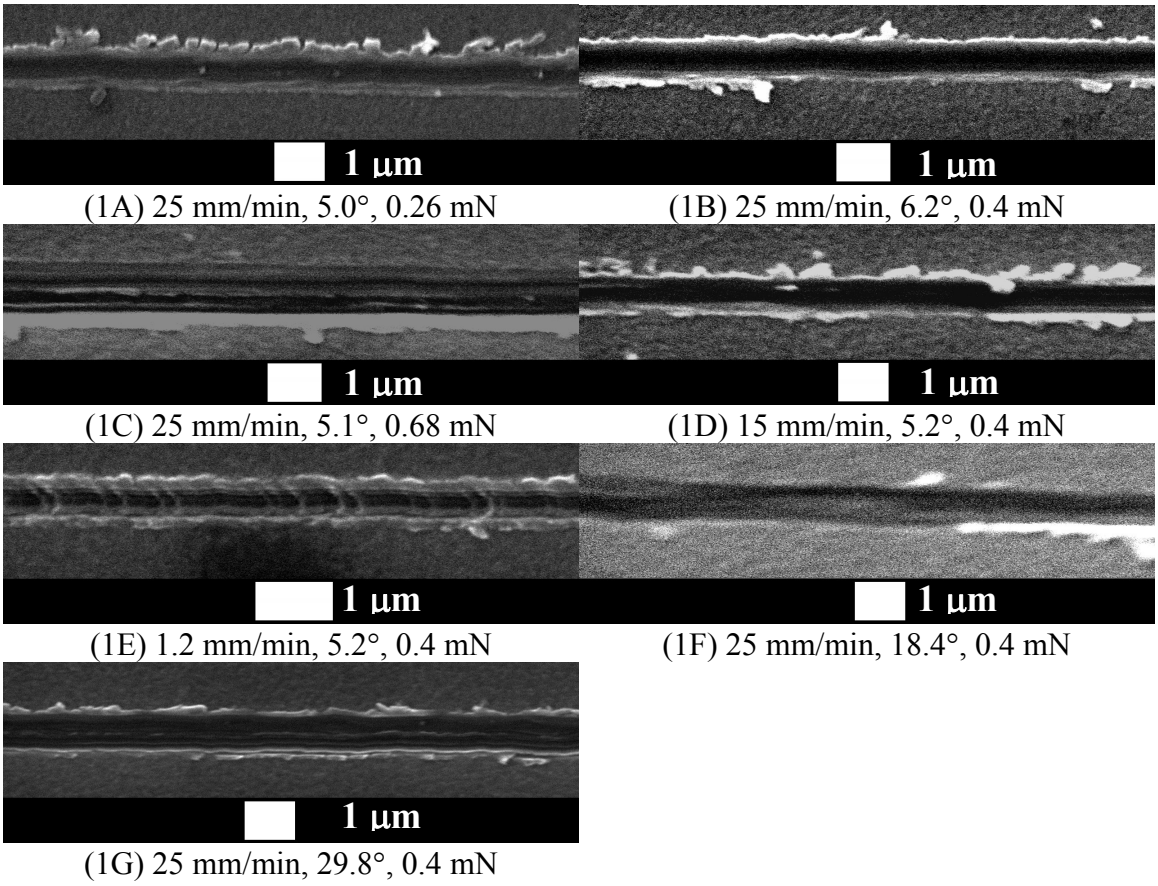


(1A) 25 mm/min, 5.0°, 0.26 mN (1B) 25 mm/min, 6.2°, 0.4 mN

(1C) 25 mm/min, 5.1°, 0.68 mN (1D) 15 mm/min, 5.2°, 0.4 mN

(1E) 1.2 mm/min, 5.2°, 0.4 mN (1F) 25 mm/min, 18.4°, 0.4 mN

(1G) 25 mm/min, 29.8°, 0.4 mN

Figure 4.2: SEM images of grooves cut in Experiment 1

### 4.3.1 Tool Wear

Tool wear is important in micro-groove cutting because it has a significant effect on groove shape. During Experiment 1, tool wear was expected to be significant due to the long distance cut. Tool wear was measured using SEM images of each worn AFM tip, as shown in Fig. 4.3, and the wear values are tabulated in Table 4.2. In the table, wear is the distance between the tip of each tool in its new and worn state and wear radius is the final radius of the cutting edge of each the AFM tip. Additionally, Fig. 4.4 shows SEM images of a new DT-NCHR AFM tip and worn tips from each trial.

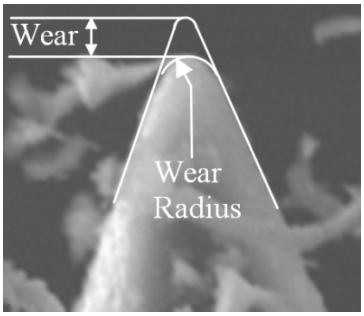


Figure 4.3: Tool wear measurement

Table 4.2: Tool wear during Experiment 1

| Test | Speed (mm /min) | Mounting Angle (deg) | Load (mN) | Major Fracture | Worn Tip Profile | Wear (μm) | Wear Radius (μm) |
|---|---|---|---|---|---|---|---|
| 1A | 25 | 5.0 | 0.26 | No | Round | 0.56 | 0.60 |
| 1B | 25 | 6.2 | 0.4 | No | Round | 0.61 | 0.37 |
| 1C | 25 | 5.1 | 0.68 | No | Round | 0.93 | 0.36 |
| 1D | 15 | 5.2 | 0.4 | Yes | Flat | 1.73 | 0.14 |
| 1E | 1.2 | 5.2 | 0.4 | No | Flat | 0.65 | 0.38 |
| 1F | 25 | 18.4 | 0.4 | Yes | Flat | 2.18 | 0.77 |
| 1G | 25 | 29.8 | 0.4 | Yes | Flat | 1.5 | 0.46 |

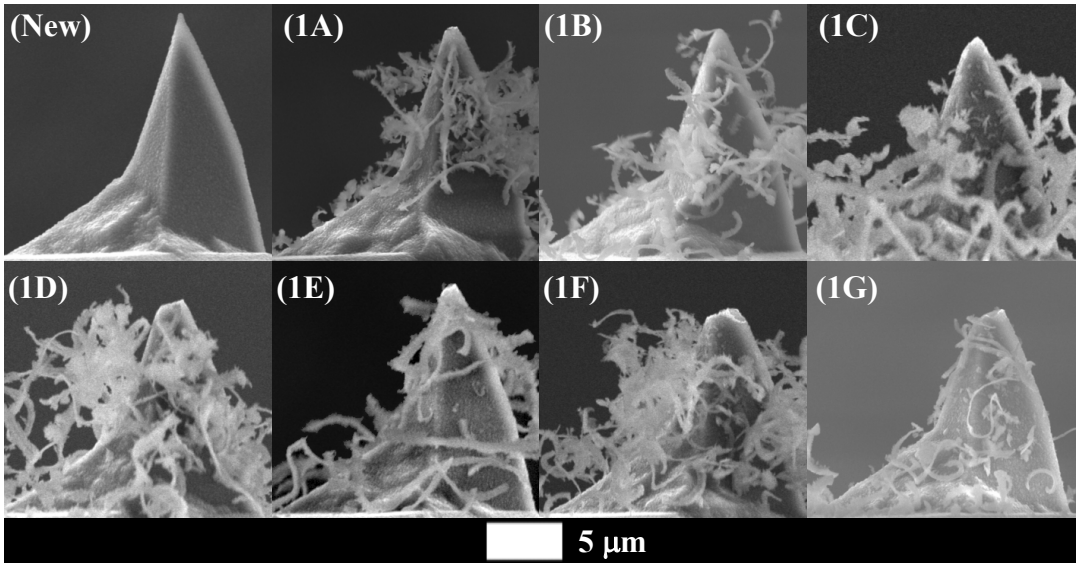


Figure 4.4: New and worn AFM probes used as flexible cutting tools

The lowest wear was seen in tests 1A and 1B where the cutting speed was 25 mm/min, the mounting angle was 5 – 6° and the applied loads were 0.26 and 0.4 mN,

respectively. In these tests the level of wear was small and the worn tools were rounded, as shown in Fig. 4.4. Hence, in Experiment 1, a low mounting angle, high cutting speed, and a moderate load resulted in low wear.

Tests 1F and 1G in Table 4.2 demonstrated an increased incidence of tool wear due to increased fracture. These two tests were conducted at high cantilever mounting angles so the rake angles were more positive than in all of the other tests. In Fig. 4.4 it can even be seen that a large chunk of the tip appears to have broken off in test 1F. Comparing tests 1A, 1B, and 1C in Table 4.2 also shows a moderate increase in tool wear with load. Also, as seen by comparing tests 1B, 1D, and 1E, lowering the cutting speed to be comparable to the speeds used when cutting inside an actual AFM (typically no greater than 1.2 mm/min) was not beneficial.

### 4.3.2 Groove Formation

AFM images of portions of the first and last grooves in tests 1A through 1G were captured after each tool pass. The captured portions included sections of the grooves in each test that were formed by one, two, three, four, and all five tool passes. Based on these images groove cross-sections were created from which the shape of each groove was extracted. By observing how the cross-sections change when multiple tool passes are used, the groove formation process can be seen. Also, by comparing the first and last groove cross-sections in each test, the effect of tool wear can be seen. Figure 4.5 shows cross-sections of the first and tenth grooves cut in tests 1A – 1C following each tool pass. Similarly, Fig. 4.6 shows cross-sections of the first and tenth grooves cut in tests 1D, 1F, and 1G following each tool pass. The cross-sections of the first groove from test 1E is

also shown in Fig. 4.6, but no other cross-sections are shown from that test because excessive snarling of chips attached to the tool caused the test to be ended prematurely.

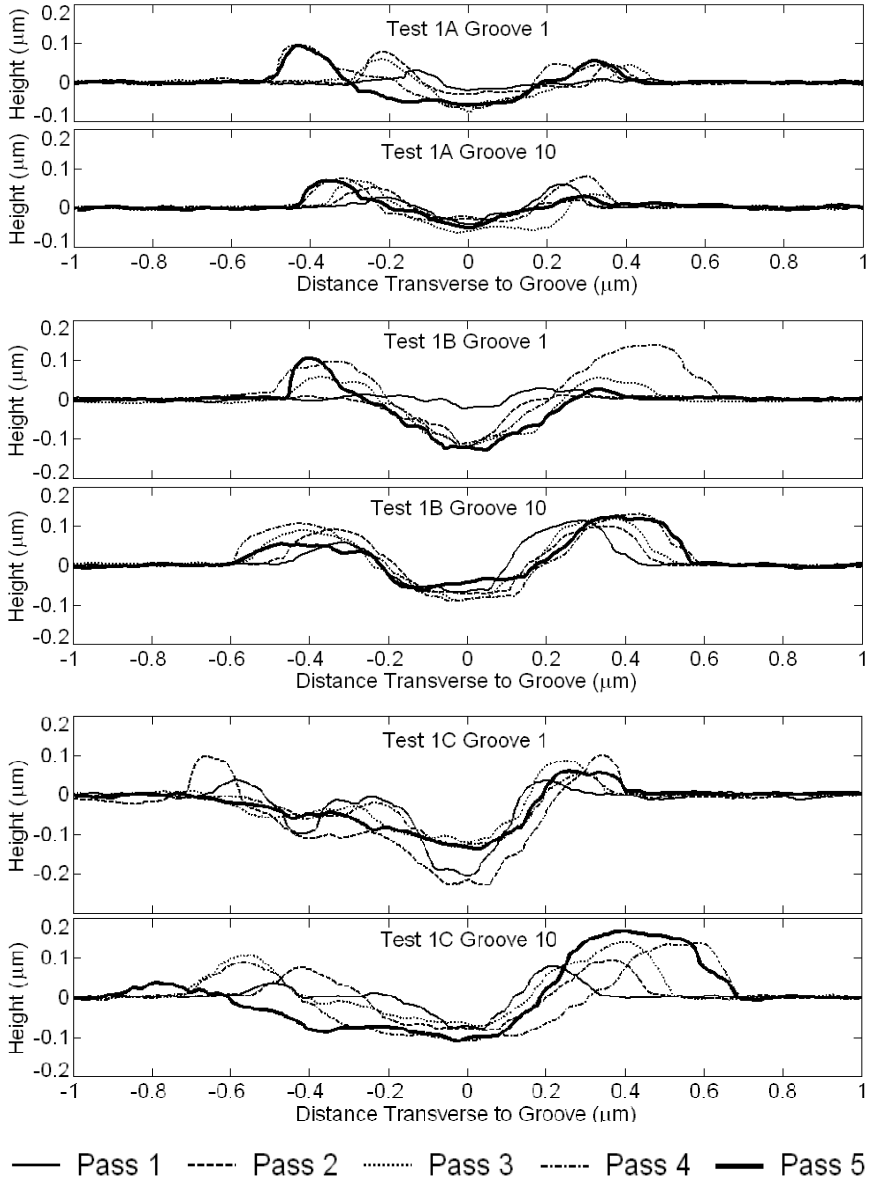


Figure 4.5: Cross-sections of the first and tenth grooves in tests 1A, 1B, and 1C following each tool pass

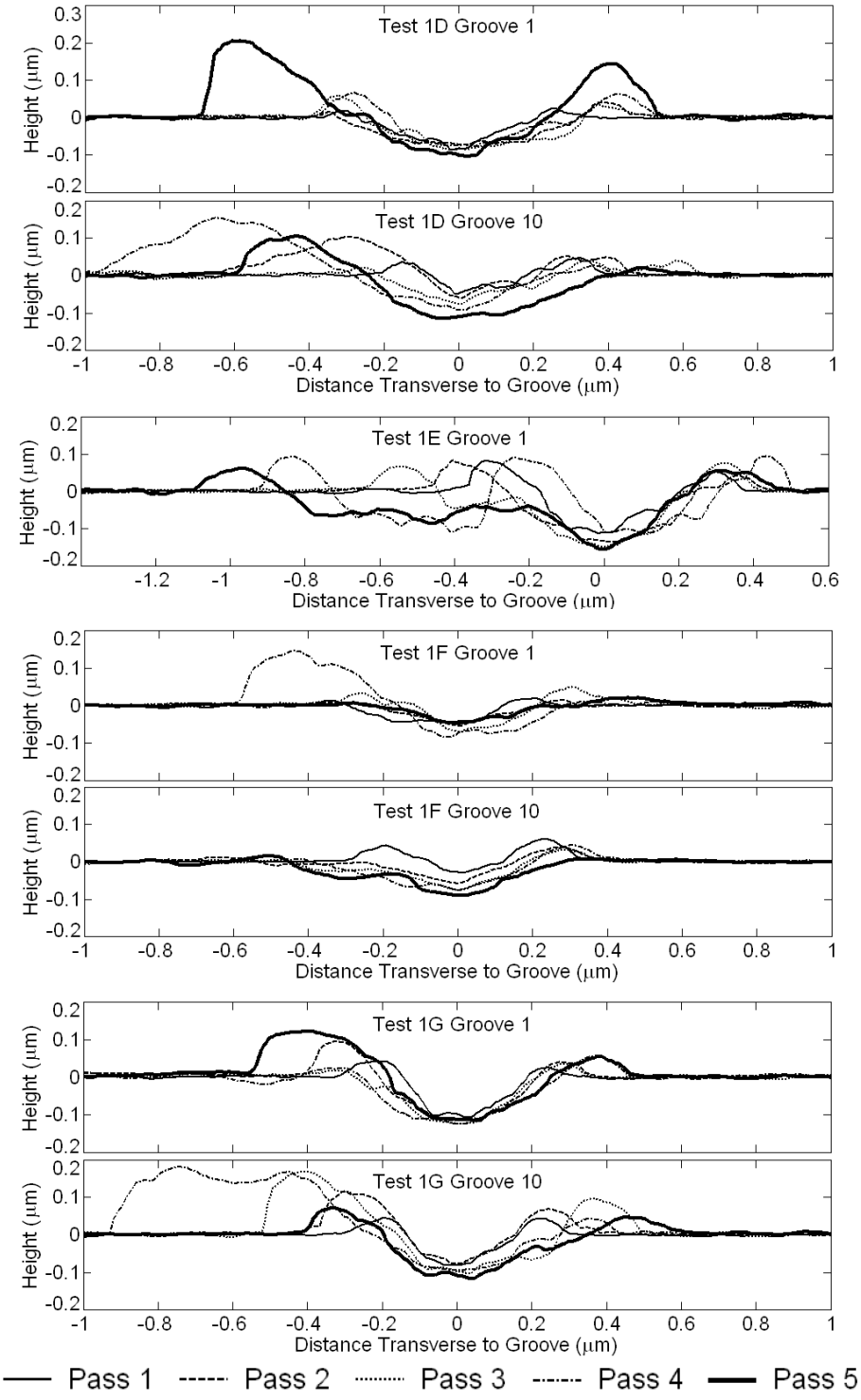


Figure 4.6: Cross-sections of the grooves in tests 1D – 1G following each tool pass

It was found that the depth of cut generally increased the most during the first couple of tool passes. The amount of material removed generally increased during all

tool passes. The widths of the grooves also increased with each tool pass, which is expected due to the pyramidal shape of each AFM tip. Reductions in depth occasionally occurred after a tool pass and were likely due to burrs or chips from a previous pass being pushed down into the groove. Such events occurred more often when the tool was worn. It was also found that multiple tool passes resulted in a more uniform depth of cut over the course of a groove.

The groove depths achieved using a given cutting condition were generally less once the tool wore. However, as can be seen in test 1B in Fig. 4.5, there appears to be an outlier event involving the first groove created during the first tool pass when the tool was new. That is, the groove in the first tool pass is shallower than the groove created when the tool was worn. This did not occur in most other tests and may be due to some unaccounted for event such as a piece of debris being temporary stuck to the tool. Furthermore, it was determined that there is some variation in groove depth along the length of the groove, which may partially explain this.

Comparison of the cross-sections in the two figures shows the effect that speed has on the shape of the grooves. It can be seen that when cutting at 1.2 mm/min the grooves ended up misshapen. This may be because the large amount time required for each tool pass allowed the effects of workpiece fixturing drift and machine tool thermal drift to cause the successive tool passes to not line up well. It can also be seen that both the depth and width of a groove tended to increase with increase load, as expected. Also, at the highest tested load, test 1C, a much wider and somewhat asymmetric bowl-shaped groove resulted. This is possibly due to cantilever twisting at the high load. The effect of load and speed are examined more systematically in Experiment 2.

### 4.3.3 Chip Morphology

SEM images showed chips attached to all of the AFM probes after the tests. This indicated that shearing was present despite the very low depth of cut. The chips varied in length from 1.6 – 961 μm and varied in average width from 0.4 – 0.75 μm. Three chips types were observed: ribbon chips, washer-type helical chips, and tubular chips [132]. Each chip type is shown in Fig. 4.7. Chip morphology is examined in more detail in Experiment 2.

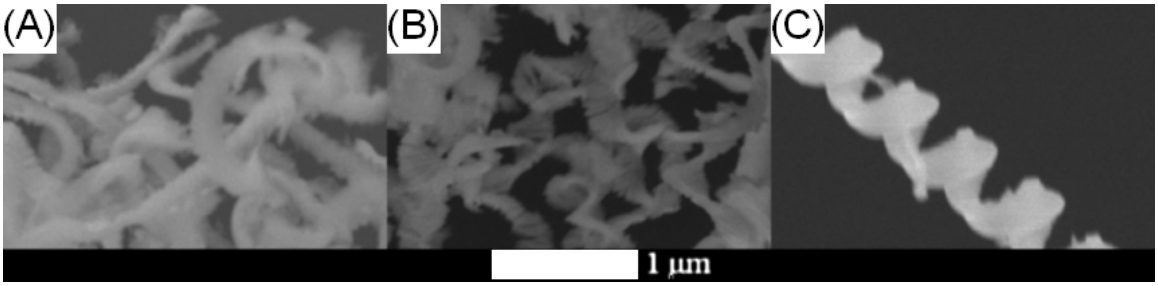


Figure 4.7: Chips seen in Experiment 1: (A) ribbon, (B) washer-type helical, and (C) tubular chips

## 4.4 Experiment 2: Short, Single Tool Pass Cuts

Following Experiment 1 it became clear that a systematic evaluation of the effects of cutting speed, tool orientation due to mounting angle, and cutting load was necessary. Wear data from Experiment 1 suggested that wear should be evaluated over shorter cuts in order to judge how much wear was due to rapidly occuring fracture and how much was due to slower abrasion. Groove formation data suggested that only one tool pass often did most of the cutting and that it would be beneficial to consider grooves formed with only one tool pass. The wear and groove geometry resulting from cutting at very low speeds (1.2 mm/min) suggested that there is little benefit in cutting so slowly.

In Experiment 2, cutting speed, mounting angle, and cutting load were varied over two levels each in a factorial scheme. During each test, six parallel 1.5 mm long straight grooves, spaced 10 μm apart, were cut using one tool pass. The test conditions are listed Table 4.3. Also, during each cut the load was ramped up to the full nominal load over the first 0.5 mm of the cut. Lastly, the angular orientation of the AFM tip was measured during groove cutting by setting the confocal laser displacement sensor into scanning mode, as described in Chapter 3, such that the laser beam continuously scanned across the AFM cantilever.

Table 4.3: Experiment 2 test conditions

| Test | 2A | 2B | 2C | 2D | 2E | 2F | 2G | 2H |
|---|---|---|---|---|---|---|---|---|
| Speed (mm /min) | 25 | 25 | 25 | 25 | 15 | 15 | 15 | 15 |
| Mounting Angle (deg) | 5 | 5 | 30 | 30 | 5 | 5 | 30 | 30 |
| Load (mN) | 0.25 | 0.5 | 0.25 | 0.5 | 0.25 | 0.5 | 0.25 | 0.5 |

## 4.4.1 Tool Wear

The worn tool from each test was examined with a SEM. Table 4.4 contains the tabulated wear data. A factorial effect analysis was performed using wear and wear radius value as the responses. Figure 4.8 shows two-way plots of the factors that affect wear. It can be seen that wear increased significantly with increased cutting load. It also increased significantly with increasing mounting angle. This latter effect was much more dramatic at the higher cutting speed and higher load. Furthermore, SEM images showed that significant tool fracture tended to occur at high mounting angles. This is consistent with the tendency of tools with more positive rake angles to experience fracture-based wear due to less material supporting the cutting edge.

Table 4.4: Tool wear data from Experiment 2

| Test | Speed (mm/min) | Mounting Angle (deg) | Load (mN) | Major Fracture | Worn Tip Profile | Wear (μm) | Wear Radius (μm) |
|---|---|---|---|---|---|---|---|
| 2A | 25 | 5 | 0.25 | No | Round | 0.25 | 0.13 |
| 2B | 25 | 5 | 0.5 | No | Round | 0.51 | 0.45 |
| 2C | 25 | 30 | 0.25 | No | Round | 0.47 | 0.39 |
| 2D | 25 | 30 | 0.5 | Yes | Jagged | 2.79 | 0.21 |
| 2E | 15 | 5 | 0.25 | No | Round | 0.41 | 0.33 |
| 2F | 15 | 5 | 0.5 | No | Round | 0.70 | 0.22 |
| 2G | 15 | 30 | 0.25 | Yes | Flat | 0.65 | 0.22 |
| 2H | 15 | 30 | 0.5 | Yes | Round | 1.64 | 0.75 |

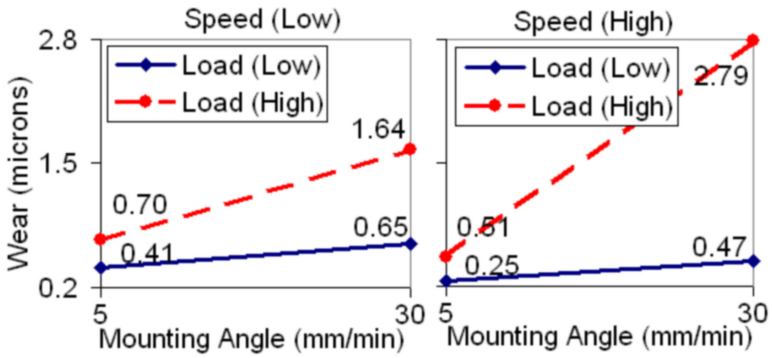


Figure 4.8: Interactions affecting wear

Figure 4.9 shows two-way plots of the factors that affect the wear radius. It can be seen that the resultant wear radius increased with increased load at low speeds and high mounting angles or at high speeds and low mounting angles. Conversely, the wear radius decreased with increased load at low speeds and low mounting angles or high speeds and high mounting angles. Note that at high mounting angles, the tip tends to experience fracture and can appear sharp while being unsuitable for cutting. The relatively large wear radius seen at a high speed, high load, and low mounting angle was probably the result of significant abrasive rounding due to the large depth of cut at that condition.

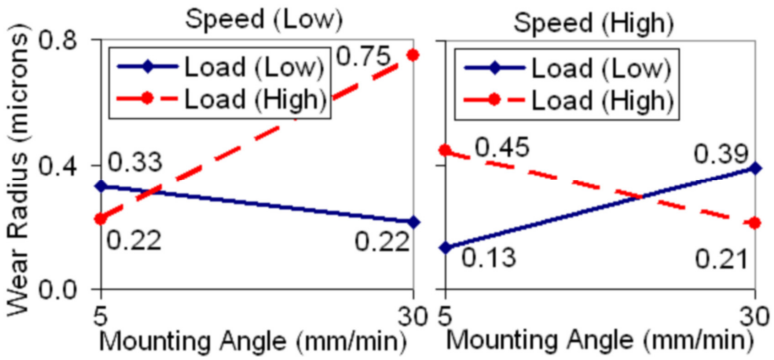


Figure 4.9: Interactions affecting wear radius

Comparison of the lowest wear conditions in the first and second experiments (tests 1A & 1B and tests 2A & 2B, respectively) showed that the amount of wear when cutting a total of 190 mm was only 0.16 – 0.26 μm greater than the amount of wear when cutting a total of 9 mm. This indicates that the majority of wear occurred very early in each test. This is taken to be due to a small amount of fracture early in each test followed by a long, very slow period of abrasive wear.

## 4.4.2. Groove Geometry

Five AFM images were captured of each of the six grooves cut in each test. Each image covered a 3 μm by 3 μm area and images of the same groove were spaced 100 μm apart. The only exception was test 2D where the groove was too shallow to easily measure and only one image was taken. AFM images from the first groove in each test are shown in Fig. 4.10: Note that the apparent side ridges in the AFM images can in some cases be folded-over burrs that appear like ridges due to limitations in AFM imaging. The folded-over nature of the burrs in Experiments 1 and 2 can be seen in SEM images of the grooves, such as those in Fig. 4.2. All the images from each test were also used to calculate parameters describing groove geometry and the calculated values are tabulated in Table 4.5.

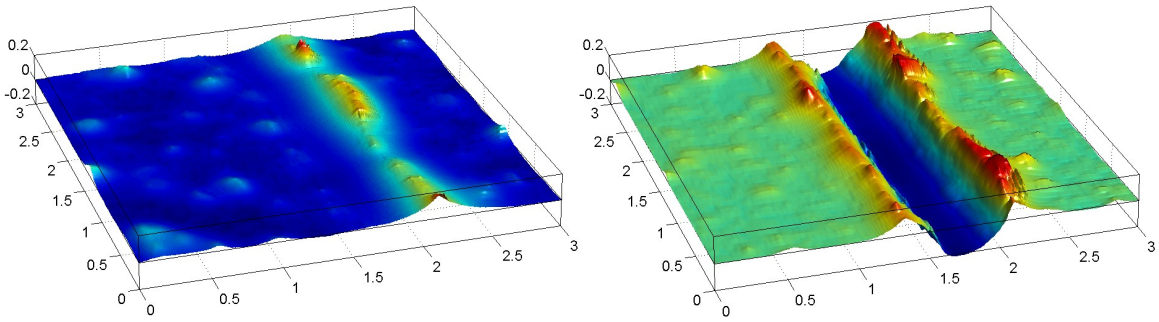

(2A) 25 mm/min, 5°, 0.25 mN



(2B) 25 mm/min, 5°, 0.5 mN

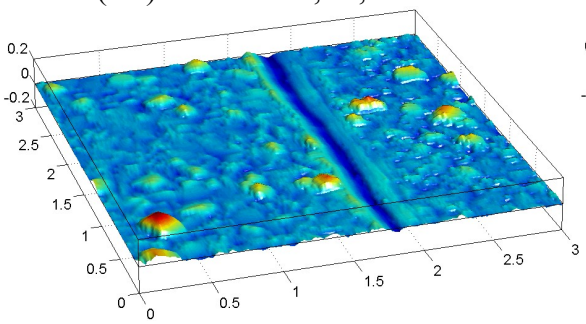

(2C) 25 mm/min, 30°, 0.25 mN

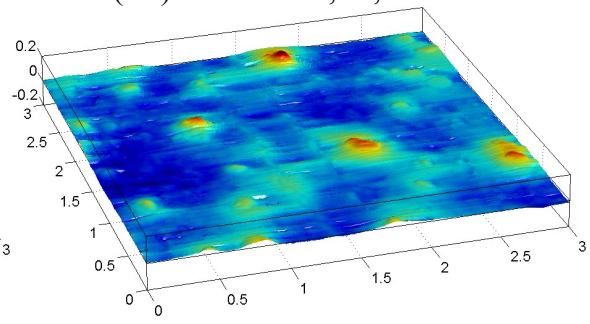

(2D) 25 mm/min, 30°, 0.5 mN

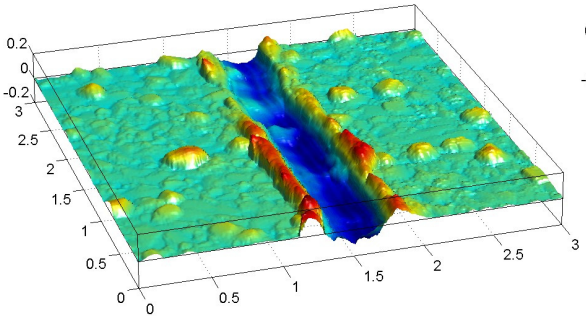

(2E) 15 mm/min, 5°, 0.25 mN

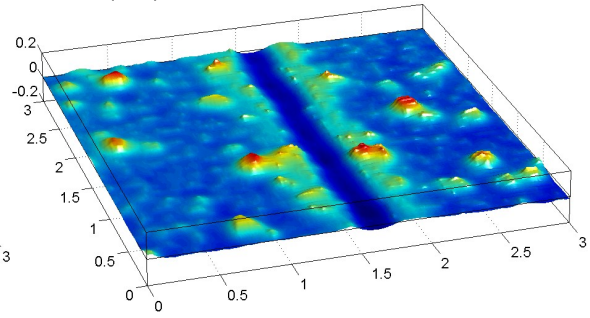

(2F) 15 mm/min, 5°, 0.5 mN

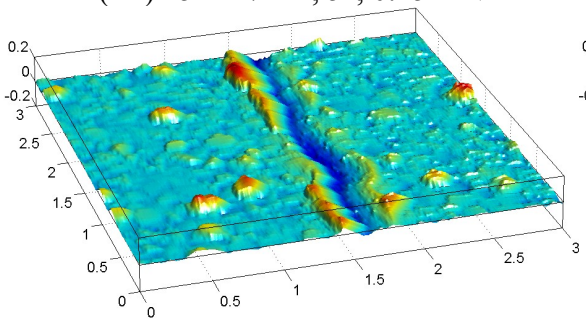

(2G) 15 mm/min, 30°, 0.25 mN

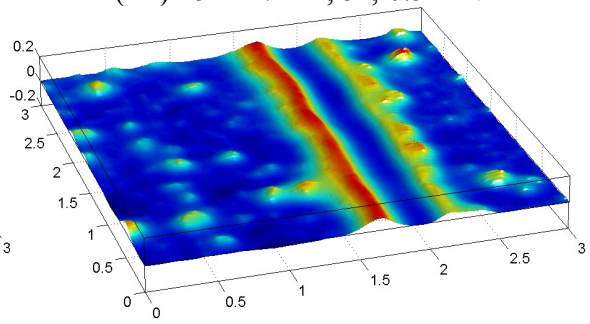

(2H) 15 mm/min, 30°, 0.5 mN

Figure 4.10: AFM images of selected Experiment 2 grooves

Table 4.5: Experiment 2 groove geometry

| Test | | 2A | 2B | 2C | 2D | 2E | 2F | 2G | 2H |
|---|---|---|---|---|---|---|---|---|---|
| Speed (mm/min) | | 25 | 25 | 25 | 25 | 15 | 15 | 15 | 15 |
| Mounting Angle (deg) | | 5 | 5 | 30 | 30 | 5 | 5 | 30 | 30 |
| Load (mN) | | 0.25 | 0.5 | 0.25 | 0.5 | 0.25 | 0.5 | 0.25 | 0.5 |
| Groove Depth (μm) | Ave | 0.00 | 0.24 | 0.05 | 0.01 | 0.05 | 0.06 | 0.05 | 0.01 |
| | Std | 0.01 | 0.02 | 0.04 | - | 0.03 | 0.04 | 0.01 | 0.02 |
| | Min | 0.00 | 0.15 | 0.00 | - | 0.00 | 0.00 | 0.00 | 0.00 |
| | Max | 0.04 | 0.29 | 0.15 | - | 0.16 | 0.18 | 0.09 | 0.07 |
| Groove Width (μm) | Ave | 0.03 | 0.54 | 0.24 | 0.34 | 0.24 | 0.39 | 0.21 | 0.05 |
| | Std | 0.06 | 0.03 | 0.10 | - | 0.11 | 0.22 | 0.05 | 0.11 |
| Groove Skewness | Ave | 0.04 | 0.06 | 0.04 | - | 0.36 | 0.05 | 0.02 | 0.01 |
| | Std | 0.27 | 0.05 | 0.38 | - | 0.72 | 0.22 | 0.27 | 0.07 |
| Groove Kurtosis | Ave | 2.16 | 2.14 | 2.34 | - | 2.96 | 2.28 | 2.17 | 2.13 |
| | Std | 0.40 | 0.05 | 0.91 | - | 2.27 | 0.43 | 0.54 | 0.06 |
| Burr Height (μm) | Ave | 0.51 | 0.42 | 0.17 | - | 0.23 | 0.31 | 0.17 | 0.36 |
| | Std | 0.29 | 0.10 | 0.08 | - | 0.14 | 0.13 | 0.08 | 0.12 |

In Table 4.5, groove depth is defined as the distance between the original surface and the lowest point in the groove. Groove width is how wide the groove is at the level of the original surface. Groove skewness and kurtosis are the same parameters used to describe the shape of a statistical distribution. The magnitude of skewness indicates the amount of asymmetry in the groove. Kurtosis indicates how square verses peaked the groove is. Lastly, burr height is an estimate of the height of a burr had it not folded over. An effect analysis was performed on each of these responses.

Figure 4.11 shows the effects of the cutting conditions on groove depth via the three-factor interaction among the variables under study. Similarly, Fig. 4.12 shows the effects of the cutting conditions on burr height via the three-factor interaction among the variables under study.

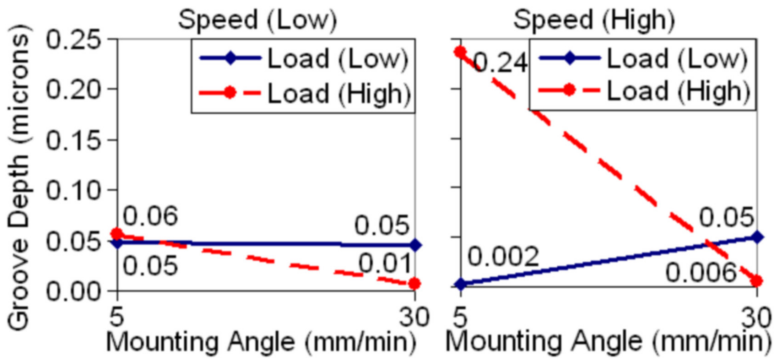


Figure 4.11: Three-factor interaction affecting groove depth

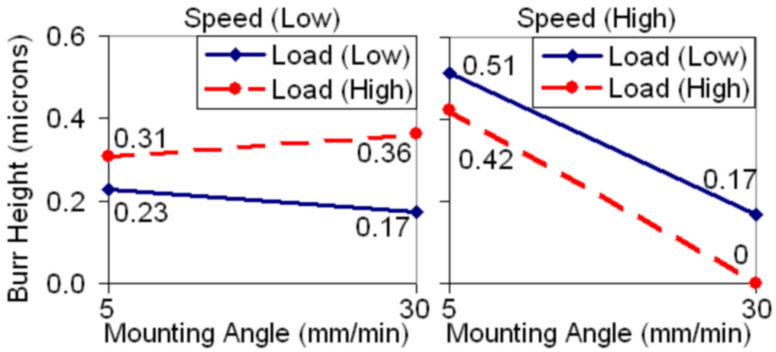


Figure 4.12: Three-factor interaction affecting burr height

It can be seen in Fig. 4.11 that groove depth generally decreased with increased mounting angle. Groove depth increased with increasing load at a low mounting angle and decreased with load at a higher mounting angle and high cutting speed. The change in groove width with cutting conditions shows similar trends, which is reasonable since the engaged portion of the AFM tip widens with increasing depth of cut. Comparison of groove skewness and kurtosis showed that squarer grooves tended to be very symmetric while more peaked grooves tended to be more skewed. Also, the test condition that resulted in the deepest groove resulted in nearly the squarest groove shape.

It can be seen in Fig. 4.12 that burr height is highly dependent on mounting angle at high speeds but not at low speeds. Burr height increases with load at low speed but decreases with load at high speed. Hence the interaction of speed with load and speed

with mounting angle is very important. Note that the zero burr height at a high mounting angle, high speed, and high load was due to the extremely small amount of material displaced. Also, burr height at a low mounting angle, high speed, and high load is large because of the large amount of material displaced.

### 4.4.3 Effective Rake Angle during Cutting

In machining, rake angle has a strong influence on cutting forces and the quality of cut surfaces. As discussed in Chapter 2, the effective rake angle is set by the radius of the tool relative to the uncut chip thickness and by the orientation of the cutting tool. In this chapter the tool orientation is allowed to vary as a function of cutting load and tool mounting angle. The value of effective rake angle for each of the cutting conditions in Experiment 2 is calculated in order to evaluate the range of possible values when using a diamond coated AFM probe as a tool and in order to better evaluate the effect of effective rake angle on cutting performance.

During cutting, the confocal laser displacement sensor was set to continuously scan across the AFM cantilever. For each cut, all of the scans taken over the fully-loaded portion of the cut were averaged and a third-order polynomial was fit to the average profile using least squares. The polynomial provided the orientation of the end of each cantilever and hence the orientation of each AFM tip / cutting geometry during cutting.

Once the orientation was known, SEM images of the sides of the AFM tips used in the experiment before and after cutting were rotated to show the orientation of the tips during actual cutting. Figure 4.13 shows images of the tool from each test where the new tip is shown on the left and the same tip after wearing is shown on the right. The left face of each tip is the rake face and each tip is shown orientated how it would have been

during cutting if the workpiece was moving from left to right across the page. The cutting edge is the lowest point in each image.

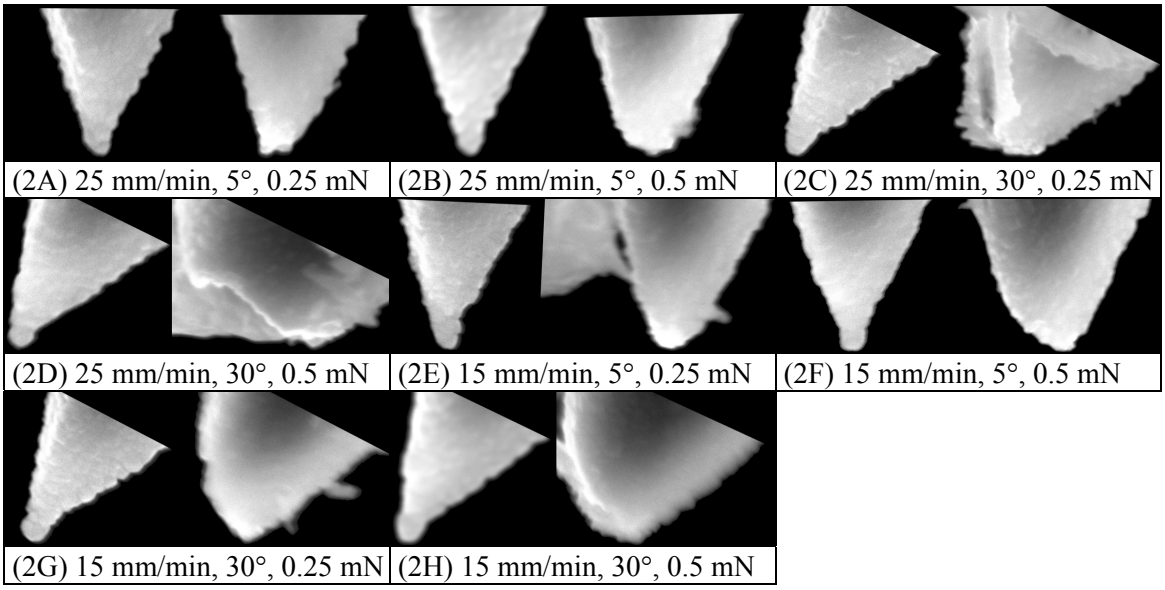


Figure 4.13: New (left) and worn (right) AFM tips in cutting orientation with rake faces on the left side

Each image was used to calculate the ideal rake angle, i.e. the rake angle calculated without taking edge radius into account, and the edge radius of the tool. Assuming that the uncut chip thickness was equal to the resultant groove depth, the effective rake angle at the start and end of each cut was calculated as described in Chapter 2.9.1. The resultant effective rake angles are listed in Table 4.6.

As can be seen in Table 4.6, the ideal rake angle could be either positive or negative depending on the mounting angle. However, the most positive effective rake angle, -40.5°, occurred when a high speed, low mounting angle, and high load was used. This means that the use of a higher mounting angle resulted in a much more positive ideal rake but the effective rake could be more negative. Also, the highly negative rake angles

observed suggest that, despite significant chip formation, a large amount of ploughing also occurred. This is supported by the presence of side burrs.

Table 4.6: Calculated rake angles during groove cutting

| Test | Speed (mm/min) | Mounting Angle (deg) | Load (mN) | Ideal Rake (deg) | | Tip / Edge Radius (μm) | | Effective Rake (deg) | |
|---|---|---|---|---|---|---|---|---|---|
| | | | | New | Worn | New | Worn | New | Worn |
| 2A | 25 | 5 | 0.25 | -17.9 | -18.3 | 0.15 | 0.13 | -87.1 | -84.4 |
| 2B | 25 | 5 | 0.5 | -19.0 | -19.0 | 0.19 | 0.45 | -40.5 | -53.0 |
| 2C | 25 | 30 | 0.25 | 10.3 | 10.3 | 0.16 | 0.39 | -71.5 | -79.7 |
| 2D | 25 | 30 | 0.5 | 9.4 | 9.3 | 0.17 | 0.21 | -78.4 | -46.8 |
| 2E | 15 | 5 | 0.25 | -14.7 | -14.7 | 0.17 | 0.33 | -64.2 | -70.4 |
| 2F | 15 | 5 | 0.5 | -18.9 | -18.9 | 0.13 | 0.22 | -66.7 | -68.8 |
| 2G | 15 | 30 | 0.25 | 11.0 | 11.0 | 0.20 | 0.22 | -69.3 | -54.1 |
| 2H | 15 | 30 | 0.5 | 8.6 | 7.6 | 0.19 | 0.75 | -81.1 | -83.7 |

### 4.4.4 Chip Morphology

An SEM was used to examine the chips stuck to each used tool and a 0.25 mm long segment of each cut. The presence of these chips indicates that at least some portion of the cuts made at each test condition involved shear-based cutting mechanics. However, this does not necessarily mean that chip formation occurred at all points in each cut. For instance, during tests 2A and 2H, which have the largest negative effective rake angles, significant groove formation, and hence chip formation, only occurred at the start of each cut and was followed by a section with very low and even zero groove depth. In the other tests, except test 2B, short sections of zero groove depth were observed where chip formation may also have not occurred, although some of these sections may be the result of debris in the groove. This variable depth phenomenon was not seen in Experiment 1, likely due to the presence of multiple tool passes.

In both Experiments 1 and 2, most of the chips shared common features. At least one side of a chip had a serrated texture typical of segmented chip formation at the

macro-scale when adiabatic shear band formation occurs due to thermo-plastic instability [87]. Such shear bands tend to occurs in materials, such as aluminum, where the decrease in flow stress due to thermal softening can be greater than the increase in flow stress due to strain hardening [87]. Additionally, most chips have wispy side-fringes from where the metal was sheared at the sides of the groove as the chip was formed.

The chips from Experiment 2 are shown in Fig. 4.14. The chip types were ribbon chips and washer-type helical chips [132], which are the same chip types that appeared in Experiment 1 at cutting speeds of 15 mm/min or higher. Examples of ribbons chips and washer-type helical chips can be seen in Fig. 4.14(2A) and 4.14(2H), respectively. Observations about the chips from each test are contained in Table 4.7.

Table 4.7: Experiment 2 chip morphology

| Test | | 2A | 2B | 2C | 2D | 2E | 2F | 2G | 2H |
|---|---|---|---|---|---|---|---|---|---|
| Speed | | 25 | 25 | 25 | 25 | 15 | 15 | 15 | 15 |
| Mounting Angle | | 5 | 5 | 30 | 30 | 5 | 5 | 30 | 30 |
| Load | | 0.25 | 0.5 | 0.25 | 0.5 | 0.25 | 0.5 | 0.25 | 0.5 |
| Chip Type | | R | R | W/R | R | R | R | R | W |
| Snarling | | Med | No | No | No | No | No | Low | No |
| Chip Length (um) | Min | 1.0 | 2.0 | 1.1 | 4.2 | 1.7 | 2.4 | 1.5 | 2.5 |
| | Max | 18.3 | 378 | 25.6 | 4.7 | 22.3 | 19.5 | 10.7 | 94.2 |
| | Mean | 6.4 | 122 | 7.2 | 4.5 | 9.3 | 7.7 | 4.6 | 25.9 |
| | Std | 5.5 | 143 | 5.6 | 0.3 | 7.2 | 7.0 | 2.5 | 26.4 |
| Width (um) | Mean | 0.64 | 0.78 | 0.51 | 1.04 | 0.75 | 0.93 | 0.43 | 0.57 |
| | Std | 0.16 | 0.20 | 0.10 | 0.26 | 0.13 | 0.17 | 0.12 | 0.12 |
| Chip Type Key | | | (R)ibbon (W)asher-Type Helical | | | | | | |

Table 4.7 shows the average chip widths to be larger than the average groove widths, suggesting partial ploughing and attachment of some of the burrs to the chips. Average chip width and average groove width also showed the same tends with cutting conditions. This behavior suggests that only one chip was formed at a time.

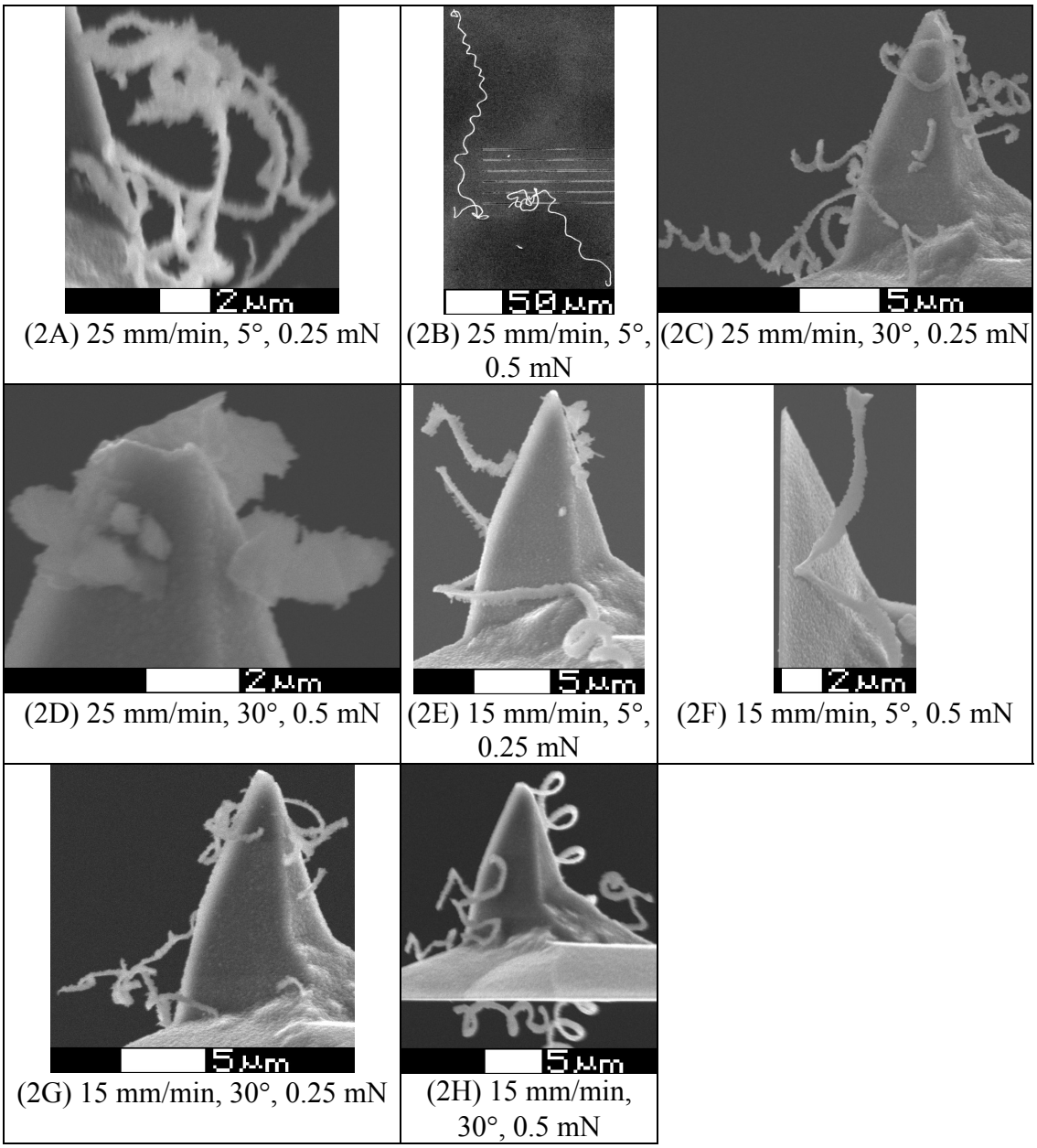


(2A) 25 mm/min, 5°, 0.25 mN

(2B) 25 mm/min, 5°, 0.5 mN

(2C) 25 mm/min, 30°, 0.25 mN

(2D) 25 mm/min, 30°, 0.5 mN

(2E) 15 mm/min, 5°, 0.25 mN

(2F) 15 mm/min, 5°, 0.5 mN

(2G) 15 mm/min, 30°, 0.25 mN

(2H) 15 mm/min, 30°, 0.5 mN

Figure 4.14: Example chips from test 2A and test 2H

It was also found that the number of tool passes had a significant effect on chip morphology. For instance, when using only one tool pass in test 2A, ribbon-type chips resulted, but when using five tool passes in test 1A snarled washer-type helical chips resulted. Additionally, the washer-type helical chips in Experiment 2 were less tightly coiled and only occurred at high mounting angles. By contrast, high mounting angles

resulted in ribbon chips and some chips that could be broken up washer-type helical chips in Experiment 1. This change in chip morphology is likely due to the very shallow depth of cut following the first tool pass.

## 4.5 Experiment 3: Continuous Curved Cut

During the second experiment, the cutting of short straight groove was evaluated. However, for many manufacturing applications, a curved groove may be desirable. In order to evaluate the ability to cut such grooves a third experiment was conducted.

The best condition from Experiment 2 was identified as a speed of 25 mm/min, a mounting angle of 5°, and a nominal load of 0.5 mN. This condition was used to conduct test 3A. In this test, the translational stages and workpiece rotary stage of the mMT were used to cut a continuous spiral pattern. The inner radius of the spiral was 236 μm, the spacing between revolutions was 3 μm, and groove length was 82 mm. A section of the spiral shaped groove is shown in Fig. 4.15. The groove curvature is clearly visible and the groove is both well-formed and continuous.

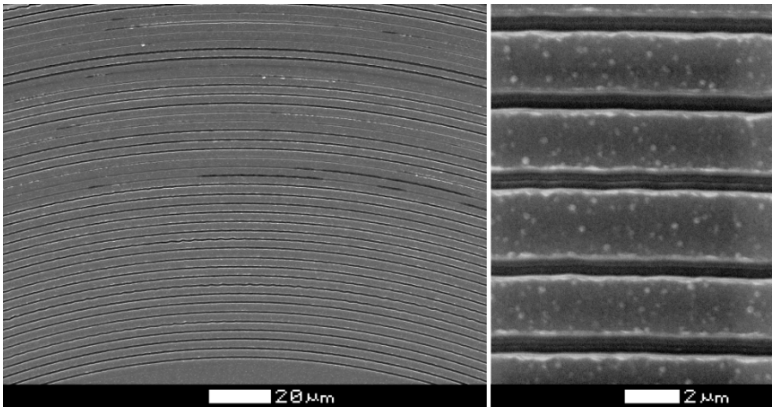


Figure 4.15: SEM images of a groove cut in a spiral pattern

AFM images were taken of sections from the first fifteen revolutions of the groove, i.e., over the first 24 mm. An AFM image from the first revolution is shown in

Fig. 4.16. It was found that the bottom of the groove was tilted slightly so that the deepest part of the groove was on the side of the groove centerline closer to the center of the spiral. A like cause is that forces generated during the cut that were transverse to the direction of cut caused the AFM cantilever to twist. The tilt might be corrected by using an AFM tip with appropriate side relief angles to minimize forces on the tool due to contact with the groove sidewall, or by using a more torsionally-stiff AFM cantilever.

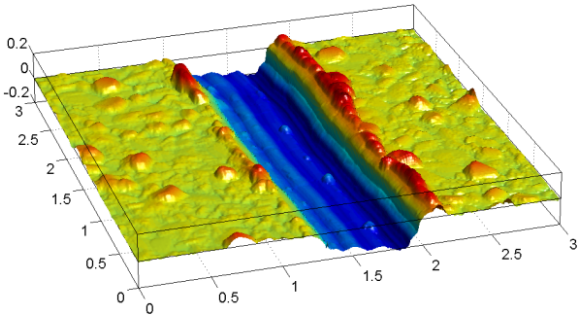


Figure 4.16: AFM image of a spiral-shaped groove section

Fig. 17 shows plots of the groove depth and groove width as a function of distance cut. Groove depth decreased over the course of the cut, which is consistent with results from Experiment 1 that indicate a reduction in groove depth with wear. This reduction happens early in the cut and then stabilizes, which supports the existence of an initial period of fast tool wear followed by a period of much slower tool wear.

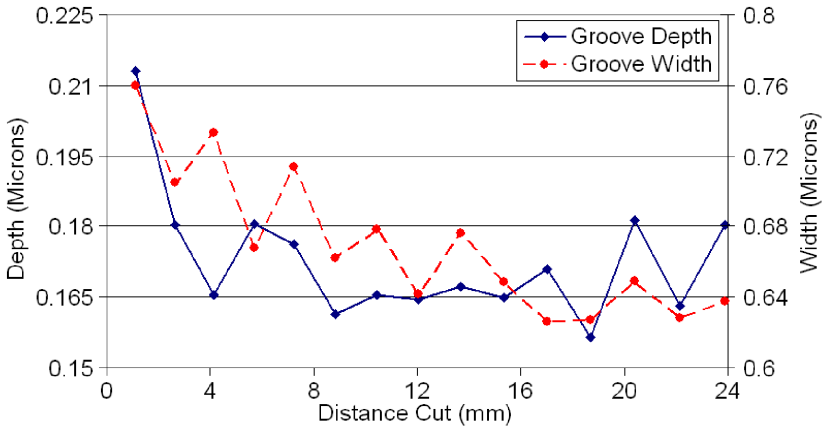


Figure 4.17: Groove depth and width vs. distance cut

## 4.6 Discussion of Results

In this chapter, the performance of the developed micro-groove cutting process was evaluated via three experiments where diamond-coated AFM probes were used as tools. These experiments showed that the process has great promise for use in producing micro-grooves. For instance, curved grooves as long as 82 mm with depths up to 0.29 μm could be cut using a single tool pass and cutting speeds at least as high at 25 mm/min.

It was found that even at the very small size scale involved, significant chip formation occurred during groove cutting. However, there is also evidence that considerable ploughing of workpiece material occurred, particularly when using low loads or cutting conditions that give rise to highly negative effective rake angles. Groove geometry was found to be highly dependent on cutting conditions, and for the tools used, the best grooves were formed when using the highest cutting speed, highest cutting load, and lowest probe mounting angle tested. Groove depth consistency was also found to be improved by the use of multiple tool passes.

The only major problem identified was the presence of significant tool wear, which decreases groove quality, decreases groove precision, and can in extreme cases render it impossible to cut a recognizable micro-grooved. It was found that tool wear was the most severe when using a high mounting angle because catastrophic fracture of the AFM tips tended to occur. This is likely because increasing the mounting angle increases the rake angle of the tool and decreases the amount of material supporting the cutting edge, which is an issue also seen with macro-scale tools. However, even when there was not catastrophic tool fracture, there was still significant wear, which consisted of a initial

period of fast more limited fracture-based wear followed by a long period of slow abrasive wear.

Therefore, it can be concluded that initial experiments showed that the micro-groove cutting process might be able to meet the process requirements outlined in Chapter 1. However, commercial diamond-coated AFM probes are simply not suitable for use as tools because they are too limited in terms of their geometries, are too fragile, and wear too heavily. This is not unreasonable since AFM probes are optimized for use in metrology and are not intended for use as cutting tools in such a demanding application as micro-groove cutting. However, since this wear is largely fracture-based the solution to the problem is to simply design a cutting geometry that is more structurally sound. Furthermore, by switching to a hard monocrystalline tool material like diamond or cubic boron nitride, instead of using polycrystalline diamond-coated silicon, the issue of abrasive wear can also be mitigated. The design, fabrication, and testing of such improved flexible cutting tools is the subject of the next chapter.

# Chapter 5

# Design and Fabrication of Flexible Micro-Groove Cutting Tools

## 5.1 Chapter Introduction

### 5.1.1 Motivation

In the previous chapter the viability of the micro-groove cutting process, described in Chapter 3, was demonstrated. However, it was also shown that commercial AFM probes, even if coated with polycrystalline diamond, are not very good cutting tools. In particular, AFM probes like the ones used in the previous chapter are shaped such that only grooves with bowl-shaped cross-sections can be produced. Additionally, it was shown that such probes are not robust enough to withstand the forces they are subjected to when cutting under the conditions described in the previous chapter, which results in highly undesirable tool fracture.

However, the poor performance of the commercial AFM probes was not totally unexpected. This is because commercial AFM probes are optimized for metrology applications where they are subjected to extremely small forces on the order of micronewtons. However, the much more demanding cutting process described in this work subjects the tool to forces on the order of a few millinewtons. This motivates the development of tool geometries specifically intended for used with the micro-groove cutting process rather than just relying in existing AFM probe geometries. The design, fabrication, and testing of such tools is the subject of this chapter.

### 5.1.2 Overview

This chapter addresses design and fabrication of flexible cutting tools with suitable geometries for micro-groove cutting. This topic is addressed by proposing a general set of cutting geometry design principles. These principles were established through examination of successful tool geometries used for groove cutting at the macro-scale and through consideration of the sorts of tool geometries that can be fabricated at the micro-scale. In particular, the capabilities and limitations of fabrication by focused ion beam (FIB) machining were considered. A set of fabrications steps capable of producing a wide range of geometries is also presented, and the implementation of these steps using commercially available equipment is discussed.

## 5.2 Flexible Tool Design Principles

In the previous chapter, it was found that AFM probes are not robust enough to serve as effective cutting tools due to their geometry. Additionally, such probes are limited in terms of the groove cross-sections they can produce. Therefore, new tools were developed to reduce or eliminate these problems.

The new tools consist of a flexible cantilever with a piece of single-crystal diamond, with a prescribed cutting geometry, attached to one end. Other materials such a cubic boron nitride (CBN) can also be used for cutting grooves in ferrous materials. In this work, these tools were fabricated by modifying single-crystal diamond AFM probes via focused ion beam (FIB) machining, which was identified as suitable for achieving the types of geometries required for an effective cutting tool.

Cutting geometry requirements imposed by groove cutting in general were found by considering the shapes of existing tools that are also suitable for groove cutting such

as shaping tools, planing tools, and parting tools Requirements imposed by tool fabrication were found by considering the capacities and limitations of FIB machining. Requirements imposed by the cutting process were found by considering the results of the experiments described in the previous chapter. These requirements are listed below and an example tool geometry that meets these requirements is shown in Fig. 5.1.

1. The cutting edge radius, $r_e$, should be as small as possible to minimize ploughing and maintain a more positive effective rake angle.
2. There should be plenty of material behind the cutting edge to support it so that it does not break off due to tool fracture like was seen in the previous chapter.
3. The tool should have a suitable end clearance angle, $\beta_e$, and side clearance angles, $\beta_{s1}$ and $\beta_{s2}$, to minimize rubbing between non-cutting faces of the tool and the workpiece. Such rubbing can cause twisting of the tool during curvilinear cuts, can cause the tool to not cut straight, and may contribute to burr formation.
4. Sharp corners should be avoided where the cutting geometry is joined to the rest of the tool in order to minimize stress concentrators that could cause premature tool breakages. Rather, fillets should be used where possible.
5. It should be possible to fabricate the tool using only through cuts because precise depth control during FIB machining is difficult.
6. It should be possible to easily cut the geometry out of a tool blank shaped like a three-sided pyramid since most diamond AFM probes will initially have this geometry.
7. As described in Chapter 3, during process planing a tool deflection and mounting angle is selected that insures that a desired load and rake angle is achieved. It is desirable for the mounting angle to at least be a few degrees in order to insure that the

cutting geometry, and not any other part of the tool, contacts the workpiece. Hence, the rake face should be cut in an orientation that insures that this is possible.

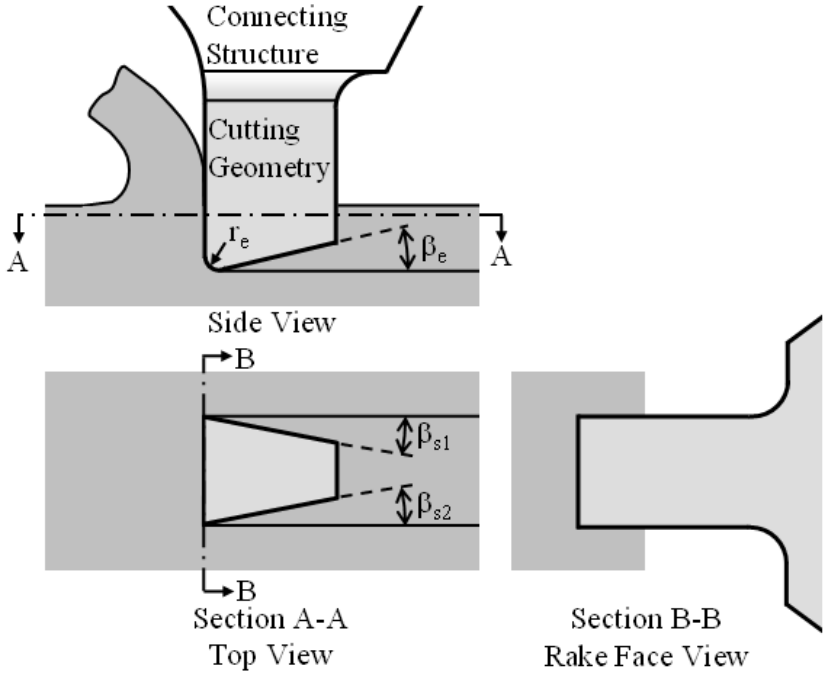


Figure 5.1: Groove cutting geometry schematic

Figure 5.2 shows progressively greater magnifications of an actual flexible cutting tool with a similar cutting geometry to the one shown in Fig. 5.1. This tool, and all other tools described herein, was fabricated from a diamond AFM probe manufactured by Micro Star Technologies that consists of a single-crystal diamond AFM tip bonded to a sapphire cantilever with a metallic adhesive. The cantilever is similarly bonded to a sapphire substrate. Additionally, the probe is glued to a small aluminum plate using a silver-filled epoxy in order to facilitate handing. The method by which this tool was fabricated is described in the next subsection.

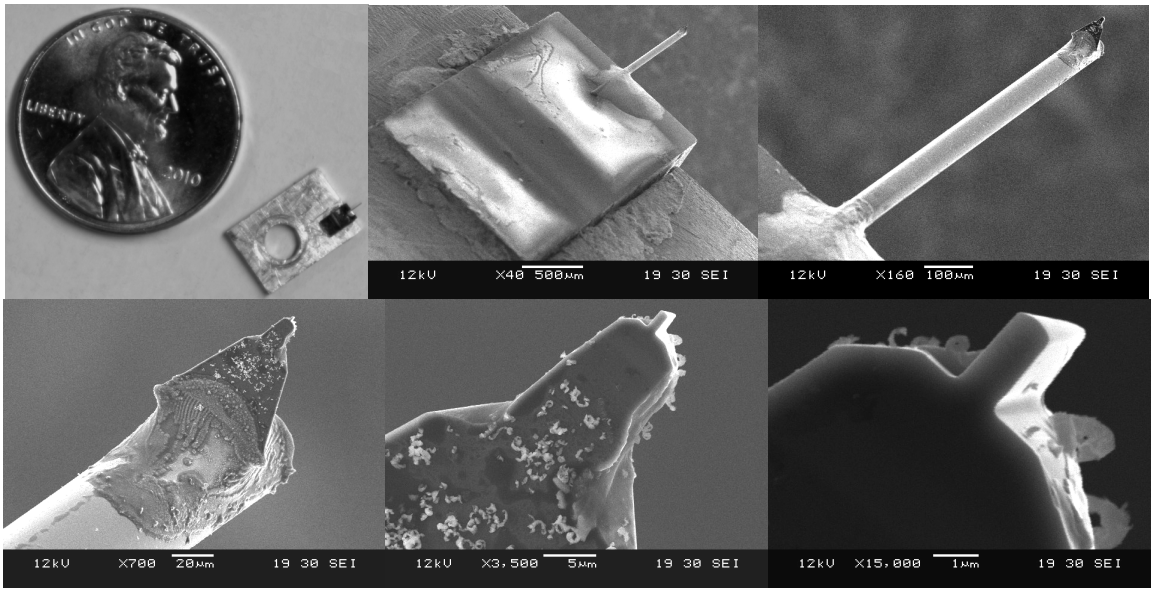


Figure 5.2: Example FIB machined flexible diamond tool with a rectangular rake face

## 5.3 Tool Fabrication Process Plan

Cutting tools have been fabricated by modifying commercial single-crystal diamond tipped AFM probes using a FEI Dual Beam 235 FIB machine. During fabrication, the diamond tipped AFM probes essentially serve as tool blanks that were selected because they already had much of the required tool geometry. The particular probes used had a diamond tip with a three-sided pyramidal geometry. Hence, the tool fabrication process becomes a series of FIB machining steps required to cut a tool geometry out of a blank shaped like a three-side pyramid. However, the FIB machining process could also be used with diamond blanks, or blanks made of other hard materials, which do not initially have a pyramidal shape.

For tools with one straight cutting edge, like the tool shown in Fig. 5.2, modification of this diamond tip involves making four through cuts. These cuts are shown in Fig. 5.3, where the solid gray region is removed in each cut and the tip is oriented such that the ion beam points into the page. The first cut forms the rake and end

clearance faces. The second and third cuts form the side clearance faces. The fourth cut intersects the rake face to form the cutting edge.

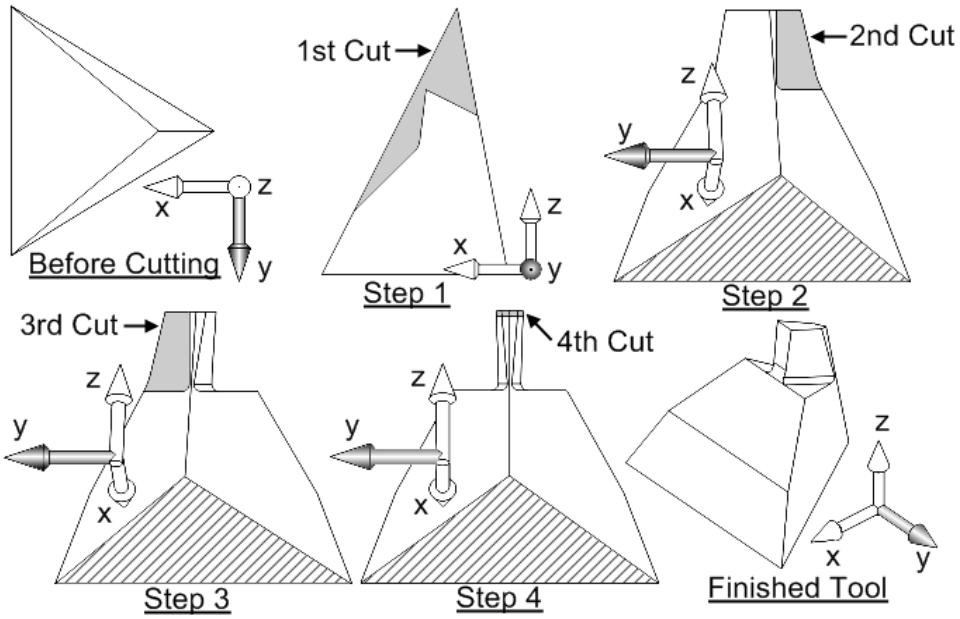


Figure 5.3: Single crystal diamond tool fabrication steps

The use of through cuts, the directions of the cuts, and the sequence of the cuts were selected to mitigate three problematic issues associated with FIB machining. The first issue is that it is difficult to control the exact depth of cut when machining using a focused ion beam. This is because the depth of cut, as a function of time, depends on many factors including ion beam current, how fast the beam is swept over the workpiece, the workpiece material, the crystalline orientation of the material, and the angle of incidence of the beam. Furthermore, when cutting a blind pocket it can be difficult to even judge what the depth of cut is. The use of through cuts exclusively, eliminates the difficulties associated with this issue because it is very easy to determine when a through cut is complete by taking an image of the tool blank using the same ion beam that is doing the cutting.

The second issue is that in order to align a workpiece relative to the ion beam, it is necessary to use the same ion beam to image the workpiece much a electron beam would be used in an SEM. During imaging the ion beam is set to a lower beam current than when intentionally cutting to reduce the material removal rate. However, any finished face facing the ion source will still be etched and degraded due to the imaging process. This issue is dealt with by orienting the sample such a critical face of the tool never faces the ion beam. For instance, in the first cut, the face of the tool blank that faces the ion beam is the same face that is to be removed in the third cut. Also, in the last three cuts only the backside of the tool, opposite the rake face, ever faces the ion source.

The third issue is that the ion beam does not consist of an infinity thin stream of ions that can be perfectly described with a vector. Rather the beam consists of a Gaussian distribution of ions that is spatially centered on a vector describing the beam direction. This means that when cutting, most of the ions will strike a target location, but some ions will also strike points around the target location. Hence, if a pocket is cut by rastering the ion beam on a set area, all of the edges and corners of the pocket will be rounded.

The third issue, which could potentially cause excessive rounding of the cutting edge, is also dealt with by cutting from the direction opposite of the rake face during the last three cuts. This is because when cutting through a piece of material, a sharper edge is formed on the side furthest from the ion source because the bulk of the material shields that edge from the Gaussian distribution of ions that round the edge formed on the side facing the beam [20]. The fourth cut in particular is intended to take advantage of this in order to get the sharpest possible cutting radius, which was 50 - 64 nm is most cases.

However, if a rake face shape such as a v-shape or curved shape does not lend itself to the use of a fourth cut, that step can be eliminated at the cost of a larger cutting edge radius in the neighborhood of 100 nm.

## 5.4 Tool Fabrication Procedure

The previous subsection described a series of FIB cuts that can be used to modify an existing single-crystal diamond AFM probe, henceforth referred to as a tool blank, in order to produce a tool geometry suitable for cutting micro-grooves. Now the implementation of these cuts using a FEI Dual Beam 235 FIB machine is described.

The exterior of the FEI Dual Beam 235 FIB machine along with its control console is shown in Fig. 5.4, and the interior of its vacuum chamber is shown in Fig. 5.5. Both an electron beam column and an ion beam column are incorporated into the machine, which are each terminated by a pole piece within the vacuum chamber. The electron column is orientated vertically and the ion column is titled so that it is set 52° from vertical. The presence of these two columns allows the same machine to be used for scanning electron microscopy, FIB microscopy, and FIB machining. The difference between FIB microscopy and FIB machining is that a much lower beam current is used in the former than the latter. However, some etching of a sample will still occur when imaging with an ion beam.

The sample to be imaged / cut is typically mounted onto a standard aluminum SEM sample stub that can be rotated using a motorized stage. This rotary stage in turn sits on a motorized 3-axis stage. Lastly, the 3-axis stage sits on a motorized sample tilt stage. This 5-axis movement is useful for sample positioning, but is limited in regards to achievable sample orientations because of limits on stage travel imposed by the confines

of the vacuum chamber of the machine and by the placement of delicate components within the vacuum chamber.

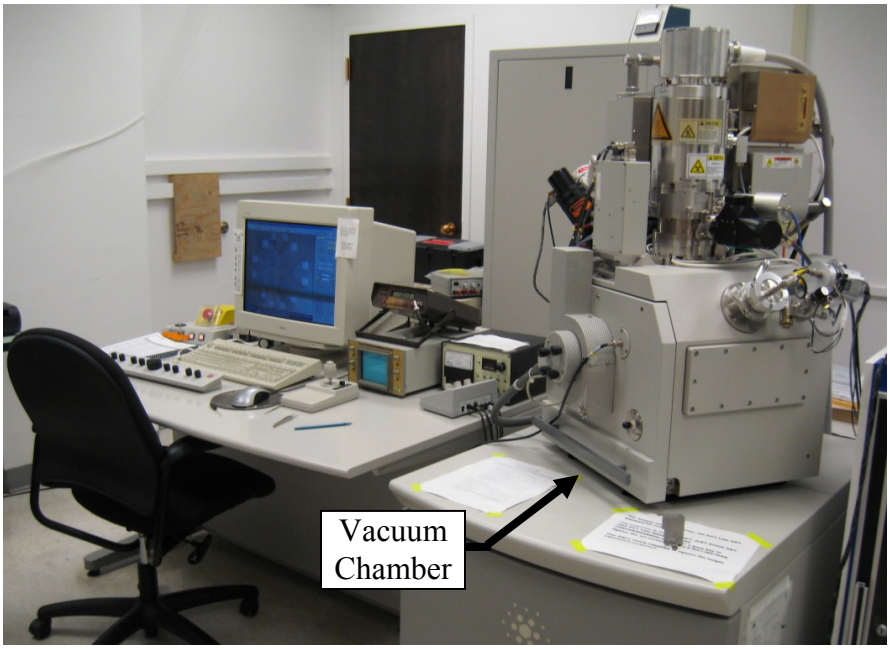


Figure 5.4: FEI Dual Beam 235 FIB machine exterior

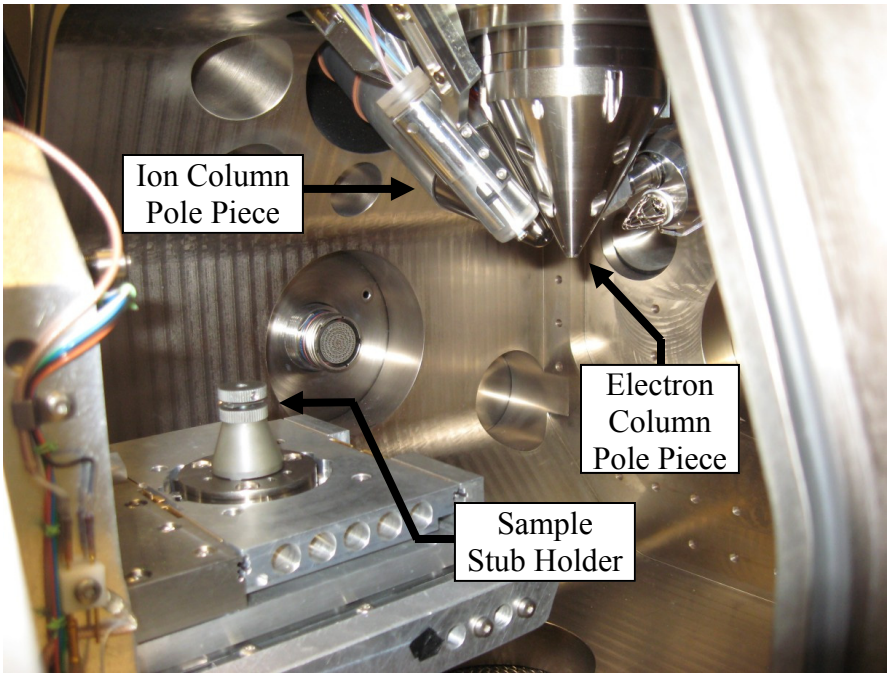


Figure 5.5: FEI Dual Beam 235 FIB machine vacuum chamber

In order to make the through cuts shown in Fig. 5.3 the tool blank must be rigidly mounted to a sample stub, and there must be electrical contact between the tool blank and sample stub. The tool blank must also be precisely positioned and aligned relative to the direction of the ion beam prior to each cut. Due to limitations in the travel of the five positioning stages, the later requirement means that the tool blanks must be mounted to a sample stub in specific orientations instead of arbitrarily.

Figure 5.6A shows one of the AFM probes that are used as tool blanks. As indicated by the scale bar in the image, the chip that the cantilever is mounted to is very small and can be difficult to handle. To ease handling, some of the blanks were glued into divots in small aluminum plates using an electrically conductive silver filled epoxy, as shown in Fig. 5.6B. Therefore, a way of mounting either of the configurations in such a way as to enable the four cuts in Fig. 5.3 is required.

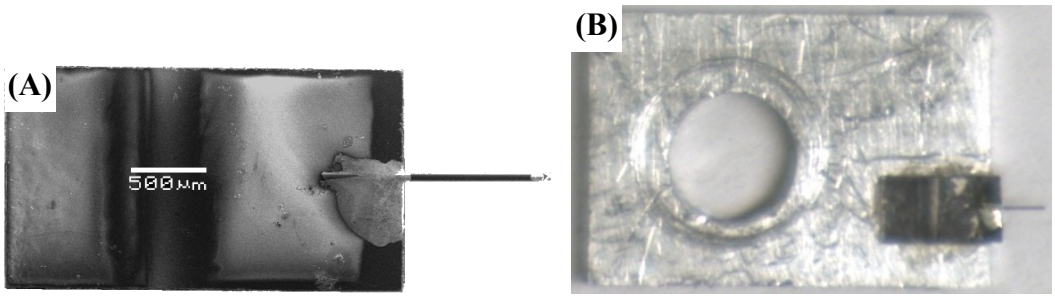


Figure 5.6: Tool blanks

In order to make the first cut, the tool blank must be oriented such that the ion beam travels in a direction perpendicular with the tool cantilever, as shown in Fig. 5.7A. Additionally, to make the last three cuts, the tool blank must be oriented such that the ion beam travels in a direction coincident with the axis of the cantilever and towards the chip the cantilever is bonded, as shown in Fig. 5.7B.

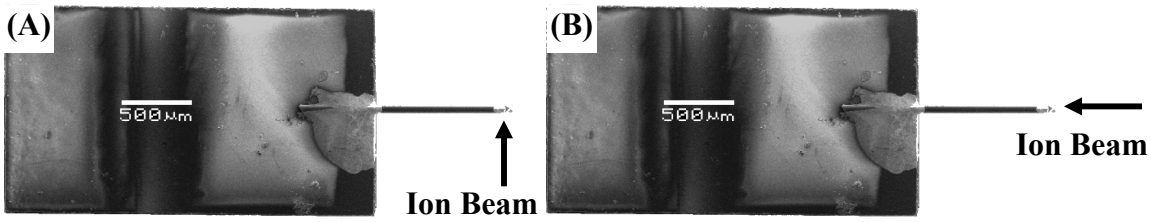


Figure 5.7: Required ion beam directions in first cut (A) and last three cuts (B)

The ion beam in the FEI Dual Beam 235 FIB machine travels in a direction 52° from vertical. Due to limits in the travels of the machine stages, this means that the tool blanks must be mounted to a 45°-angle sample stub during machining on order for the required orientations to be achievable. A common way for attaching a sample to such a sample stub would be to use double-sided carbon tape. However, this proved to not be rigid enough and allowed too much tool blank movement during FIB machining. To alleviate this issue, a fixture was fashioned, shown in Fig 5.8A, that incorporates a vice that can hold the stand-alone tool blanks shown in Fig. 5.6A and that incorporates bolt holes to allow for fixturing of the mounted blanks shown Fig. 5.6B.

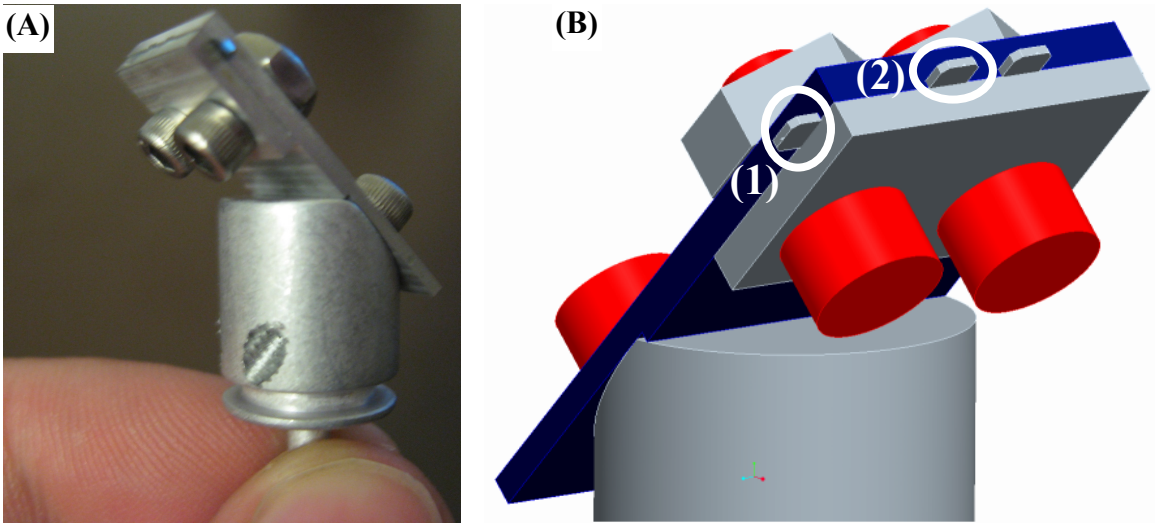


Figure 5.8: Fixture for use in FIB machining AFM probe

The fixture is oriented within the FEI Dual Beam 235 FIB machine as shown in Fig. 5.9. During the first cut, the fixture holds the blank in the first orientation labeled in Fig. 5.8B. This allows the ion beam to strike the side of the blank as shown in Fig. 5.7A. Prior to the second cut, the blank is removed from the fixture and replaced in the second orientation labeled in Fig. 5.8B. This allows the ion beam to strike the side of the blank as shown in Fig. 5.7B, which is necessary for the last three cuts. These two different fixturing orientations were required due to limitations in the travel of the FIB machine stages. However, a machine with a different stage configuration would not have this issue. This would be beneficial since manually changing the position of a blank in the fixture requires venting and subsequent pumping down of the FIB vacuum chamber, which takes approximately 30 minutes to complete.

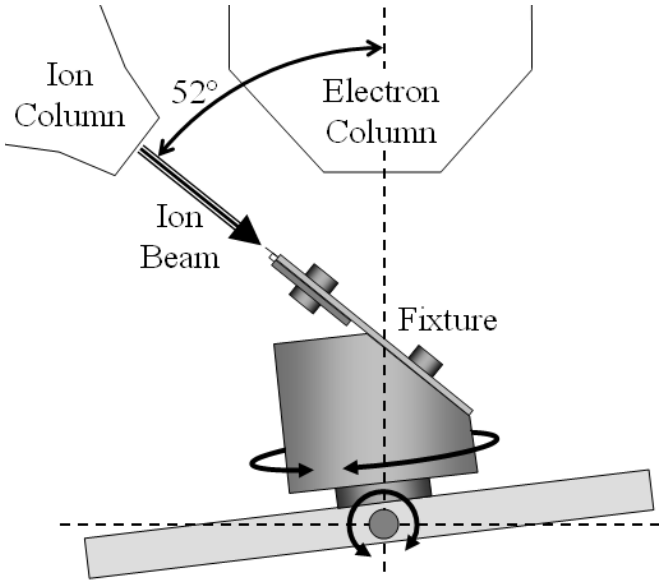


Figure 5.9: Arrangement of fixture inside FEI Dual Beam 235 FIB during tool fabrication

During FIB machining, the ion beam removes material by repeatedly sweeping the beam over areas where material is to be removed. The trajectory that the beam follows, and hence of shape of the specified area, is controlled by a beam trajectory file.

This file is generated by software included with the machine that accepts a bitmap image where areas to be machined area in black and areas to be left alone are in white and a value indicating the distance per pixel in the bitmap image. In addition to generating the beam trajectory file, the software also specifies the magnification that the machine should be set to during machining using the beam trajectory file generated. Example images suitable for producing a tool like the one in Fig. 5.2 and are shown in Fig. 5.10.

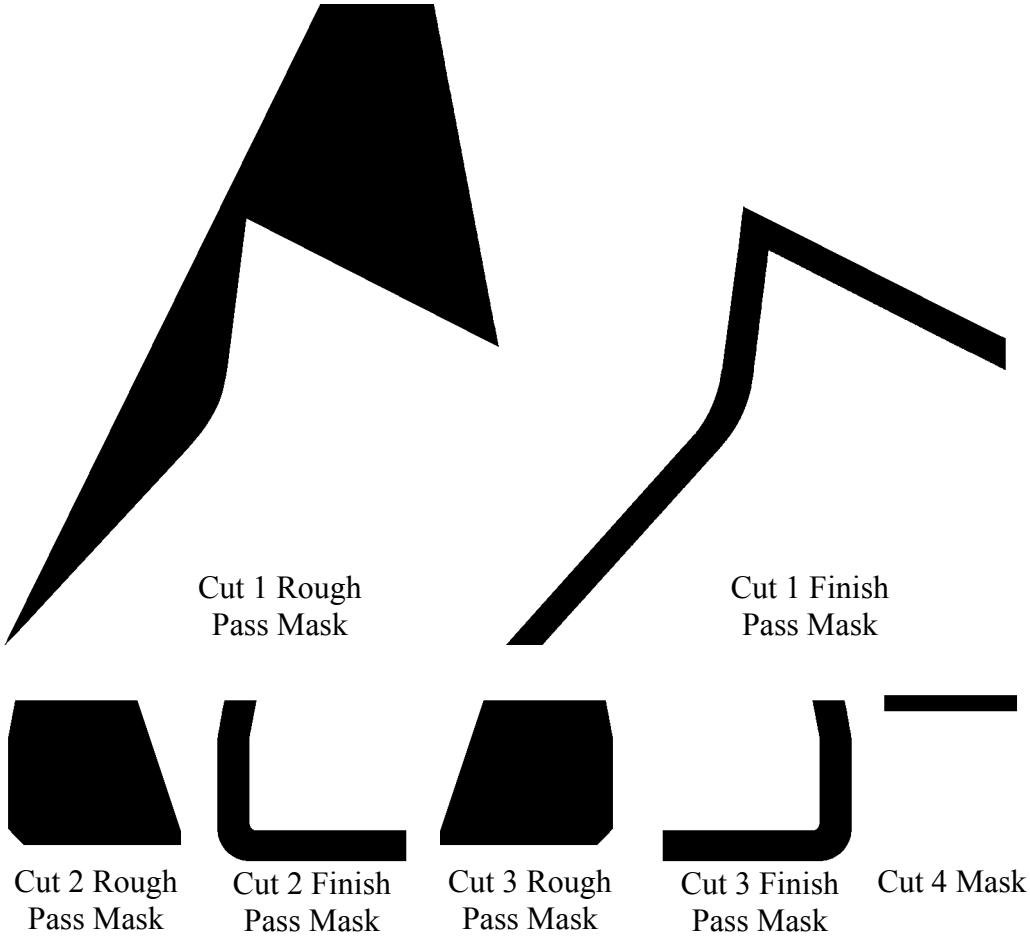


Figure 5.10: Image masks used during FIB machining

Once the beam trajectory files have been prepared and the fixture is placed within the FIB machine, the following steps are followed to make each of the cuts. First, the ion beam current is set low enough current that images can be taken of the blank using the

ion beam without the blank being etched very quickly (~ 10 pA) and the beam trajectory file for the cut is loaded. Second, the blank is imaged with the ion beam in real time, and the area to be cut appears superimposed on the image. The machine is set to the magnification provided by the software that produced the beam trajectory file and its stages are adjusted to get the area to be cut to line up with the appropriate location on the blank. The ion beam path can also be electronically shifted slightly to allow for extremely fine alignment adjustments. Third, the ion beam is set to scan along the path indicated by the beam trajectory file and the ion beam current is increased (~500 – 7000 pA). High ion beam currents, which result in fast but lass controlled cutting, are useful for hogging out material and lower ion beam currents are useful for finish passes. Fourth, periodically, the machine is momentarily set back into imaging mode in order to see how far the cut has progressed. Each FIB cutting operation is allowed to continue until the ion beam has removed all required material.

## 5.5 Chapter Summary

This chapter described the design and fabrication of flexible cutting tools with cutting geometries intended to be significantly more effective than the geometries of the commercial AFM probes used as tools in the Chapter 4. This involved the proposal of several tool design principles, introduction of a versatile tool fabrication procedure, and discussion of how this procedure was implemented using a commercial FIB machine. In the next chapter, a series of experiments are described that evaluate the effectiveness of the new tool geometries introduced in this chapter.

# Chapter 6

# Experiments Using FIB Machined Flexible Single-Point Cutting Tools

## 6.1 Chapter Introduction

In the previous chapter a method of fabricating flexible cutting tools with geometries tailored to micro-groove cutting was described. This chapter addresses evaluation of the performance of these tools when used to cut micro-grooves under various conditions. This is accomplished by describing six experiments that evaluate micro-groove cutting under different conditions and while using different tool geometries. The first four of these experiments involve cutting individual grooves that are spaced far enough apart to avoid complicating effects such as displaced material from one groove being involved in the formation of another groove. These experiments establish relationships between process parameters, i.e., cutting load, cutting speed, and tool shape, and process outputs including groove shape, groove quality, tool wear, and chip morphology. Of these relationships, the one between cutting conditions and groove shape is of particular interest because, due to the flexible nature of the tools, depth of cut cannot be controlled directly but rather is a function of cutting conditions, tool geometry, and workpiece material.

Tools capable of cutting relatively wide rectangular grooves, suitable for micro-fluidics and surface texturing applications, are used in the first and fourth experiments where one micron wide grooves are cut using various cutting loads and speeds. A

narrower tool, suitable for cutting rectangular grooves that could be used in high-density micro-heat exchangers, is used in the second experiment. A tool suitable for cutting compound v-shaped grooves that could be used in optical applications such a light guides is used in the third experiment where the capability of achieving a desired groove shape with close tolerance is considered. Note that compound v-shaped grooves, instead of simple v-shaped grooves, were considered because they represented a feature that was more difficult to manufacture and that had an actual application in LCD light guides.

The last two experiments explore interactions between existing grooves and grooves that are being cut because there are applications where such interactions are unavoidable. Such interactions may occur in micro-optics applications, where grooves may need to be so closely spaced that material deformed during the formation of one groove is involved in the formation of another groove. Also, when forming surface texturing patterns or networks of micro-fluidic channels it may be necessary to intersect a new groove and an existing groove. For these reasons, the effects of cutting one micron wide parallel grooves in close proximity to each other were considered in a fifth experiment. Also, the effects of cutting intersecting grooves under varying machining conditions and with different groove patterns were considered in a sixth experiment.

## 6.2 Tools Used in Experiments

Three single-crystal diamond tools were fabricated and each tool was examined with an SEM in order to quantify the actual geometry that was achieved. For example, Fig. 6.1 shows several images that describe tool D1. The characteristics of each tool are listed in Table 6.1. The listed back rake angles and end clearance angles are achieved when the tool is held such that the end of the bent cantilever is at a 7° angle with respect

to the workpiece surface, which is a condition that was enforced during all experiments. Also, the shape of the rake face of each tool is shown in Fig. 6.2.

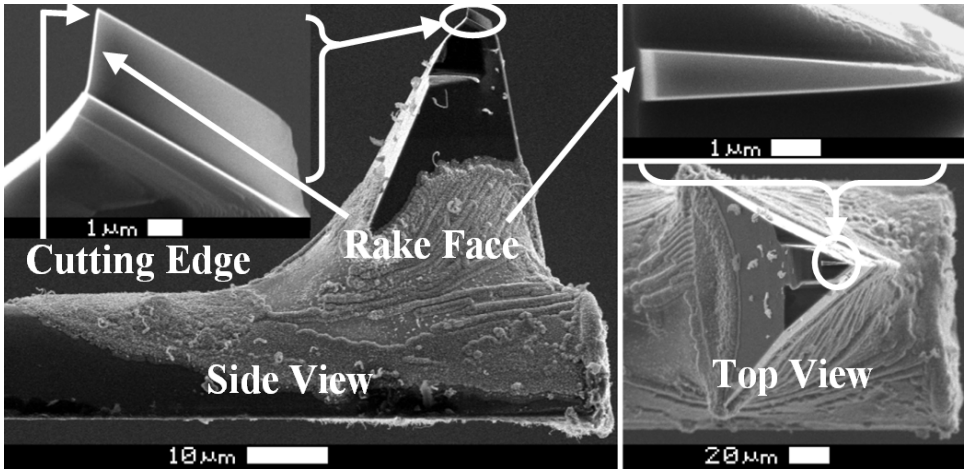


Figure 6.1: Overall shape of diamond tool D1

Table 6.1: Fabricated diamond tools

| Tool | D1 | D2 | D3 |
|---|---|---|---|
| Cantilever Stiffness (N/m) | 100 | 100 | 102 |
| Shape | Rectangle | Rectangle | Compound-V |
| Back Rake Angle (°) | 0 | 0 | 0 |
| End Clearance Angle (°) | 20 | 20 | 10 |
| Side Clearance Angles (°) | 2.98 | 5.0 | ~ 7.0 |
| | 3.59 | 3.5 | ~ 7.0 |
| Width (µm) | 1.05 | 0.411 | N/A |
| Edge Radius (nm) | 62 | 50 | 97 |
| Max Depth of Cut (µm) | 2.32 | 2.38 | 2.03 |

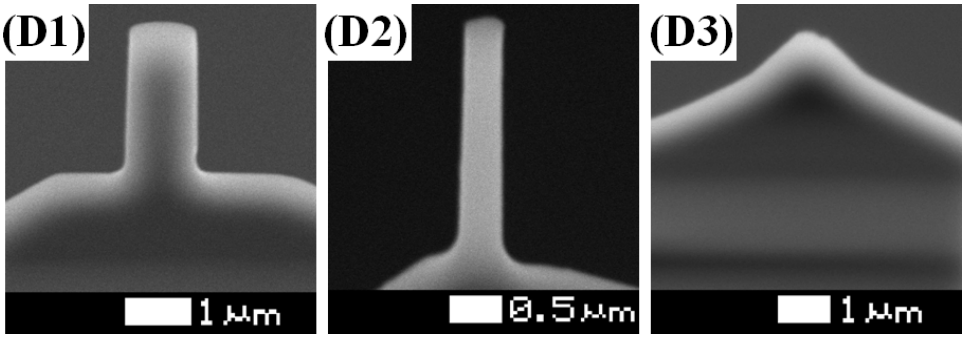


Figure 6.2: Rake face profiles of fabricated diamond tools

Tools D1 and D2 were to have rectangular rake faces and were produced via the four FIB cuts previously described. Figure 6.1 shows an example of this type of tool. As can be seen in Fig. 6.2, the overall shape of the rake face of each tool was fairly close to an actual rectangle. By contrast, tool D3 in Fig. 6.2 had a compound v-shaped rake face where the two included angles were 90° and 120°. When fabricating this tool, the fourth FIB cut was not used, which is the reason for the larger edge radius listed in Table 6.1. Also, some undesired rounding of the tip of the rake face was present, but this can be reduced through improved control of the FIB machining process.

## 6.3 Experimental Procedure

The groove cutting procedure employed in this set of experiments was identical to the procedure described in Chapter 3. Following each experiment, an SEM was used to characterize the micro-grooves, examine chips attached to the tool and workpiece, and to measure tool wear. An AFM, loaded with a high-aspect ratio silicon AFM probe, was also used to measure groove geometry. However, this latter measurement was complicated by the fact that the portion of the AFM probe that contacted each groove is of a similar size scale as each groove. This caused some measurement distortion, shown in Fig. 6.3, despite the use of high-aspect ratio probes.

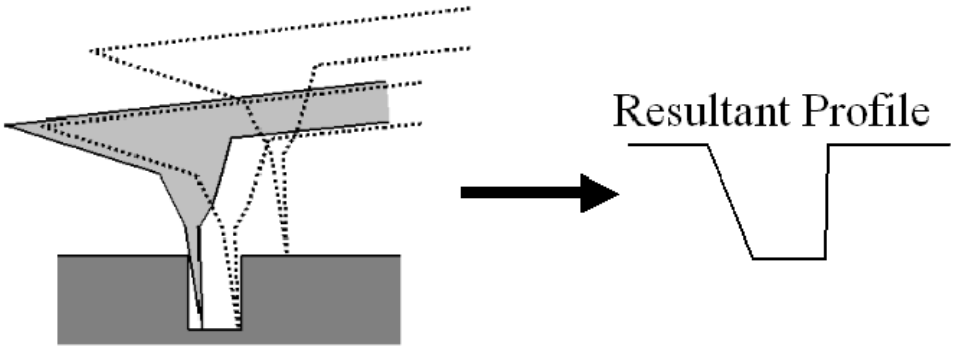


Figure 6.3: AFM measurement distortion

The distortion is caused by the finite aspect ratio of the AFM tip and any tilt in the tip relative to the groove. In particular, the latter distortion source causes one side of a measured groove to appear to have a shallower slope than is actually present. AFM probes with tilted tips were used in an attempt to compensate for this, but variations in the angle the AFM equipment held the probe and sample at insured that some tilt-based distortion was still present and must be accounted for when interpreting the AFM images.

## 6.4 Solitary Groove Cutting Experiments

Experiments were conducted to evaluate the factors that affect groove depth, groove shape, and tool wear. Hence tool load, cutting speed, and tool shape were varied during four experiments, as described in Table 6.2. In the first three experiments cutting speeds were limited to those used with some success in the previous chapter. In the fourth experiment, an effort was make to determine if significantly higher speed cutting could be performed successfully or if such high cutting speeds would break the tool.

Table 6.2: Conditions for Experiments 1, 2, 3, and 4

| Exp. | Tool | Tool Passes | Speeds (mm/min) | Loads (mN) | Total Distance Cut (mm) |
|---|---|---|---|---|---|
| 1 | D1 | 3 | 25, 50 | 0.3, 0.4, …1.3, 1.4 | 122.4 |
| 2 | D2 | 5 | 25, 50 | 0.6, 0.8, 1.0, 1.2 | 52.0 |
| 3 | D3 | 3 | 50 | 0.3, 0.4, …1.3, 1.4 | 61.2 |
| 4 | D1 Resharpened | 1 | 50, 100, 200, 300, 400 | 0.3, 0.5, 0.7, 0.9, 1.1, 1.3 | 180.0 |

In each experiment, a separate groove was cut using each experimental condition where the conditions for a given experiment consisted of all combinations of the corresponding speeds and loads given in the table. The workpiece in each experiment was a 3.1 μm thick film of thermally evaporated aluminum deposited onto a silicon substrate. The order in which the conditions were used was selected randomly in

Experiments 1, 2, and 3. However, in Experiment 4, speeds were tested in ascending order in order to determine at what speed, if any, that the tool would fail. The order the loads were tested in was still selected randomly.

### 6.4.1 Exp. 1 - Rectangular Groove Cutting Results

Over the course of Experiment 1, a total distance of 122.4 mm was cut in aluminum, and tool wear was evaluated by comparing SEM images of the tool before and after cutting. It was found that the only change in tool geometry was a small increase in cutting edge radius from 62 nm to 81 nm. Therefore, tool wear is not expected to have had a significant effect on groove formation for the material considered.

AFM images were captured of sections of the workpiece representative of each cutting condition after each tool pass. It was found that relatively high-aspect ratio grooves could be created. However, this caused the type of AFM measurement distortions described earlier in this paper. This is seen by scanning a section of a groove, rotating the sample 180°, taking another scan of the groove, and then matching up the two scans. Figure 6.4 shows cross-sections assembled from two such scans of a groove cut at 50 mm/min with a 1.1 mN load. The actual geometry is best represented by the left half of the solid line and the right half of the dashed line.

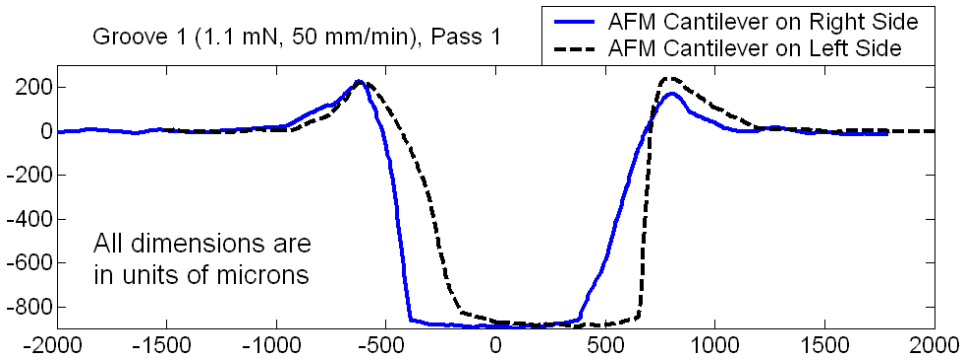


Figure 6.4: Groove cut at 50 mm/min with a 1.1 mN load

As can be seen in Fig. 6.4, the grooves were rectangular in shape. However, it would have been impractical to create composite cross-sections, like in Fig. 6.4, for every groove. Hence, it should be noted that for all other cross-sections shown in this chapter, one of the sidewalls may appear less vertical that it actually is. In this experiment, for example, the left sidewall is more representative of the actual geometry.

Cross-sections of the grooves cut at 25 mm/min are shown in Fig 6.5 following each tool pass. Similar cross-sections of the grooves cut at 50 mm/min are shown in Fig. 6.6. It was found that rectangular groove cross-sections were produced under all cutting conditions when the measurement distortion is taken into account. All groove increased in depth following each tool pass. Also, all grooves had side burrs with sizes dependent on cutting conditions. Groove shape was found to not be affected by cutting speed.

The depths of the grooves are plotted in Fig. 6.7. As can be seen in the figure, groove depth increased with increased load and with an increased number of tool passes, but cutting speed had very little effect on the depth of cut. Furthermore, the increase in depth of cut with load was more quadratic in nature than linear. It can also be seen that groove depth increased the most during the first tool pass, increased less during the second tool pass, and increased even less during the last tool pass. The spread of the data points for any given condition indicates that variations in groove depth are not large relative to the depth of cut, which is an improvement compared to the results presented in Chapter 4 and indicates the potential to achieve good relative tolerances.

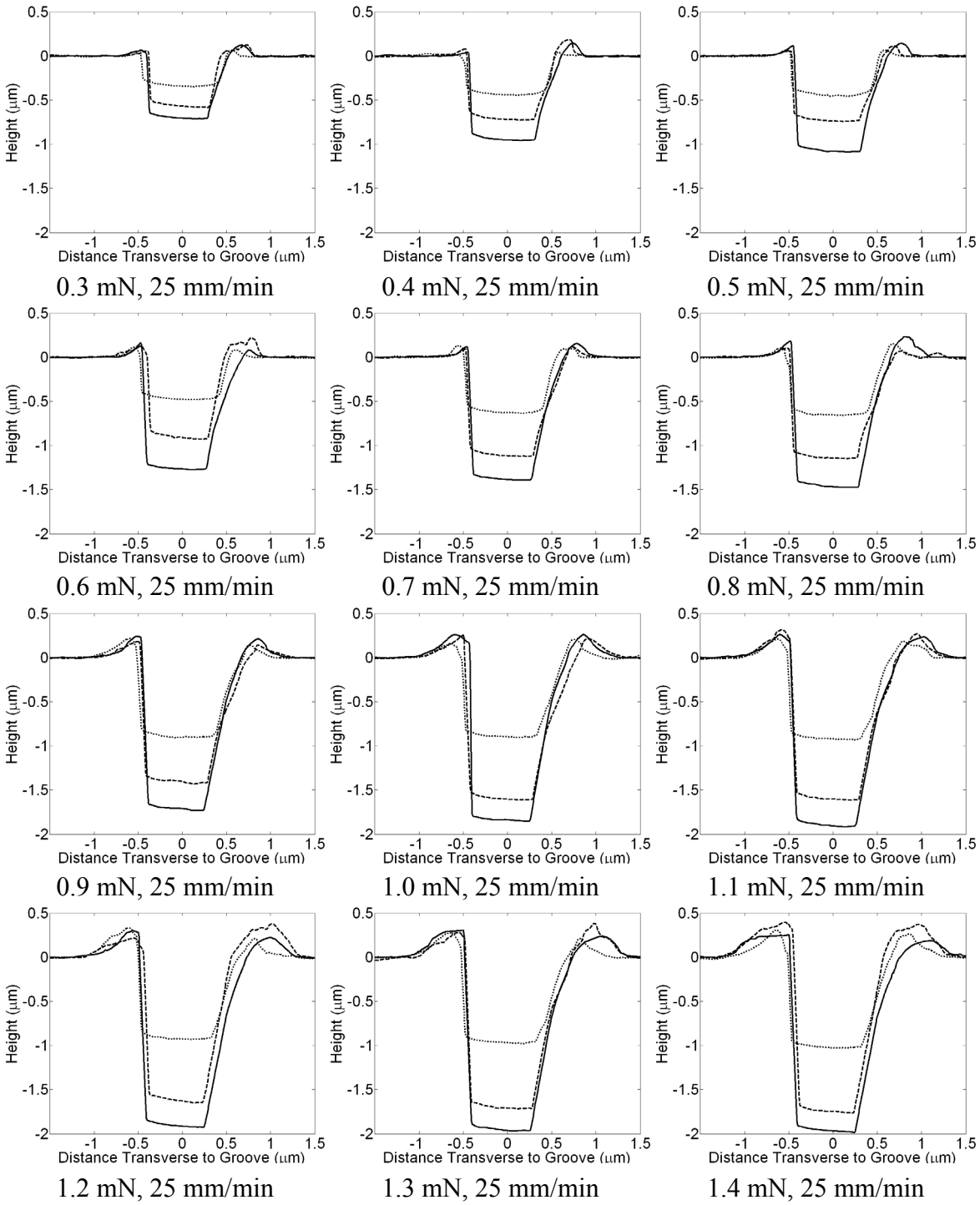


Figure 6.5: Rectangular grooves cut at 25 mm/min following each tool pass

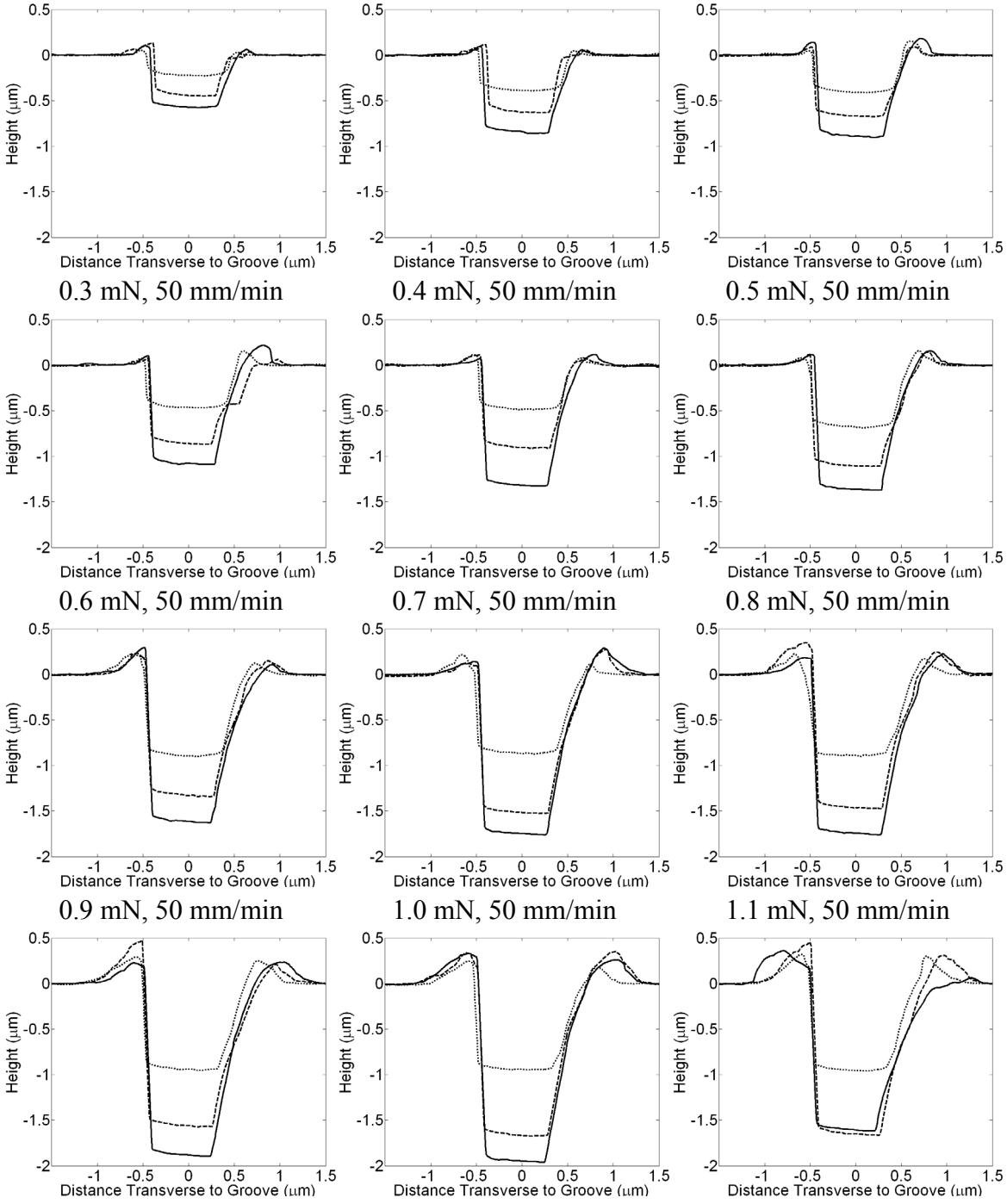


Figure 6.6: Rectangular grooves cut at 50 mm/min following each tool pass

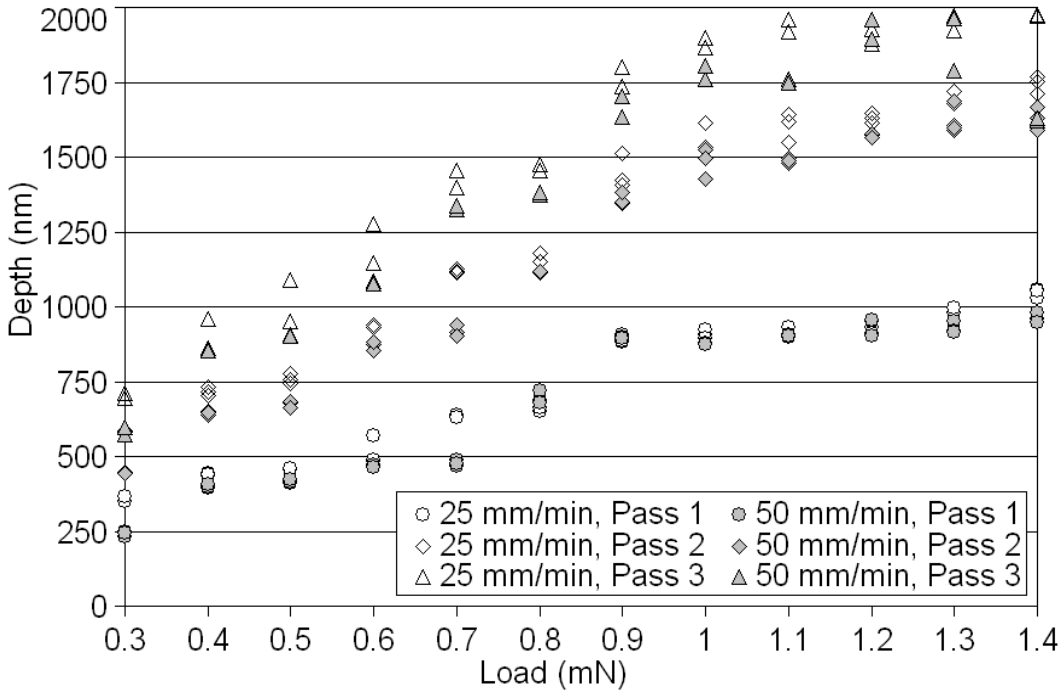


Figure 6.7: Rectangular groove depth under different conditions

Burrs were generated on the top edges of all of the grooves. The size of these burrs was found to directly relate to the depth of cut and number of tool passes used. This can be seen in Fig. 6.8 where burr height is plotted vs. groove depth following the first, second, and third tool passes. It can be seen that when one tool pass was used, burr height increased nearly linearly with groove depth until a depth of about 850 nm was achieved, at which point burr height increased dramatically. Additionally, when two tool passes were used, a similarly dramatic increase in burr height occurred when a groove depth of about 1500 nm was achieved. This suggests that for the material considered there is a critical depth of cut per tool pass of about 750 - 800 nm, which is independent of cutting speed, in the range considered, and will result in significant burr formation if exceeded. Hence, the maximum depth of cut per tool pass appears to be limited by acceptable burr size.

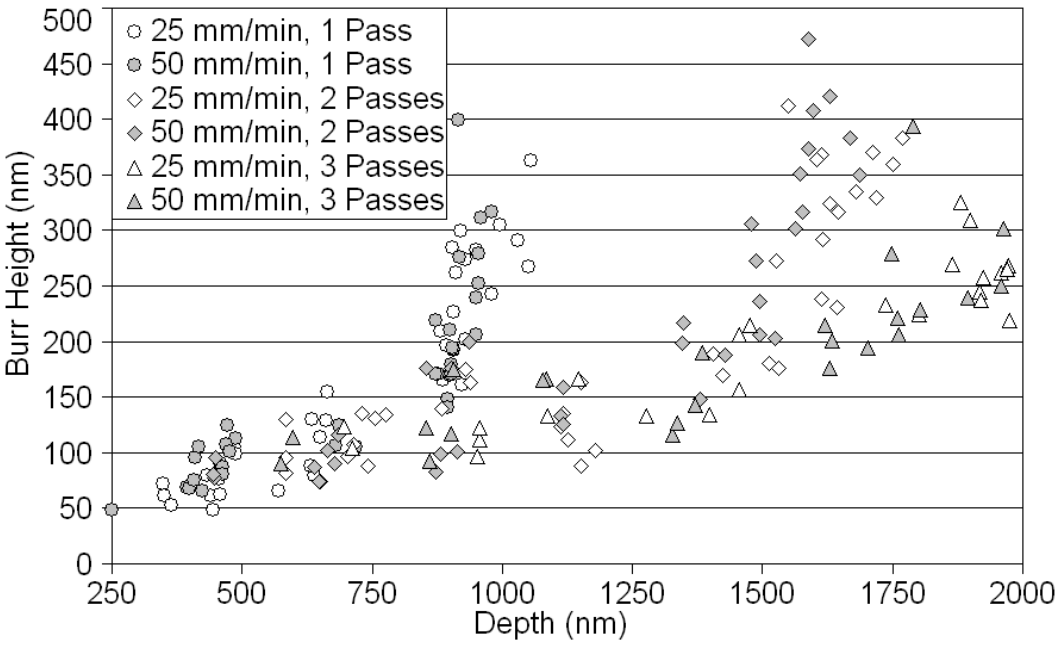


Figure 6.8: Rectangular groove burr height at different depths of cut

In addition to being used to create groove cross-sections, AFM images of the grooves were also used to see how the depths of the grooves varied along a cut. Variations in depth of cut can be caused by effects such a machine tool dynamics, tool dynamics, or cutting process-based variations in cutting forces. For instance, the AFM probe modified to construct tool D1, used in this experiment, has a natural frequency of 36.7 kHz. Hence, when cutting at 50 mm/min, the period of groove depth variations caused by undamped cantilever vibrations at resonance would be 22.7 nm. Furthermore, this period will increases with the introduction of damping. Hence, it is desirable to examine the frequency of depth variations. It is also desirable for depth variations to be as small as possible in order to achieve the best possible groove depth tolerances. Hence, examination of groove depth variation magnitude is also desirable.

In order to extract either depth variation magnitude or frequency it is necessary to extract a line profile describing the depth of the groove floor. The magnitude of the

variations can then be seen by plotting this profile. The frequency of the variations can be found by using the known cutting speed to relate distance along the profile to time and then getting the frequency spectrum using a fast Fourier transform (FFT).

However, extraction of frequency information is complicated by limitations in the Digital Instruments / Veeco Dimension 3100 AFM used in the work. Specifically, when scanning a sample, the AFM is only capable of capturing 512 data points in any direction. I.e., a AFM image can never contain more than 512 x 512 data points. This means that if an image is taken of a small area, high frequency variations in groove depth can be observed but low frequency variations cannot. Conversely, if an image is taken of a large area, low frequency variations can be seen by high frequency variations cannot as per the Nyquist sampling theorem. Also, since the scanning stages of the AFM do not have built in position sensors, stitching images of small adjacent areas together is not a practical means of circumventing the 512 point limit.

Therefore, in order to see both low and high frequency variations in groove depth in the direction of cut, images were taken of selected grooves with scan sizes of 5 μm, 10 μm, 20 μm, and 40 μm. Hence, the images with a 5 μm scan size contained high frequency information and each progressively larger image contacted progressively lower frequency information. Figure 6.9 shows the groove bottom profiles from each scan of the groove cut using one tool pass, a cutting speed of 50 mm/min, and a load of 0.7 mN. Figure 6.10 show similar profiles corresponding to the other groove examined in this manner, which is the groove that was cut using one tool pass, a cutting speed of 50 mm/min, and a cutting load of 1.2 mN. Figure 6.11 and Fig. 6.12 show the frequency spectra associated with the profiles in Fig. 6.9 and Fig. 6.10, respectively.

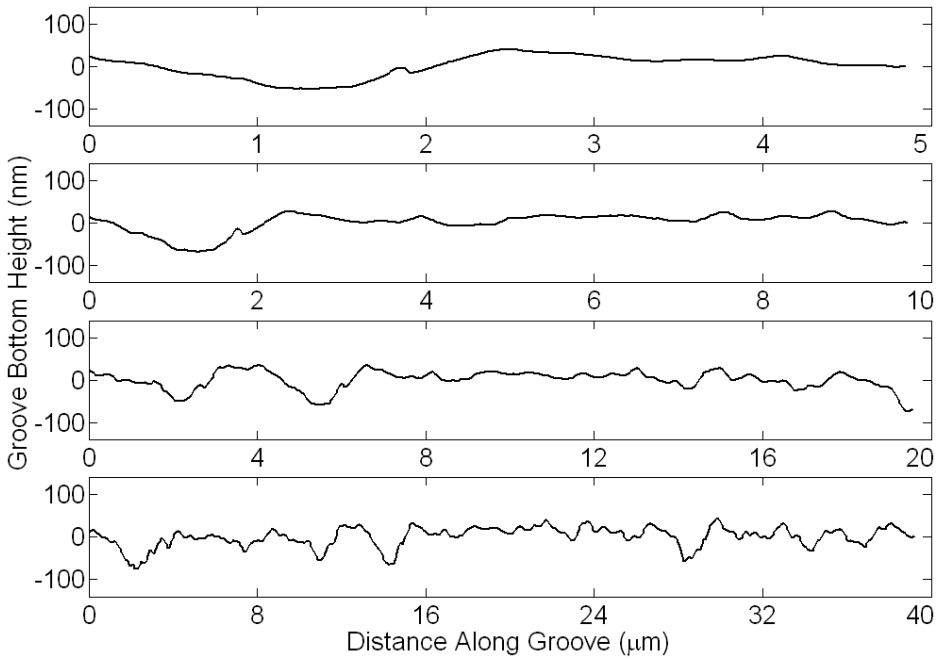


Figure 6.9: Scans at different length scales along a groove cut using one tool pass at 50 mm/min and with a 0.7 mN load

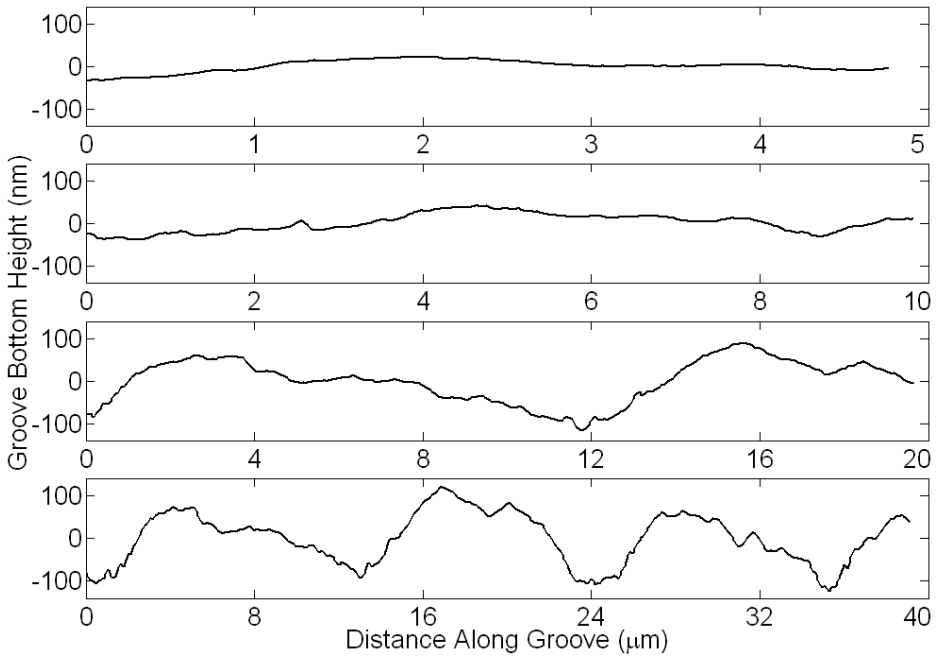


Figure 6.10: Scans at different length scales along a groove cut using one tool pass at 50 mm/min and with a 1.4 mN load

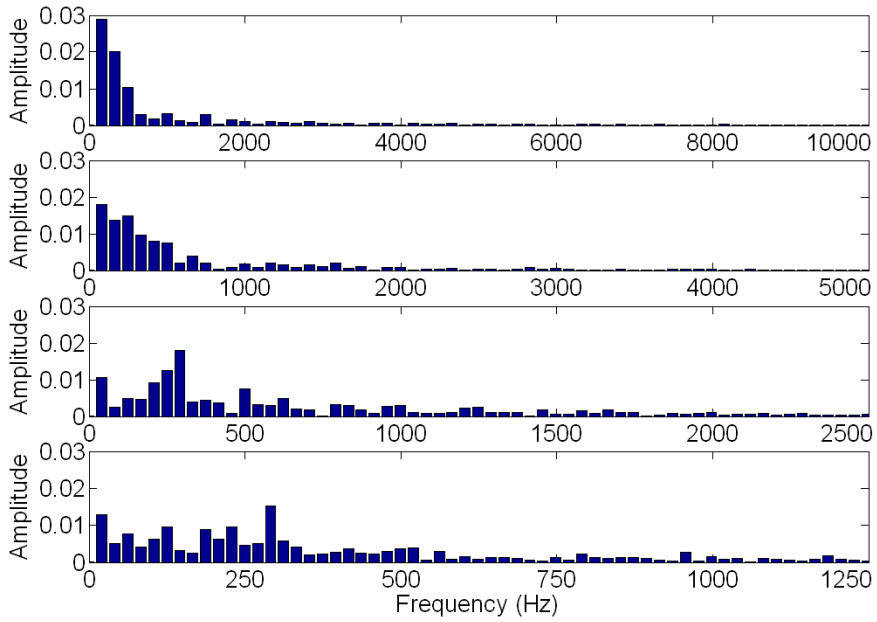


Figure 6.11: Spectrum of scans at different length scales along a groove cut using one tool pass at 50 mm/min and with a 0.7 mN load

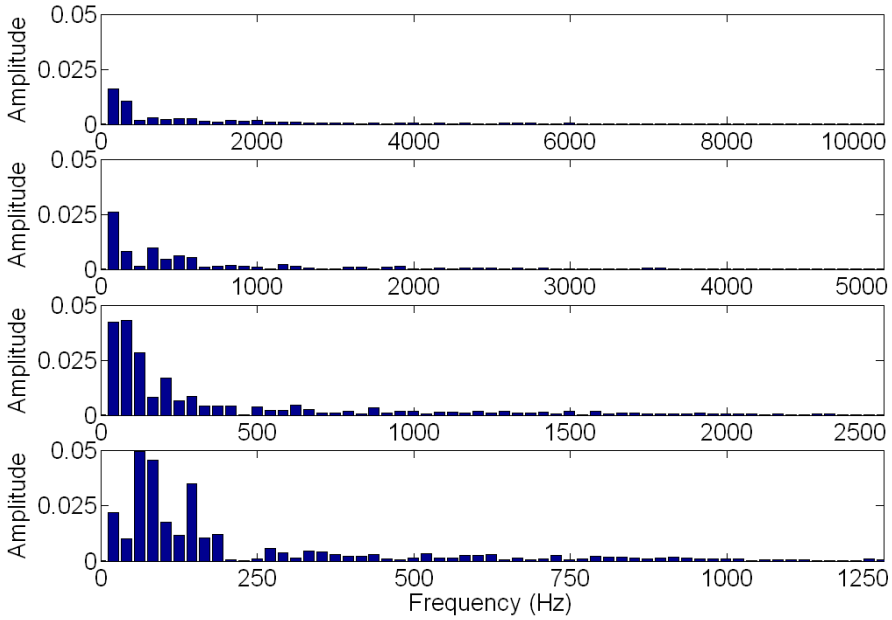


Figure 6.12: Spectrum of scans at different length scales along a groove cut using one tool pass at 50 mm/min and with a 1.4 mN load

Examination of Fig. 6.9 shows that, in the 0.7 mN case the Ra of the groove bottom was 17.7 nm. The corresponding spectra in Fig. 6.11 show that there are no

significant frequency components above 3000 Hz, the majority of depth variations occurred below a frequency of 1000 Hz, and the largest frequency component was at about 300 Hz. Therefore, the cantilever must be heavily damped because this is not nearly as high as the tool natural frequency of 36.7 kHz. It is possible that tool mass / stiffness had very little effect on the cutting process and that the variations seen are due to other dynamic phenomenon.

Examination of Fig. 6.10 shows that, in the 1.4 mN load case the Ra of the groove bottom was 50.4 nm, which is 2.85 times greater than in the 0.7 mN case. In can be seen from the corresponding spectra, shown in Fig. 6.12, that there is very little variation at frequencies above 600 Hz. Furthermore, the majority of variation occurs below 200 Hz and the largest frequency component is at 50 – 60 Hz. This is again much lower than the undamped natural frequency of the tool, and is also lower than in the 0.7 mN load case. This frequency shift might be due to increased frictional damping along the tool-chip interface, which tends to increase in length with depth of cut in traditional machining. Alternatively, the low frequency component might be introduced by the significantly greater amount of burr formation with might introduces stochastic force components.

SEM images of the grooves were also examined and it was found that long curly chips were formed and tended to be attached to the workpiece at the end of each cut. These chips, shown in Fig. 6.13A, can be easily removed after cutting by using a nitrogen blow-off, as shown by Fig. 6.13B. It is interesting to note that unlike the applications considered here, where these chips are a nuisance at best, in other applications requiring the formation of nanowires, the formation of these chips may be the primary objective.

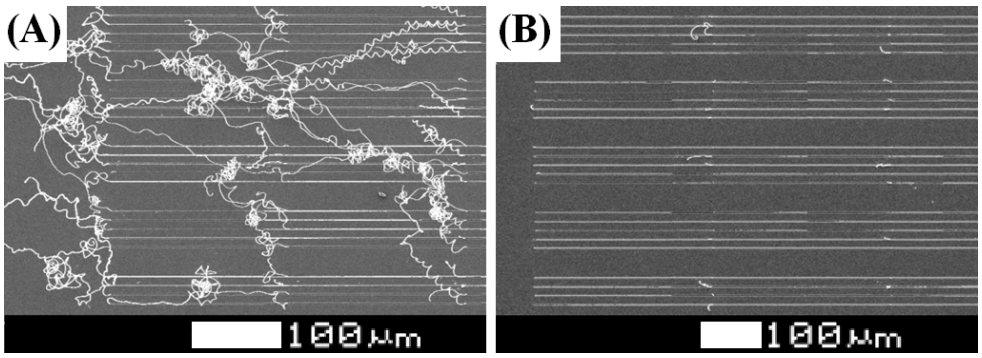


Figure 6.13: Workpiece with attached aluminum chips (A) and after chips were removed with nitrogen blow-off (B)

The chips connected to the workpiece at the end of each cut were examined. Figure 6.14 shows chips produced when cutting under two different conditions. It was found that the side of each chip that slides up the rake face of the tool during cutting is very smooth, and the opposite side of the chip has a rough serrated texture. This is consistent with chip formation at the macro-scale and was also seen in Chapter 4 when cutting with an AFM probe. Additionally, as seen in Fig 6.14B, the progressing front of deformed material at the point of chip formation has a somewhat rounded profile. A more comprehensive examination of chip morphology is provided when discussing the results from Experiment 4 later in this chapter.

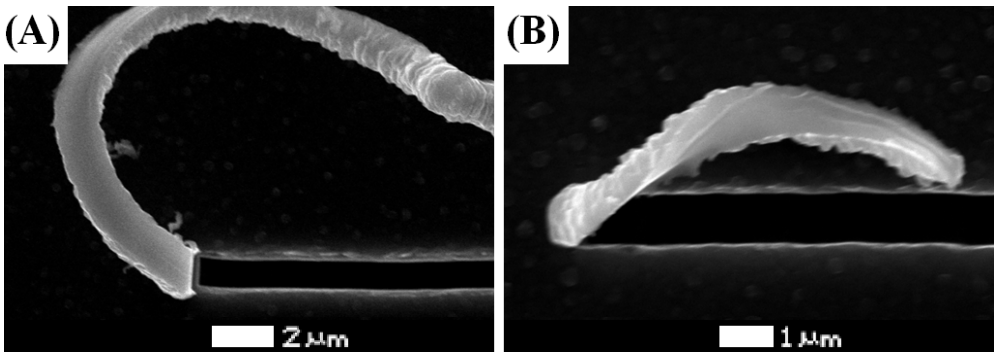


Figure 6.14: Aluminum chip formed while cutting at 25 mm/min with a 0.9 mN load (A) and at 50 mm/min with a 0.5 mN load (B)

## 6.4.2 Exp. 2 - Very Narrow Groove Cutting Results

In order to determine if narrower grooves could be produced, a second experiment was conducted where a 411 nm wide diamond tool, tool D2 in Table 6.1, was used to cut several grooves. SEM images were taken of the workpiece after each cut, and an attempt was made to capture AFM cross-sections of each groove. However due to the extreme narrowness and high-aspect ratio of the grooves, AFM images could not be captured using available AFM equipment. Therefore, less detailed information was collected via examination of SEM images and FIB cross-sections of selected grooves.

For example, an FIB machined cross-section of a groove cut using one tool pass at 25 mm/min and with a 1.2 mN load is shown in Fig. 6.15A. Note that the groove cross-section appears much more tapered than it actually is due to redeposition of sputtered ions onto the groove sidewalls during FIB machining. However, such a cross-section can still be used to estimate groove width at the workpiece surface.

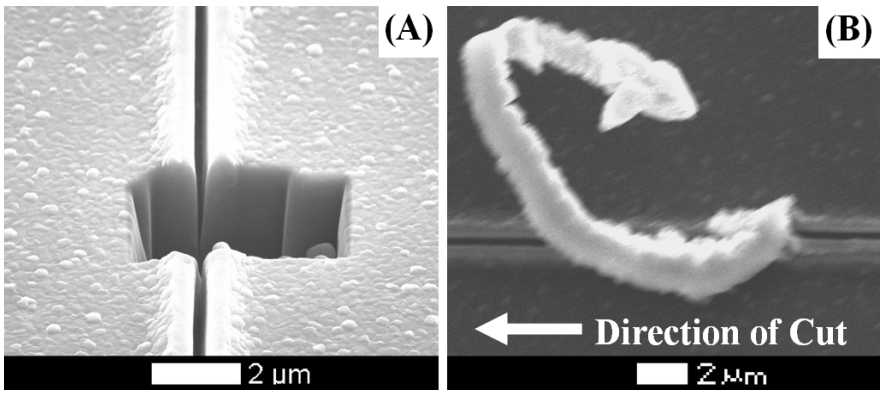


Figure 6.15: FIB Cross-section from 1st tool pass (A) and chip formed during 2nd tool pass (B) at 25 mm/min with a 1.2 mN load

It was found that no measurable tool wear occurred over the course of the 52 millimeters cut in Experiment 2. Furthermore, narrow grooves were successfully cut and

chip formation occurred in all cases. The widths of these grooves was about 300 nm, which is less than the 411 nm width of the tool and indicated the presence of 55.5 nm of elastic recovery at each sidewall.

Additionally, marks on the top workpiece surface near the grooves indicated that the tool reached its maximum possible depth of cut of 2.38 μm during some of the cuts, and that the shoulder of the tool (see Fig. 6.2B tool D2) rubbed against the workpiece. This can be seen in Fig 6.15B where the chip being formed during a second tool pass is significantly wider than the groove formed during the first tool pass. This occurred during the second tool pass when a 1.2 or 1.0 mN load was used and during the fifth tool pass when a 0.8 mN load was used. This indicates a depth of cut per tool pass of at least 1.19 μm when using a load of 1.0 mN or greater. As with the wider tool in Experiment 1, cutting speed did not appear to have had an effect on cutting behavior.

### 6.4.3 Exp. 3 - Compound V-Groove Cutting Results

A third experiment was conducted to evaluate the capability of cutting a groove with a more complex desired cross-section. The desired geometry was a compound v-shape with a 0.95 μm deep section that has an included angle of 90° that transitions to a 0.45 μm deep section with an included angle of 120°. Inspection of the resultant groove cross-sections showed that the desired cross-section was achieved when using a 1.2 mN load, as can be seen in Fig. 6.16. In the figure the actual groove cross-sections following each tool pass are shown as solid, dotted, or dashed lines, and the desired cross-section is shaded grey. The only difference between the desired cross-section and actual groove shape, when a 1.2 mN load and three tool passes were used, was slight rounding at the bottom of the groove due to the rounded tool shape shown in Fig. 6.2.

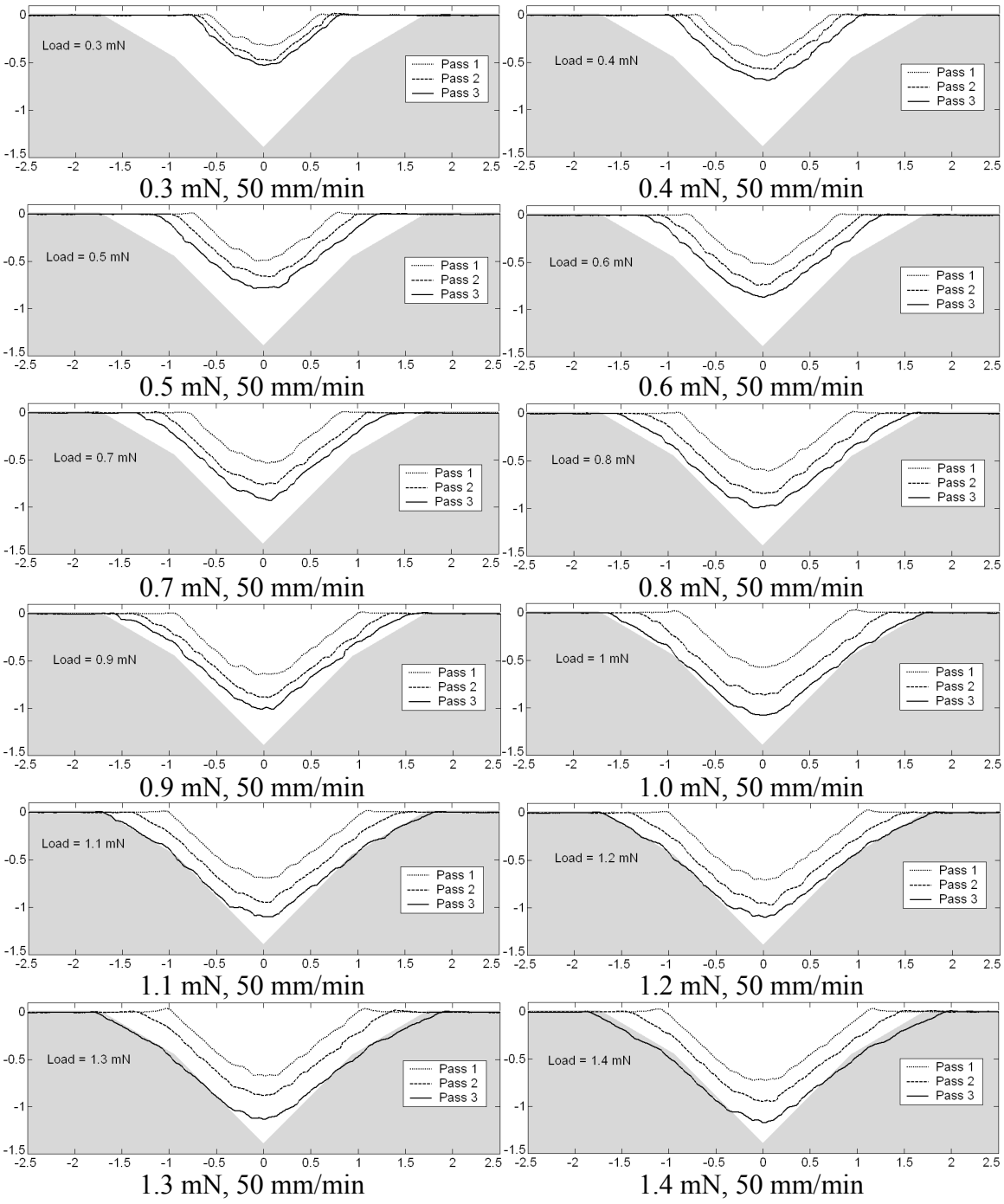


Figure 6.16: All experimental compound v-groove cross-sections with desired cross-section shaded grey (units in microns)

Side burr formation was observed when cutting the grooves. However, as shown in Fig. 6.17, these burrs were much smaller than the burrs that occurred when cutting

grooves with rectangular cross-sections. In this experiment the largest burr height was 38 nm when cutting with a 1.3 mN load and only one tool pass. By contrast, burr heights between 50 and 250 nm were observed when cutting rectangular grooves at depths of cut below the critical depth of cut per tool pass, as shown in Fig. 6.8.

As can be seen in Fig. 6.17, the majority of the burr formation occurred in the first tool pass and the burr height was reduced in subsequent tool passes so that burr height following the third tool passes never exceeded 10 nm. This reduction in burr height following the second tool pass with a v-shaped cutting tool is consistent with results in the literature concerning micro-scale shaping/planing with v-shaped diamond tools at a size scale about one order of magnitude larger [21].

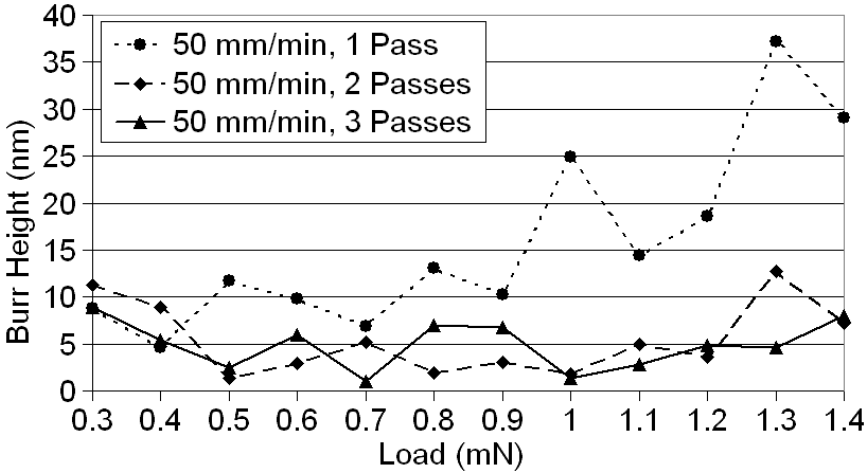


Figure 6.17: Burr heights associated with compound v-grooves

### 6.4.4 Exp. 4 – High-Speed Micro-Groove Cutting Results

Experiment 4 examined the effects of cutting at higher speeds that used previously. I.e., speeds up to 400 mm/min vs. speeds of 25 – 50 mm/min. The exact cutting conditions are given in Table 6.2. The goal of the experiment was to determine if it would be possible to use higher cutting speeds in order to achieve more desirable material removal rates or if there would be undesirable effects such a tool breakage or poorly formed grooves. Following the experiment, tool wear was measured, groove cross-sections where characterized, and chip morphology was characterized.

The experiment was conducted using tool D1 following several tests, not discussed herein, in which the tool accumulated a large amount of polymer debris due to handling that rendered it impossible to determine if the tool was too worn to be used again or not. Therefore, step four of the FIB fabrication procedure described in Chapter 5 was repeated in order to resharpen the tool. The new edge radius of the tool was 67 nm.

During the experiment a total distance of 180 mm was cut where distances of 84, 24, 24, 24, and 24 mm were cut at speeds of 50, 100, 200, 300, and 400 mm, respectively. It was found that no tool breakage occurred and the edge radius of the tool only increased by 15 nm as a result of wear. This is slightly less wear than seen in Experiment 1 at speeds of 25 and 50 mm/min.

AFM images were captured of each groove and these images were used to create groove cross-sections, which are plotted in Fig. 6.18. Note the due to AFM measurement distortion, which was discussed previously, the left side of each cross-section is more representative of the actual groove geometry than the right side.

Figure 6.18 shows that rectangular shaped grooves of good quality were achieved in all cases. Also, both the overall shape of each groove and the amount of burr formation remained the same regardless of cutting speed. However, depth of cut appears to be affected by cutting speed such that shallower depths of cut for a given cutting load are generally achieved when cutting at higher speeds. However, this trend cannot be stated with certainty since the order of the cuts was not randomized out of necessity.

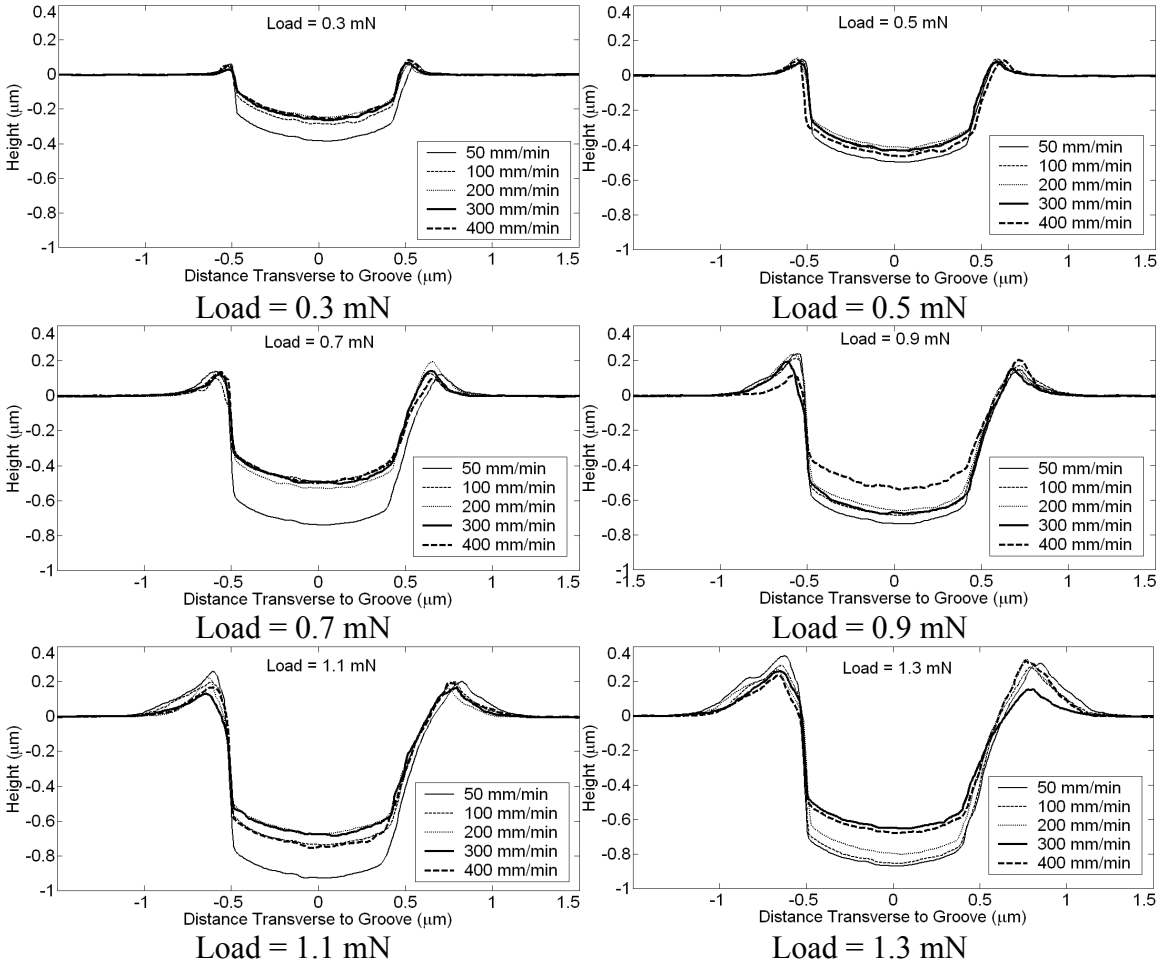


Figure 6.18: Groove cross-sections cut at speeds between 50 and 400 mm/min

Many of the grooves were terminated with chip roots that connected to intact chip segments of various lengths, as observed previously in Experiment 1. These chips could have been easily removed via the use of a compressed air blow-off, but were retained

because they enabled chip morphology to be related to cutting conditions by carefully imaging the chips with an SEM. Figures 6.19, 6.20, 6.21, 6.22, and 6.23 show SEM images of chips formed at cutting speeds of 50, 100, 200, 300, and 400 mm/min, respectively. In each figure, chips formed using different cutting loads are identified. If an image of a chip formed using a load of 0.3, 0.5, 0.7, 0.9, 1.1, or 1.3 mN is not present in a figure, it is because the chip separated from the workpiece prior to examination and hence could not be imaged.

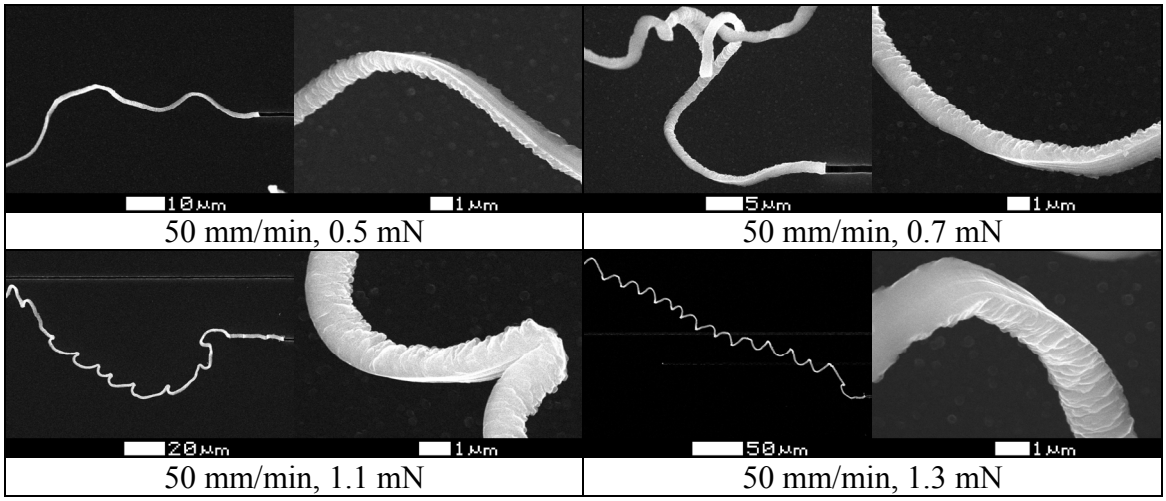


| 50 mm/min, 0.5 mN | 50 mm/min, 0.7 mN |
|---|---|
| 50 mm/min, 1.1 mN | 50 mm/min, 1.3 mN |

Figure 6.19: Chips formed at speeds of 50 mm/min

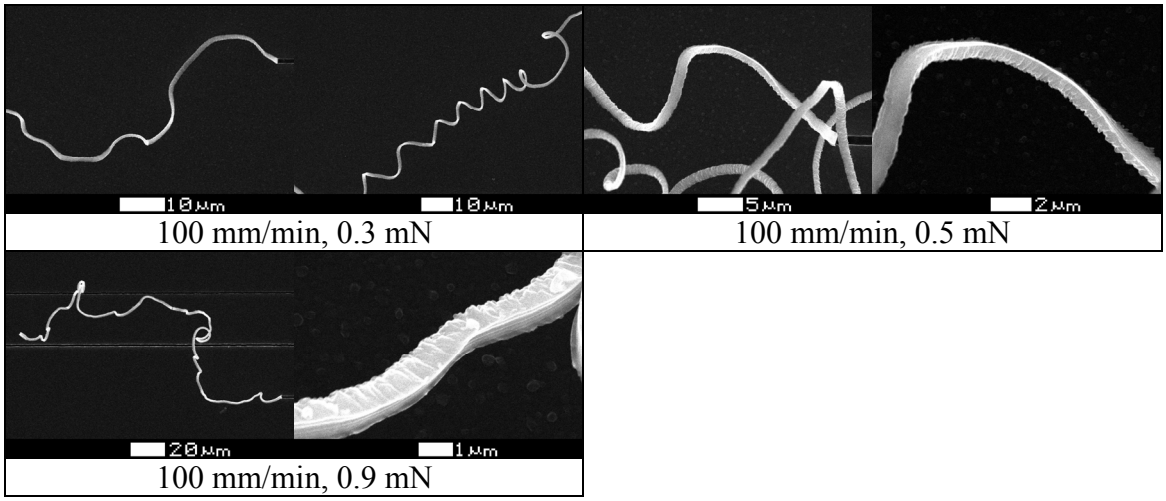


| 100 mm/min, 0.3 mN | 100 mm/min, 0.5 mN |
|---|---|
| 100 mm/min, 0.9 mN | |

Figure 6.20: Chips formed at speeds of 100 mm/min

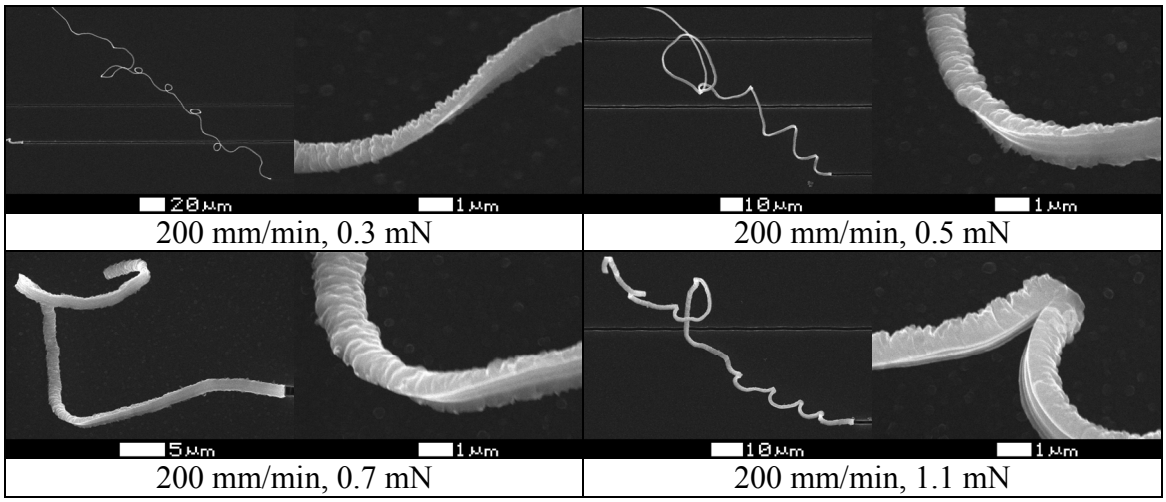


| 200 mm/min, 0.3 mN | 200 mm/min, 0.5 mN |
|---|---|
| 200 mm/min, 0.7 mN | 200 mm/min, 1.1 mN |

Figure 6.21: Chips formed at speeds of 200 mm/min

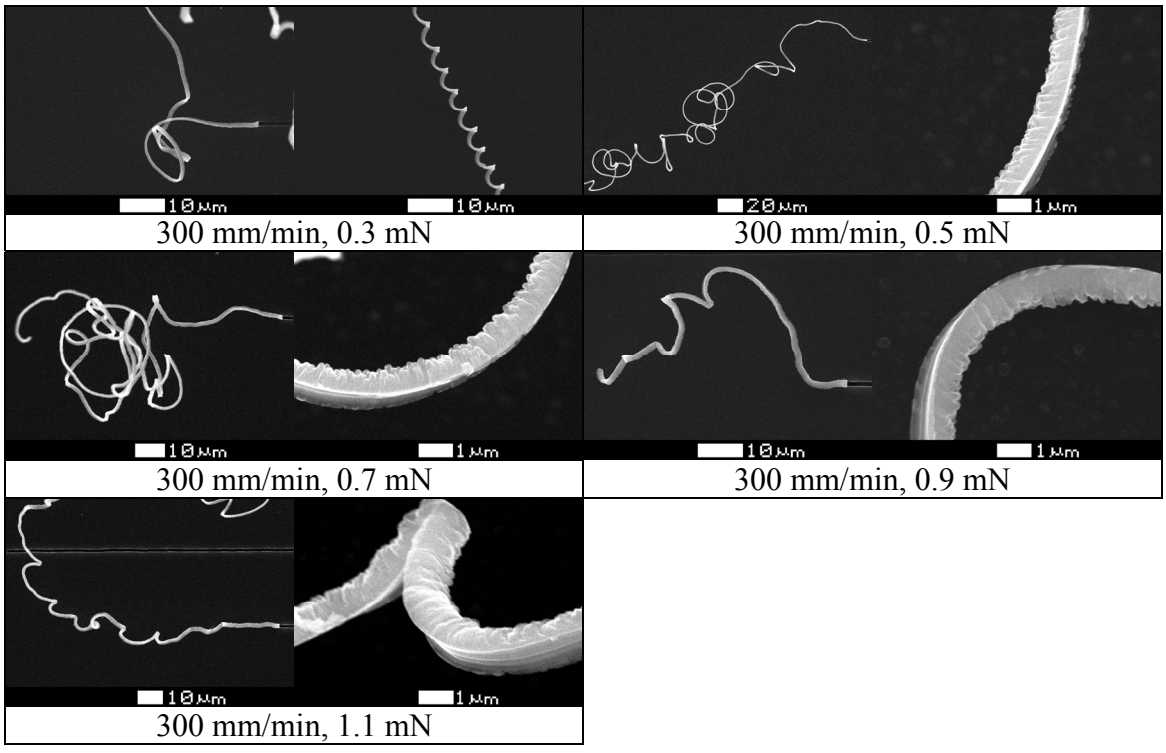


| 300 mm/min, 0.3 mN | 300 mm/min, 0.5 mN |
|---|---|
| 300 mm/min, 0.7 mN | 300 mm/min, 0.9 mN |
| 300 mm/min, 1.1 mN | |

Figure 6.22: Chips formed at speeds of 300 mm/min

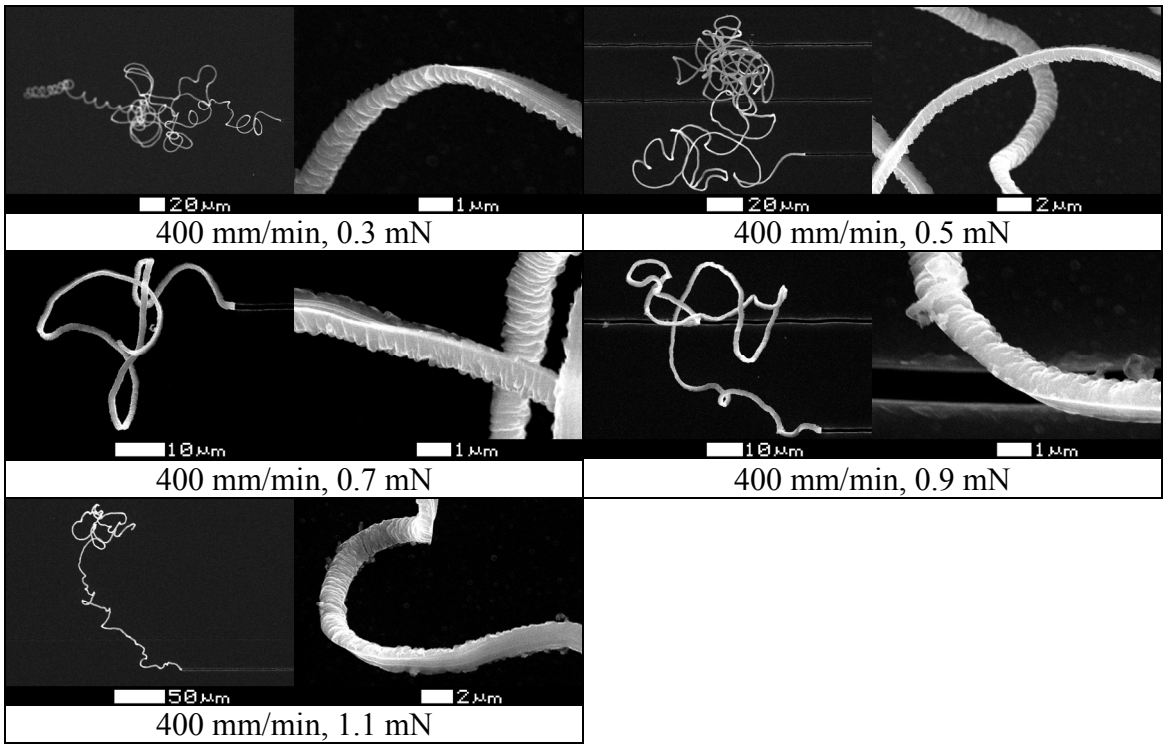


Figure 6.23: Chips formed at speeds of 400 mm/min

Examination of Figs. 6.19 – 6.23 shows that all of the chips were either ribbon type or washer-type helical as seen previously when cutting with AFM probes in Chapter 4. Chips formed at a low 0.3 mN load, and hence with low depth of cut, tended to form tightly curled washer-type helical chips. When the load was increased to 0.5 – 0.9 mN, straighter but still wavy ribbon type chips tended to form. At loads of 1.1 mN and higher chips tended to include kinks where the chip must have gotten caught on the tool geometry and buckled. Such an effect is intentionally induced in macro-scale cutting, via the use of a chip-breaker tool geometry, in order to break continuous chips into more manageable lengths. However, due to the extremely ductile nature of the pure aluminum workpiece, the chips do not appear to break even when buckled. Lastly, the only speed related effect observed is than when cutting at 50 mm/min wash-type helical chips can form at higher loads than when cutting at speeds of 100 mm/min and higher.

Based off the groove cross-sections and images of the chips, parameters describing each cut were found and are tabulated in Table 6.3. Note that the listed chip thickness and chip width values are actually the mean of at least three measurements. Also, it should be noted that since the experiment did not make use of a quick-stop apparatus, chip formation that occurred at the very end of a cut was not at the actual cutting speed due to tool deceleration. Care was taken to only measure chip width and chip thickness at points on the chips sufficiently far from a chip root to insure that the measured portion of the chip formed at the tested cutting speed. Note that no values are given in the table for cases where this was not possible due to the chip being too short.

Examination of the table shows that the greatest effect due to changes in cutting speed is a change in depth of cut. Additionally, as the depth of cut increases or decreases, the chip thickness similarly increases or decreases. Groove width, burr height, and chip width do not appear to be significantly affected by changes in cutting speed. The effect of increasing the cutting load appears to be similar regardless of the cutting speed used.

Table 6.3: Chip and groove characteristics in Experiment 4

| Speed (mm/min) | Load (mN) | Chip Thickness (μm) | Chip Width (μm) | Groove Depth (μm) | Groove Width (μm) | Burr Height (μm) |
|---|---|---|---|---|---|---|
| 50 | 0.3 | | | 0.389 | 1.022 | 0.074 |
| 50 | 0.5 | 0.76 | 1.16 | 0.501 | 1.050 | 0.106 |
| 50 | 0.7 | 1.10 | 1.40 | 0.746 | 1.156 | 0.151 |
| 50 | 0.9 | | | 0.751 | 1.138 | 0.211 |
| 50 | 1.1 | 1.13 | 1.51 | 0.928 | 1.203 | 0.246 |
| 50 | 1.3 | 1.24 | 1.89 | 0.882 | 1.181 | 0.348 |
| 100 | 0.3 | 0.64 | 1.01 | 0.287 | 0.983 | 0.069 |
| 100 | 0.5 | 0.78 | 1.21 | 0.443 | 1.054 | 0.110 |
| 100 | 0.7 | | | 0.492 | 1.134 | 0.137 |
| 100 | 0.9 | 0.93 | 1.46 | 0.693 | 1.131 | 0.209 |
| 100 | 1.1 | | | 0.757 | 1.176 | 0.222 |
| 100 | 1.3 | | | 0.850 | 1.158 | 0.305 |
| 200 | 0.3 | 0.50 | 0.99 | 0.250 | 0.990 | 0.063 |
| 200 | 0.5 | 0.72 | 1.14 | 0.418 | 1.065 | 0.111 |
| 200 | 0.7 | | | 0.530 | 1.073 | 0.174 |
| 200 | 0.9 | | | 0.660 | 1.111 | 0.213 |
| 200 | 1.1 | 1.08 | 1.59 | 0.682 | 1.198 | 0.204 |
| 200 | 1.3 | | | 0.776 | 1.145 | 0.303 |
| 300 | 0.3 | 0.48 | 0.98 | 0.267 | 0.970 | 0.066 |
| 300 | 0.5 | 0.74 | 1.19 | 0.431 | 1.049 | 0.090 |
| 300 | 0.7 | 0.90 | 1.33 | 0.503 | 1.083 | 0.151 |
| 300 | 0.9 | | | 0.675 | 1.163 | 0.187 |
| 300 | 1.1 | 1.10 | 1.70 | 0.687 | 1.212 | 0.170 |
| 300 | 1.3 | | | 0.668 | 1.182 | 0.229 |
| 400 | 0.3 | 0.50 | 1.09 | 0.257 | 0.976 | 0.079 |
| 400 | 0.5 | 0.79 | 1.19 | 0.464 | 1.096 | 0.111 |
| 400 | 0.7 | | | 0.500 | 1.104 | 0.132 |
| 400 | 0.9 | 1.02 | 1.48 | 0.570 | 1.132 | 0.182 |
| 400 | 1.1 | 1.10 | 1.68 | 0.750 | 1.184 | 0.205 |
| 400 | 1.3 | | | 0.687 | 1.159 | 0.293 |

## 6.5 Interactions between Grooves

### 6.5.1 Exp. 5 - Cutting Closely Spaced Grooves

A fifth experiment was conducted to examine the effects of cutting very closely spaced parallel micro-grooves. Two sets of grooves were cut into a workpiece, which consisted of a 3.1 μm thick film of thermally evaporated aluminum deposited onto a silicon substrate, using the conditions given in Table 6.4. Each set contained seven parallel grooves that were spaced such that the gap between each pair of grooves was as given in the table. The 1.05 μm wide tool D1 from Table 6.1 was used immediately after it had been used in Experiment 1 and then examined since no appreciable tool wear had occurred. Resharpening of the tool for use in Experiment 4 did not occur until later.

Table 6.4: Experiment 5 – Closely spaced parallel grooves

| Set | Speed (mm/min) | Load (mN) | Passes | Gaps Between Grooves (μm) |
|---|---|---|---|---|
| 1 | 50 | 1.4 | 1 | 3, 2, 1.5, 1.0, 0.75, 0.5 |
| 2 | 50 | 0.7 | 2 | 3, 2, 1.5, 1.0, 0.75, 0.5 |

An SEM image of the first set of grooves, which were each formed by a single tool pass at a load of 1.4 mN, is shown in Fig. 6.24A. A similar image of the grooves in the second set, which were each formed by two tool passes and a 0.7 mN load, is shown in Fig. 6.24B. AFM cross-sections of the two sets are shown in Fig. 6.25, which shows that groove depths achieved in both sets were about 1.0 μm. This means that in the first set, the critical depth of cut per tool pass of 750 – 800 nm is exceeded (recall the earlier discussion of Fig. 6.8), which caused significant burr formation. In the second set this value is not exceeded and burr formation is minimal.

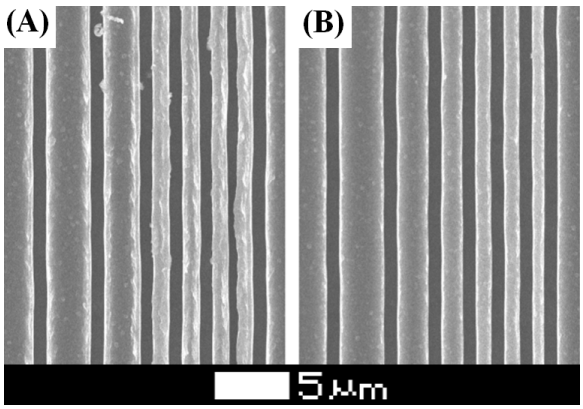


Figure 6.24: SEM images of parallel grooves cut using one tool pass at a 1.4 mN load (A) and two tool passes at a 0.7 mN load (B)

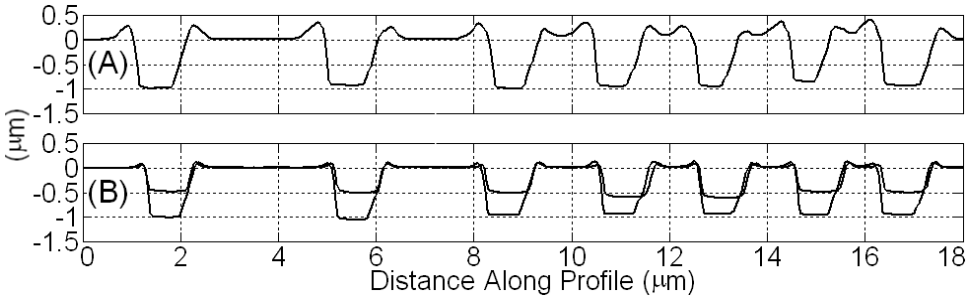


Figure 6.25: Cross-sections of parallel grooves cut using one tool pass at a 1.4 mN load (A) and two tool passes at a 0.7 mN load (B)

Via SEM image processing, the mean widths of the ridges of material between each pair of grooves were found. The mean ridge widths are plotted in Fig. 6.26 verses the command distance between grooves. Ideally, these two values would be identical. However, as can be seen in the figure, using one tool pass and a relatively high load caused significant deviation between the command and actual values. This may be due to the presence of significant burr formation that affects the width of the ridge of material between two grooves.

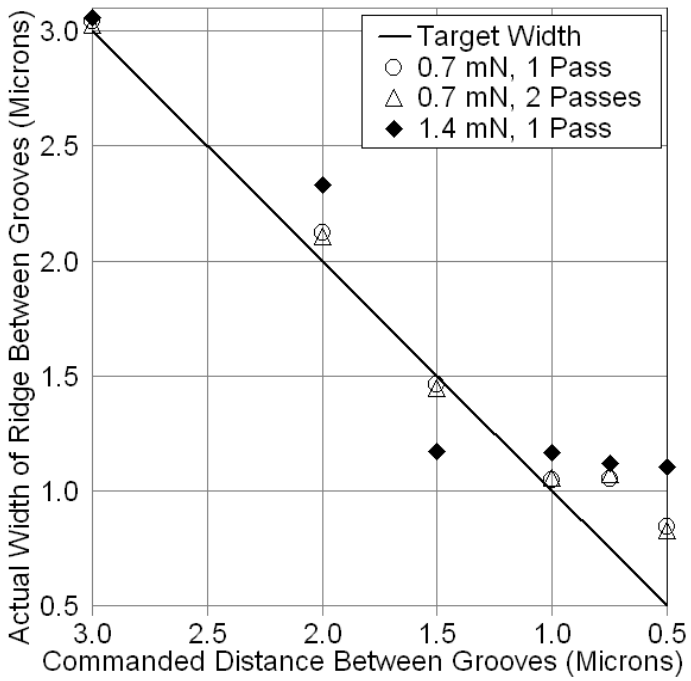


Figure 6.26: Ridges between closely spaced grooves

When very small distances between grooves were commanded, the actual ridge widths tended to be larger than commanded. Due to this effect, the minimum commanded width of a ridge of material between two 1 μm wide and 1 μm deep grooves that matched the actual width was about 1 μm for the tested tool and material combination. A likely cause is elastic recovery of the ridge material. That is, during cutting, material on the ridge sidewalls is compressed and then elastically recovers as the tool moves on. Such compression and recovery was responsible for grooves being 111 nm narrower than the tool used to cut them in Experiment 2. Additionally, when forming a very narrow ridge of material between grooves, the ridge may bend over slightly due to cutting forces and then spring back once the tool has moved on. Such bending and spring back would become more pronounced as a ridge of a set height is made thinner, which would cause it to act more like a cantilever.

### 6.5.2 Exp. 6 - Cutting Intersecting Grooves

A sixth experiment was conducted to examine the effects of one groove intersecting another groove, or another group of grooves. The experiment considered the effect of the depths of the grooves, the effect of the angle at which the grooves intersected, and the differences between intersecting a lone groove and intersecting a group of closely spaced parallel grooves with narrow ridges of material between them.

The 1.05 μm wide tool and workpiece material from Experiment 5 were used after it was found that the tool was not appreciably worn, and the cutting speed was 50 mm/min. All grooves were cut using one 0.7 mN tool pass, two 0.7 mN tool passes, or three 0.85 mN tool passes, which resulted in groove depths of 0.5, 1.0, and 1.5 μm, respectively.

There were three test sets in the experiment, and in each set there were 18 test sites. At each site, a different combination of intersected groove depth, intersecting groove depth, and intersection angle was used so that all combinations of the values in Table 6.5 were represented. Individual grooves were intersected in the first set. In the second set, parallel grooves spaced 2.0 μm apart were intersected. In the third set, parallel grooves spaced 1.0 μm apart were intersected.

Table 6.5: Experiment 6 – Intersecting grooves

| | | |
|---|---|---|
| All Sets | Intersected Groove Depths | 0.5, 1.0, 1.5 μm |
| | Intersecting Groove Depths | 0.5, 1.0, 2.0 μm |
| | Intersection Angles | 45°, 90° |
| Set 1 | Individual grooves were intersected | |
| Set 2 | Parallel Grooves spaced 2.0 μm apart were intersected | |
| Set 3 | Parallel Grooves spaced 1.0 μm apart were intersected | |

In the first test set of Experiment 6, the effect of individual grooves intersecting was evaluated. Figure 6.27 shows all of the intersections where vertical grooves, cut from top to bottom, intersected existing horizontal grooves at a 90° angle. Figure 6.28 shows similar intersections except the angle of intersection is 45°. Again, the intersecting grooves were cut from top to bottom and the existing grooves were horizontal. Note that in both figures, the intersecting grooves were spaced progressively closer together so that the two rightmost vertical grooves in each image were spaced only 1 μm apart.

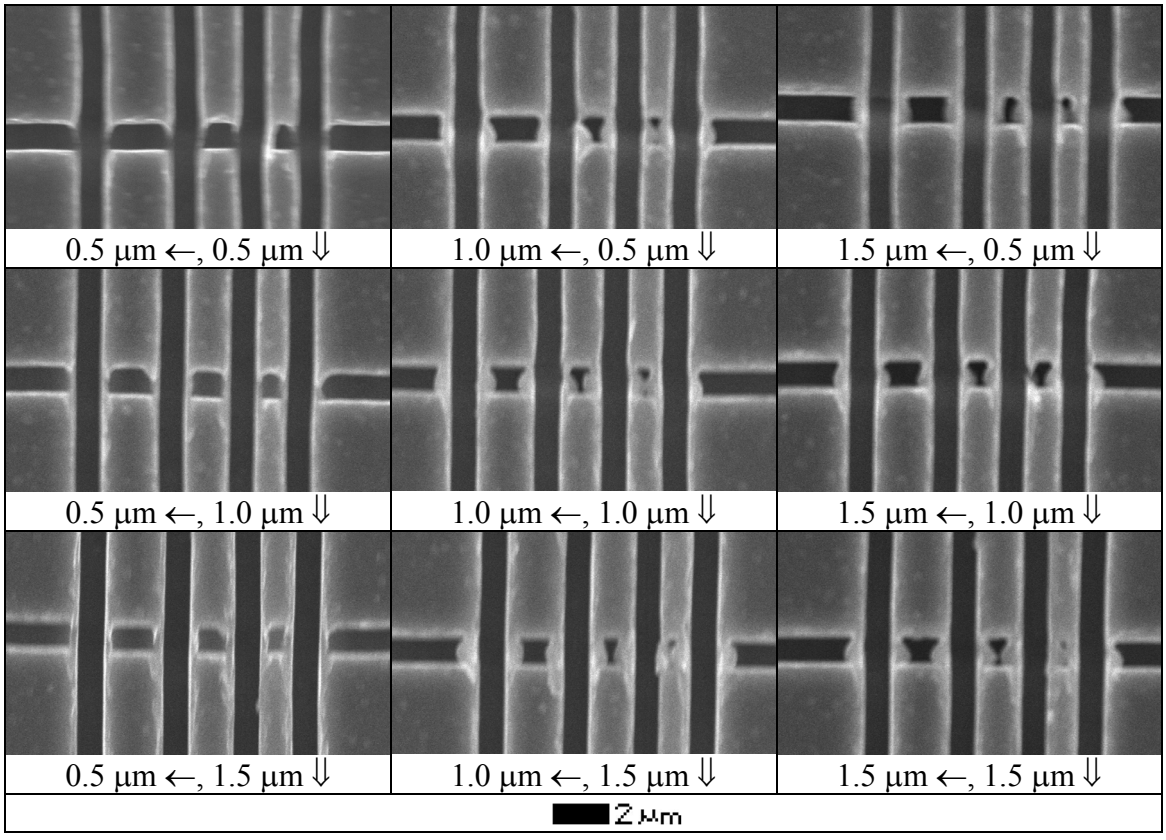


Figure 6.27: 0.5, 1.0, and 1.5 μm deep grooves intersecting at a 90° angle

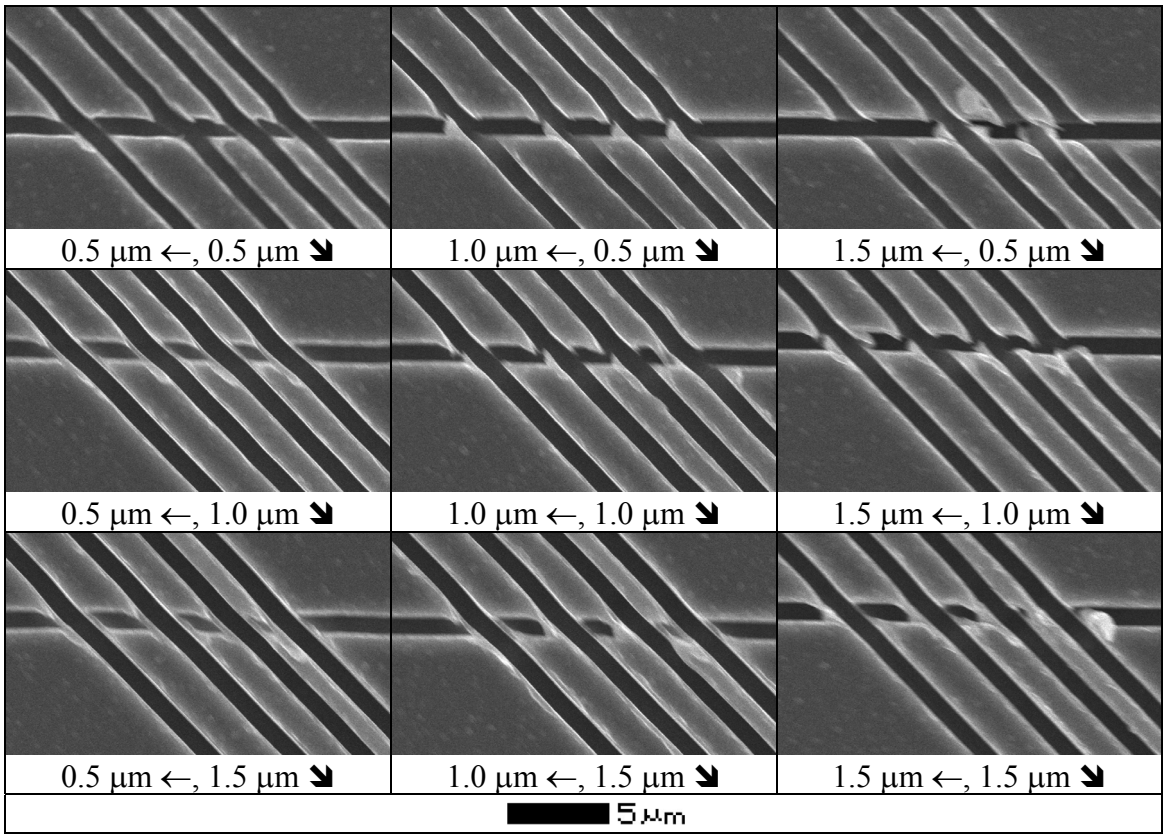


Figure 6.28: 0.5, 1.0, and 1.5 μm deep grooves intersecting at a 45° angle

As can be seem in Fig 6.27 and Fig. 6.28, four grooves intersected an existing groove at each test site. These intersections presented no problems during cutting. Furthermore, it was possible for parallel intersecting grooves spaced as close as 1 μm apart to be cut without significant distortion of the ridge of material between the grooves either before or after intersecting the existing groove.

AFM images were taken of selected intersections where grooves with depths of 0.5 and 1.5 μm intersected at a 90° angle. Five 2D profiles were constructed based on each image. One of the profiles showed the cross-section of the groove being intersected and the four other profiles showed variations in depth along the bottoms of the four intersecting grooves. These 2D profiles are shown in Fig. 6.29 where the direction of cut was from left to right.

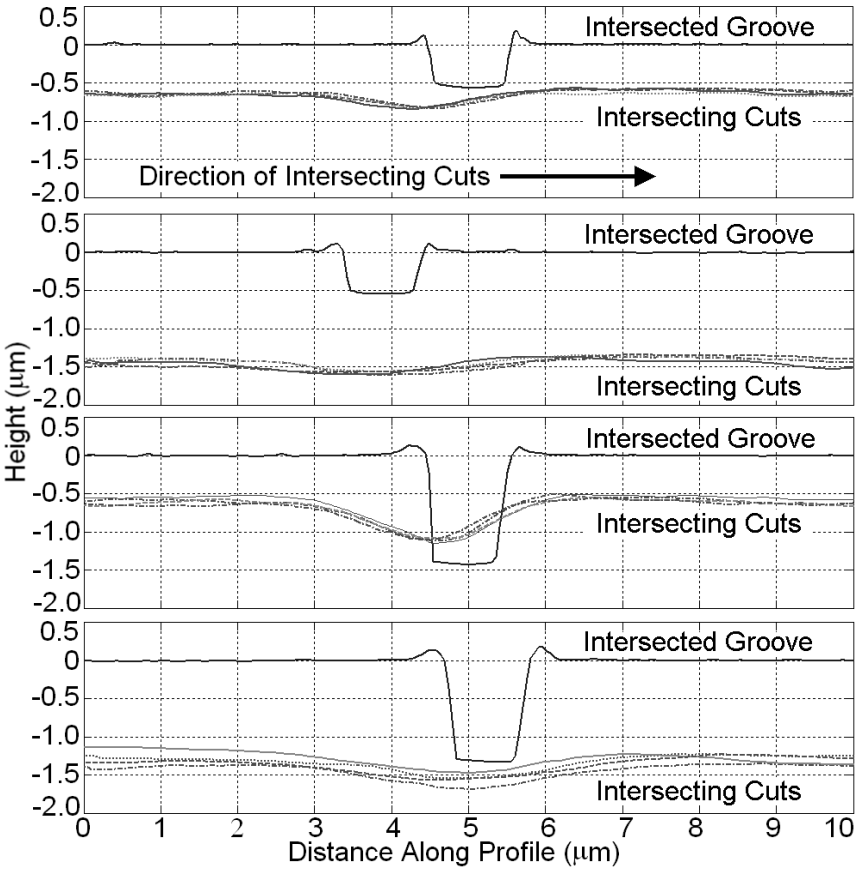


Figure 6.29: Cross-sections of intersected grooves and profiles of the bottoms of intersecting grooves

As can be seen in Fig. 6.29, there was a slight dip in the bottom of each intersecting groove. This was expected since cutting is a constant load operation and there is not as much material to remove when intersecting an existing groove. Also, each dip started 1 – 1.5 μm before the tool reached the sidewall of the groove being intersected. This may have been caused by the collapse of the thin wall of material between the rake face of the tool and the sidewall of the groove about to be intersected in the moments before the grooves actually crossed. Provided that the intersected groove is not much deeper than the intersecting groove, it appears that the dip will be small in magnitude and unlikely to be problematic.

Exit burr formation, as depicted in Fig. 6.30, occurred during all intersections. This was expected because, when cutting the intersecting groove, the tool exits from the cut when it breaks though the sidewall of the existing groove, which is a known source of burr formation in machining [133]. Furthermore, the pure aluminum workpiece is highly ductile and prone to experiencing burr formation when cut.

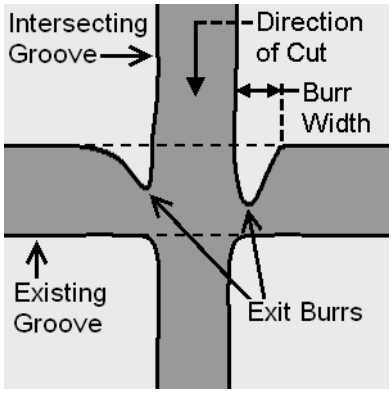


Figure 6.30: Exit burr formation during groove intersection

As a result of exit burr formation, it was found that burrs tended to block the groove being intersected. For example, exit burrs formed during the intersection of 0.5 μm deep grooves result in partial blockage of the intersected horizontal groove, as shown in Fig. 6.27. Exit burrs fully block the intersected horizontal groove in Fig. 6.27 in the case where two 1.5 μm deep grooves intersected. These burrs are generally as tall as the groove is deep. Additionally, the widths of these burrs varied depending on the intersection conditions, which suggests that the amount of material incorporated into each burr also varied.

These results indicate that burr formation will tend to be present at groove intersections. The approach required to deal with these burrs depends on the application. For instance, in applications such as surface texturing or micro-heat exchanger fabrication, the presence of burrs at intersection sites may be perfectly acceptable. In

fact, for some surface texturing applications, burr formation might be used advantageously to achieve a particular pattern such as pockets to retain lubricant. In other applications, such as micro-fluidics, full blockage of a channel by burrs would be undesirable. In such cases burr reduction and/or removal strategies would have to be employed. One means of reducing burr formation would be to avoid the use of highly ductile work material if the application allows such latitude. Another method may be to use multiple tool passes to cut the grooves and to alternate back and forth between using a tool pass to cut a groove to be intersected and using a tool pass to cut an intersecting groove, which would result in shallower intersections and hence less burr formation. Burr reduction might also be accomplished via selection of better tool geometry or cutting conditions. Burr removal might also be accomplished via an operation such as chemical etching, which could take advantage of the relatively large surface area and small volume of the burrs to attack them much faster than the surrounding grooves.

In the second test set in Experiment 6, the effect of intersecting parallel grooves spaced 2.0 μm apart was evaluated. Figure 6.31 shows vertical grooves intersecting existing horizontal grooves spaced 2.0 μm apart. In these images the angle of intersection was 90°, and the intersecting grooves were cut from top to bottom. Additionally, Fig. 6.32 shows an identical set of intersections except that the angle of intersection is 45°. Note that in both figures, the intersecting grooves were spaced progressively closer together so that the two rightmost vertical grooves in each image were spaced only 1 μm apart.

It was found that when intersecting grooves with 2 μm wide ridges between them at a 90° angle, no distortion of the ridges occurred except for the appearance of exit burrs.

In the 45° angle cases there was some waviness induced in the intersecting grooves due to uneven loading / unloading of the tool, but the appearance of entrance and exit burrs was the only ridge distortion observed. Furthermore, this was the case even when the intersecting grooves were spaced as close as 1 μm apart.

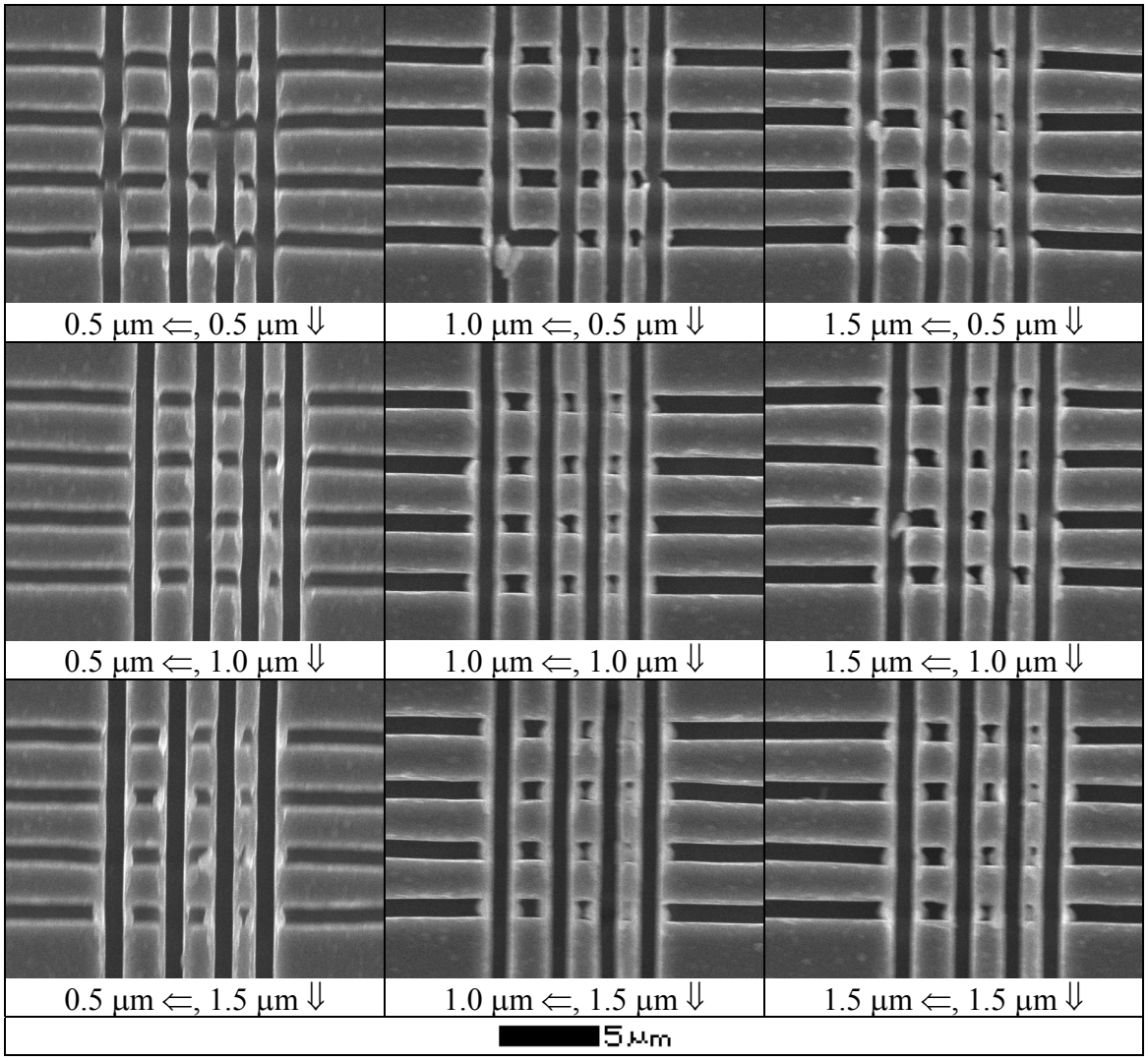


Figure 6.31: 0.5, 1.0, 1.5 μm deep grooves intersecting parallel horizontal ridges that are 2.0 μm wide at a 90° angle

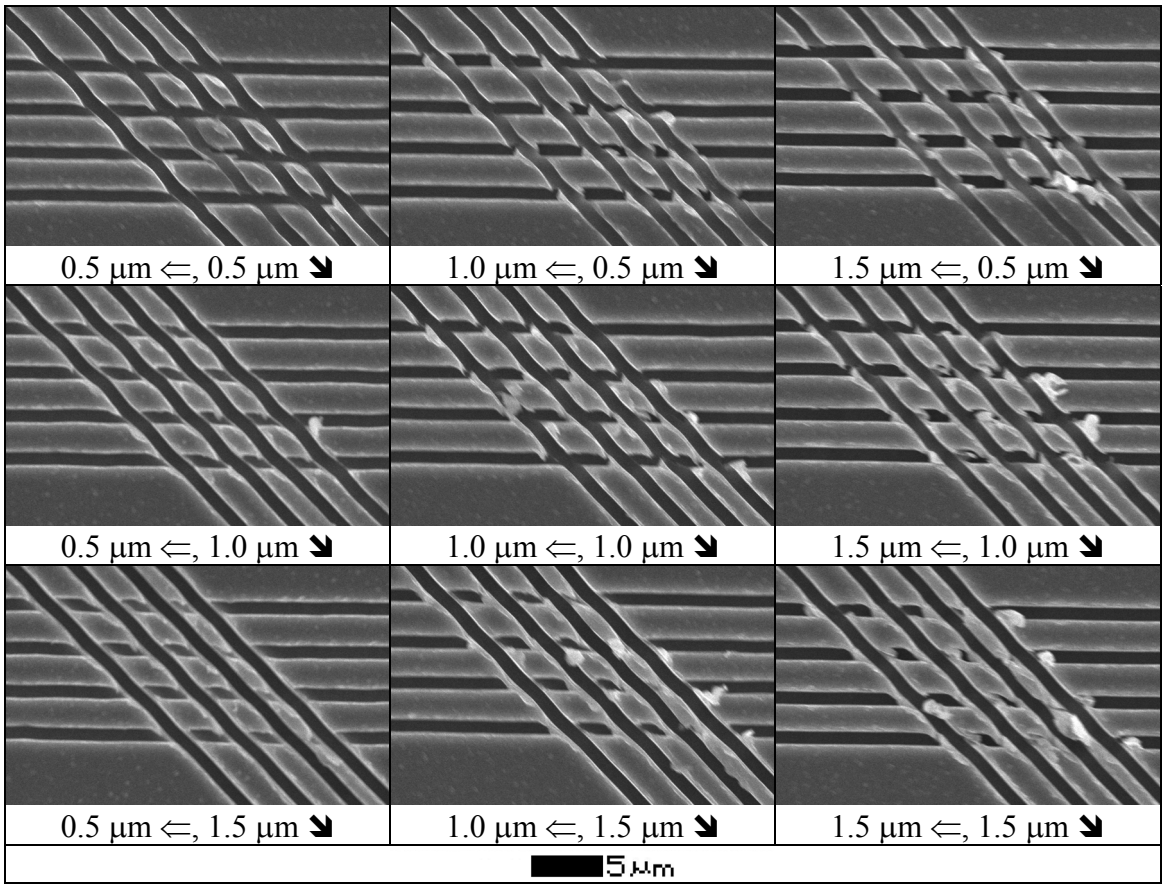


Figure 6.32: 0.5, 1.0, 1.5 μm deep grooves intersecting parallel horizontal ridges that are 2.0 μm wide at a 45° angle

The third test set in Experiment 6 was identical to the second test set except that the grooves being intersected were spaced only 1.0 μm apart. Hence, the ridge of material between each intersected groove was half as thick as in the previous test set. Figure 6.33 shows vertical grooves intersecting existing horizontal grooves spaced 1.0 μm apart. In these images the angle of intersection was 90°, and the intersecting grooves were cut from top to bottom. Additionally, Fig. 6.34 shows an identical set of intersections except that the angle of intersection is 45°.

It was found that the presence of thinner ridges resulted in significant ridge deformation when groove depth exceeded 0.5 μm. However, the amount of deformation

was not as pronounced in the 45° angle cases. Also, in the 45° angle cases, the deformation of the ridges appears to occur mostly on the side of each new groove corresponding to the side of the tool that exited from the cut first. These results demonstrate the importance of cutting conditions during intersection of micro-grooves when cutting through very thin ridges of material.

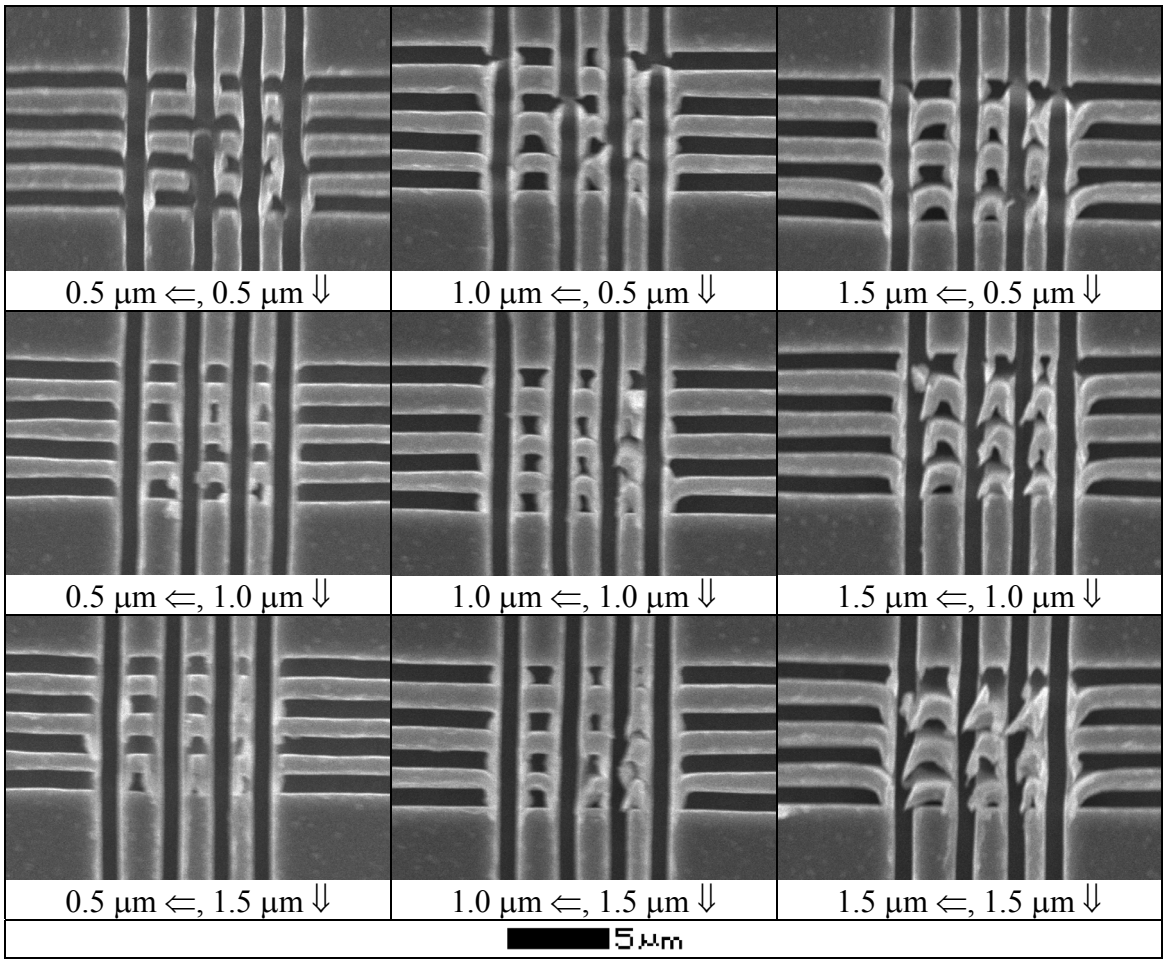


Figure 6.33: 0.5, 1.0, 1.5 μm deep grooves intersecting parallel horizontal ridges that are 1.0 μm wide at a 90° angle

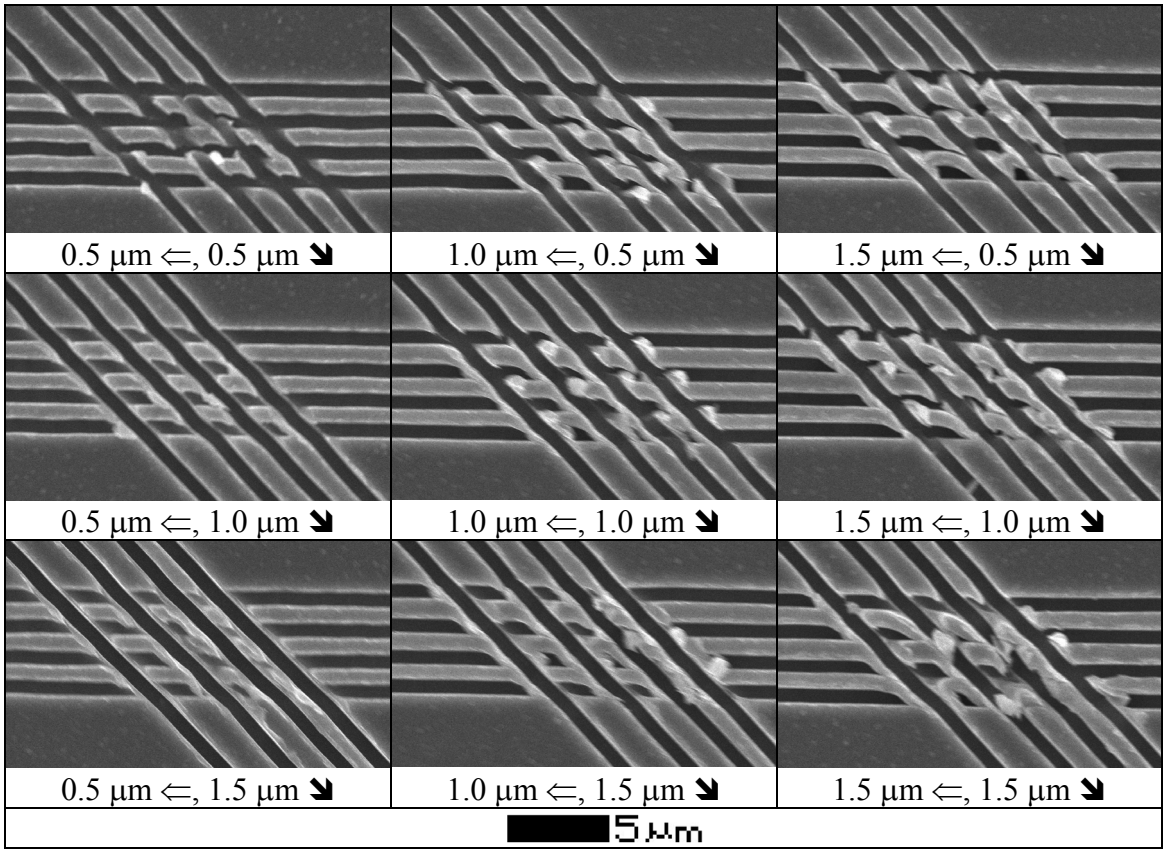


Figure 6.34: 0.5, 1.0, 1.5 μm deep grooves intersecting parallel horizontal ridges that are 1.0 μm wide at a 45° angle

## 6.6 Experimental Conclusions / Summary

Testing of flexible cutting tools with geometries suitable for micro-groove cutting was the subject of this chapter. Testing consisted of six experiments in which micro-grooves with rectangular and compound v-shapes were cut in pure aluminum. These experiments evaluated the effects of cutting conditions and the effects of grooves intersecting or being cut in close proximity to each other. The conclusions from these experiments are as follows:

1. Focused ion beam modification of diamond AFM probes, as described in Chapter 5, can be used to produce flexible micro-scale groove cutting tools as narrow as 411 that have very effective cutting geometries. Furthermore, these tools are capable of withstanding the forces they are subjected to during cutting much more effectively than the commercial AFM probes used as tools in the previous chapter.
2. Grooves with one micron wide rectangular cross-sections could be repeatably cut in aluminum and the depth of cut could be well controlled by setting the cutting load. The relationship between groove depth and both cutting load and the number of tool passes is nonlinear. Cutting speed only has a small effect on groove depth. Also, it was found that there is a critical depth of cut per tool pass beyond which will result in greatly increased burr formation.
3. Grooves as narrow as 300 nm but about 2 μm deep can be cut using the developed process. A measurable amount of elastic recovery of the sidewalls of the grooves was observed, and therefore when such narrow grooves are cut, elastic recovery must be taken into account to achieve a prescribed groove width.
4. The ability of cutting compound v-shaped grooves was demonstrated. It was also found that a desired groove shape could be readily achieved when using a tool with identical geometry to the desired geometry. Burr formation was much smaller than when cutting rectangular grooves. Furthermore, burr formation was reduced even more after using a second tool pass.
5. Grooves were cut in aluminum at speeds as high as 400 mm/min with less tool wear than when cutting at lower speeds of 25 – 50 mm/min. Furthermore, groove quality and the amount of burr formation was found to not be strongly effected by cutting

speed. Hence, it appears that cutting at higher speeds up to at least 400 mm/min is beneficial.

6. Chips were found to remain attached to a workpiece, via their chip roots, following most micro-groove cutting operations. These chips can be easily removed by blowing compressed air across the workpiece, and if left undisturbed can also be used to examine chip morphology corresponding to a particular cut. It was found that chip morphology is primarily affected by cutting load, and hence depth of cut, during experiments where 1 μm wide grooves were cut in aluminum. Specifically, at lower loads curly washer-type helical chips were formed. At higher loads, wavy ribbon chips were formed. At the two highest loads tested, bucked chips were formed that would likely be discontinuous if the workpiece material was not as ductile.
7. One micron wide and deep parallel grooves, cut in pure aluminum, can be spaced about one micron apart controllably. If a closer spacing was commanded, the ridge of material between the grooves became wider than commanded, which is likely due to elastic recovery. In order to get the thinnest possible ridge of material between grooves, it was found that the depth of cut per tool pass should be kept low enough to avoid large amounts of burr formation, which affect ridge geometry.
8. Grooves can be successfully cut that intersect existing grooves without affecting the characteristics of the intersected groove after the intersection point. The depth of the intersecting groove briefly dips before the intersection point, possibly due to collapse of the sidewall of the intersected groove.
9. Exit burr formation occurs during groove intersection, but it is expected that exit burr size can be reduced by avoiding the use of highly ductile work materials, if the

application allows such latitude, or by using other established burr reduction and/or removal techniques.

10. If an intersected ridge of material between two existing grooves is too thin and has too high of an aspect ratio, it can deform during intersection. However, sufficiently low aspect ratio ridges do not experience significant deformation.

In conclusion, based on the experiments described in this chapter, it was found that the use of the improved flexible cutting tools described in Chapter 5 enables the production of high-quality micro-scale grooves, which can be cut at speeds up to at least 400 mm/min. However, even with the use of these very good tools there are still some issues that need to be addressed such as how to minimize side burr formation, how to minimize exit burr formation, and how to better control the morphology of the chips in order to enable chip control strategies. A more fundamental understanding of the cutting process is required in order to address these issues than can be readily achieved via experimentation. Hence, finite element simulation of the micro-groove cutting process is the subject of the next chapter.

# Chapter 7

# Finite Element Modeling of the Developed Micro-Groove Cutting Process

## 7.1 Introduction

### 7.1.1 Motivation

In the previous chapters the micro-groove cutting process has been studied via experimentation. This has resulted in the development of flexible tools that produce high-quality grooves, and has allowed cutting load to be correlated with depth of cut for a given tool geometry and workpiece material. However, experimental studies do not reveal all the pertinent information about the cutting process, and hence there is a limit on how much process improvement can be achieved without the use of very large test matrices. For example, because of the size-scale of the process it has not been possible to observe the cutting action directly, and hence information about chip formation and chip flow has been lacking. Also unavailable is the stress / strain distributions within a workpiece and information on how a workpiece deforms as a tool passes through it. These limitations drive the need for a model of the cutting process, which is the subject of this chapter.

### 7.1.2 Model Scope

In this chapter, a cutting model is developed for the purpose of simulating the types cuts described in Experiment 4 in Chapter 6. Additionally, the model should be

able to simulate what happens when one groove intersects an existing groove, which results in exit burr formation as seen in Experiment 6 in Chapter 6. In order to accomplish this, several process features must be addressed by the model, some of which are not typically addressed by models in the literature.

In the experiments of interest, a tool with a width of 1.05 μm was used to cut grooves with depths of approximately 0.25 to 1.0 μm using orthogonal cutting. Hence, the width of the cut grooves was 1.05 - 4.2 times the depth of cut. This invalidates the plane strain assumption often used in the literature to simplify orthogonal cutting into a 2D problem. Hence, the micro-groove cutting process involves distinctly 3D stress and strain fields that must be captured. Direct evidence of this is seen in experiments where the shapes of the chip roots indicate spreading of the material ahead of a tool.

The workpiece material consists of a 3.1 μm thick film of thermally evaporated aluminum deposited on a flat silicon substrate. During cutting, stress fields are expected to extend below the cutting edge of the tool and these fields may be affected by the transition from aluminum to silicon, which have different material properties. Therefore, the configuration of the workpiece material must be accounted for by the model.

Side burrs and exist burrs were observed during experiments described in the previous chapter. These burrs are of concern because they affect the ability to produce groove cross-sections with a specified tolerance. Hence, a comprehensive model must be able to predict side and exit burr formation, which is also 3D process. Furthermore, correct burr prediction involves correctly handling separation of chip material from the workpiece at the sides of the chip, which indicates that the modeled section of the

workpiece must include not just the chip but also enough material to the side of the chip to correctly handle workpiece deformation during chip separation.

The tooling using in Experiment 4 in Chapter 6 had a slightly rounded bottom, as shown in Fig. 7.1, as a result of limitations in how sharp a feature could be produced by FIB machining. For this particular tool, the rounded end of the tool is well described by an arc with a radius of 893 nm. Hence, the depth of cut at the center of groove is less than at the sides of a groove. This results in non-uniform uncut chip thickness and must be accounted for by a model that is to correctly predict chip flow. Also, the side edges of the tool were rounded to a radius of approximately 60 nm, which must also to be accounted for since this could have an effect on burr formation.


Figure 7.1: Rake face of the tool used in Experiment 4 in Chapter 6

In summary, the micro-groove cutting model to be developed in this chapter must be able to handle the 3D stress / strain fields present due to the plane strain assumption being invalid. The model must be able to account for the workpiece material configuration used in experiments. It must also accuracy predict side burr formation and exit burr formation. To accomplish this, separation between not just the bottom of the chip and the workpiece but also the side of the chip and the workpiece must be handled correctly. The model should also be able to predict chip flow with sufficient accuracy to

be able to correctly predict chip curl. Lastly, rounded features on the FIB machined tools need to be handled by the model. The need to handle the 3D stress / strain fields present during cutting, to handle chip separation at the side of the chip, to account for rounded tool geometry, and to predict side burr formation sets this model apart from existing machining models.

## 7.2 Overall Modeling Approach

### 7.2.1 Model Type

Several types of machining models exist: analytical models, mechanistic models, molecular dynamics (MD) models, and finite element models. Analytical and mechanistic models are not well suited for predicting complex 3D surface morphology resulting from a groove cutting operation. MD models provide accurate representations of the cutting process and resultant machined surface, but simulation volumes large enough for simulation of micro-scale cutting are computationally prohibitive [100 - 102]. Finite element models can represent the micro-scale cutting processes in a way that is computationally feasible and can provide detailed information about the cutting process. Therefore, a finite element model is used in this work. Additionally, the Lagrangian finite element formulation is used so that transient events such as exit burr formation can be modeled. The general purpose finite element software, Abaqus version 6.9 us used to implement the model.

### 7.2.2 Consistent Units

In several finite element software packages, such as Abaqus 6.9, there is no built-in set of units used by the software. Rather, all calculations performed by the software

assume consistent units. That is, a set of units where no conversion factors are necessary to specify derived units in terms of fundamental units. Furthermore, the set of consist units used when providing inputs, such as material properties and element dimensions, determines the set of consist units in which outputs are provided.

Two common sets of consistent units are given in Table 7.1. The MKS system is commonly used and is also known as the SI system of units. However, in this work the mmNS system is used because it is more suitable when working with small dimensions such as those seen in a micro-scale cut. This is because the use of the MKS system would result in such small numerical values that round-off errors might become an issue.

Table 7.1: Consistent units

| | Meter / Kilogram / Second (MKS) System | Millimeter / Newton / Second (mmNS) System |
|---|---|---|
| Length | Meter | Millimeter |
| Time | Second | Second |
| Mass | Kilogram | Tonne (1000 Kg) |
| Force | Newton | Newton |
| Temperature | Degree Celsius | Degree Celsius |
| Area | $(\text{Meter})^2$ | $(\text{Millimeter})^2$ |
| Volume | $(\text{Meter})^3$ | $(\text{Millimeter})^3$ |
| Velocity | Meter / Second | Millimeter / Second |
| Pressure | Newton / Meter | MPa |
| Stress | Newton / Meter | MPa |
| Energy | Joule | mJ |

## 7.2.3 Integration Scheme

Using the general purpose Abaqus finite element software, solutions can be acquired through an implicit dynamic analysis procedure (Abaqus/Standard) or through an explicit dynamics procedure (Abaqus/Explicit). The explicit dynamics procedure evaluates a large number of small time increments where a central-difference time integration rule is used. During each increment a tiny change in the state of each element

in the model is calculated based on the state of the elements at the start of the increment and any load / boundary conditions applied during the increment. This procedure is suitable for analysis of short dynamic events, complex contact conditions, large deformations, and does not suffer from convergence problems that can arise when using direct-integration. Hence, Abaqus/Explicit was selected for use in this work.

This explicit dynamics procedure imposes the requirement that the time required for a signal, such as a stress wave, to propagate through any element in the mesh must be less than the time increment used. Otherwise, the model becomes unstable and gives erroneous results. This requirement can result in the need for very tiny time increments, which can render simulations of even short periods of time computationally infeasible. Therefore, it is desirable to use as large of a time increment as possible without causing the model to become unstable, which is that task that Abaqus automatically performs.

An estimate of the largest stable time increment imposed by the purely mechanical response of a model is given by Equations (7.1) – (7.4), where $\Delta t_{mech}$ is the time estimate, $L_{min}$, is the dimension of the smallest element in the mesh, $\rho$ is the material density, $\nu$ is Poisson's ratio, and E is the modulus of elasticity [122]. Additionally, if thermal effects are to be considered, Equations (7.5) – (7.6) provide a separate estimate $\Delta t_{thermal}$, where k is the material thermal conductivity and c is the specific heat [122]. The smaller of the two estimates is close to the actual stable time increment.

(7.1) $$\Delta t_{mech} \approx \frac{L_{\min}}{C_d}$$

(7.2) $$C_d = \sqrt{\frac{\hat{\lambda} + 2\hat{\mu}}{\rho}}$$

(7.3) $$\hat{\lambda} = \frac{E\nu}{(1+\nu)(1-2\nu)}$$

(7.4) $$\hat{\mu} = \frac{E}{2(1+\nu)}$$

(7.5) $$\Delta t_{thermal} \approx \frac{L_{\min}{}^2}{2\alpha}$$

(7.6) $$\alpha = \frac{k}{\rho c}$$

## 7.2.4 Element Selection Considerations

As can be seen in Equations (7.1) and (7.5), the stable time increment decreases as the dimension of the smallest element in the model decreases. For example, using Equations (7.1) - (7.4) to calculate $\Delta t_{mech}$, it can be found that for aluminum the largest stable time increment imposed by the mechanical response of the model is 3.3 x $10^{-12}$ seconds when a element size of 20 nm is used, which is the approximate element size required to accurately simulate uncut chip thickness on the order of 250 nm. As a result, over 300 million time increments are required for each millisecond simulated. Such a large number of increments are not practical given current computer hardware.

To alleviate this issue, mass scaling can sometimes be used. Mass scaling involves artificially increasing material density by some multiplier in order to reduce $\Delta t_{mech}$. This is practical in lower speed deformation simulations where inertial effects are limited, but cannot be used in high-speed simulations, such as those of ballistics impact. Fortunately, machining at the micro-scale involves relatively low speed deformations and

hence a mass scaling factor of 5000 is used. This decreased the number of increments required per millisecond to a more practical 4.35 million.

As can be seen in Equation (7.5) the situation is worse with regards to the thermal stable time increment because said increment reduces with the square of the smallest element dimension. At larger size scales, this is not a problem because $\alpha$ is generally small. However, with a 20 nm element $\Delta t_{thermal}$ becomes a prohibitively small $2.3 \times 10^{-12}$ seconds, and mass scaling cannot be used to alleviate this issue. This renders modeling of thermal conduction during cutting computationally infeasible at the size scale of interest without resorting to a new computational framework.

Fortunately, there is evidence that thermal softening is not very significant in machining of aluminum at the size scale of interest. In fact, the size effect seen when cutting using small uncut chip thickness has been partially attributed to an increase in material shear strength due to a decrease in tool-chip interface temperature [105, 134]. This explains the results of experiments where Al 7075-T6 was machined using diamond tools, with similar radii as the ones used in this work, where the amount of friction was seen to increase with decreasing uncut chip thicknesses below about 700 nm [135]. Additionally, in a study where machining of Al 5083-H116 was modeled with finite elements, it was shown via calculations based on Oxley's method [136] that the change in flow stress due to the temperature rise when cutting as fast at 10 m/min, with chip loads similar to those used in this work, should be negligible, which was supported by experimentally validated simulations [109]. Since cutting speed in this work is no greater than 0.4 m/min, thermal effects should also be negligible and are ignored.

It should be noted however, that the evidence that suggests that thermal effect can be ignored regards situations where the tool and workpiece have high thermal conductivities, such as aluminum. Other metals such a copper, some brasses, and some bronzes also have high thermal conductivities, and hence thermal effects can likely be ignored when simulating micro-scale cuts in them as well. However, thermal effect would need to be more carefully considered when simulating cuts in materials, such as titanium, that have very low thermal conductivities.

Abaqus has many different types of element types suitable for different problems. 8-node linear reduced integration elements (C3D8R) with "relax stiffness" hourglass control were selected because they are suitable for modeling problems without thermal effects and with large deformations. All element settings were the Abaqus default, which is deemed suitable for use in the model.

### 7.2.5 Chip Separation Criteria

In finite element modeling of orthogonal cutting processes in 2D, a common approach is to model the chip and the uncut workpiece as two separate pieces that are somehow tied together until a separation criterion is met. Other researchers have used various element failure criteria that enable elements underneath, and possible within, a chip to fail under suitable conditions and subsequently be removed from the simulation [35, 108, 114, 124, 126]. In this work, element failure is used to model chip separation since this is an approach that is readily implemented in Abaqus / Explicit and because there is evidence of this being a physically realistic approach [35, 108].

During preliminary debugging simulations, not described in this chapter, all elements in the workpiece were permitted to fail if a failure criterion was met. However,

this lead to problems with the algorithm that handles contact between the tool and workpiece, which renders simulation results highly unreliable. Therefore, element failure is limited to zones of sacrificial elements in order to render tool workpiece contact better behaved. This approach has been successfully used by other researchers in 2D simulations, where the sacrificial elements comprised a single layer underneath the chip [35, 108]. In order to extend this approach to 3D, a single layer of elements beneath the chip is allowed to fail and a region of elements on the side of the chip is allowed to fail. This is described in more detail in subsequent sections.

## 7.3 Material Model

### 7.3.1 Overview

Correct modeling of material properties is necessary in order to achieve accurate simulation results. In this work, simulations were limited to those that represent the experiments conducted in the previous chapter, so that the simulations can be validated with experimental results. To accomplish this, it is necessary to be able to model the thermally evaporated aluminum film that was cut, the silicon substrates the film sits on, and the single crystal diamond that makes up the cutting geometry of the tool. Of course, simulations of micro-groove cutting with any other combination of materials could also be performed provided that the corresponding material properties are acquired.

The thermally evaporated aluminum film is expected to behave as a ductile metal and both elastically and plastically deform. Therefore, both elastic and plastic material properties are required. Additionally, in order for a chip to be able to separate from the workpiece, material properties must be specified that enable failure of elements that make up the aluminum film. By contrast, both diamond and silicon are brittle materials that

tend to fracture rather than plastically deform. Fracture of the diamond or silicon is not expected because both materials are much stronger than aluminum, and such fracture was not seen experimentally. Therefore, only elastic properties need to be specified for these materials. Additionally, material density must be specified for all materials.

## 7.3.2 Elastic Properties

Elastic properties were found for single crystal silicon, single crystal diamond, and pure aluminum. Single crystal silicon has anisotropic elastic properties that are readily available in the literature [137]. In Abaqus 6.9, such a material can be modeled though the use of a stiffness matrix in the form given by Equation (7.7) where the tensor on the left side of the equation is the stress tensor and the tensor on the right side of the equation is the strain tensor. Table 7.2 provides the inputs to the stiffness matrix that result in the material being orientated such that the 1-direction and 3-direction lie along the [110] crystalline directions and the 2-direction lies along the [100] crystalline direction. Material density is also included in the table.

$$\begin{Bmatrix} \sigma_{11} \\ \sigma_{22} \\ \sigma_{33} \\ \tau_{12} \\ \tau_{13} \\ \tau_{23} \end{Bmatrix} = \begin{bmatrix} D_{1111} & D_{1122} & D_{1133} & 0 & 0 & 0 \\ D_{1122} & D_{2222} & D_{2233} & 0 & 0 & 0 \\ D_{1133} & D_{2233} & D_{3333} & 0 & 0 & 0 \\ 0 & 0 & 0 & D_{1212} & 0 & 0 \\ 0 & 0 & 0 & 0 & D_{1313} & 0 \\ 0 & 0 & 0 & 0 & 0 & D_{2323} \end{bmatrix} \begin{Bmatrix} \varepsilon_{11} \\ \varepsilon_{22} \\ \varepsilon_{33} \\ \gamma_{12} \\ \gamma_{13} \\ \gamma_{23} \end{Bmatrix} \tag{7.7}$$

Table 7.2: Single crystal silicon properties at room temperature

| | | | | |
|---|---|---|---|---|
| Stiffness Matrix | D1111 | 194,360 MPa | D3333 | 194,360 MPa |
| | D1122 | 63,900 MPa | D1212 | 79,560 MPa |
| | D2222 | 165,700 MPa | D1313 | 50,900 MPa |
| | D1133 | 35,240 MPa | D2323 | 79,560 MPa |
| | D2233 | 63,900 MPa | | |
| Density | 2300 Kg/m$^3$ [138] | | | |

Single crystal diamond and pure aluminum can be treated as isotropic elastic solids. The elastic properties and density for diamond are listed in Table 7.3 and the same properties for aluminum are listed in Table 7.4. Note that the modulus of elasticity for diamond is 12.68 times higher than aluminum. Hence, very little deformation of the diamond is expected during cutting. Furthermore, simulation of a material with such a high modulus of elasticity would result in a very small stable time increment, as discussed previously. Therefore, diamond was approximated as a perfectly rigid material, which should not significantly affect accuracy.

Table 7.3: Diamond properties at room temperature [39]

| | |
|---|---|
| Modulus of Elasticity | 862,500 MPa |
| Poisson's Ratio | 0.2 |
| Density | 3360 Kg/m$^3$ |

Table 7.4: Aluminum properties at room temperature

| | |
|---|---|
| Modulus of Elasticity | 68,000 MPa [39] |
| Poisson's Ratio | 0.33 [139] |
| Density | 2698.9 Kg/m$^3$ [39] |

## 7.3.3 Aluminum Flow Stress Model

In order to accurately simulate a machining process, suitable flow stress data must be acquired. Ideally the data should be collected for the exact same alloy machined, at the same heat treat, and at the same size scale. The data set should also include data at all

the strains and strain rates that are present during the machining process. This is because, small changes in alloy composition and heat treat can have significant effects on material properties. Also, apparent material strength has been shown to increase at smaller size scales [140]. Both strains and strain rates can also be as very high, which results in considerable strain hardening and strain rate hardening.

Unfortunately, it is not always possible to meet this ideal, and approximate values must be used. This is in part because the high strain and strain rate testing required involves the use of specialized equipment and published data is not available for many alloys. Also, the equipment required to collect high strain rate data, such as the split Hopkinson pressure bar apparatus [141], is limited to macro-scale testing.

Since high-strain rate micro-scale test apparatus is not available, macro-scale properties were used as an approximation. This was deemed the best choice because of the importance of strain rate hardening in machining and due to the very limited amounts of micro-scale flow stress data. Also, since little data is available for the 99.99% pure aluminum used in this work, data for 99% pure fully annealed Al 1100-0 was used.

Room temperature flow stress curves were collected from the literature for Al 1100-0 or similar alloys differing only slightly in purity or heat treat. Some very high strain rate data was also found for vapor deposited aluminum. The material, heat treat, test method, and strain rate, for each flow-stress curve are listed in Table 7.5. Note that when shear stress and strain data was found, the Mises criterion was assumed to be applicable and the material was assumed to be incompressible so that tensile stress-strain curves could be found through the use of Equations (7.8) and (7.9) [142] where $\sigma$ is tensile stress, $\tau$ is shear stress, $\varepsilon$ is tensile strain, and $\gamma$ is shear strain.

(7.8) $$\sigma = \tau\sqrt{3}$$

(7.9) $$\varepsilon = \frac{\gamma}{\sqrt{3}}$$

Table 7.5: Room temperature stress-strain curves

| Material Description | Heat Treatment | Test | Strain Rate ($sec^{-1}$) | Reference |
|---|---|---|---|---|
| Al 1100-0 | | CSHPB | 800 | [142] |
| Al 1100-0 | | TSHB | 800 | [142] |
| Al 1100-0 | | QS | 0.0045 | [142] |
| Ann. Com. Pure | Ann. @ 600° F 2 hr, F.C. | QS | 0.00167 | [141] |
| Ann. Com. Pure | Ann. @ 600° F 2 hr, F.C. | QS | 0.56 | [141] |
| Ann. Com. Pure | Ann. @ 600° F 2 hr, F.C. | CSHPB | 1750 | [141] |
| Al 1100 | Ann. @ 650° F 2 hr, F.C. 24 hr | QS | 0.002875 | [143] |
| Al 1100 | Ann. @ 650° F 2 hr, F.C. 24 hr | QS | 0.015 | [143] |
| Al 1100 | Ann. @ 650° F 2 hr, F.C. 24 hr | QS | 0.1 | [143] |
| Al 1100 | Ann. @ 650° F 2 hr, F.C. 24 hr | DDI | 910 | [143] |
| Al 1100 | Ann. @ 650° F 2 hr, F.C. 24 hr | DDI | 1450 | [143] |
| Al 1100 | Ann. @ 650° F 2 hr, F.C. 24 hr | DDI | 1850 | [143] |
| Al 1100 | Ann. @ 650° F 2 hr, F.C. 24 hr | DDI | 2500 | [143] |
| Al 1100 | Ann. @ 650° F 2 hr, F.C. 24 hr | DDI | 3210 | [143] |
| Al 1100 | Ann. @ 650° F 2 hr, F.C. 24 hr | DDI | 3750 | [143] |
| Al 1100 | Ann. @ 650° F 1.5 hr, F.C. | TSHB | 490 | [144] |
| Al 1100 | | PSI | 61776 | [145] |
| Al 1100 | | PSI | 103345 | [145] |
| Al 1100 | | PSI | 107387 | [145] |
| Al 1100 | | PSI | 118356 | [145] |
| Vapor Deposited | | PSI | 2309401 | [145] |
| Vapor Deposited | | PSI | 2886751 | [145] |

| | |
|---|---|
| CSHPB | Compressive Split Hopkinson Pressure Bar |
| TSHB | Torsional Split Hopkinson bar |
| QS | Quasi-Static |
| DDI | Direct Disk Impact |
| PSI | Pressure Shear Impact |
| Ann. | Annealed |
| F.C. | Furnace Cooled |

The flow stress data is plotted in Fig. 7.2 for plastic strains between 0 and 0.5. Note the sharp increase in flow stress that occurs at strain rates of higher than several thousand $sec^{-1}$. Generally, in finite element modeling, this data is fit to a function that is be used by the software to rapidly compute flow stress for a given strain and strain rate. One such empirical function commonly used in metal cutting simulations is the Johnson-Cook flow stress model [146]. For example, this model has been used in 2D finite element simulations of micro-scale cutting in aluminum 2024-T3 [35].

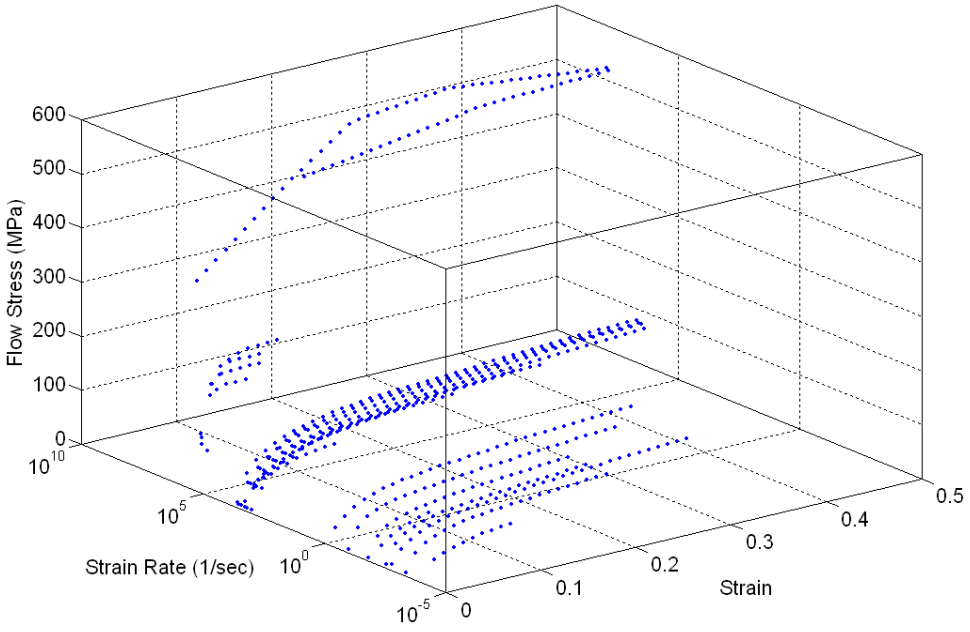


Figure 7.2: Stress-strain curves at various strain rates

However, attempts to fit a material model to the data showed that the Johnson-Cook plasticity model fit the data up to a strain rate of a few thousand $sec^{-1}$ moderately well, but high-strain rate behavior was not captured. I.e., the marked increase in flow stress at strain rates of $10^4$ $sec^{-1}$ and higher was not captured. Furthermore, since this high strain rate data was captured for vapor deposited aluminum, it is particularly applicable. Hence, a different empirical flow stress equation had to be developed.

Examination of curves of flow stress vs. strain rate, where each different curve represents behavior at a different strain, shows that all the curves have about the same shape. This is seen by normalizing each curve by the flow stress at a strain rate of 0.00167 $sec^{-1}$ to produce the normalized curves shown in Fig. 7.3. Hence there is not a strong coupling between the effects of strain and strain rate. Therefore, the flow stress can be described with a single stress-strain curve that is adjusted by some strain rate dependent flow stress multiplier curve.

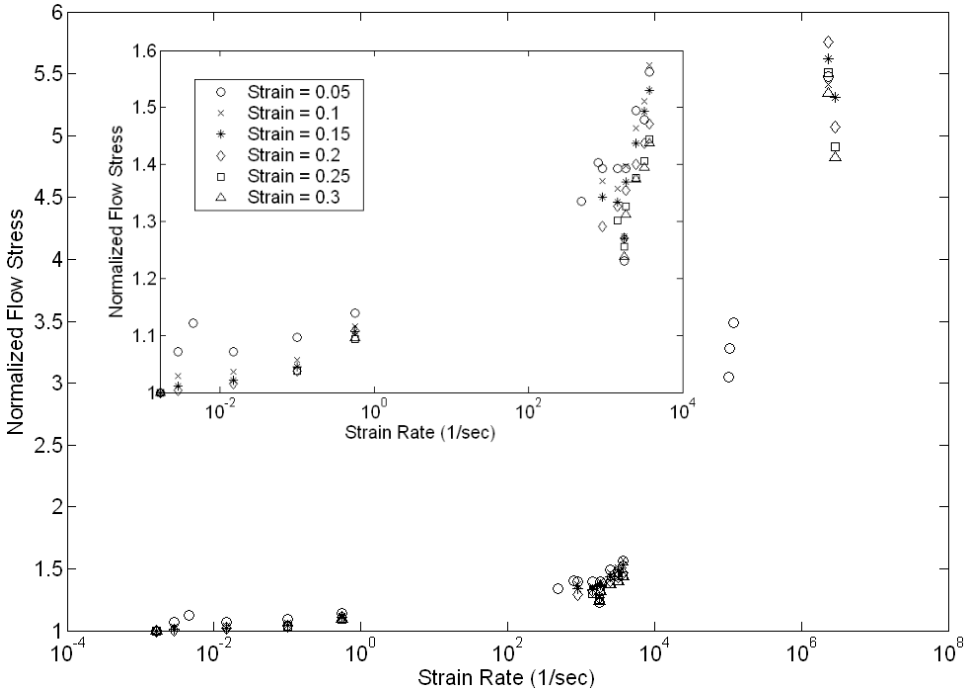


Figure 7.3: Relationship between normalized flow stress and strain rate for Al 1100-0

A piecewise stress multiplier function is described by Equations (7.10) – (7.13) where R is the stress multiplier, $\dot{\bar{\varepsilon}}^{pl}$ is the equivalent plastic strain rate, $\varepsilon_t$ is the strain rate where one function transitions to another, $\varepsilon_o$ is the quasi-static strain rate, and all other values are empirically fit constants. The strain rate function $f_1$ is in the form used in a relatively low strain rate flow stress model for 1100-0 [143], and $f_2$ is in the form used in the Johnson-Cook plasticity model [146].

(7.10)
$$R(\dot{\bar{\varepsilon}}^{pl}) = \begin{cases} f_1(\dot{\bar{\varepsilon}}^{pl}) & \text{if } \dot{\bar{\varepsilon}}^{pl} \le \dot{\varepsilon}_t \\ f_2(\dot{\bar{\varepsilon}}^{pl}) & \text{if } \dot{\bar{\varepsilon}}^{pl} > \dot{\varepsilon}_t \end{cases}$$

(7.11)
$$f_1(\dot{\bar{\varepsilon}}^{pl}) = \frac{1}{\left[1 - \frac{\log(\dot{\bar{\varepsilon}}^{pl} / \dot{\varepsilon}_o)}{\log(D_o)}\right]^p}$$

(7.12)
$$f_2(\dot{\bar{\varepsilon}}) = C * \log\left(\frac{\dot{\bar{\varepsilon}}^{pl}}{\dot{\varepsilon}_o}\right) + f_1(\dot{\varepsilon}_t) - C * \log\left(\frac{\dot{\varepsilon}_t}{\dot{\varepsilon}_o}\right)$$

(7.13)
$$\frac{d f_1(\dot{\varepsilon}_t)}{d\dot{\bar{\varepsilon}}^{pl}} = \frac{d f_2(\dot{\varepsilon}_t)}{d\dot{\bar{\varepsilon}}^{pl}}$$

The function was fit to the data in Fig. 7.3 using a least squares regression, which resulted in the fit shown in Fig. 7.4 and the constants given in the first five columns of Table 7.6. This fit had an $R^2$ regression value of 0.99.

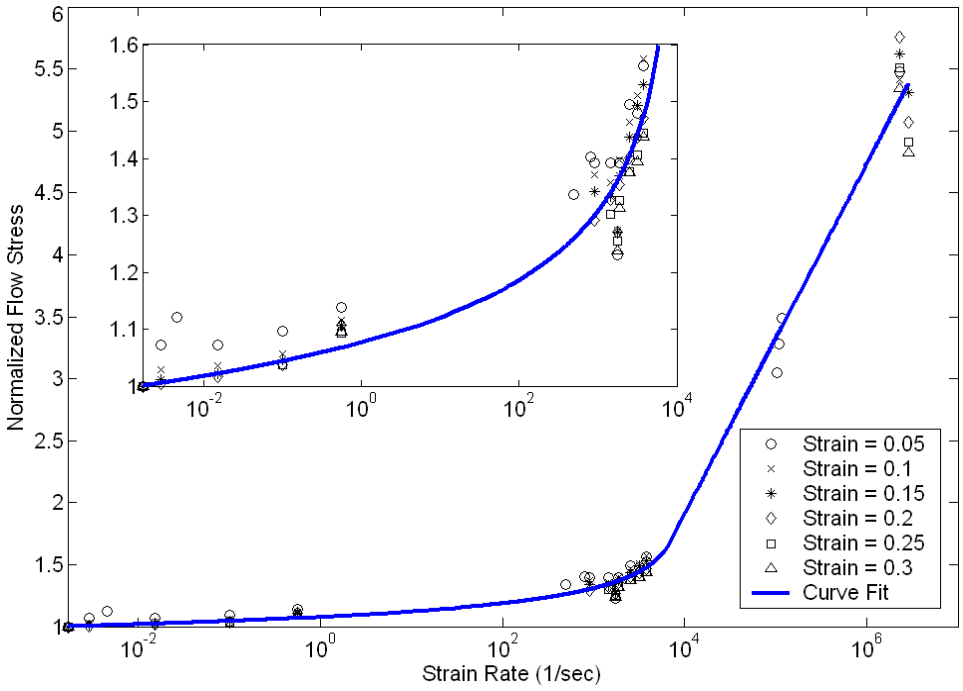


Figure 7.4: Curve fit to the normalized flow stress data

Table 7.6: Flow stress data fit parameters

| $\dot{\varepsilon}_o$ | $D_o$ | p | $\dot{\varepsilon}_t$ | C | A | B | n |
|---|---|---|---|---|---|---|---|
| 0.00167 | 5,988,024 | 0.139677 | 6820 | 1.41057 | 25.44 | 123.23 | 0.3215 |

The flow stress values in each stress-strain curve from the literature were divided by the values from the curve in Fig. 7.4 at each corresponding strain rate. This caused all the stress-strain curves to line up fairly well, as shown in Fig. 7.5. A function given by Equation (7.14), which is the strain rate independent portion of the Johnson-Cook plasticity model, was then fit to these adjusted curves. In the equation, σo is the quasi-static flow stress, $\bar{\varepsilon}^{pl}$ is the plastic equivalent strain, and A, B, and n are parameters. The parameters were found via least squares fit regression and are given in the last three columns of Table 7.6.

(7.14) $$\sigma^o = A + B\left(\bar{\varepsilon}^{pl}\right)^n$$

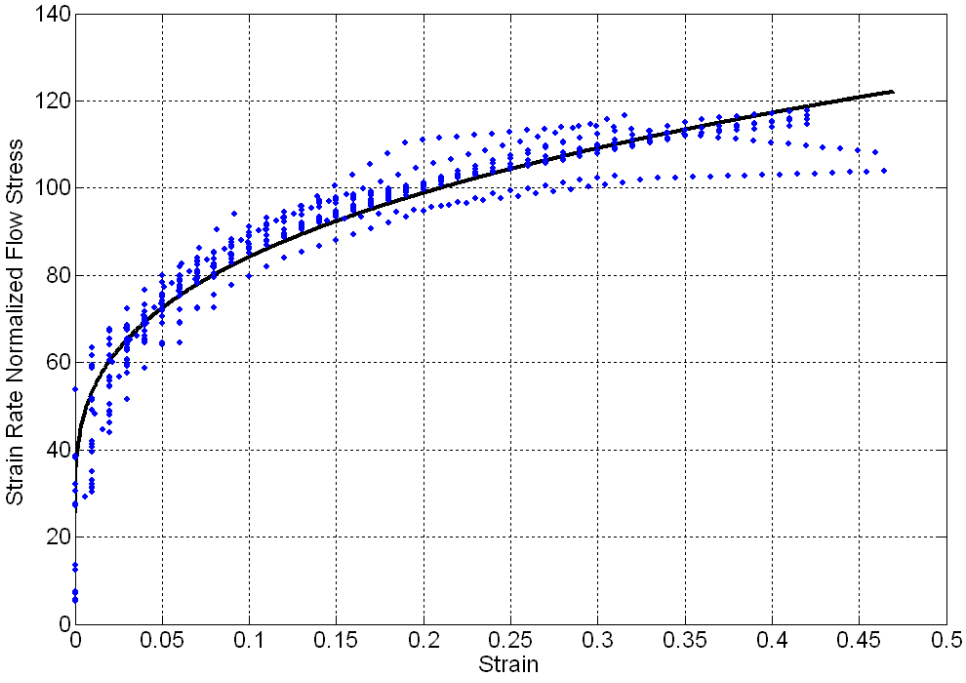


Figure 7.5: Strain rate normalized stress-strain curves and fit curve

The final stress/strain/strain rate relationship is described by Equation (7.15) where $\bar{\sigma}$ is the flow stress. This resultant function is shown as curves in Fig. 7.6, while actual data points are shown as dots. As can be seen in the figure, the stress-strain-strain rate relationship is described fairly well.

(7.15) $$\bar{\sigma} = \sigma^{o}\, R$$

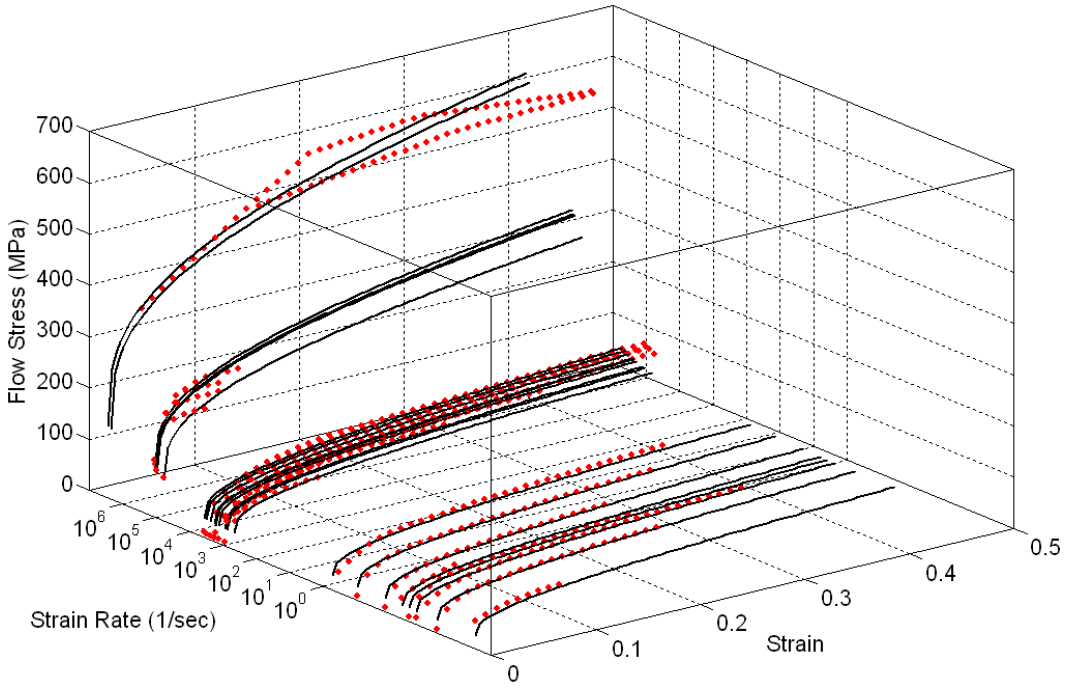


Figure 7.6: Stress-strain data at various strain rates and material model calculated curves

## 7.3.4 Aluminum Failure Model

In order to model separation of a chip from a workpiece, selected elements in the model are permitted to fail, and hence a material failure criterion for aluminum is necessary. The Johnson-Cook damage model [147] has been used by several researchers [35, 125, 126] for this purpose in 2D finite element simulations of metal cutting. This model is used to predict when material has become damaged. Following the initiation of damage, the properties of the damaged material can be made to degrade, which is

followed by material failure. Alternatively, the material can be assumed to immediately fail upon damage initiation, which is a commonly used approach in metal cutting that is also be used here.

In this work a slightly modified Johnson-Cook damage model is used, which is already implemented in Abaqus 6.9 [122], was used to determine when elements become damaged and are deleted. Using this model, elements are assumed to become damaged during a time increment where a damage parameter, $\omega_D$, reaches unity. This damage parameter is found in each time step by summing all instantaneous damage parameter values, $\Delta\omega_D$, from the current and previous time steps. This can be seen in Equations (7.16) and (7.17) where $\Delta\bar{\varepsilon}^{pl}$ is the change in plastic equivalent strain during a time increment, and $\bar{\varepsilon}_D^{pl}$ is the equivalent plastic strain at the onset of damage based on the material state during a given time increment.

$$\omega_D = \sum \Delta\omega_D \geq 1 \tag{7.16}$$

$$\Delta\omega_D = \frac{\Delta\bar{\varepsilon}^{pl}}{\bar{\varepsilon}_D^{pl}\left(\eta, \dot{\bar{\varepsilon}}\right)} \geq 0 \tag{7.17}$$

The value of $\bar{\varepsilon}_D^{pl}$ is given by Equation (7.18) where $d_1$ – $d_5$ are material dependent parameters, $\dot{\bar{\varepsilon}}^{pl}$ is the plastic equivalent strain rate, $\dot{\varepsilon}_o$ is a parameter used to non-dimensionalize the strain rate, $\hat{\theta}$ is the nondimensional temperature, and $\eta$ is the stress triaxiality, which is the negative of the pressure stress divided by the Mises stress. The modification from the original Johnson-Cook formula only causes the sign of parameter $d_3$ to be opposite from the originally published form. Also, since thermal effects are neglected, $\hat{\theta}$, remains zero at all times and the value of $d_5$ is irrelevant.

(7.18) $$\bar{\varepsilon}_D^{pl}\left(\eta,\dot{\bar{\varepsilon}}\right)=\left[d_1+d_2\,e^{\left(-d_3\,\eta\right)}\right]\left[1+d_4\,Ln\left(\frac{\dot{\bar{\varepsilon}}^{pl}}{\dot{\varepsilon}_o}\right)\right]\left(1+d_5\,\hat{\theta}\right)$$

The values of $d_1 - d_4$ could not be found for high purity evaporated aluminum or even Al 1100-0 in the literature. Instead, the most relevant values for $d_1 - d_3$ are as reported for Al 1100-H12 [148], which is a work hardened version of Al 1100-0. Note that the sign of $d_3$ is opposite what it would be using the published Johnson-Cook model due to the modified version used in Abaqus. The most relevant value of $d_4$ is the value reported for Al 2024-T3 [149]. These parameter values are listed in Table 7.7.

Table 7.7: Modified Johnson-Cook damage model parameters

| $d_1$ | $d_2$ | $d_3$ | $d_4$ | $\dot{\varepsilon}_o$ |
|---|---|---|---|---|
| 0.071 | 1.248 | 1.142 | 0.007 | 1 |

# 7.4 Contact Modeling

## 7.4.1 Contact Algorithm

Contact between the tool and workpiece and between the workpiece and itself is modeled using the general contact algorithm in Abaqus 6.9. Friction is modeled using a extended coulomb friction model, described by Equation (7.19), where frictional shear stress, $\tau_{fric}$, is given by a constant coefficient of friction, $\mu$, if the predicted frictional shear stress is below a set limit, $\tau_{crit}$. If the predicted frictional shear stress exceeds the limit, the limit itself is used by the model. This approach is based on the work of [150] and has been successfully used by several researchers [35, 103, 109, 125]. The basis for the approach is that the pressure on the rake face during machining can become so high that the frictional shear stress exceeds the shear strength of the material at the interface

between the chip and rake face, which causes seizing of a thin contact layer on the chip and localized plastic flow of the underlying chip material.

$$\tau_{fric} = \begin{cases} \mu p_{contact} & \text{if} \quad \mu p_{contact} < \tau_{crit} \quad (sliding) \\ \overline{\tau}_{crit} & \text{if} \quad \mu p_{contact} \geq \tau_{crit} \quad (sticking) \end{cases} \tag{7.19}$$

## 7.4.2 Range of Physically Realistic Friction Values

The correct values of μ and $\tau_{crit}$ must be found in order to get good model predictions. One means of accomplishing this is to run simulations using several sets of values and select the values that provide predictions that are closest to experimental results, which is the approach taken in this work. However, since simulations are expected to be time consuming, a study of the literature is used to narrow the range of values that need to be examined.

The most relevant experimental friction data found in the literature was from an experimental study where large grained high purity (99.999% pure) aluminum workpieces that were annealed for 30 minutes at 400° C were cut using orthogonal machining with a single crystal diamond tool that had an edge radius of 200 nm and a 0° rake angle [94]. The lowest cutting speed used was 300 mm/min, which is the same speed used in some experiments from the previous chapter, the shallowest depth of cut was 10 μm, and a cutting fluid (Ecoline™) was applied to the tool and workpiece prior to each experiment, which unfortunately changes the friction conditions. The study showed that the coefficient of friction varied considerably from grain to grain, but for a finer grained material the mean value would be most representative, which is 0.15. Therefore, since cutting fluid was used, this value forms a lower bound on range of values that may be suitable for the current simulations.

Additionally, several researchers have conducted finite element simulations using coefficient of friction that were later validated with experiments. One study involved simulating orthogonal cutting of Al 2024-T3 with diamond tools at speeds of 150 m/min and 180 m/min and with an uncut chip thickness of 105 μm [35, 108]. In that study, the coefficient of friction was 0.2 and a max allowable frictional shear stress of 20 MPa worked well. The low max allowable frictional shear stress was attributed to thermal softening of material at the tool – chip interface. Another study involved simulating cutting of Al 5083-H116 using a diamond tool with an edge radius of 5 microns at a speed of 200 m/min. A coefficient of friction of 0.14 and max allowable frictional shear stress of 135 MPa was found to be effective in that study [107]. Yet another study simulated cutting of hot extruded Al 1100 using silicon a nitride based ceramic tool insert. It was found that at a cutting speed of 0.6 m/sec a constant coefficient of friction of 0.27 gave the best results. Based on these results, it was concluded that, for tool / workpiece material combinations closest to the experiments described in the previous chapter, the coefficient of friction is likely between 0.15 and 0.27.

A common way of finding the max allowable friction shear stress, $\tau_{crit}$, appears to be to try several values until one is found that causes the model to give results consistent with experiments [35, 107 - 109]. In another instance, the value of $\tau_{crit}$ was set slightly higher than a material shear strength value associated with complete failure of the material, which was used for chip separation modeling [151]. Lastly, $\tau_{crit}$ can be estimated via careful evaluation of experimental cutting forces and observation of the area of seized chip contact [125], which can be found via a quick stop test [150]. Since sufficient cutting force data does not exit for the experiments described in the previous

chapter, the approach of running simulations to see the effect of varying $\tau_{crit}$ is used, as described later in this chapter.

## 7.5 Model Geometry

The previously selected 8-node elements are used to construct the workpiece used in the model, and the tool is mesh using rigid elements. The overall mesh is shown in Fig. 7.7. In the figure the direction of cut is indicated and it can be seen that the model makes use of half symmetry in order to reduce the amount of computer time required.

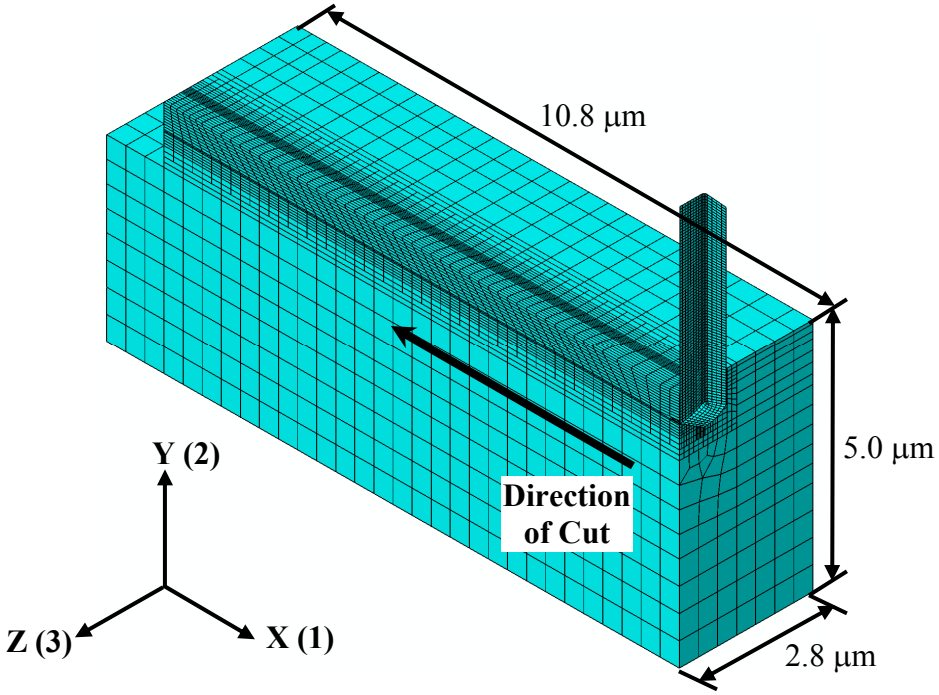


Figure 7.7: Overall model geometry

The workpiece portion of the model consists of five parts that are meshed separately than joined using surface-based mesh tie constraints, which perform interpolation over interfaces where mating nodes do not line up perfectly. The five parts are identified as the cut work (Fig. 7.8A), uncut work (Fig. 7.8B), support work 1 (Fig. 7.8C), support work 2 (Fig 7.8D), and end support (Fig. 7.8E). Note that all of the workpiece elements are assigned aluminum material properties except elements in the

bottom 2 μm of support work 2 and end support parts, which are assigned silicon material properties, where the [100] crystalline direction is coincident with the y-axis as it is defined in Fig. 7.7. Additionally, two sets of aluminum material properties are used, one the does not allow for element failure and deletion and one that does, in order to handle separation of the chip from the workpiece.

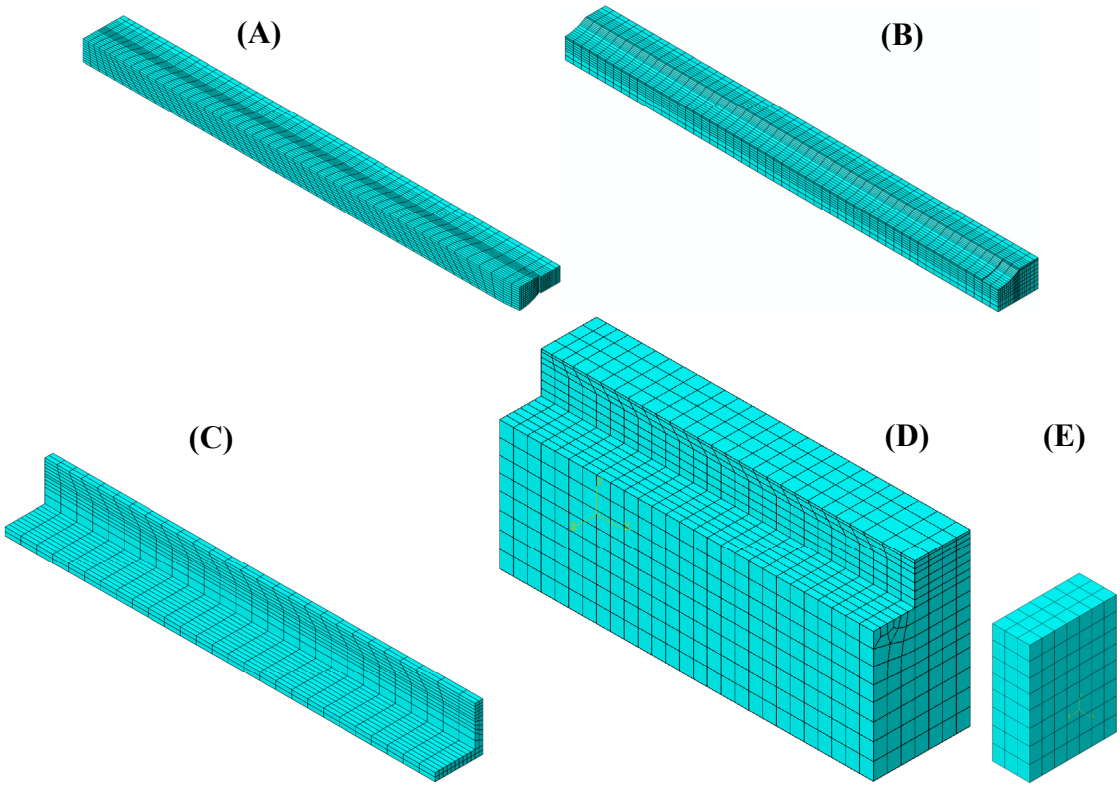


Figure 7.8: Workpiece components

Figure 7.9 indicates the regions that are capable of material failure in order for chip formation to occur. A 3D view of a portion of the workpiece is shown in Fig. 7.9A, and a cross-sectional view of the mesh in a plane normal to the direction of cut is shown in Fig. 7.9B. Workpiece elements that are allowed to fail if the Johnson-Cook damage criterion is met are darkly shaded and elements that are not allowed to fail are more lightly shaded. Notice that the elements that can fail make up a single layer of elements

below the uncut chip and an eight element wide region of elements on the side of the uncut chip. This configuration insures that the bottom of the chip separates from the workpiece exactly at the cutting edge of the tool, which is a good approximation provided that the tool is sharp. The side of the chip is allowed separate from the workpiece anywhere in the selected region, since the exact location when separation should occur is not initially known.

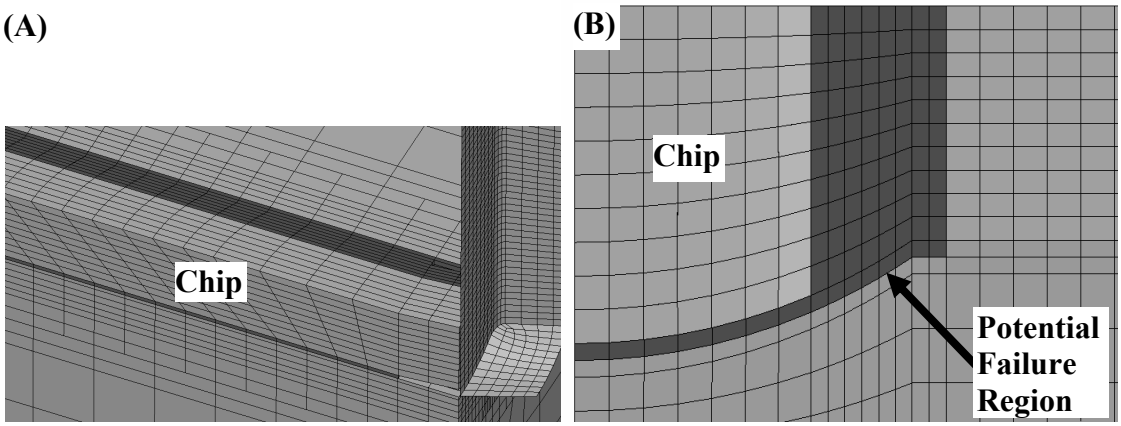


Figure 7.9: Material failure regions

Three features were introduced to facilitate chip formation without any element becoming misshapen to the point where simulation accuracy suffers. As shown in Fig. 7.10, a 40° tilt was introduced into the mesh in the direction of cut in order to pre-compensate for element skew induced by shearing over the course of the simulation. Hence, the amount of skew experienced by an element at any time during a simulation is more limited, which increases simulation accuracy since highly skewed elements are not as accurate. Such an approach has been previously used by several researchers in 2D simulations [35, 104, 123]. Additionally, as shown in Fig. 7.11, a crack with a 5° opening angle and a 400 nm depth was introduced where the tool initially enters the workpiece in order to encourage steady state chip formation to occur earlier in the

simulation than it would occur otherwise. Lastly, as can be seen in Fig. 7.9B and Fig. 7.11, the cross-section of the mesh was rounded to match the rounded bottom of the cutting tool used in Experiment 4 in Chapter 6.

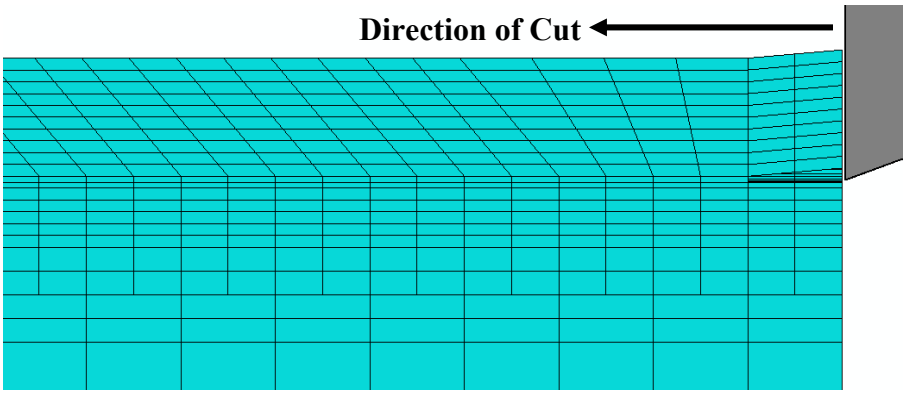


Figure 7.10: Mesh slant

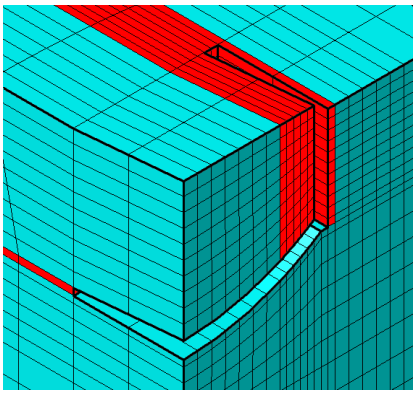

Figure 7.11: Initial crack in order to facilitate chip formation

The tool to be modeled was rounded it bottom with a radius of 893 nm. Additionally, some rounding with a radius of 60 nm was present on edges of the tool formed via a focused ion beam. This means that a completely correct model of the tool would have a rounded cutting edge and rounded non-cutting edges. However, if a rounded cutting edge is used, a very dense mesh would be required in the vicinity of the cutting edge, which would increase computer time significantly. Also, in order for separation of the chip to occur there would have to be a region of elements in line with

the cutting edge capable of failure, which would cause the contact problem that motivated the use of a line of fallible elements below the chip to return.

Fortunately, a 60 nm cutting edge radius is sharp enough to approximate as infinitely sharp in this work. The justification for this is that a chip will separate from a workpiece when the uncut chip thickness exceeds the minimum chip thickness, which is a material dependent fraction of the cutting edge radius. For aluminum the minimum chip thickness is 40% of the cutting edge radius [152] or 24 nm in this case. Such a small minimum chip thickness relative to the depth of cut, 265 nm being the shallowest depth of cut to be simulated, indicates that over 90% of the material will travel up the rake face of the tool during actual cutting and not be affected by the presence of the edge radius. Hence, the sharp tool approximation is valid provided that exact trust force predictions, which may be affected by the presence of ploughing under the tool, are not required. This is acceptable since finite element models often do a poor job of predicting thrust forces, and hence this is not a model output that will be considered in this work

A 3D view of the tool model is shown in Fig. 7.12A. The tool was constructed from rigid 3D planar elements (R3D4) and takes advantage of half-symmetry to reduce the element count. The tool model shown in the figure has a 0° rake angle, a 20° end clearance angle, a 5° side clearance angle, and a perfectly sharp cutting edge. Also, as shown in Fig. 7.12B, the tool has a rounded bottom with a radius of 893 nm. As shown in Fig. 7.12C, the side edge of the tool also has a radius of 60 nm.

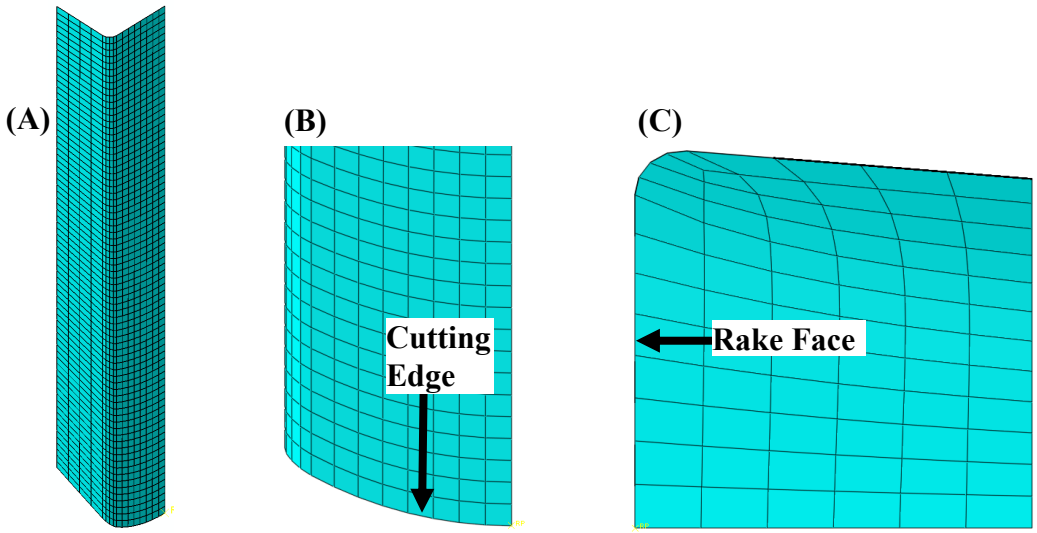


Figure 7.12: Tool mesh 3D view (A), rake face view (B), and top down view (C)

When using this tool in a simulation, all of the elements that make up the bottom of the chip should slide up the rake face of the tool. Hence, all of the nodes attached to each of these elements should also slide up the rake face. If however, one or more of the nodes that make up one of these elements manages to slide under the tool, then the associated element will become highly deformed. Such events can occur at the start of a simulation and may greatly impact the simulation results in a negative manner.

This problem can occurs because, as shown in Fig. 7.13, the failure of an element beneath the chip produces an open space between the bottom of the tool and the elements that make up the uncut workpiece. The existence of this space is purely due to finite element descritization, and in actual cutting the space would be full of material being ploughed under the tool. Hence chip material would not be able to flow into this space, i.e., the chip material would only be able to flow up the rake face because it would have nowhere else to go.

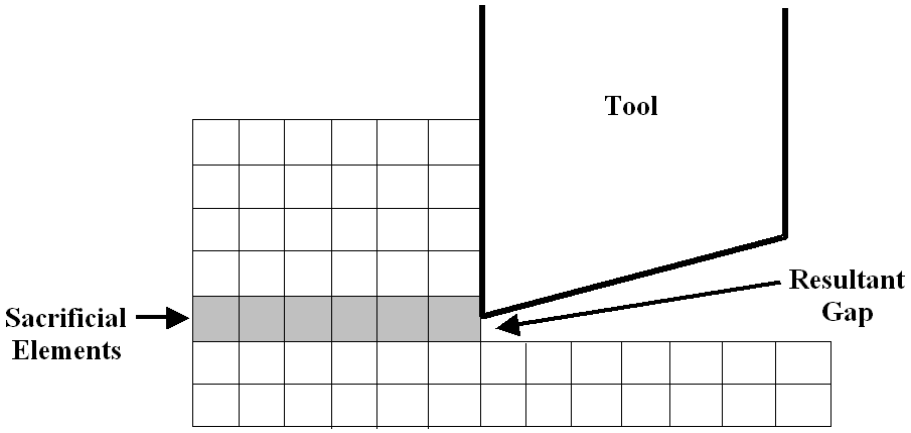


Figure 7.13: Cause of nodes being able to slide under the tool

Since it is not realistic for nodes to slide under the tool though an empty space that is only present due to the FEA descritization, some means of constraining nodes to not flow into that space is needed. This is accomplished by adding a separate rigid part placed such that it extends from the cutting edge and prevents nodes from moving in physically unrealistic manner. This chip guide is shown in Fig. 7.14A and matches up with a tool as shown in Fig. 7.14B. Since this part is not physically real, contact between the chip guide and the workpiece is taken to be frictionless.

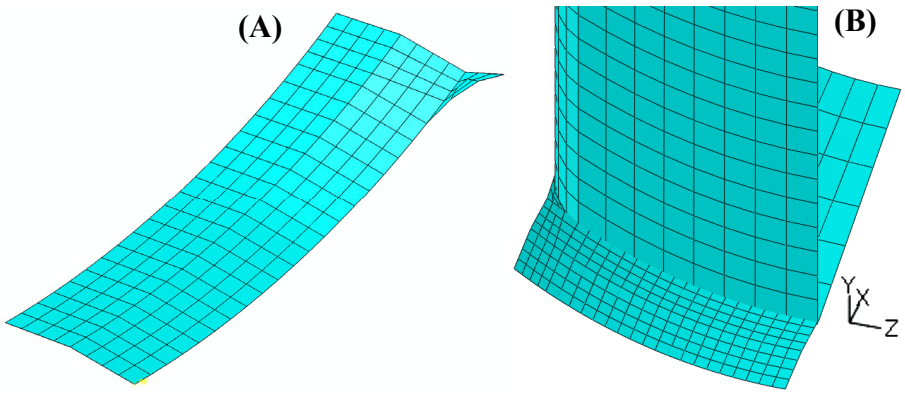


Figure 7.14: Chip guide (A) and how it mates to the cutting tool (B)

## 7.6 Boundary and Contact Conditions

A cutting full simulation is broken into five time steps: the initial step, the cut entry step, the cut established step, the cut exit step, and the cut clear step. These steps correspond establishment of initial conditions, initial entry of the tool into the workpiece, steady state cutting, exit of the tool from the workpiece, and moving the tool past the workpiece. During each step, boundary conditions are applied, maintained, or modified. Table 7.8 provides the duration of each step and indicates the boundary conditions present in each step. Figure 7.15 indicates where each boundary condition is applied except for the last two boundary conditions, which are directly applied to the tool and chip guide rigid bodies.

The boundary condition on the side of the crack, which is only active up through the second step, is intended to prevent the weakly supported material from spreading too much due to compression when the tool first enters the workpiece. Also, the boundary conditions up through the cut est. step are aimed at simulating stead state cutting. By contrast the boundary conditions are changed during the cut exit step to allow for simulation of the tool to exiting from the other side of the workpiece.

Table 7.8: Boundary conditions

| Time Step | Initial | Cut Entry | Cut Est. | Cut Exit | Cut Clear |
|---|---|---|---|---|---|
| Duration (msec) | 0.0 | 0.242 | 1.32 | 0.6 | 0.25 |
| Fixed X Entry B.C. | Nodes fixed in x-dir | | | | |
| Fixed Z Crack B.C. | Nodes fixed in z-dir | | Inactive | | |
| Pinned Sides B.C. | Nodes fixed in all directions | | | | |
| Pinned End B.C. | Nodes fixed in all directions | | | | |
| Pinned Exit B.C. 1 | Nodes fixed in all directions | | | Inactive | |
| Pinned Exit B.C. 2 | Nodes fixed in all directions | | | Inactive | |
| Symmetry B.C. | Symmetry about xy-plane | | | | |
| Tool Vel B.C. | Inactive | -5 mm/sec in x-dir | | | |
| Chip Guide Vel B.C. | Inactive | -5 mm/sec in x-dir | | Inactive | |

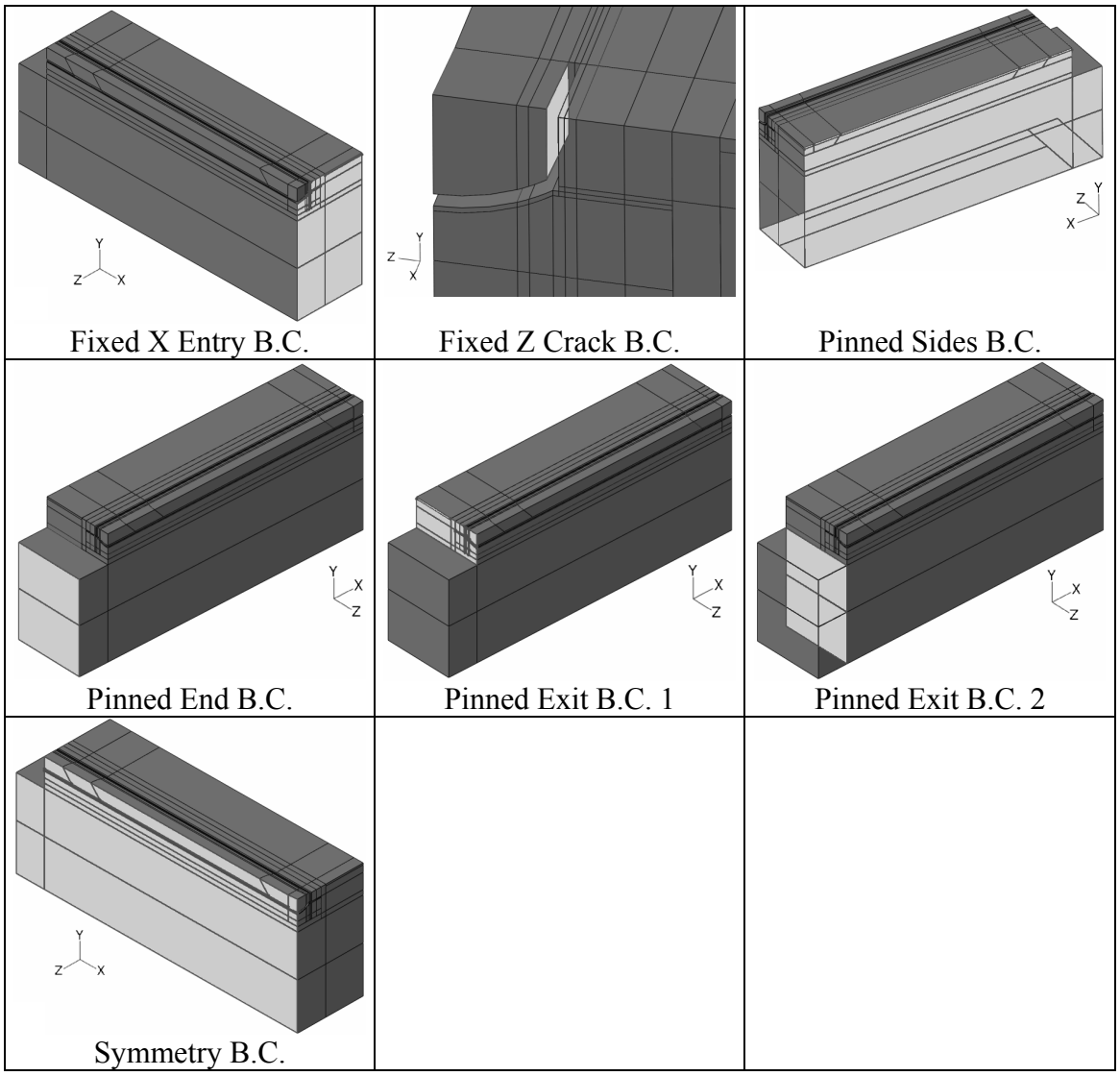


Figure 7.15: Regions where boundary conditions are applied

As mentioned previously, the workpiece consisted of five parts that were joined with surface-based mesh tie constraints. Additionally, there is a rigid tool part and a rigid chip guide part. Over the course of the simulation, different parts are enabled to have contact with each other using the Abaqus general contact algorithm, and contact conditions are assigned to each contact pair. The contact pairs during each time step and the corresponding contact conditions are given in Table 7.9. Note that the change in contact conditions during the cut exit step is intended prevent the chip guide from

affecting the exit burr formation process and is acceptable because the situation that causes the chip guide to be necessary only occurs early in the simulations.

Table 7.9: Contact pairs and conditions

| Part 1 | Part 2 | Friction Model | Steps |
|---|---|---|---|
| Tool | Cut Work | Extended Coulomb Friction | All |
| Chip Guide | Cut Work | Frictionless | Initial, Cut Entry, Cut Est. |
| Cut Work | Cut Work | Extended Coulomb Friction | All |
| Cut Work | Uncut Work | Extended Coulomb Friction | Cut Exit, Cut Clear |

# 7.7 Friction and Material Failure Strain Effects

## 7.7.1 Motivation

In order for the model to be useful for predictions it is necessary to find all model parameters that could not be found with confidence in the literature. Specifically, the coefficient of friction, $\mu$, must be found and the max possible frictional shear stress at the interface between the tool and chip, $\tau_{crit}$, must be found. Also, since the Johnson-Cook damage parameters were found for a material that had experienced much more work hardening than the actual workpiece material, these parameters might require adjustment. These tasks are accomplished by running simulations while using different combinations of parameter values, and then comparing simulation and experimental results. Multiple experimental conditions are simulated so that the parameters are not erroneously set to values that work well for one condition but do not work well at all for other conditions.

Once the correct parameters are found, results can be evaluated in order to gain an understanding of the cutting process that cannot be gained experimentally. Additionally, useful insight into the cutting process can be gained by examining how model behavior changes as parameters of interest are changed.

## 7.7.2 Selected Experimental Cases

Experiment 4 in Chapter 6 was conducted using cutting speeds of 50 mm/min to 400 mm/min. It is desirable to simulate the highest speed cases because the computer time required for a simulation depends on how much time must be simulated, which is in turn dependent on how long it takes for a tool to travel a long enough distance to observe cutting mechanics. However, the grooves produced in the 400 mm/min case were slightly wavy, likely due to the cutting action occurring faster than the limited bandwidth laser sensor and feedback control could easily handle. Therefore, simulations of some of the cuts made at 300 mm/min were performed instead.

Three load cases were selected for simulation: 0.3 mN, 0.7 mN, and 1.1 mN. For convenience, Table 7.10 lists the groove shape and chip characteristics that were present in each selected case during Experiment 4 in Chapter 6. Also, Fig. 7.16 shows the cross-sections of each of the grooves. Recall that due to distortion in AFM measurements, the left sides of the cross-sections are more representative of the actual groove shape than the right sides, which appear more sloped than they actually are.

Table 7.10: Selected groove and chip characteristics from Experiment 4 in Chapter 6

| Conditions | Load (mN) | 0.3 | 0.7 | 1.1 |
|---|---|---|---|---|
| | Speed (mm / min) | 300 | 300 | 300 |
| Groove Shape | Mean Depth (μm) | 0.267 | 0.503 | 0.687 |
| | Mean Width (μm) | 0.970 | 1.083 | 1.212 |
| | Left Burr Height (μm) | 0.052 | 0.148 | 0.146 |
| | Right Burr Height (μm) | 0.080 | 0.153 | 0.193 |
| Chip | Mean Chip Thick (μm) | 0.475 | 0.901 | 1.102 |
| Characteristics | Chip Thick Std (μm) | 0.025 | 0.022 | 0.043 |
| | Mean Chip Width (μm) | 0.976 | 1.332 | 1.703 |
| | Chip Width Std (μm) | 0.023 | 0.044 | 0.025 |
| | Curl Radius (μm) | 1.673 | > 2.76 | > 2.76 |

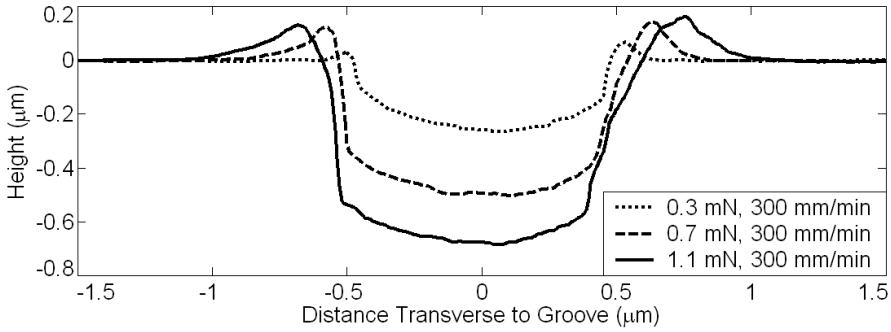


Figure 7.16: Selected groove cross-sections from Experiment 4 in Chapter 6

Additionally, for purposes of comparison to simulation results, the chip roots and chip curl during the selected cases was examined in more detail. Figure 7.17 shows the chip roots with the cutting tool superimposed on then. The images have been stretched at scaled so that they line up correctly. Figure 7.18 shows chips formed from the same cuts. Based on these images, it is shown that the chip curls in each case once it separates from the tool. In the 0.3 mN load case, the chip curl radius was 1.673 μm. In the other cases the curl radius due to cutting mechanics alone could not be measured directly, since the chip ran into the upper portion of the tool, as can be seen in Fig. 7.17B and Fig. 7.17C. In these cases, the chip curl radius was greater than 2.76 μm since this is the radius below which the chip would clear the tool. The radii are listed in Table 7.10.

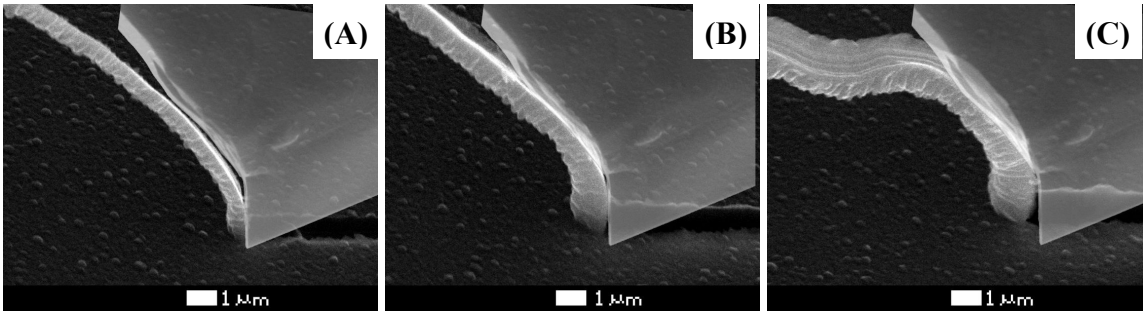


Figure 7.17: Chip roots formed when cutting at 300 mm/min in the 0.3 mN (A), 0.7 mN, (B) and 1.1 mN (C) cases

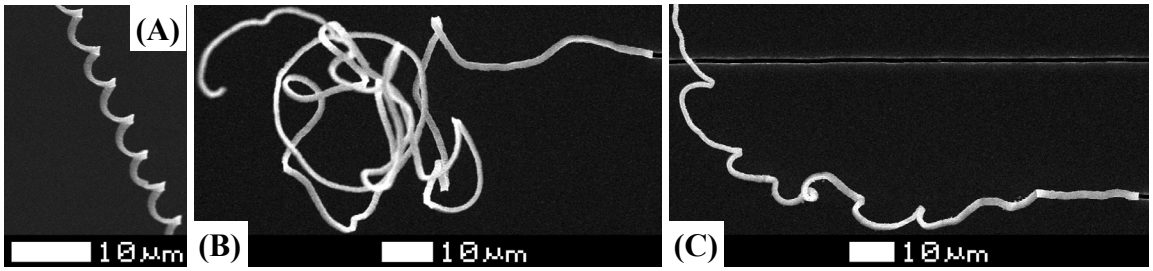


Figure 7.18: Chip formed when cutting at 300 mm/min in the 0.3 mN (A), 0.7 mN, (B) and 1.1 mN (C) cases

## 7.7.3 Estimating the Max Allowable Frictional Shear Stress

A common way of estimating the max allowable friction shear stress, $\tau_{crit}$, is to run simulations with several values until one is found that causes the model to give results consistent with experiments [35, 107 - 109]. In another instance, the value of $\tau_{crit}$ was set slightly higher than a material shear strength value associated with complete failure of the material [151]. Alternatively, $\tau_{crit}$ can be estimated via evaluation of experimental cutting forces and observation of the area of seized chip contact [125], which can be found via a quick stop test [150].

In the current case, experimental data does not exist and useful values have not been founded in the literature. Therefore, several finite element model runs were performed using different values of $\tau_{crit}$: 100, 200, 300, and 400 MPa. In each run, the coefficient of friction is assumed to be 0.2, the depth of cut is 500 nm, and the cutting speed is 300 mm/min. The material properties used were the same given previously in this chapter in Table 7.2, Table 7.4, Equations (7.10) – (7.15), Table 7.6, and Table 7.7. These runs enabled observation of changes in chip shape and estimation of the shear strength of the work hardened material at the tool-chip interface.

It was found that chip shape did not change significantly due to changes in $\tau_{crit}$. Also, there were not very large changes in the work hardened material shear strength at the interface between the chip and tool. This can be seen in Fig. 7.19A where the shear strength values at each node along the interface are plotted. In each case, the mean material shear strength is about 300 MPa along the rake face, which indicates that most of the work hardening occurred in the primary shear zone.

Additional, simulations were run to determine if the mean material shear strength at the interface remains 300 MPa when the coefficient of friction is varied. These simulations used coefficients of friction of 0.15, 0.20, 0.25, and 0.3 where $\tau_{crit}$ was set to 300 MPa and all other simulation values were as before. It was found that work hardened material shear strength at the interface is not strongly affected by the coefficient of friction in the range of 0.15 to 0.30, as shown in Fig. 7.19B.

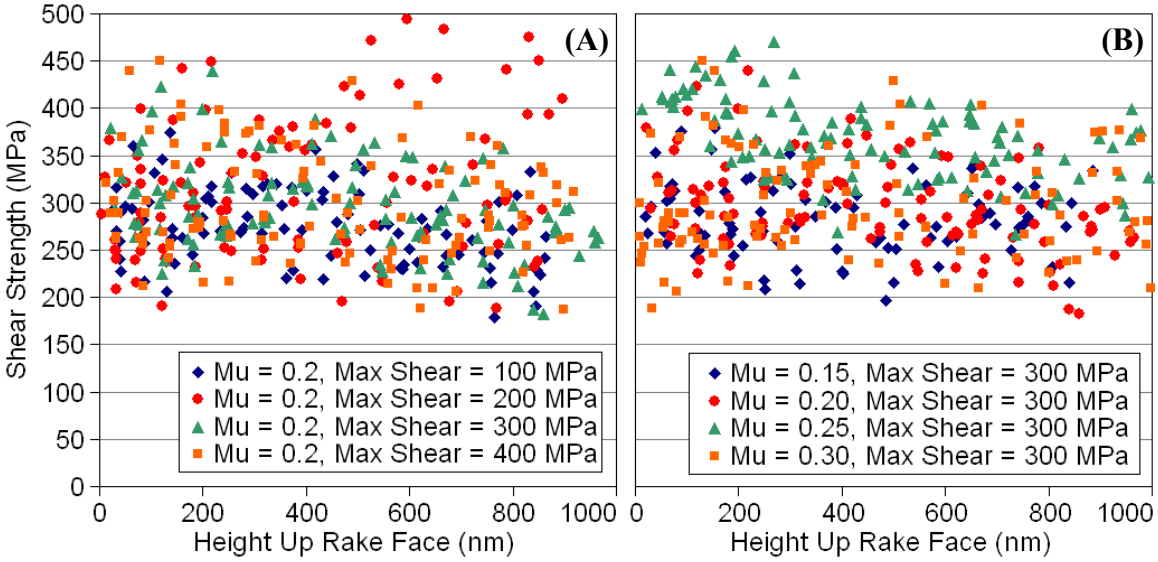


Figure 7.19: Shear strength of material due to work hardening of material along rake face

Except for a few hot spots, the contact pressures at the rake face – chip interface are low enough that frictional shear stress is not nearly as high as the work hardened

shear strength of the chip material at the interface, which is likely why changing the value of $\tau_{crit}$ does not have a large effect on simulation results. This can be seen in Fig. 7.20, which shows the contact pressures along the rake face mostly do not exceed 800 MPa in all of the simulations, which results in a frictional shear stress of only 240 MPa even if a coefficient of friction as high as 0.3 is used. Hence, very little sticking is expected to occur. This is consistent with results reported by [150] where sticking did not occur during cutting at what are considered low speeds for conventional macro-scale metal cutting. This is fortuitous since it means that the $\tau_{crit}$ value used in the simulations does not need to be as accurate as it would have to be otherwise. Hence, in the remainder of the work $\tau_{crit}$ is taken to be 300 MPa.

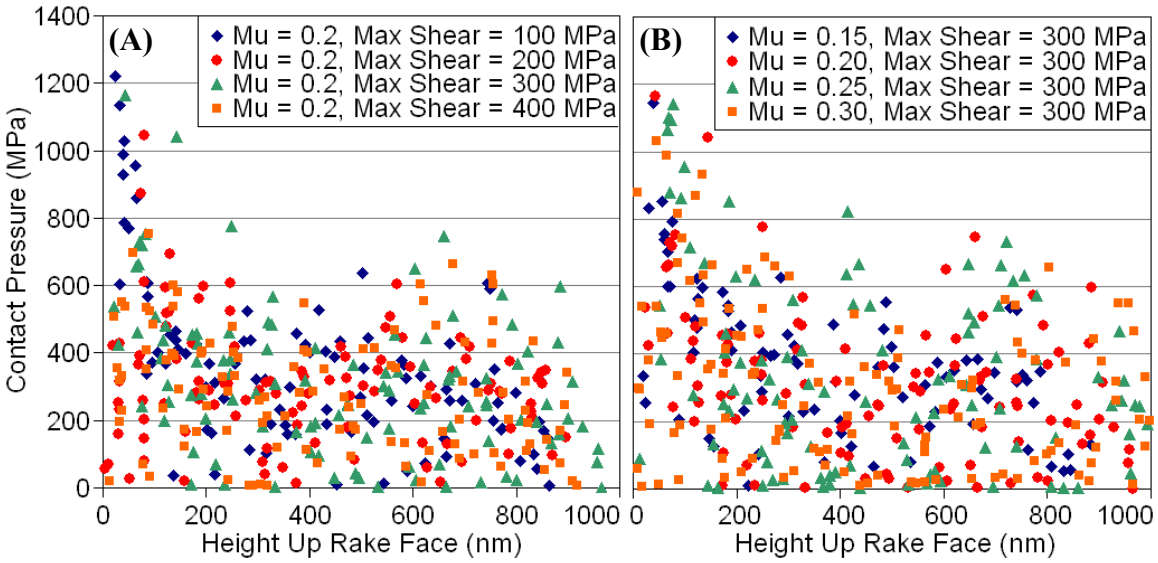


Figure 7.20: Contact pressures at various heights up the tool rake face

## 7.7.4 Finding Coefficient of Friction and Material Failure Values

The coefficient of friction can have a significant effect on model output and must be set accurately. Also, the amount of plastic equivalent strain required for material failure can affect burr formation and must be modeled correctly. To find the correct

values to use several simulations were run and the simulation outputs are compared to the previously described experimental results. Once again, in all the simulations the material properties used were the same given previously in this chapter in Table 7.2, Table 7.4, Equations (7.10) – (7.15), Table 7.6, and Table 7.7.

The simulations were run at a speed of 300 mm/min and depths of cut of 265 nm, 500 nm, and 720 nm. These depths are the mean depths during several different experiments conducted using cutting loads of 0.3, 0.7, and 1.1 mN, respectively. For each depth, all combinations of two coefficients of friction, $\mu$, and two Johnson-Cook damage model $d_2$ values were simulated. The values of $\mu$ used were 0.20 and 0.25. Parameter $d_2$ was used as a variable because, as shown in Equation (7.18), it has the strongest effect on the value of plastic equivalent strain required for material failure. One of the $d_2$ values was 1.248, which is that value reported for Al 1100-H12 in the literature [148] and might be too high due to the work hardening present in that material. The other $d_2$ value of 0.9 and was selected arbitrarily.

After the simulations had each progressed to the point of capturing steady state chip formation, model outputs were compared to experimental results to see what combination of $\mu$ and $d_2$ offers the best predictions overall. This is accomplished by evaluating the effect of these parameters on chip thickness, burr height, chip curl radius, and groove shape, each of which can be obtained from the model and measured experimentally. Figure 7.21 shows the simulated chip thickness results plotted along side the experimentally measured chip thicknesses. Additionally, the side burr height was found in each of the simulations. Figure 7.22 shows the simulated heights along with the experimentally measured burr heights. Note that there are two overlapping bars shown

for each experimental result in order to show the measured height of side burrs on the left and right side of each groove.

| Depth of Cut (nm) | Coefficient of Friction | J-C, D2 Value |
|---|---|---|
| 265 | 0.20 | 1.248 |
| 265 | 0.20 | 0.9 |
| 265 | 0.25 | 1.248 |
| 265 | 0.25 | 0.9 |
| 267 | Experimental | |
| 500 | 0.20 | 1.248 |
| 500 | 0.20 | 0.9 |
| 500 | 0.25 | 1.248 |
| 500 | 0.25 | 0.9 |
| 503 | Experimental | |
| 720 | 0.20 | 1.248 |
| 720 | 0.20 | 0.9 |
| 720 | 0.25 | 1.248 |
| 720 | 0.25 | 0.9 |
| 687 | Experimental | |

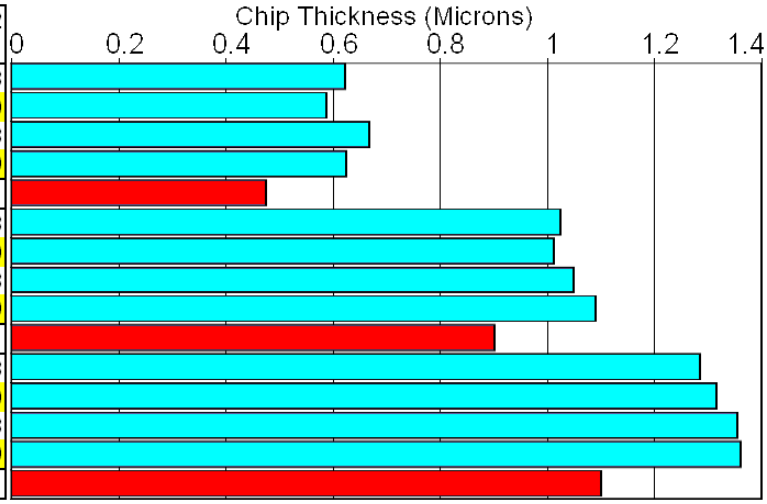


Figure 7.21: Simulated and experimental chip thickness

| Depth of Cut (nm) | Coefficient of Friction | J-C, D2 Value |
|---|---|---|
| 265 | 0.20 | 1.248 |
| 265 | 0.20 | 0.9 |
| 265 | 0.25 | 1.248 |
| 265 | 0.25 | 0.9 |
| 267 | Experimental | |
| 500 | 0.20 | 1.248 |
| 500 | 0.20 | 0.9 |
| 500 | 0.25 | 1.248 |
| 500 | 0.25 | 0.9 |
| 503 | Experimental | |
| 720 | 0.20 | 1.248 |
| 720 | 0.20 | 0.9 |
| 720 | 0.25 | 1.248 |
| 720 | 0.25 | 0.9 |
| 687 | Experimental | |

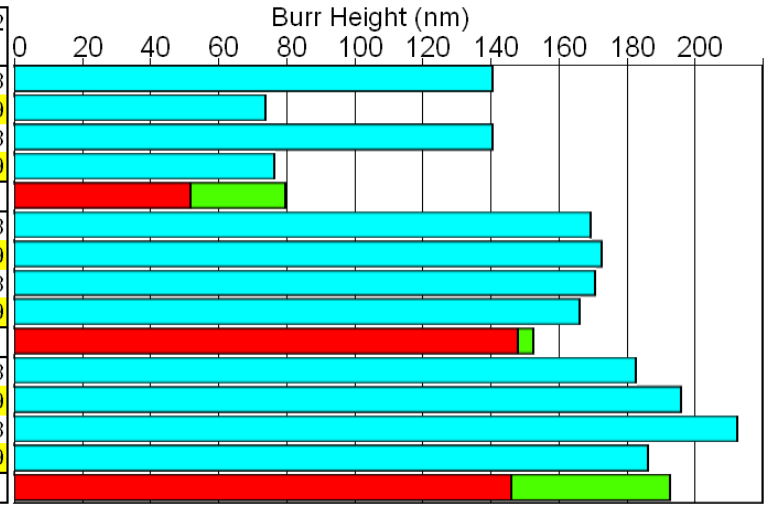


Figure 7.22: Simulated and experimental side burr heights

As shown in Fig. 7.23, during simulations where the depth of cut is 265 nm and $d_2$ is 0.9, the top of the side burr would peal away leaving behind a smaller side burr that more closely matched the experimental burr height. For all other conditions, burr pealing did not occur. Since the amount of material pealing away is so small, this might represent an actual occurrence, which would not be observable.

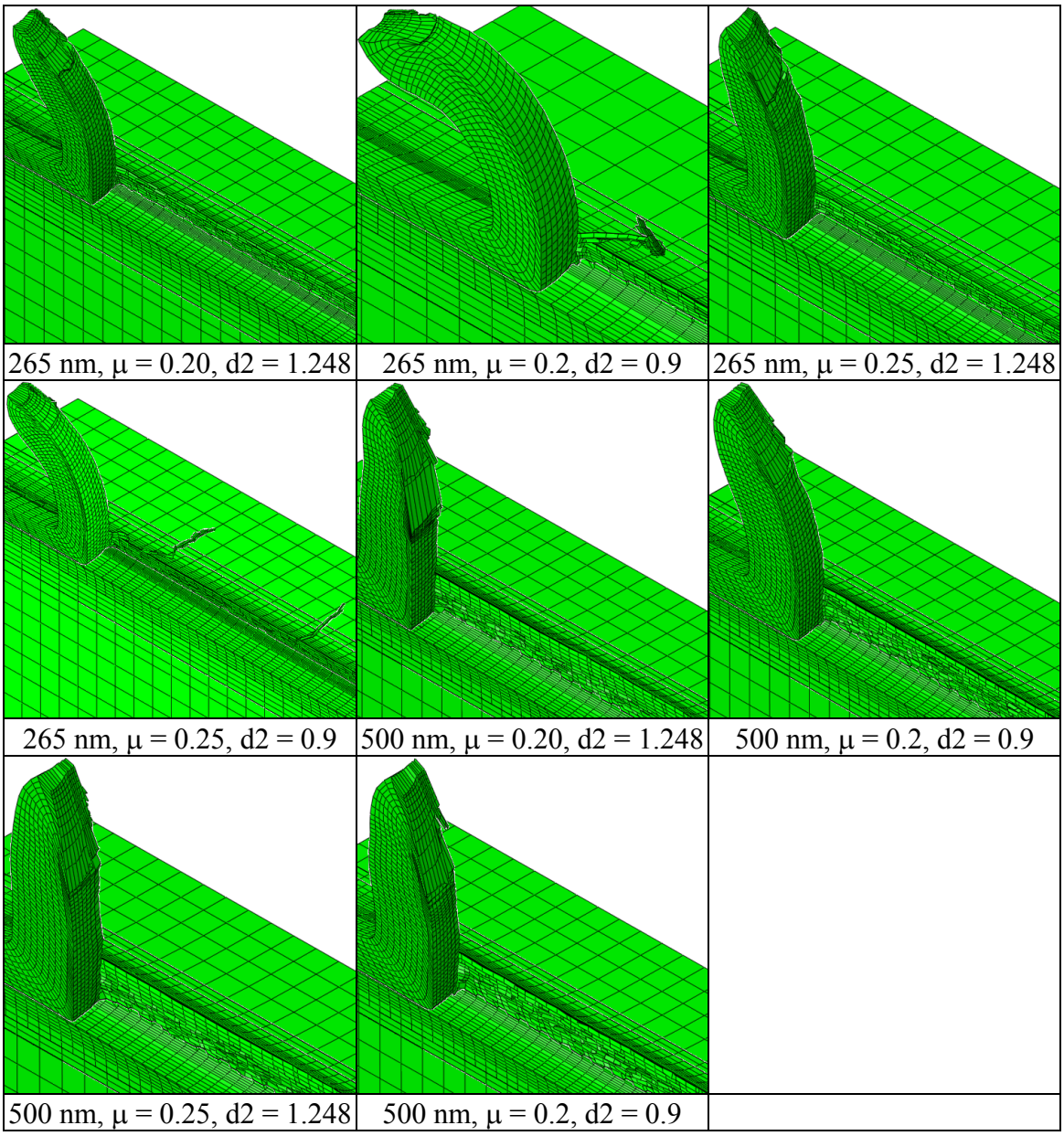


Figure 7.23: Burr pealing seen in some simulations

Figure 7.24 shows plots of the groove cross-sections from the 265 nm depth of cut simulations with the experimental cross-section superimposed on each plot. Figure 7.25 and Fig. 7.26 show a similar set of plots from simulations with a 500 nm and 720 nm depth of cut, respectively. In each figure, the shading indicates the predicted plastic equivalent strain (PEEQ). Note the experimental cross-sections do not line up as well on

the right sides of the grooves due to distortion introduce by AFM measurement. Also, the experimental and predicted groove bottoms are at different depths due to the deletion of the layer of sacrificial elements below the chip during simulations and due to slight difference in the experimental and simulated depths of cut.

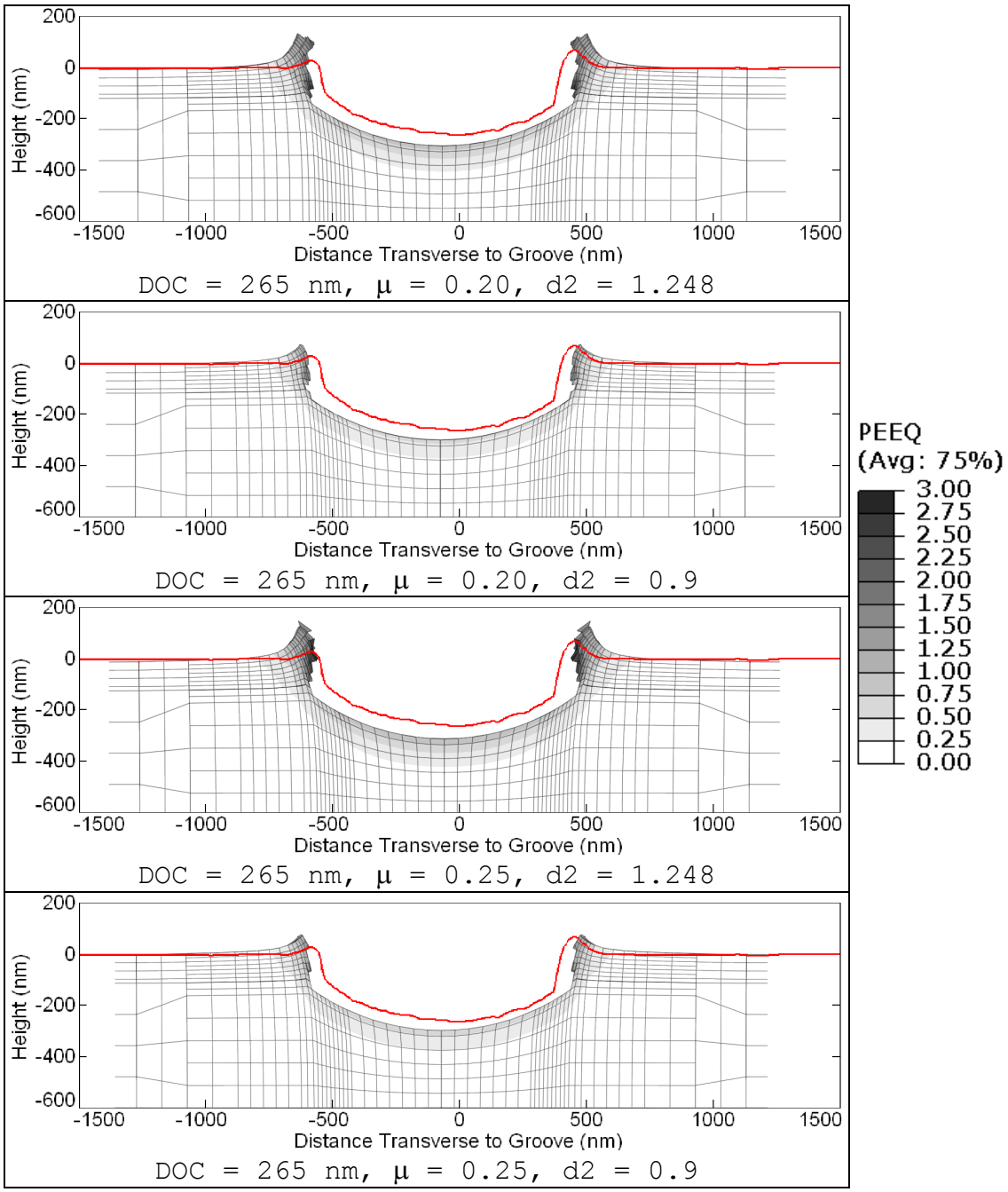


Figure 7.24: Experimental and simulated cross-sections of a shallow cut

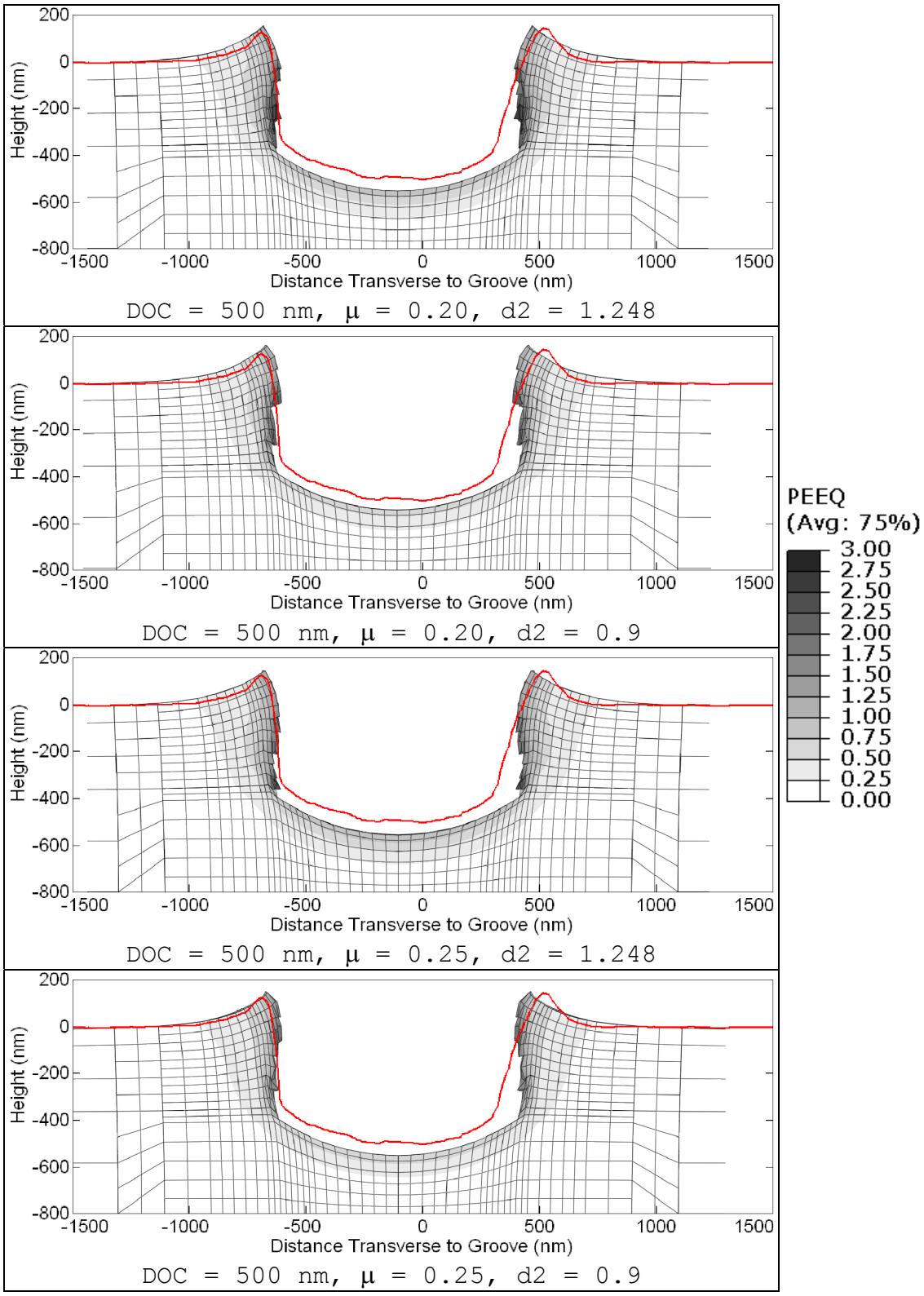


Figure 7.25: Experimental and simulated cross-sections of a moderately deep cut

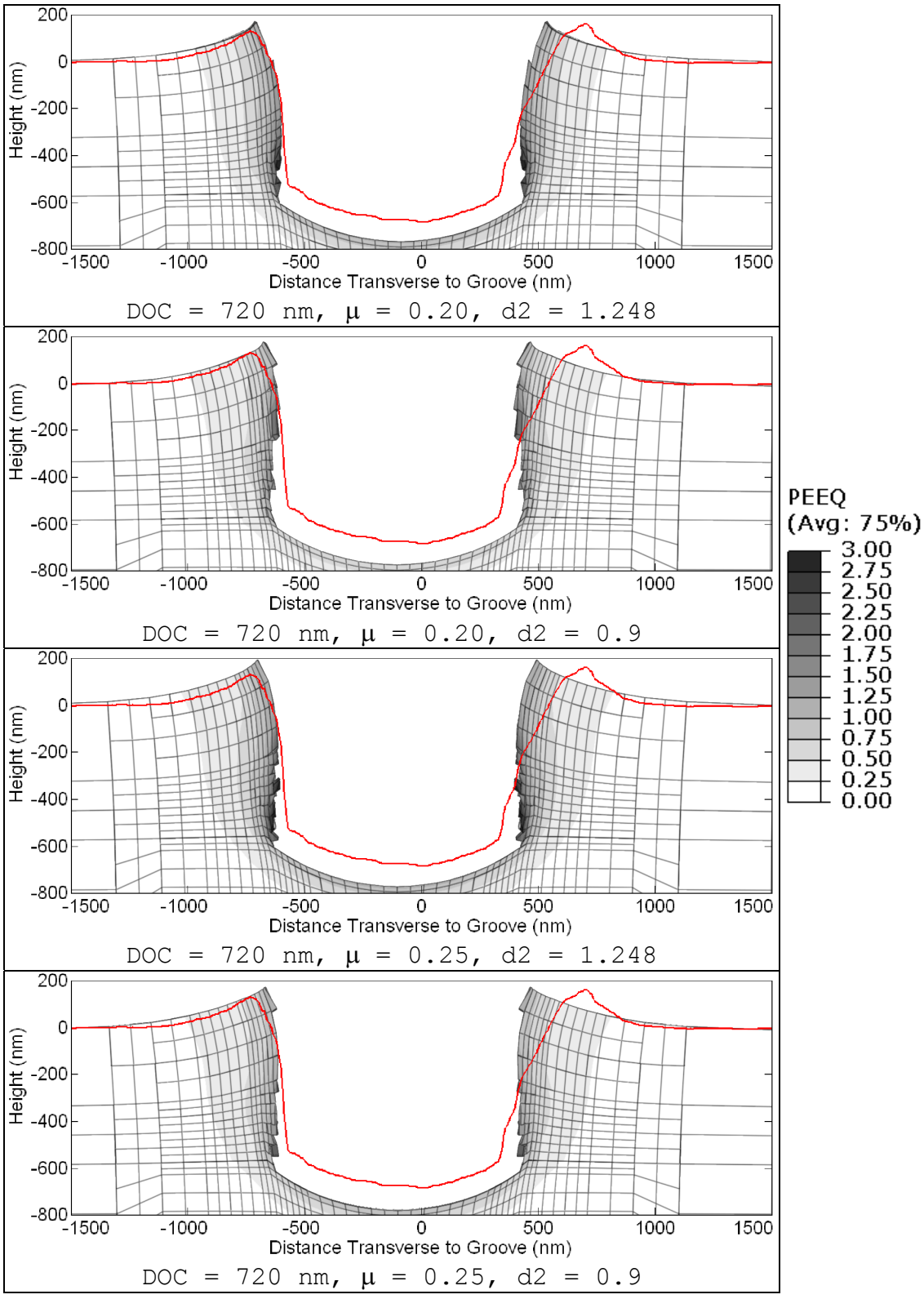


Figure 7.26: Experimental and simulated cross-sections of a deep cut

In order to see the curl of the simulated chips, the positions of the nodes along the symmetry plane that contact and then separate from the rake face were extracted from each simulation and plotted. Figures 7.27, 7.28, and 7.29 show plots of the chip shapes in the 265 nm, 500 nm, and 720 nm depth of cut simulations, respectively. In each plot the darkened line segment towards the bottom of the plot represents nodes that experienced contact with the rake face.

Based on the plots, the simulated chip curl radius was calculated for each simulation where there was enough data points to successfully fit a circle to the chip profile after separation from the rake face. The radii are plotted in Fig. 7.30 along with the experimentally determined chip curl radii. Note that the bars for the 503 nm and 687 nm depth of cut cases encompass the right side of the plot because it could only be determined that that actual radius was greater than 2.76 based experimental data. Lastly, Table 7.11 contains all the simulation results for easy comparision reference.

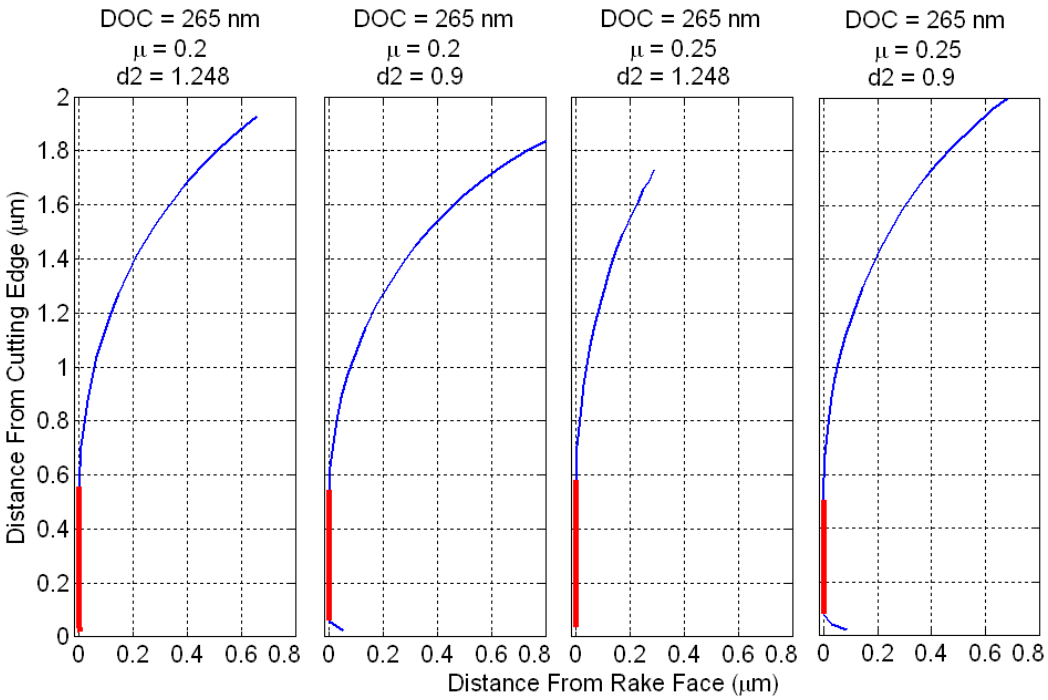


Figure 7.27: Simulated chip curl during simulations with a 265 nm depth of cut

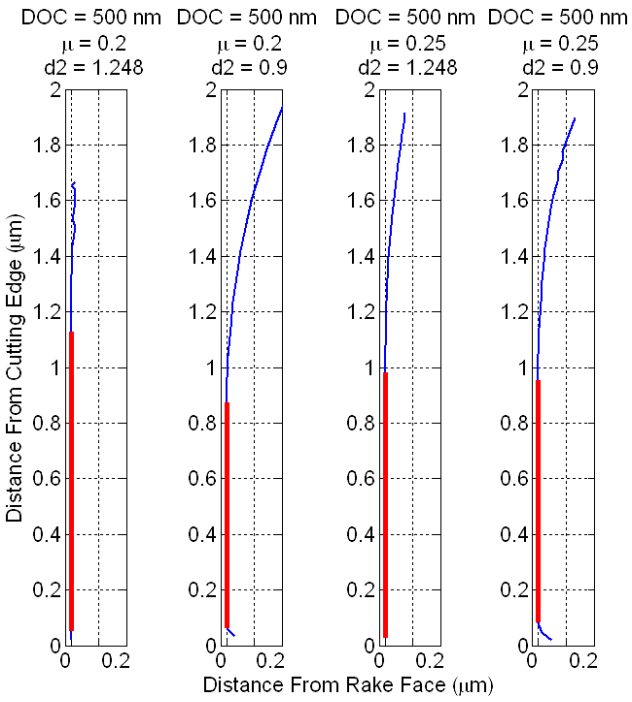


Figure 7.28: Simulated chip curl during simulations with a 500 nm depth of cut

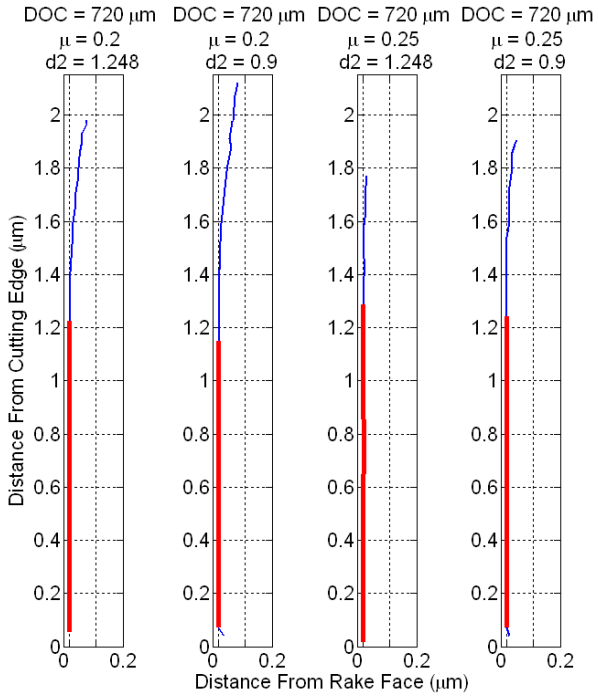


Figure 7.29: Simulated chip curl during simulations with a 720 nm depth of cut

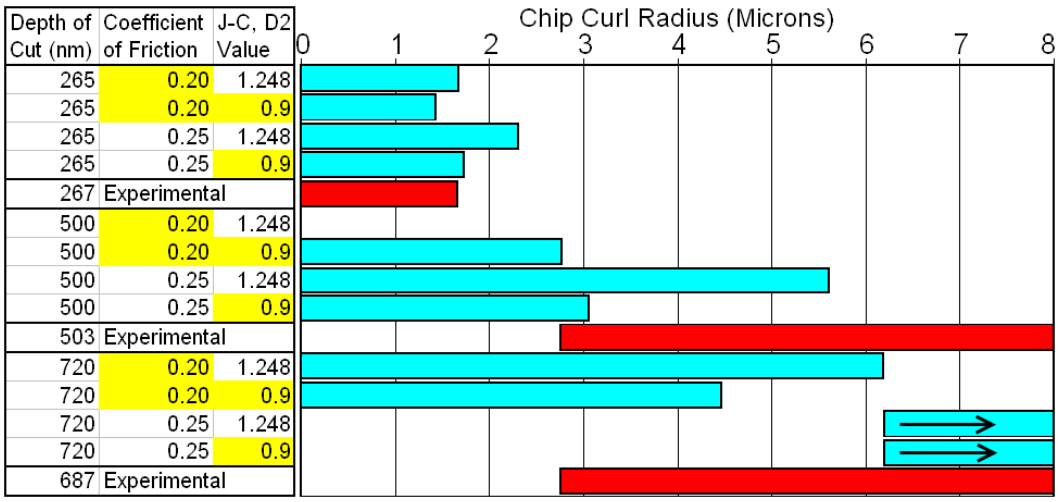


Figure 7.30: Simulated and experimental chip curl radii

Table 7.11: Tabulated results from simulations and experiments

| Depth of Cut (nm) | Coefficient of Friction | J-C, D2 Value | Center Chip Thick (μm) | Contact Length (μm) | Burr Ht (nm) | Curl Radius (μm) |
|---|---|---|---|---|---|---|
| 265 | 0.20 | 1.248 | 0.624 | 0.577 | 141 | 1.688 |
| 265 | 0.20 | 0.9 | 0.588 | 0.568 | 74 | 1.442 |
| 265 | 0.25 | 1.248 | 0.668 | 0.629 | 141 | 2.316 |
| 265 | 0.25 | 0.9 | 0.626 | 0.613 | 76 | 1.742 |
| 267 | Experimental | | 0.475 | | 52, 80 | 1.673 |
| 500 | 0.20 | 1.248 | 1.026 | 1.176 | 170 | |
| 500 | 0.20 | 0.9 | 1.013 | 0.919 | 173 | 2.778 |
| 500 | 0.25 | 1.248 | 1.049 | 1.046 | 171 | 5.619 |
| 500 | 0.25 | 0.9 | 1.090 | 1.005 | 166 | 3.071 |
| 503 | Experimental | | 0.901 | | 148, 153 | > 2.76 |
| 720 | 0.20 | 1.248 | 1.285 | 1.328 | 183 | 6.196 |
| 720 | 0.20 | 0.9 | 1.315 | 1.263 | 196 | 4.4816 |
| 720 | 0.25 | 1.248 | 1.356 | 1.395 | 212 | Large |
| 720 | 0.25 | 0.9 | 1.361 | 1.333 | 186 | Large |
| 687 | Experimental | | 1.102 | | 146, 193 | > 2.76 |

The simulations results were examined to determine the best values of $\mu = 0.2$ and $d_2$. Examination of Fig. 7.21 shows that predicted chip thickness increases with increased depth of cut depth of cut, which is consistent with experimental results. Furthermore, the amount of increase due to a change in depth of cut is almost the same as the experimentally observed increase. However, the predicted thickness was larger then the

experimentally observed thickness in all cases. It is also shown that the predicted thickness always increased with an increased coefficient of friction and varied inconsistently when $d_2$ was changed.

Burr height predictions also captured the trend of increased burr height with increased depth of cut, as shown in Fig. 7.22. However, the magnitude of the burr height is overpredicted by nearly 100% at a low depth of cut unless $d_2$ is set to 0.9, which causes the prediction to be correct to within the level of experimental uncertainly. Setting, $d_2$ to 0.9 at larger depths of cut also improved prediction accuracy. Changing the coefficient of friction, however, had inconsistent results. The importance of $d_2$ is expected because burr formation is strongly affected by separation of material at the side of the chip, which is in turn affected by the material failure criteria. Furthermore, the $d_2$ value from the literature of 1.248 was expected to be too high because the material the results were reported for had been work hardened significantly.

Examination of the cross-sections in Fig. 7.24 – Fig. 7.26 showed that overall groove shape was predicted fairly well in most cases. Once again, setting of $d_2$ equal to 0.9 resulted in much better predictions in the 265 nm depth of cut case. In the 500 nm depth of cut case, changing $d_2$ had little effect, but there was some benefit to increasing the coefficient of friction. In the 720 nm depth of cut case a lower coefficient of friction gave better prediction, but the change was not very significant.

As shown in Fig. 7.30, the chip curl radius was predicted to increase with increased depth of cut, which is consistent with experimental results. The radius decreases when $d_2$ is decreased and increases when the coefficient of friction increases. In the 265 nm depth of cut case, goods predictions were achieved when $\mu = 0.2$ and d2 =

1.248 and also when $\mu = 0.25$ and d2 = 0.9. At 500 nm and 720 nm depths of cut, all predicted curl radii are in the potential experimental range

In light of the model's intended use, correct chip flow and burr shape prediction are considered important. Hence, use of parameters that result in a slightly less accurate chip thickness prediction in order to get a significantly more accurate burr height and chip curl prediction is deemed acceptable. The best results were deemed to be achieved when $\mu = 0.25$ and $d_2 = 0.9$. This is primarily due to the large decrease in burr height and chip curl radius prediction accuracy at lower depths of cut when other values were used.

# 7.8 Finite Element Model Validation

## 7.8.1 Model Accuracy

Experimentally measurable outputs from simulations using the values for $\tau_{crit}$, $\mu$, and $d_2$ found in the previous sections are tabulated in Table 7.12. These models outputs are the chip thickness at the symmetry plane, the predicted side burr height, and the predicted chip curl radius. The table also lists the experimentally measured values and the error in the predictions given by the model.

Table 7.12: Model prediction accuracy

| Exp. Depth of Cut (nm) | Sim. Depth of Cut (nm) | Characteristic | Exp. Value | Sim. Value | Error |
|---|---|---|---|---|---|
| 267 | 265 | Chip Thickness (μm) | 0.475 | 0.626 | 31.8% |
| 503 | 500 | | 0.901 | 1.090 | 21.0% |
| 687 | 720 | | 1.102 | 1.361 | 23.5% |
| 267 | 265 | Side Burr Height (nm) | 52, 80 | 76 | 0% |
| 503 | 500 | | 148, 153 | 166 | 8.5% |
| 687 | 720 | | 146, 193 | 186 | 0% |
| 267 | 265 | Chip Curl Radius (μm) | 1.673 | 1.742 | 4.1% |
| 503 | 500 | | > 2.76 | 3.071 | |
| 687 | 720 | | > 2.76 | > 3.071 | |

It can be seen in Table 7.12 that chip thickness prediction errors are within 21.0 – 31.8 %. Burr height prediction errors are within 0.0 – 8.5 %. Chip curl prediction error is only 4.1% in the case when simulation results and experimental results could be directly compared and appears acceptable in all other cases. Therefore, the model is providing acceptably accurate results, and the model material properties given earlier in the chapter and the inputs found in the previous section will be used in all further simulations described in this work.

## 7.8.2 Validity of 3D Modeling Requirement

Two dimensional finite element models are commonly used to simulate orthogonal metal cutting because of the accompanying reduction of required computer resources. However, it was argued earlier in this chapter that a 3D model would be required to capture the pertinent mechanics of the micro-groove cutting process. Model outputs are evaluated here to confirm these arguments.

In order to approximate the stress / strain state of a 3D cutting process using a 2D model, the plain stain assumption is typically made. Using this assumption, out-of-plane components of the strain tensor are assumed to be zero, i.e., with a coordinate system defined as in Fig. 7.7, the $\varepsilon_{33}$ strain tensor component is assumed zero. Alternatively, the plane stress assumption can be made when the out-of-plane components of the stress tensor are zero, i.e., with a coordinate system defined as in Fig. 7.7, the $\sigma_{33}$ stress tensor component is zero. Hence, if the simulation results show that both this components are not very small then 2D approximations are not valid and will give erroneous results.

A top-down view of a workpiece surface during a simulated cut is shown in Fig. 7.31, where the depth of cut is 500 nm and the rake angle is 0°. Hence, the camera is

looking in the negative y-direction such that z-axis appears vertical in the figure. Tensile out-of-cutting plane components of the plastic strain and stress tensors are indicated in the figure via grayscale shading. It is clear that both these components are far too large to be approximated as zero. In fact, out-of-plane tensile plastic strain is as high as 0.45 and out-of-plane compressive stress is as high as 130 MPa. Hence, any 2D approximation of the micro-groove cutting process is completely incorrect, and the 3D model is required. This validates the arguments made earlier in this chapter.

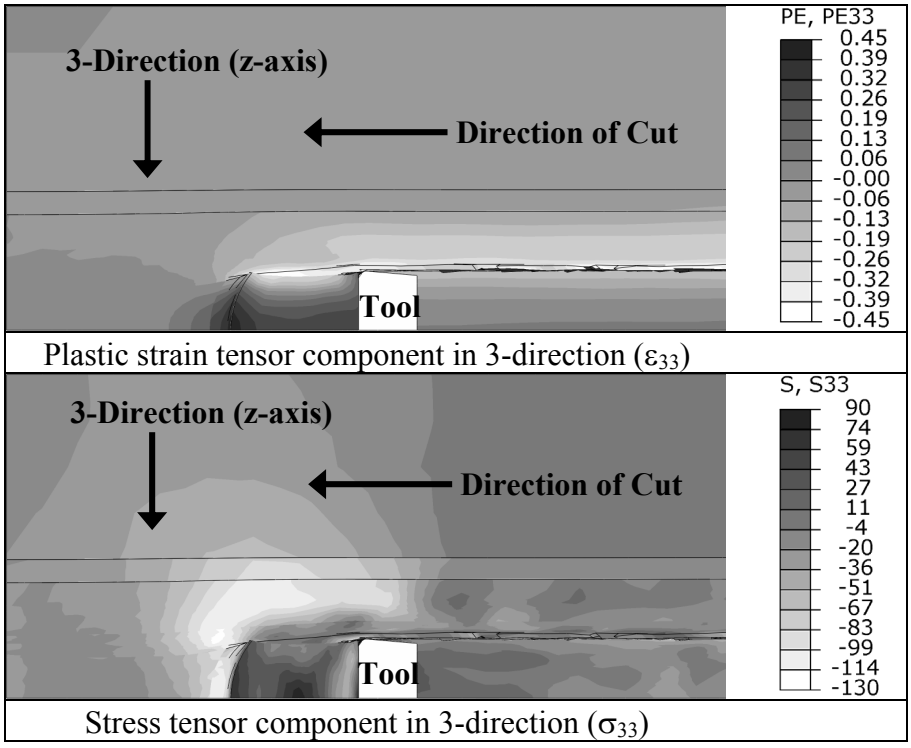


Figure 7.31: Out of cutting plane tensile plastic strain / stress ($\varepsilon_{33}$ / $\sigma_{33}$) for a 500 nm deep cut using 0° rake angle tool

## 7.9 Chapter Summary

In this chapter, the development of a finite element model of micro-groove cutting was described. This model addresses the need to handle the 3D stress / strain fields

present during micro-groove cutting, to handle chip separation at the side of a chip, to account for rounded tool geometry, and to predict side burr formation during steady state cutting. The model is also capable of simulating exit burr formation when a tool exits from a workpiece.

Model inputs were extracted from the literature where possible. When literature values could not be found, the model was run using different inputs values and used to simulate cutting during three experiments from Chapter 6. The model inputs that resulted in the most accurate predictions of the experimental results were selected for further use.

It was shown that when using the selected model parameters, good agreement is achieved between the model and experimental results. Specifically, chip thickness prediction errors are within 21.0 – 31.8 %, burr height prediction errors are within 0.0 – 8.5 %, and chip curl prediction error is only 4.1% in cases where simulation and experiment results could be compared. Additionally, it was shown that out-of-cutting plane stress and strain components are large enough that the use of a 3D model is justified since 2D approximations cannot capture the stress/strain fields present.

In the next chapter, the model is used to examine process mechanics during steady state cutting at different depths of cut and with different rake angles. Exit burr formation, when a tool exits the workpiece is also examined. Those results will in turn be used to gain a better understanding of the micro-groove cutting process, which can be used to implement process improvements.

# Chapter 8

# Model-Based Micro-Groove Cutting Process Study

## 8.1 Design of Simulation Experiments

In the previous chapter, a 3D finite element model of the cutting process was developed that addresses the 3D stress / strain fields present during micro-groove cutting, addresses chip separation at the side of a chip, accounts for rounded tool geometry, predicts side burr formation, and can predict exit burr formation. This model also was validated using experimental results. In this chapter, the model is used to simulate micro-groove cutting at three different depths of cut and with two different rake angles. Selected results from these simulations are examined in detail with the goal being to gain a better understanding of the micro-groove cutting process, which can be used to implement process improvements.

The geometry of the model is shown in Fig. 8.1. The 1, 2, and 3 directions of the stress / strain tensors correspond to the x, y, and z directions, respectably, as shown in the figure. The tool travels in the negative x-direction. The model makes use of half-symmetry and the symmetry plane lies parallel to the x-y plane. The materials that make up the top 3 μm and bottom 2 μm of the model are aluminum and single crystal silicon, respectively. The model is long enough in the cutting direction to ensure steady-state cutting is achieved, and exit burr formation can be examined by continuing to cut until the tool exits from the mesh. All stress values are reported in MPa.

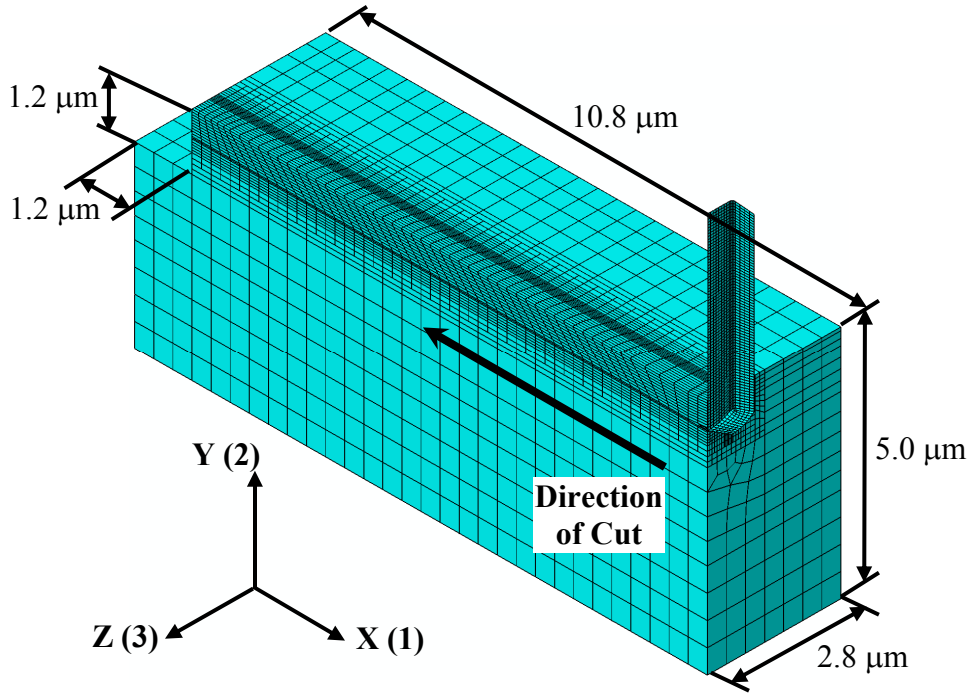


Figure 8.1: Overall model geometry

Simulations were conducted using all combinations of the depths of cut of 254 nm, 500 nm, and 720 nm as well as the rake angles of 0° and 10°. In each of these simulations the cutting speed was 300 mm/min and cutting was allowed to progress until steady-state chip formation occurred. Additionally, in the case of a 500 nm depth of cut and a 0° rake angle, exit burr formation was simulated.

Figure 8.2, Fig. 8.3, and Fig. 8.4 show the simulated geometries of the workpieces, mirrored about the symmetry plane, during steady-state cutting when the depth of cut is 264 nm, 500 nm, and 720 nm, respectively. In all cases, it can be seen that a chip separates from the workpiece, flows up the rake face, and separates from the rake face. Side burrs are formed on the side of each groove. Also, ahead of each chip, a rounded prow of material rise out of the workpiece.

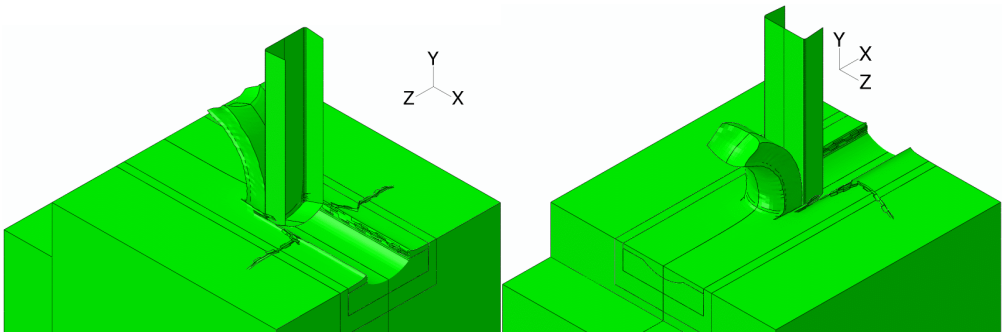


254 nm depth of cut, 300 mm/min, 0° rake angle

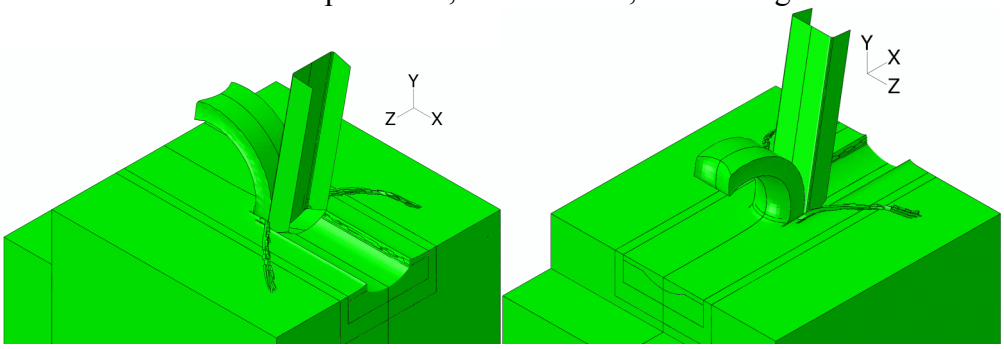


254 nm depth of cut, 300 mm/min, 10° rake angle

Figure 8.2: Predicated steady-state workpiece shapes when the depth of cut is 265 nm

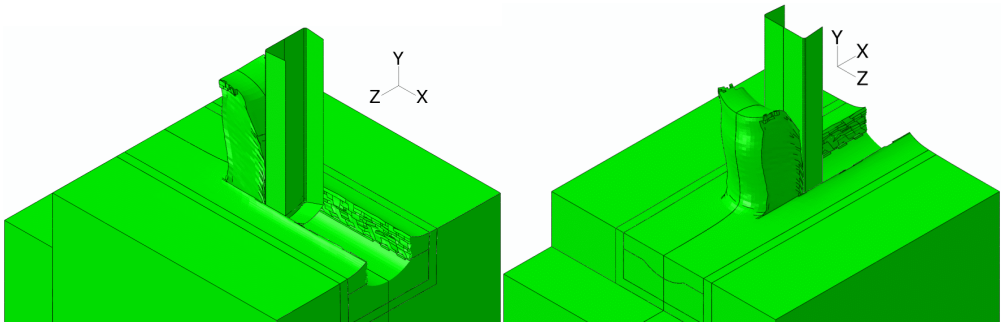


500 nm depth of cut, 300 mm/min, 0° rake angle

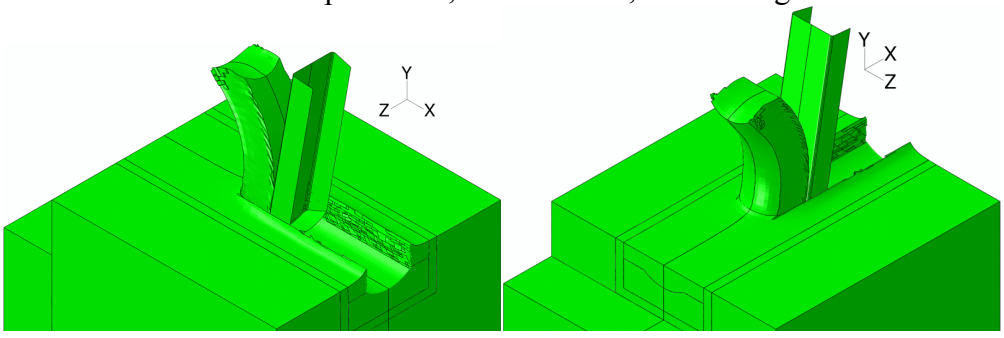


500 nm depth of cut, 300 mm/min, 10° rake angle

Figure 8.3: Predicated steady-state workpiece shapes when the depth of cut is 500 nm

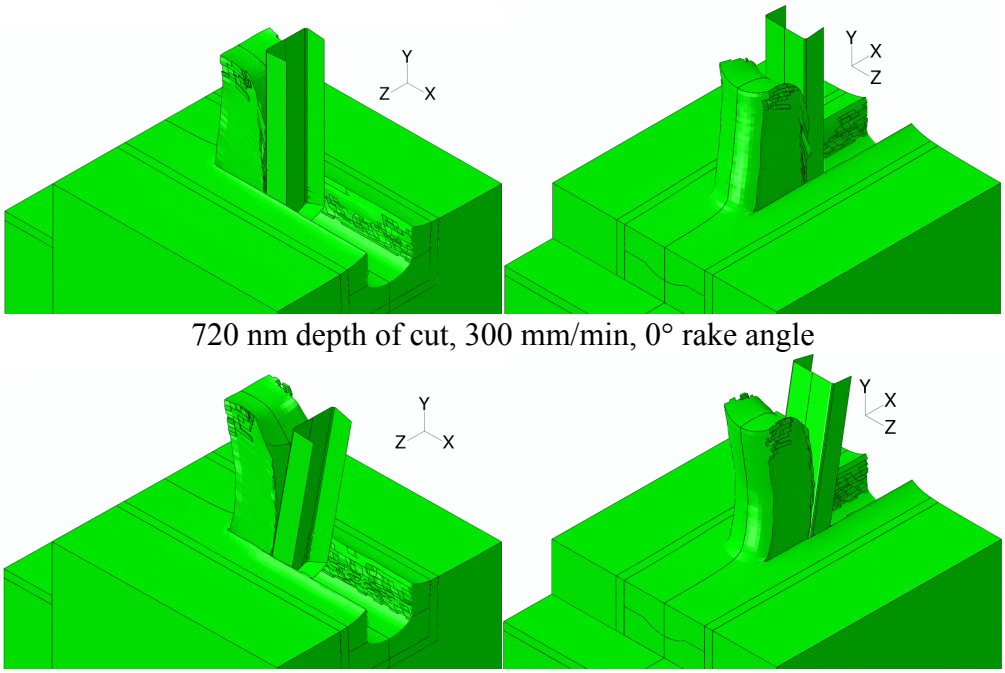


720 nm depth of cut, 300 mm/min, 0° rake angle

720 nm depth of cut, 300 mm/min, 10° rake angle

Figure 8.4: Predicated steady-state workpiece shapes when the depth of cut is 720 nm

In the next section, fundamental micro-groove cutting process characteristics including cutting forces, chip curl, chip thickness, and the stress / strain distributions present throughout the thickness of the chips are examined for each of the six simulated conditions. Then, in the following section, out-of-cutting plane effects that result in side burr formation are examined, and a sequence of events that occur during side burr formation is described. Afterwards, in another section, exit burr formation is examined, and a sequence of events leading to exit burr formation is described. Lastly, a discussion of the potential for the delamination of a soft thin film on a substrate when micro-grooves are cut into the film is presented. A summary of the results from the chapter follows.

## 8.2 Fundamentals of the Micro-Groove Cutting Process

In micro-groove cutting experiments, the load applied to the tool normal to the workpiece surface is controlled and balances with the process dependent thrust force in

order to set the depth of cut. However, the force in the cutting direction has not been measured experimentally due to its extremely small magnitude. Conversely, finite element simulations tend to not do a good job of predicting thrust forces, but can accurately predict force in the cutting direction. Hence, cutting force predictions in the direction of cut, which are shown in Fig. 8.5, are discussed here. Note that the plot shows the output of the half symmetry model, which gives half the actual cutting forces.

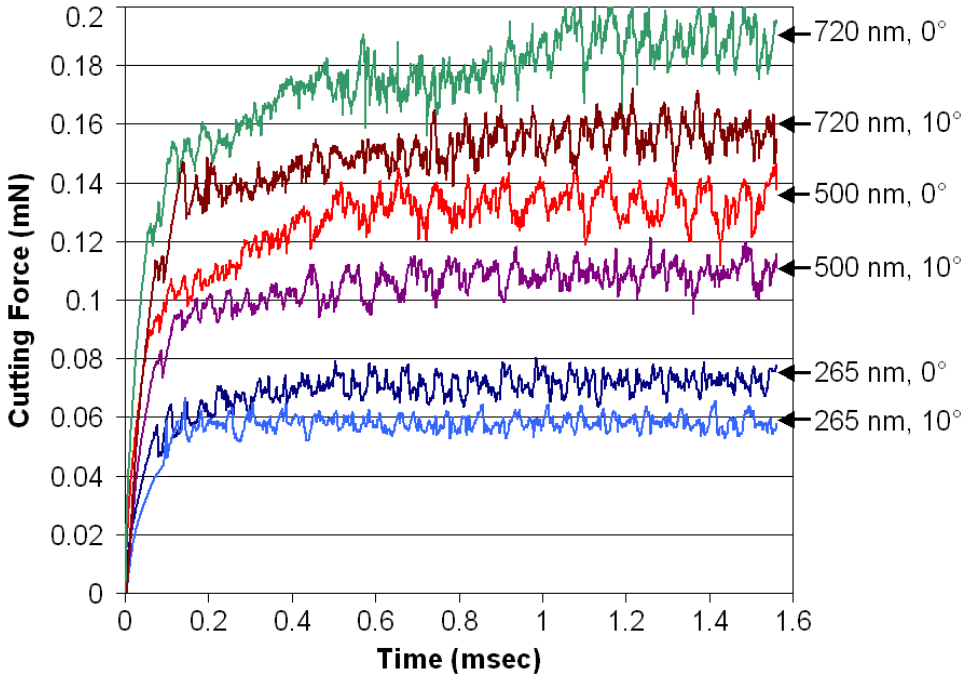


Figure 8.5: Predicted cutting forces in direction of cut

As can be seen in Fig. 8.5, the cutting force initially ramps up at the start of a cut when the tool enters the workpiece and then continues to rise until reaching a constant value indicative of steady-state cutting. Oscillations in cutting force are due to the failure and deletion of discrete elements as a part of chip separation. This is an artifact of the finite element model and would not be expected to occur during actual cutting.

The simulations indicate that the steady-state cutting force magnitudes increase linearly with an increase in depth of cut and decrease with increased rake angle, which is

consist with conventional machining. Also, the amount of decrease in cutting forces that occurs when the rake angle is increased is greater when the depth of cut is large. Note that cutting forces are small compared to the thrust forces. This can be seen by recalling that in experiments using similar cutting conditions as in the simulations, and a 0° rake angle, the thrust forces were 0.3 mN, 0.7 mN, and 1.1 mN for depths of cut of 267 nm, 503 nm, and 687 nm, respectively. Due to a lack of experimental data this result cannot be directly verified. However, the large difference between cutting forces and thrust forces is noteworthy because it is generally not seen in conventional micro-scale cutting. From a tool design perspective, this indicates that the ability of a tool to withstand high thrust forces might be more critical than its ability to withstand high forces in the cutting direction.

Simulation results were also evaluated at the symmetry plane in order to examine chip flow, the primary shear zone, and the secondary shear zone. Figure 8.6 shows the deformed meshes during steady-state chip formation. Note that the tops of the chips are truncated so that portions of the chips formed prior to the establishment of steady-state conditions are not shown. In each case, the chip smoothly separates from the workpiece along the plane of elements under the chip that are permitted to fail. Also, although the elements that make up the chips are deformed by shear, due to the initial slant of the mesh, this deformation is kept to an acceptable level. Comparison of the meshes shows that chip thickness, tool-chip contact length, and chip curl radius all vary with cutting conditions, which is expected. The numerical values are listed in Table 8.1.

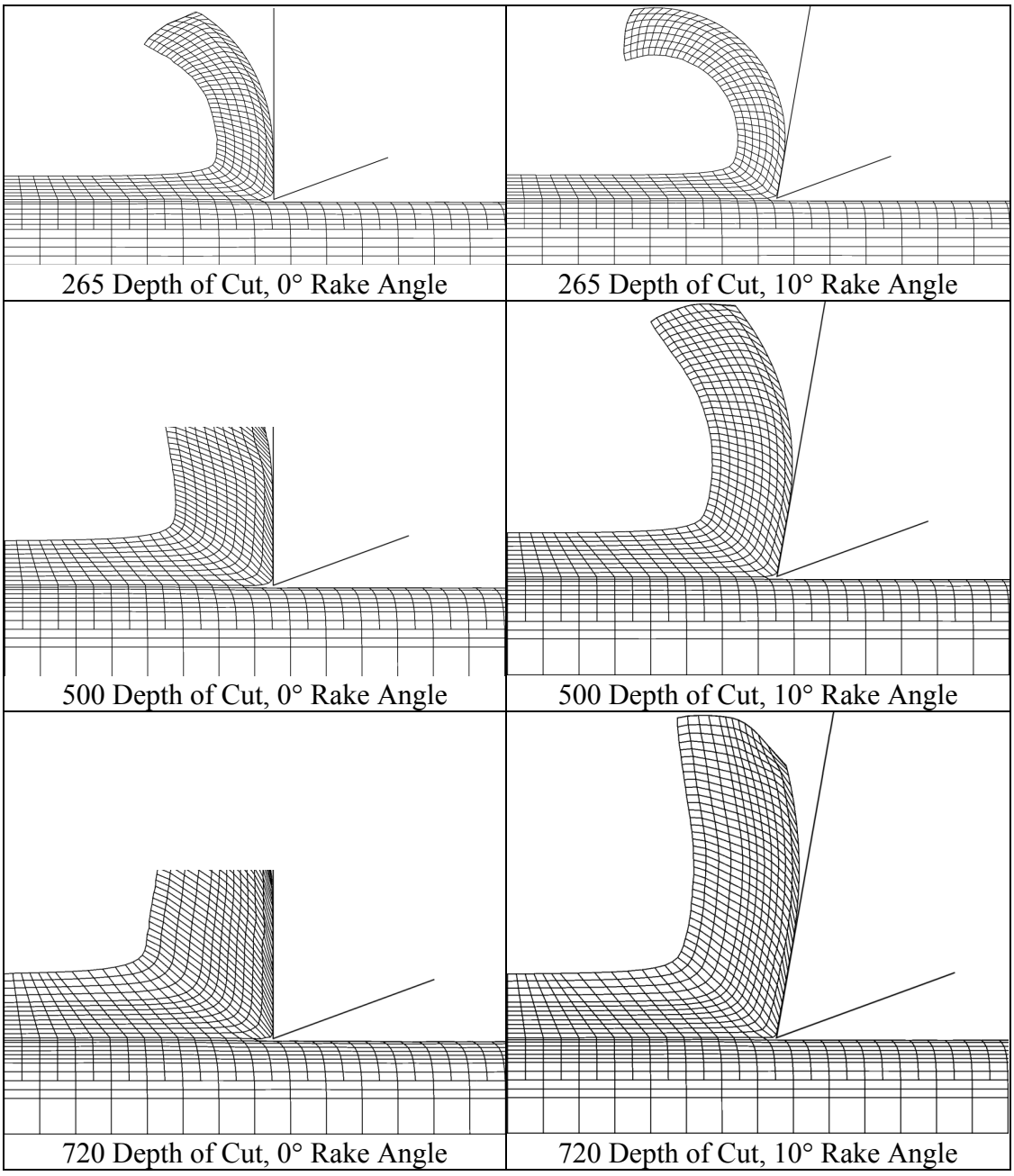


Figure 8.6: Deformed mesh at the symmetry plane during steady-state cutting

Table 8.1: Predicted steady-state chip shapes

| Rake Angle (deg) | 0 | 0 | 0 | 10 | 10 | 10 |
|---|---|---|---|---|---|---|
| Depth of Cut (nm) | 265 | 500 | 720 | 265 | 500 | 720 |
| Chip Thickness (μm) | 0.626 | 1.090 | 1.361 | 0.526 | 0.898 | 1.181 |
| Contact Length (μm) | 0.613 | 1.005 | 1.333 | 0.510 | 0.810 | 1.137 |
| Curl Radius (μm) | 1.742 | 3.071 | Large | 1.452 | 2.798 | 4.844 |

As indicated in Table 8.1, chip thickness, tool-chip contact length, and the chip curl radius all decrease when the rake angle is increased from 0° to 10°. By contrast, chip thickness, tool-chip contact length, and the chip curl radius all increase when the depth of cut in increased. Hence, in order to set these chip flow characteristics at a given depth of cut it may be necessary to adjust the rake angle by changing the tool orientation. Setting of chip flow characteristics in this manner might be desirable because a chip breaker geometry will only be effective if chip characteristic are within a range dependent on the chip breaker geometry, and at the micro-scale it is not practical to adjust the configuration of a chip breaker to accommodate changes in chip characteristics. Also, if micro-groove cutting is being used to create micro-wires, i.e., the chip is the desired product, control of the chip thickness and chip curl would be desirable.

The stress and strain states of the chips and underlining workpieces are also examined at the symmetry plane. Figure 8.7 shows the Von Mises stresses in each simulated case. Similarly, Fig. 8.8 shows the plastic equivalent strains at the symmetry plane. It can be seen that the most intense stresses in the symmetry plane occur at the cutting edge. Other areas of lower, but still relatively intense, stresses are the primary and second shear zones, which are clearly delineated by the stresses present. Note that the same Von Mises stress magnitudes tends to be present through each shear zone. Also, chip material that has moved past the shear zones is much less stressed.

The plastic equivalent strain is highest in the secondary shear zone in all cases. The amount of plastic strain, and hence the amount of work hardening increases when the depth of cut is increased. Also, increasing the rake angle causes the majority of the plastic strain to become concentrated in the side the chip that passes through the

secondary shear zone. By contrast, plastic strain is more evenly distributed throughout the chip when the rake angle is 0°. This also changes the distribution of work hardening in the chip, which must be taken into account if a chip breaker is to be designed. Since uniform strength through the thickness of the chip cannot be assumed.

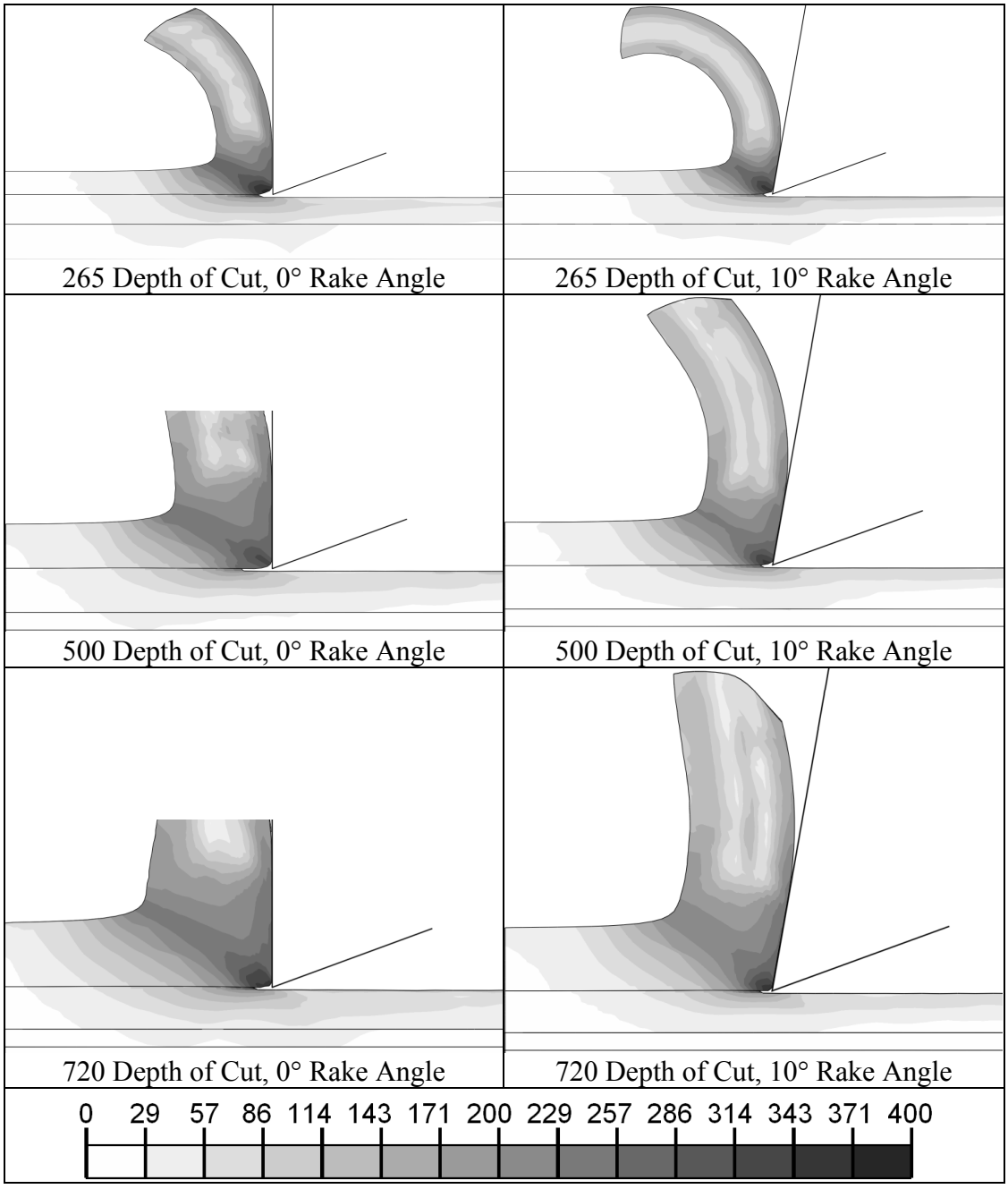


Figure 8.7: Predicted Von Mises stresses at the symmetry plane

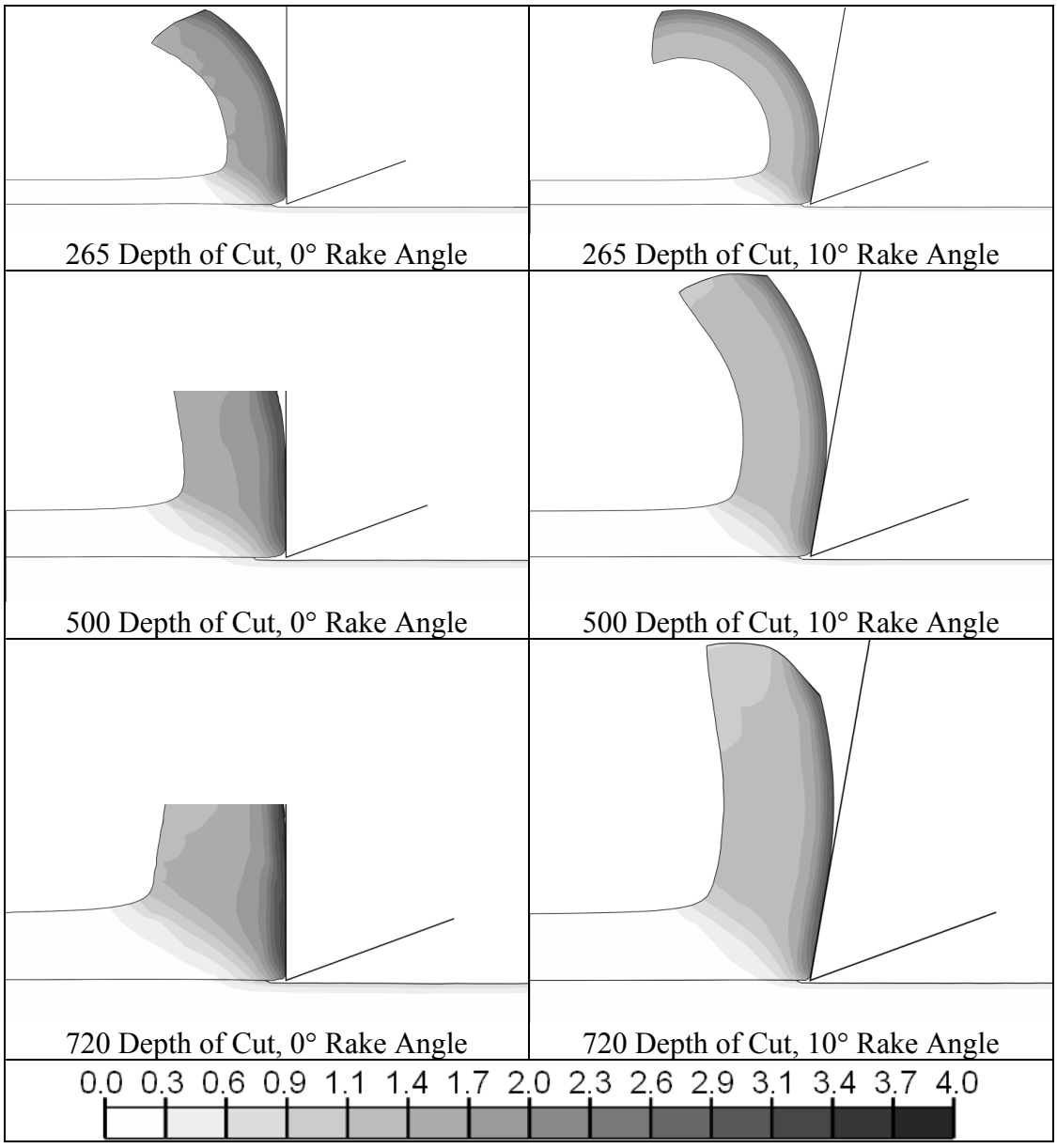


Figure 8.8: Predicted plastic equivalent strains at the symmetry plane

# 8.3 Out-of-Cutting Plane Causes of Burr Formation

## 8.3.1 Out-of-Cutting Plane Material Flow

The action at the symmetry plane only partly describes chip formation because the micro-groove cutting process is inherently 3D, and hence out-of-cutting plane deformation must be accounted for. Such deformation can be seen in Fig. 8.9, which

provides a top down view of the workpiece during steady-state cutting at a depth of cut of 500 nm. In the figure, the workpiece is moving from left to right and the tool is stationary. It can be seen that material ahead of the tool is compressed and either becomes part of the chip or is forced to flow around the tool. This is indicated by the arrows in the figure. Such material flow strongly affects side burr formation.

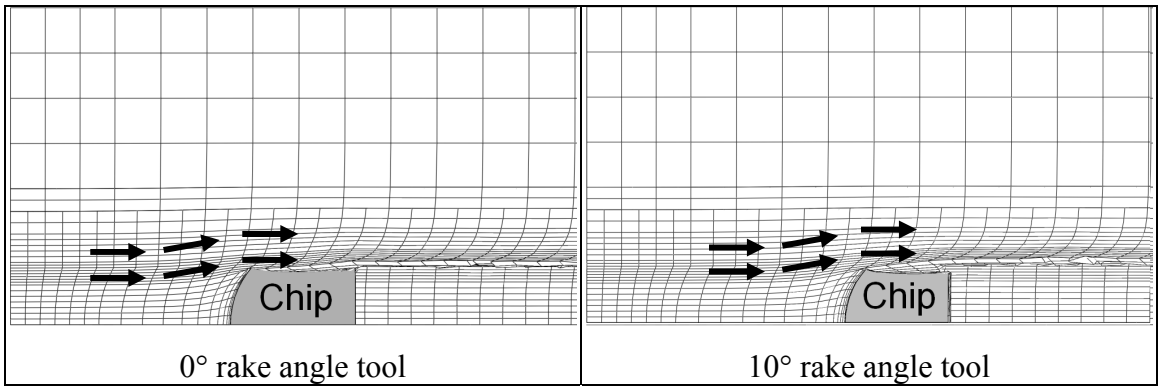


Figure 8.9: Top-down view of deformed mesh from simulating a 500 nm deep cut

## 8.3.2 Out-of-Cutting Plane Stress and Strains

To understand the state of the workpiece surface cutting it is necessary to not only consider stresses and strains on the surface of the workpiece, but to also consider subsurface stress and strains. This is accomplished by evaluating the stresses and strains at several elevations in the y-direction relative to the top surface of the workpiece, where the coordinate system is as defined in Fig. 8.1.

Figure 8.10 shows the Von Misses stresses in a workpiece at four different elevations relative to the workpiece surface when the depth of cut is 500 nm and the rake angle is 0°. In the first image, the camera is looking down on the workpiece from a height of 0.45 μm above its surface. Hence, the stresses on the workpiece surface and on the newly formed groove bottom are shown. In the other three images, slices of the

workpiece are shown at depths of 0.2 μm, 0.4 μm, and 0.6 μm below the workpiece surface, which corresponds to 40%, 80%, and 120% of the depth of cut, respectively. Similarly, Fig. 8.11 shows the corresponding plastic equivalent strains.

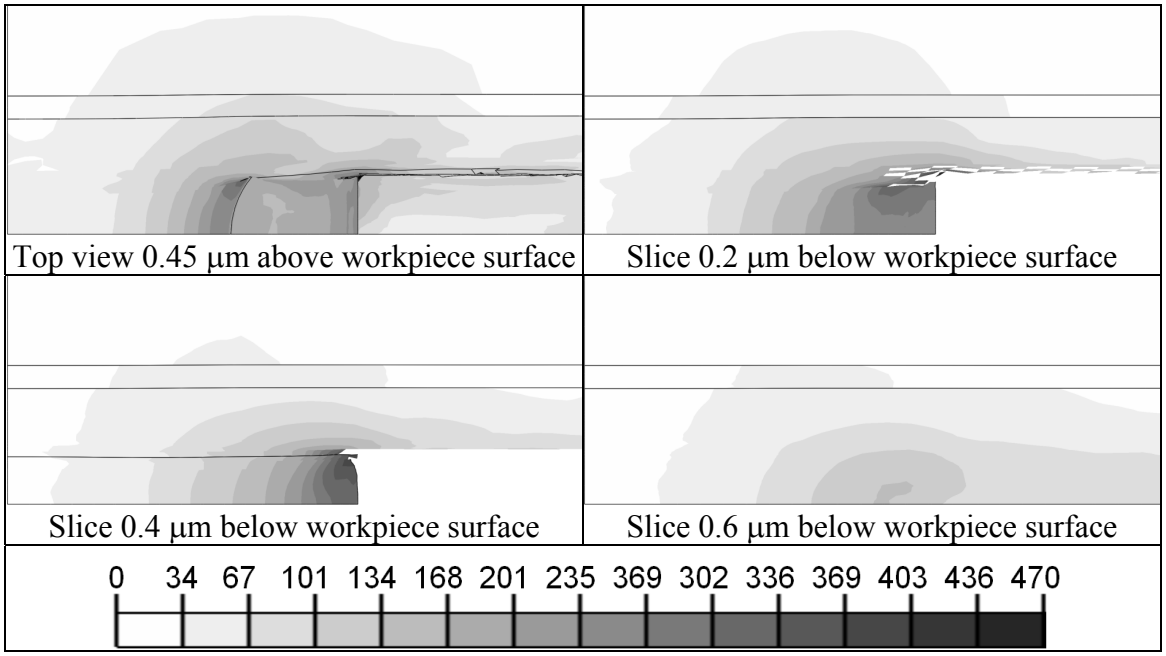


Figure 8.10: Mises stress slices: 0° rake angle and 500 nm depth of cut

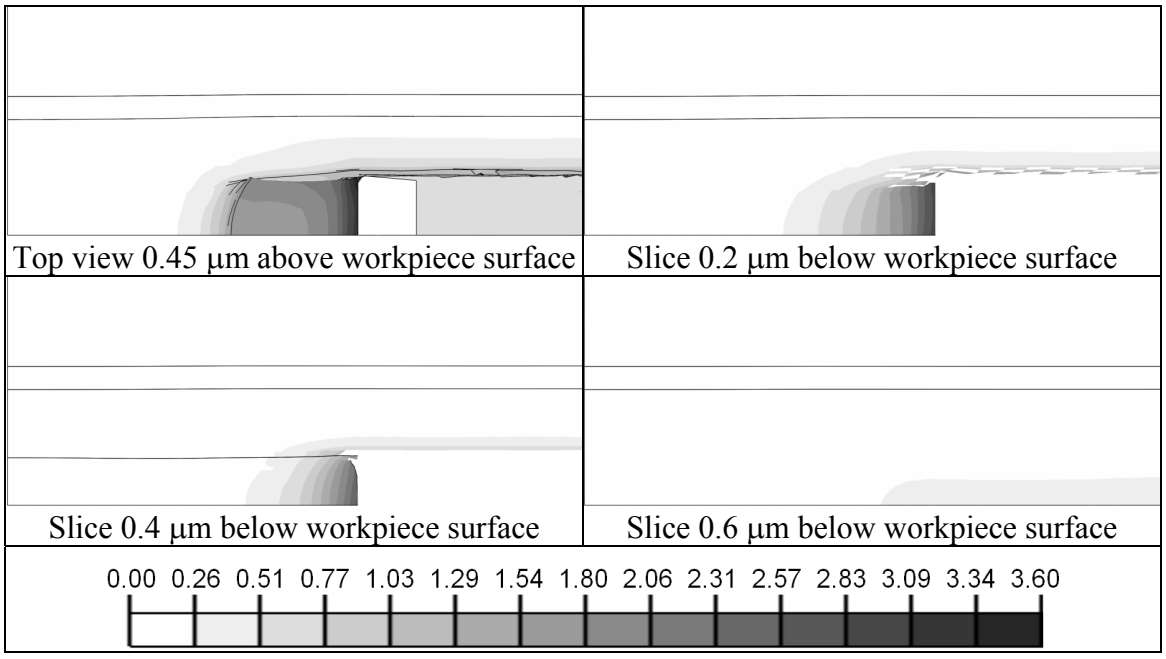


Figure 8.11: Plastic equivalent strain slices: 0° rake angle and 500 nm depth of cut

The case where a 500 nm deep groove is cut using a 10° rake angle is also considered. Figure 8.12 and Fig. 8.13 show the Von Misses stresses and plastic equivalent strains, respectively, at the same four locations as in the previous two figures.

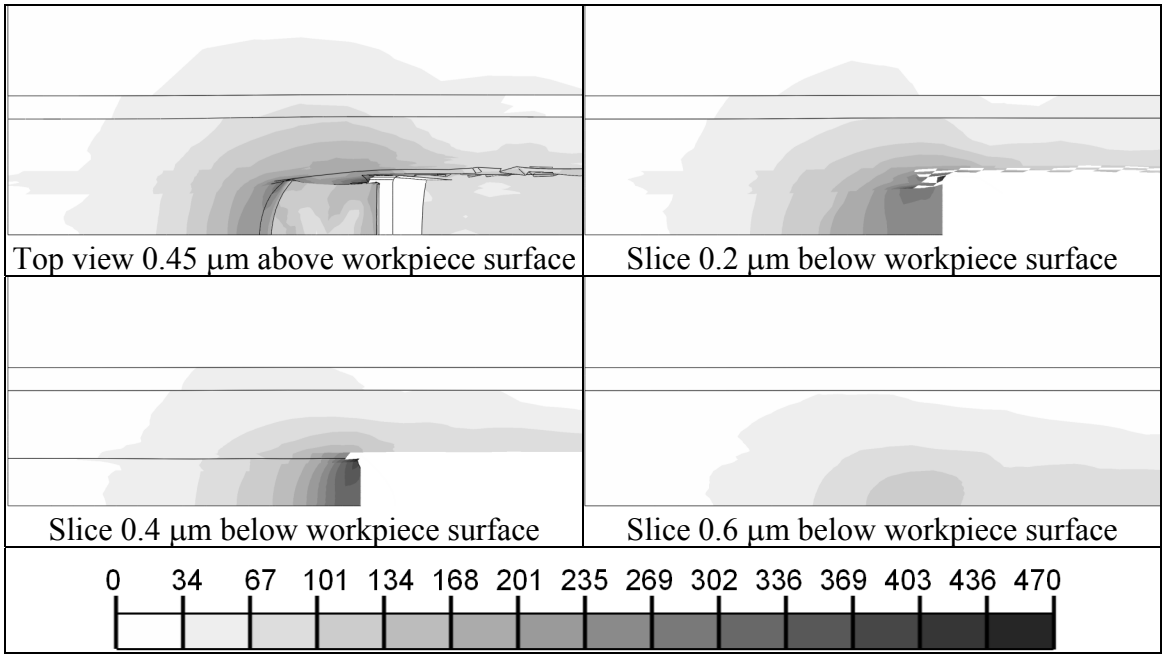


Figure 8.12: Mises stress slices: 10° rake angle and 500 nm depth of cut

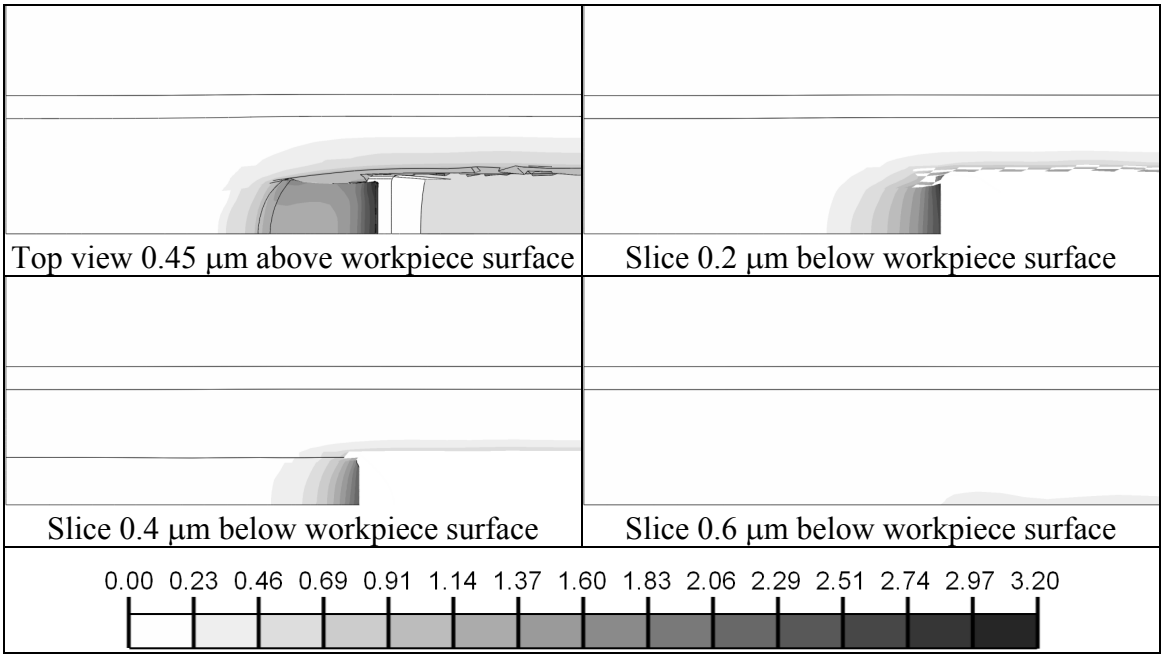


Figure 8.13: Plastic equivalent strain slices: 10° rake angle and 500 nm depth of cut

Examination of Fig. 8.10 – Fig. 8.13 shows that region of high Von Mises stress and plastic equivalent strain extends ahead of the cutting tool, to the side of the cutting tool, and below the cutting tool. The magnitude of strain fails off much more quickly that the stress. Also, at a given distance from the cutting zone, the plastic equivalent strain is fairly uniform. Where it is not uniform is within the chip itself where plastic equivalent strain is highest in the secondary shear zone but also fairly high at the side of the chip where it separates from the workpiece. Strain in the center of the chip, away from the secondary shear zone, is relatively low.

The shape of the stress field is interesting because the area of highest stresses is near the edge of the tool where the rake face meets the side clearance face and also near where the side of the chip starts to separate from the workpiece. This appears to be due to a stress concentration effect induced by the sharp edge of the tool and / or the sharp edge where the separating chip joins with the sidewall of the newly formed groove. As a result, a spike shaped region of elevated stress extends from the side of the chip root in the direction of cut. The magnitude of this effect might be controllable by varying the sharpness and shape of the tool where the rake angle meets the side clearance face, which could be of value because the high Von Misses stresses in this region appear to be a important component of the material failure that results in separation of the side of the chip from the workpiece.

Both the regions of significant stress and strain are smaller when using a tool with a 10° rake angle compared to a tool with a 0° rake angle, and the magnitude of the plastic equivalent strain is also less. This indicates that a more positive rake angle may be

beneficial in cases when deformation of material around the groove must be kept to a minimum, such as when cutting delicate closely spaced features.

### 8.3.3 Side Burr Formation and Chip Formation Steps

Side burr formation is not instantaneous and cannot be readily explained by showing the deformed shape of the workpiece, stress field, or strain field at any instant in time. Rather, the deformation of the workpiece must be considered as a function of time as the tool passes through it. Therefore, a slice of the workpiece is considered that lies parallel to the y-z plane and is located 7.5 μm from the start of the cut, as shown in Fig. 8.14. As the tool approaches the slice, the deformation, stress state, and strain state of the material that makes up the slice is considered at each point in time that is outputted by the model. Hence, evaluation of images of the slice presented sequentially shows the formation of the side burr and the process by which the chip separates from the workpiece.

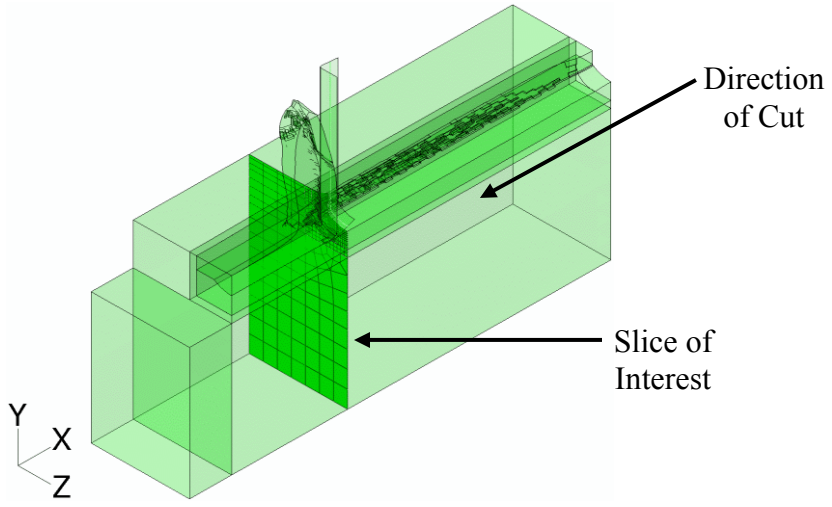


Figure 8.14: Workpiece mesh slice 7.5 μm from the start of the cut

Images of the deformed shape of the selected slice of the workpiece and the Von Mises stresses present in the slice at various stages of side burr formation and chip

separation are shown in Fig. 8.15 for the case of a 500 nm deep cut with a 0° rake angle tool. In each image the line of symmetry is on the right side. Also, the tool, which is not shown, is traveling in a direction pointed out of page. The distance provided below each image is how much more distance the tool must travel for the cutting edge of the tool to pass through the selected slice. A negative value indicates that the tool has already passed through the slice. A similar set of images, shown in Fig. 8.16, give the plastic equivalent strains in the slice at the same times as in Fig. 8.15.

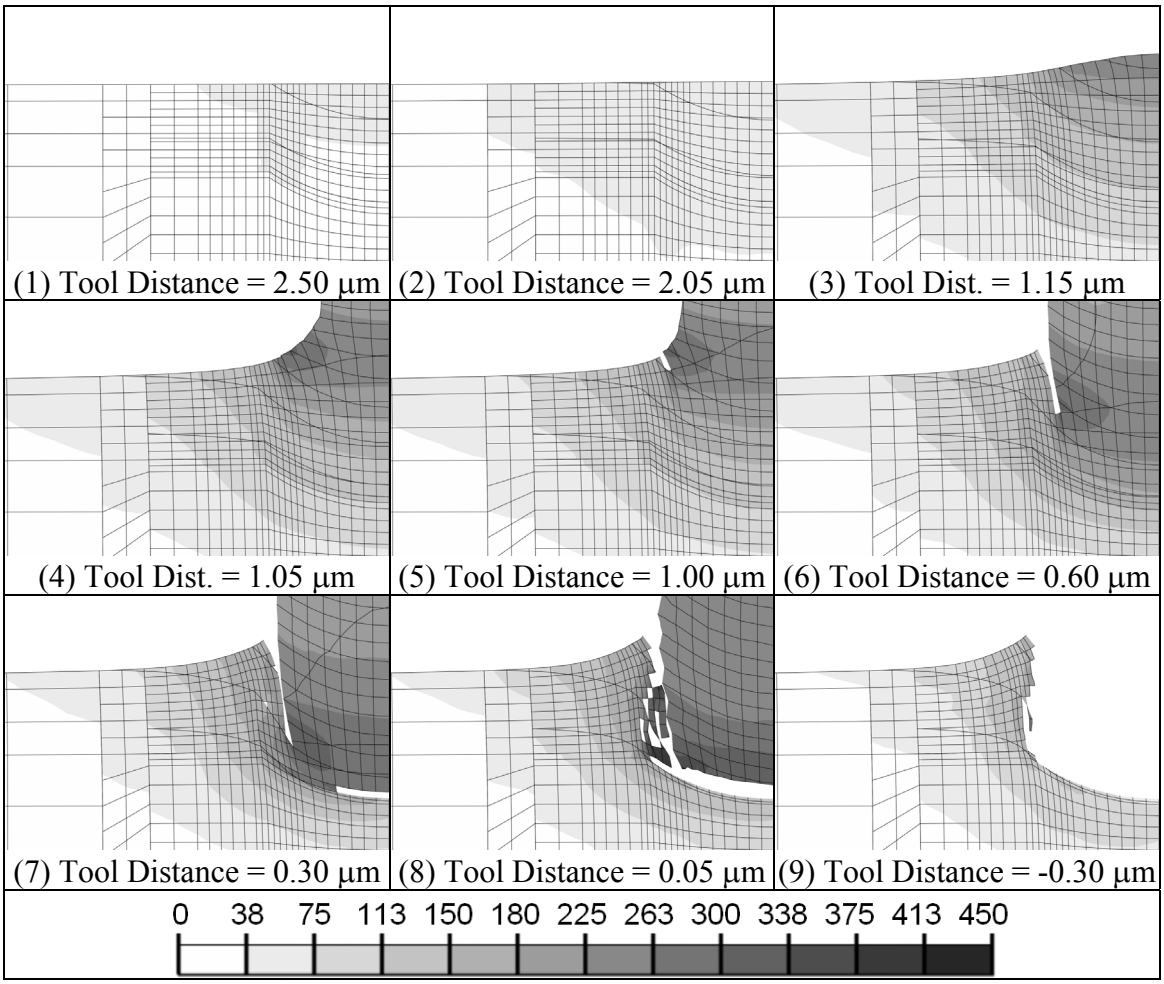


Figure 8.15: Von Mises stress during side burr formation: 500 nm DOC, 0° rake

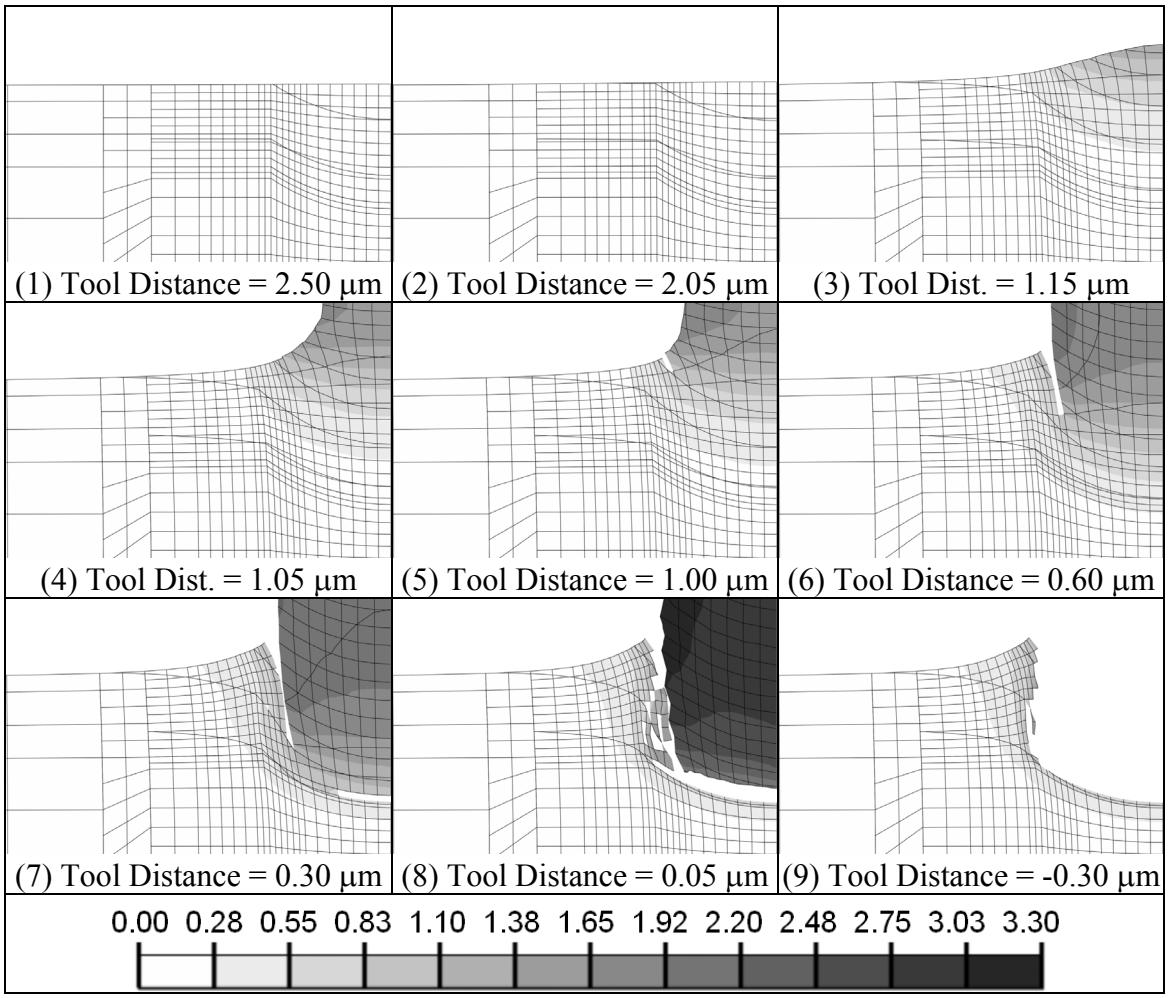


Figure 8.16: Plastic equivalent strain during side burr formation: 500 nm DOC, 0° rake

Figure 8.15 and Fig. 8.16 show a sequence of steps that occur as the tool approaches and passes through the selected slice. This sequence is as follows where each step corresponds to an image in the figures:

1. (Tool Distance = 2.50 μm) A small amount of stress is induced in a semi-circular region near the surface of the workpiece at the line of symmetry.
2. (Tool Distance = 2.05 μm) Stress spreads out radially from the point where the symmetry line meets the surface of the workpiece and a slight uplifting of the material near the symmetry line occurs.

3. (Tool Distance = 1.15 μm) Material near the line of symmetry is pushed up and forms a prow of material ahead of the tool. Stresses form a noticeable gradient where stress is highest within the prow and decreases when moving away from the prow. Noticeable plastic strains are also present within the prow and reduce when moving away from it.
4. (Tool Distance = 1.05 μm) The prow of material ahead of the tool starts to transition into a chip. The material that is raised up on the side farthest from the line of symmetry starts forming what will become the side burr. At the corner where the raised material meets the workpiece surface, intense localized stresses are generated. This is due to the spike shaped region of stress shown in Fig. 8.10 and Fig. 8.12 that is likely caused by a stress concentrator effect, as described previously.
5. (Tool Distance = 1.00 μm) Material at the workpiece surface in the region of high localized stress fails and forms a notch. Material on the side of the notch opposite the line of symmetry is now differentiated as a small side burr.
6. (Tool Distance = 0.60 μm) The notch becomes a crack that extends downwards into the workpiece with the region of high localized stress remaining at its bottommost end. Material on the side of the crack opposite of the chip starts to be pushed sideways away from the chip so that it can flow around the tool as shown in Fig. 8.9. This compresses the material below the burr, which causes it to be squeezed upward and increase the height of the burr.
7. (Tool Distance = 0.30 μm) Material fails below the chip near the line of symmetry, which forms a crack underneath the chip. This crack spreads sideways away from the line of symmetry to release the bottom of the chip. Material not included in the chip

continues to flow sideways around the tool, become compressed, and push upward, which further increases the height of the side burr.

8. (Tool Distance = 0.05 μm) The cracks below the chip and on its side meet to separate the chip from the workpiece. The side burr is done growing at this point.
9. (Tool Distance = -0.30 μm) The tool passes through the slice of material of interest and takes the chip material with it. The groove is fully formed at this point.

The sequence that occurs when cutting a 500 nm deep groove using a 10° rake angle is also shown. The configuration of the selected slice and the Von Mises stresses are shown in Fig. 8.17. The corresponding plastic equivalent strain is shown in Fig 8.18.

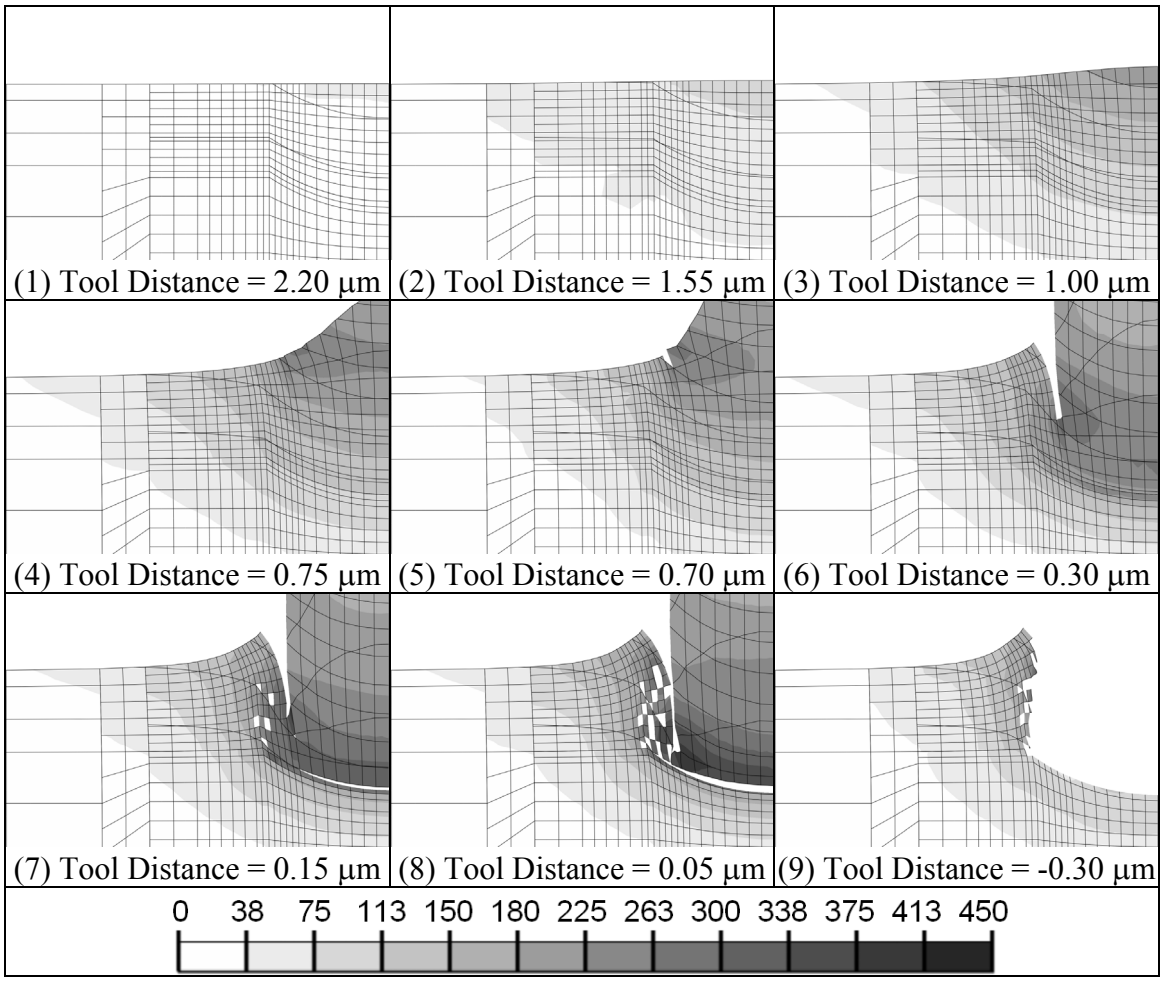


Figure 8.17: Von Mises stress during side burr formation: 500 nm DOC, 10° rake

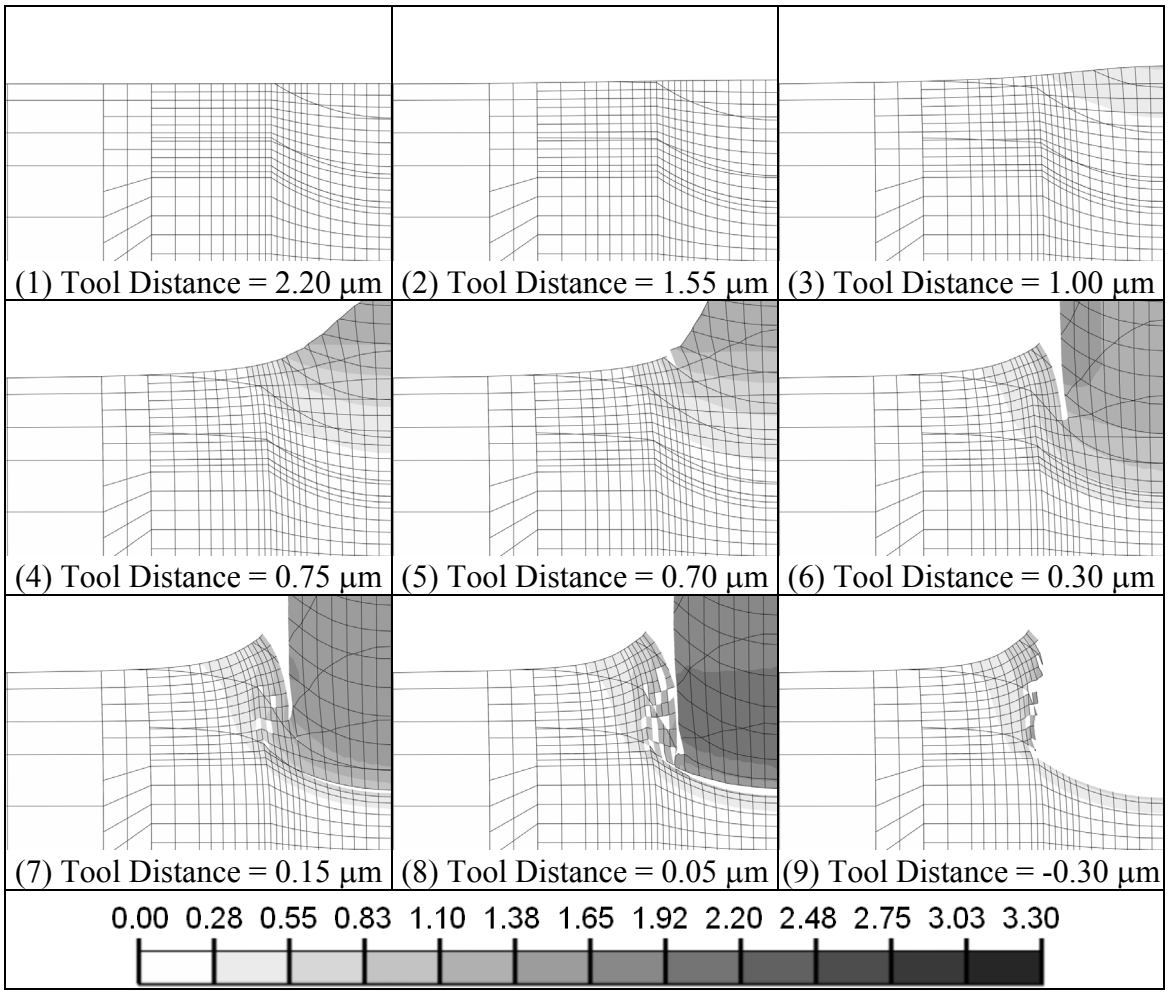


Figure 8.18: Plastic equivalent strain during side burr formation: 500 nm DOC, 10° rake

Figure 8.17 and Fig. 8.18 show that when a 10° rake angle is used, the same sequence of side burr and chip formation events occurs. However, the region of high stress does not penetrate as deeply into the workpiece when using a higher rake angle, which is consist with results shown previously in the chapter. Also, when using a larger rake angle, all of the steps previously described do not occur until the tool is closer to the observed slice of material. This makes sense because the rake face of the tool is leaning away from the slice of observed material instead of being oriented parallel with it. There is also slightly more increase in burr height during the phase when material is flowing

around the tool, being compressed sideways, and being squeezed upward. This difference in final burr height and in the timing of the burr and chip formation sequence can be seen in Table 8.2.

Table 8.2: Chip separation and burr formation summary

| Rake Angle (deg) | 0 | 10 | 0 | 10 |
|---|---|---|---|---|
| Depth of Cut (nm) | 500 | 500 | 720 | 720 |
| Side Burr Height (nm) | 166 | 177 | 186 | 194 |
| | Distance From Cutting Edge (μm) | | | |
| Stress Rises Noticeably | 2.80 | 2.25 | 3.10 | 2.70 |
| Prow Formation Starts | 2.05 | 1.55 | 2.20 | 1.70 |
| Side of Chip Starts to Separate | 1.00 | 0.70 | 1.20 | 0.95 |
| Bottom of Chip Starts to Separate | 0.30 | 0.15 | 0.20 | 0.15 |
| Chip Fully Separates | 0.05 | 0.00 | 0.05 | 0.00 |

Additionally, side burr formation was also considered when cutting at a depth of 720 nm. For brevity, the plots are not shown here. However, the plots appear very similar to the four previously shown plots. One difference is that significantly high stress and strain fields extended further into the workpiece. The burr height was also larger, likely due to the larger amount of material being squeezed upwards as it flows around the tool. Also, the various stages in the burr formation and chip separation sequence occur when the tool is further away from the observed slice than when using a smaller depth of cut, which corresponds to the thicker chip produced when using a larger depth of cut. This information is summarized in Table 8.2.

## 8.4 Exit Burr Formation

### 8.4.1 Comparison of Experimental Burrs and Model Predictions

In Chapter 6 it was shown that exit burrs form when one groove intersects another groove, as shown in Fig. 8.19. The burrs visible in the figure are attached to the side of

the grooves (side exit burrs). However, when exit burr formation is typically addressed in conventional orthogonal cutting, the exit burr observed is formed at the bottom of the groove due to folding over of the chip prior to separation from the workpiece (bottom exit burrs) [114, 115]. In such treatments the width of the tool tends to be much larger than the depth of cut and the plane strain modeling assumption can be used. Since this is not the case with the current process, the formation of side exit burrs is likely due to the 3D nature of the stress and strains present during the cutting process.

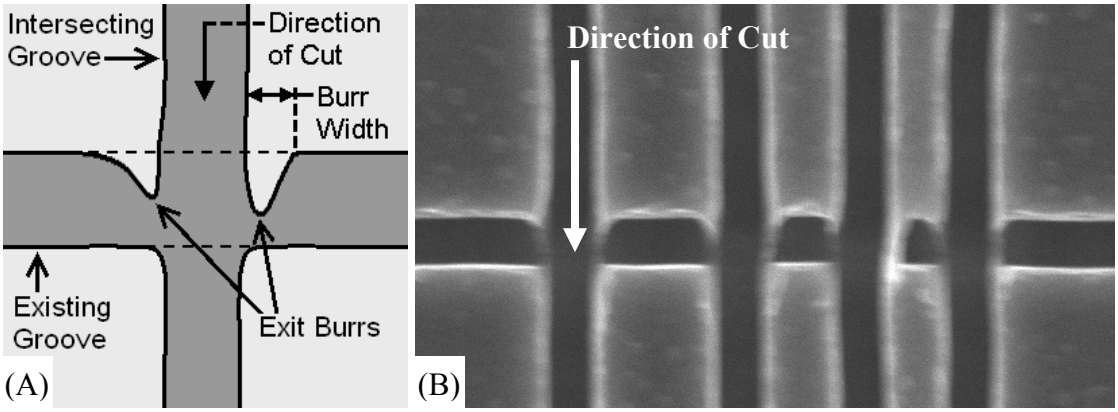


Figure 8.19: Exit burrs shown schematically (A) and via an SEM image (B)

To examine exit burr formation, the simulations using a 500 nm depth of cut and both a 0° rake angle tool and 10° rake angle tool were continued until the point when the tool exited and cleared the workpiece. The shape of the predicted exit burrs is shown in Fig. 8.20 for the 0° rake angle case, which shows both a bottom exit burr and a set of larger side exit burrs. This is consistent with the experimentally observed results in Chapter 7. Hence the model appears to capture the effects that result in side exit burr formation.

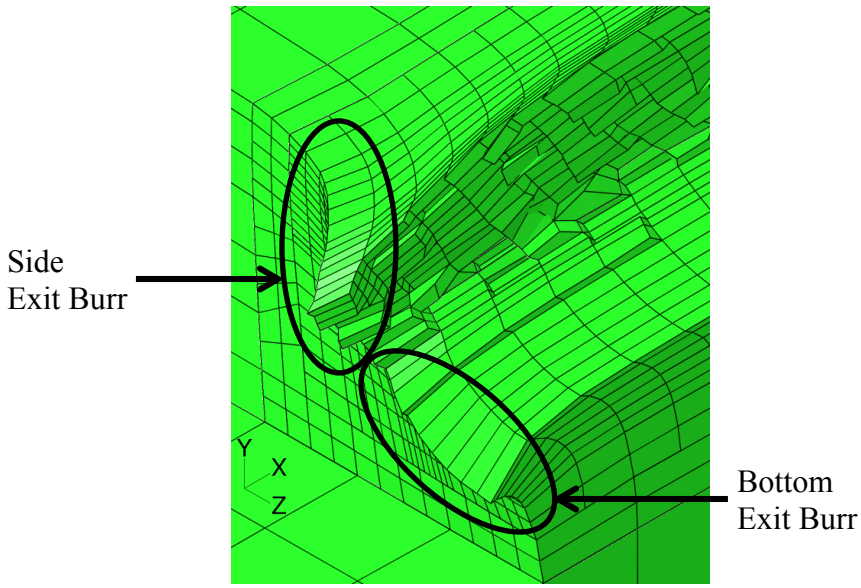


Figure 8.20: Exit burr shape predicted during a 500 nm deep cut with a 0° rake angle tool

## 8.4.2 Sequence of Events during Exit Burr Formation

In order to examine the process of burr formation, the deformation, stresses, and strains in the model were examined at each time step that was outputted by Abaqus for the 0° rake angle case. Images of the 3D geometry present during selected time steps are shown in Fig. 8.21. In each image the time after the start of the exit burr formation portion of the simulation is indicated for the purpose of synchronization with images in Fig. 22 – Fig. 25 that were taken at different time points in the simulation. Also, note that the geometry is mirrored about the symmetry plane for additional ease of interpretation.

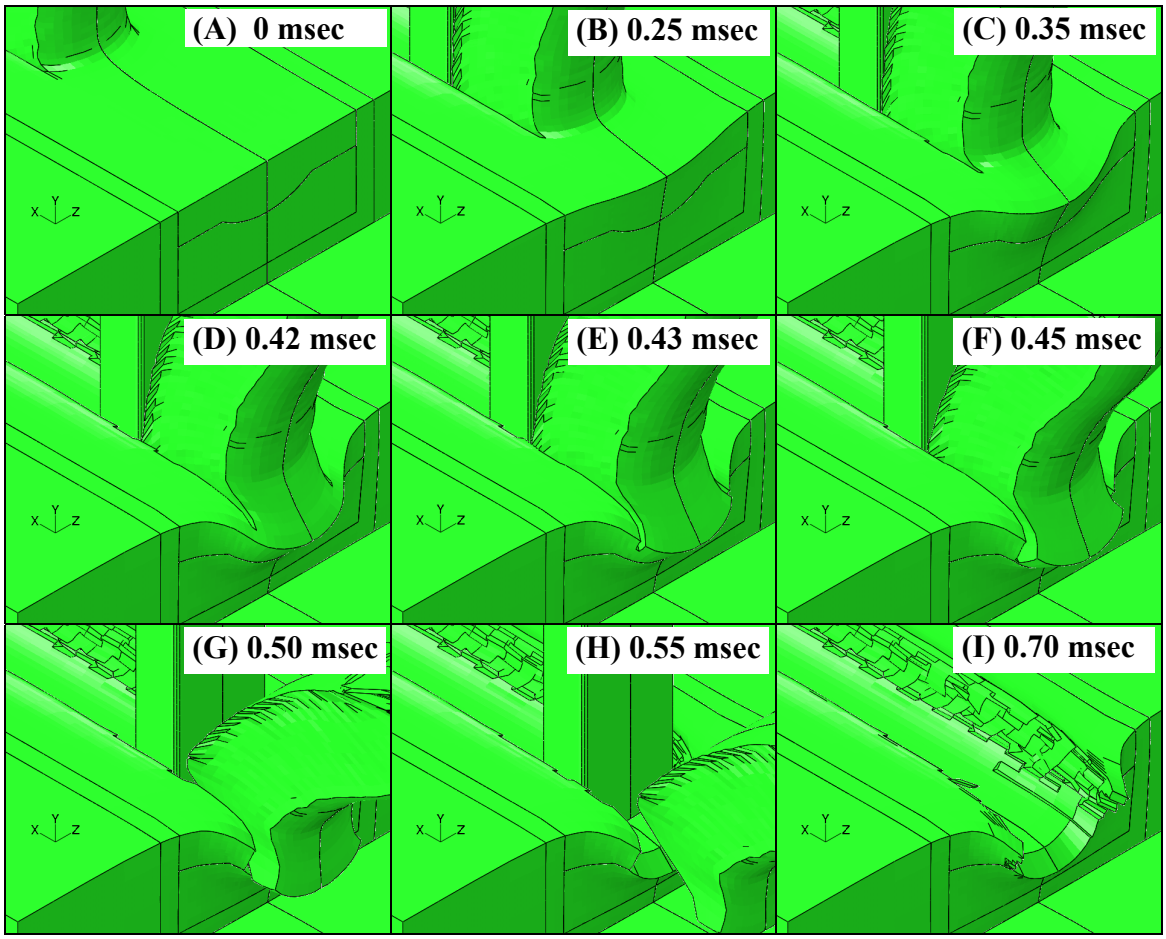


Figure 8.21: 3D view of exit burr geometry formation sequence

Additionally, in order to more clearly show the burr formation mechanism, the chip shape and Von Mises stresses were found on the plane of symmetry at selected times These stresses are shown in Fig. 8.22, where the tool is moving from right to left. Similarly, plastic equivalent strains at the symmetry plane were found at the same times and are plotted in Fig. 8.23. These two sets of images provide the same type of information about bottom exit burr formation that has been found by other researchers via 2D studies of exit burr formation. They also show how chip flow transitions to final chip removal at the end of the cut. However, despite the existence of similar data based on 2D

analysis, such results cannot be used to determine what will happen in the 3D case because, of the presence of out-of-cutting plane stresses and strains.

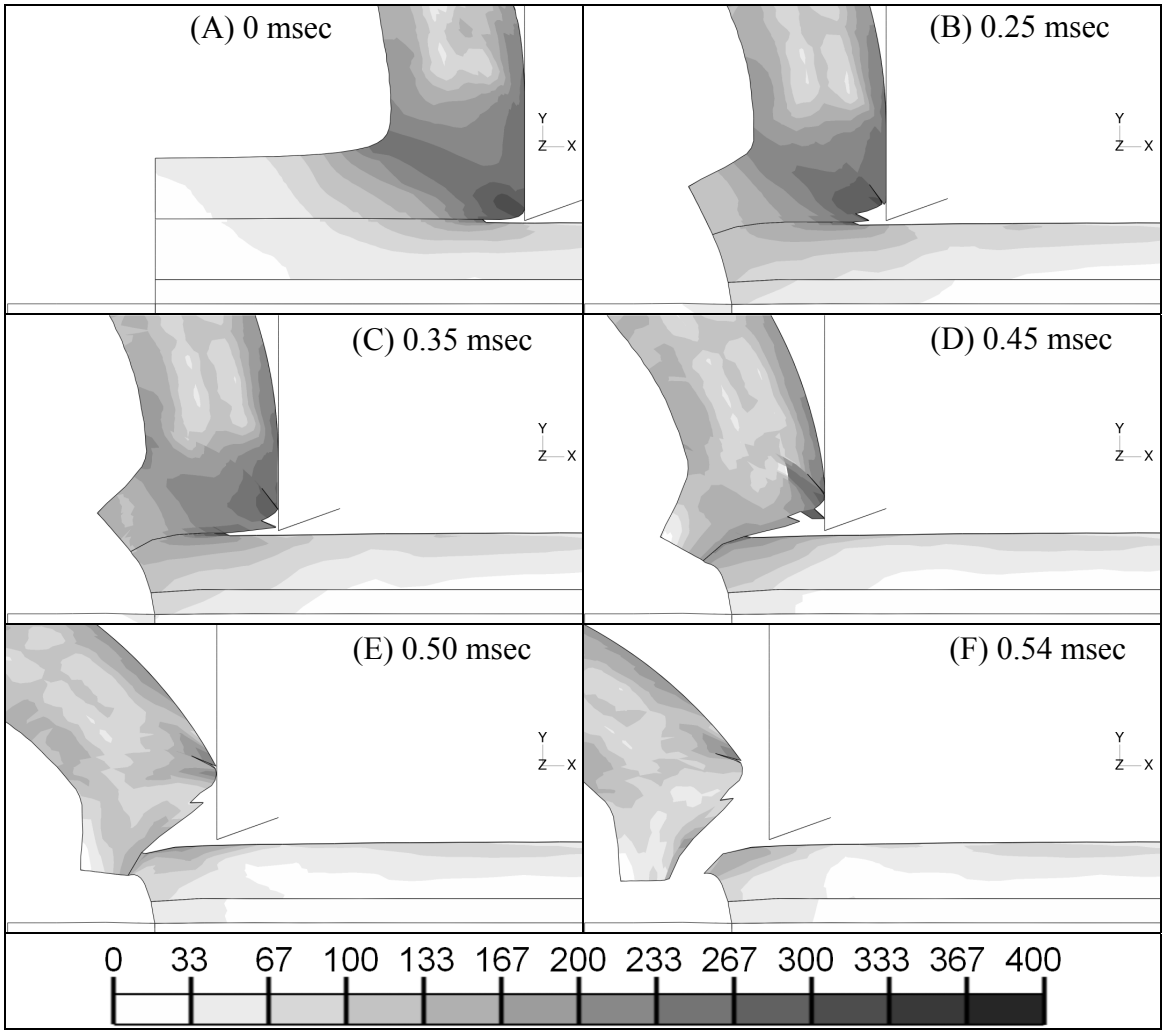


Figure 8.22: Symmetry plane view of Von Mises stresses during exit burr formation

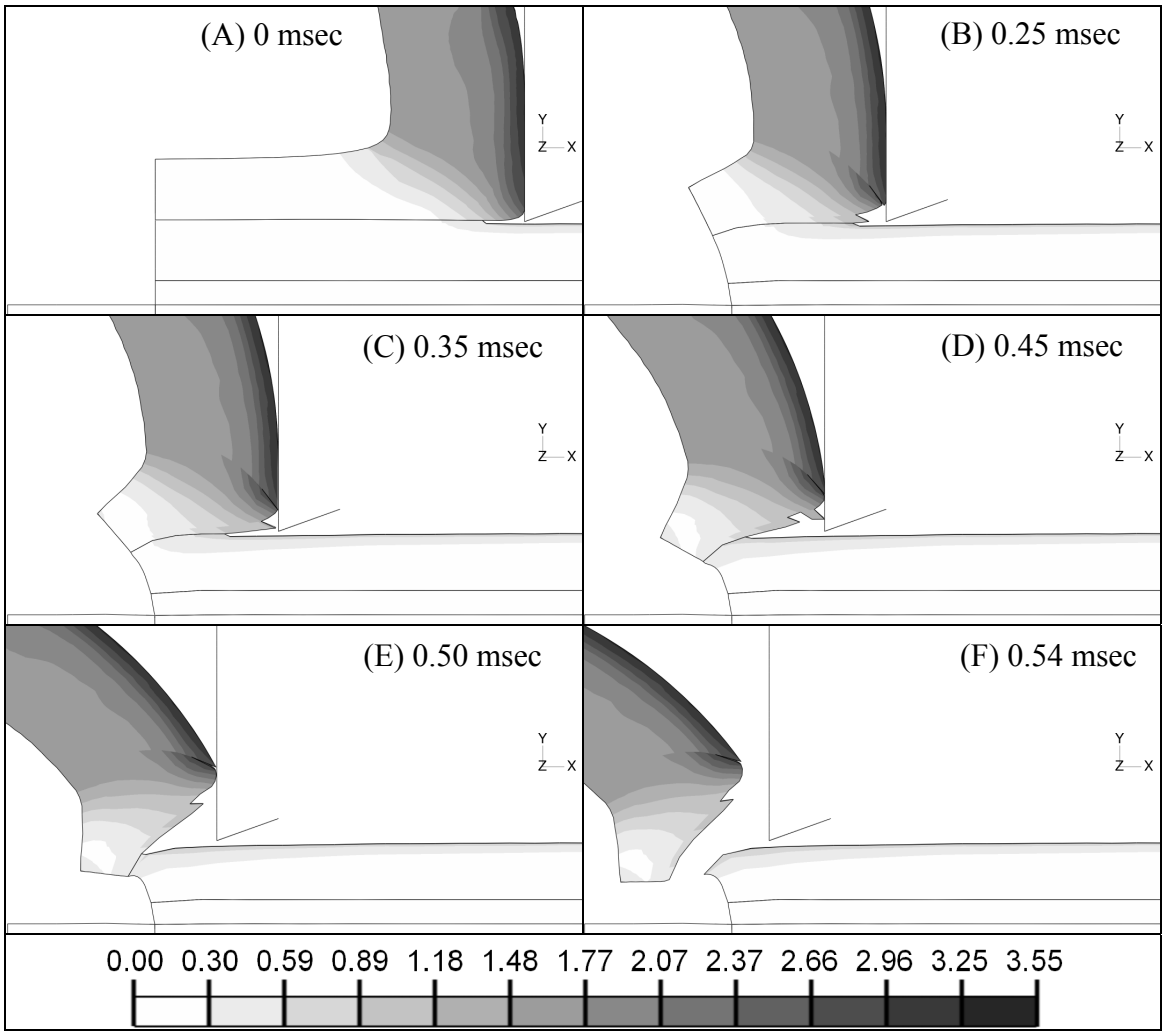


Figure 8.23: Symmetry plane view of plastic equivalent strain during exit burr formation

In addition to stress-strain information at the symmetry plane, stresses and strains were also examined on the top surface of the workpiece looking downwards in the negative y-direction. The Von Misses stresses on the surface are shown in Fig. 8.24, where the tool is moving from right to left. Similarly, plastic equivalent strains on the surface are shown at the same times in Fig. 8.25. Note that the images have been mirrored about the line of symmetry to improve clarity. Also, note that the tool appears solid white in each image and the top of the chip appears solid dark grey. This should not be taken to indicate the stress or strain in the tool or chip.

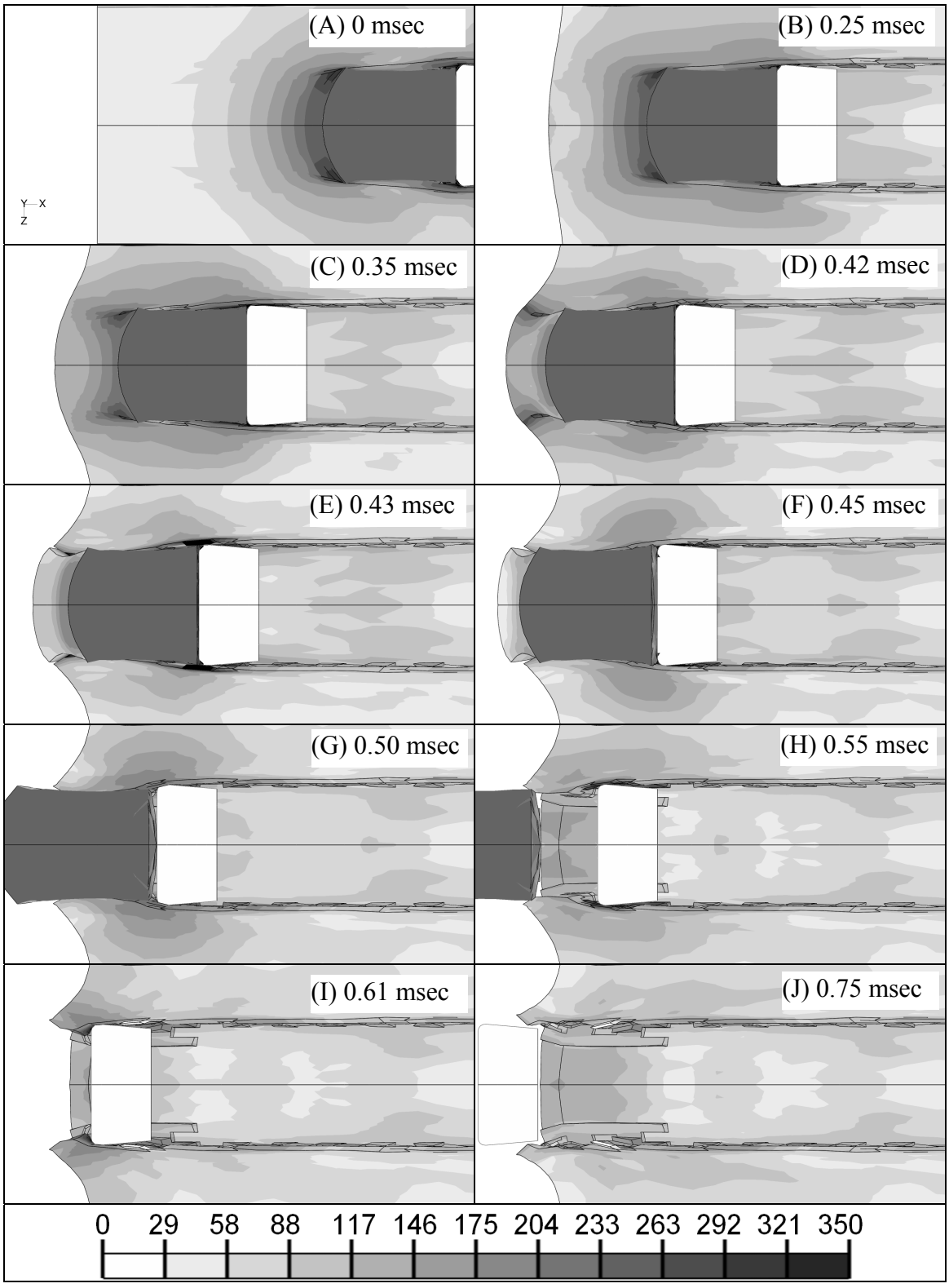


Figure 8.24: Top down view of Von Mises stresses during exit burr formation

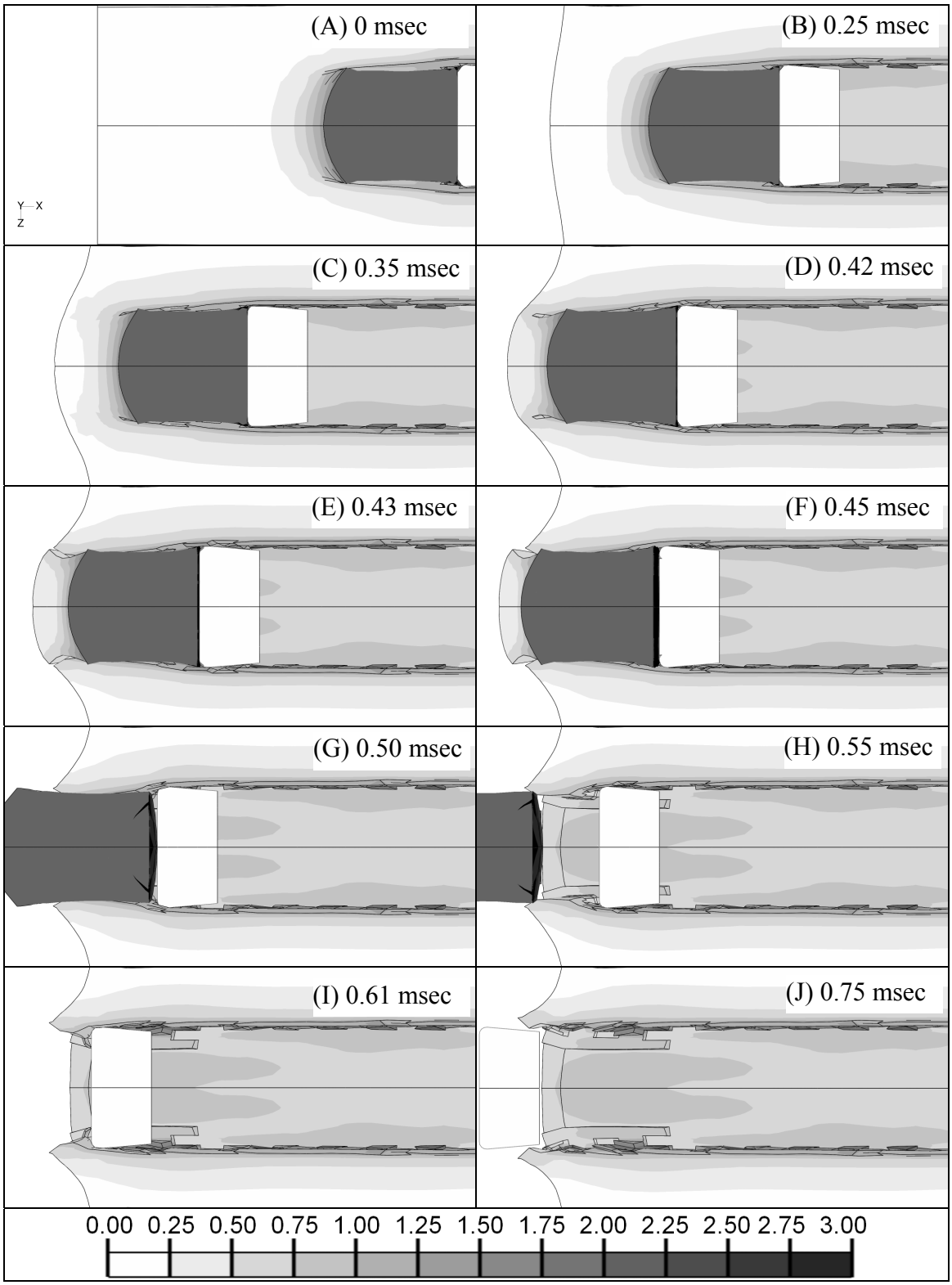


Figure 8.25: Top down view of plastic equivalent strain during exit burr formation

Using the results presented in Fig. 8.21 – Fig. 8.25, a sequence of events that results in burr formation was determined and is as follow:

1. Initially the tool is far enough from the end of the workpiece for the stresses ahead of the cut to be reduced to an insignificant level before reaching the boundary of the material. This represents steady-state cutting.
2. Significant stresses reach the end of the workpiece and the material on the side of the workpiece where the tool exits starts to bulge outward slightly as shown in Fig. 8.21B and Fig. 8.24B. This represents the start of the formation of the exit burrs.
3. As the distance between the tool and the end of the workpiece lessens, a membrane of material is formed that joins the sides and bottom of the end of the cut groove. This membrane bulges outwards and bends over as shown in Fig. 8.24C and Fig 8.22C, respectively. Also, as shown in Fig. 8.24C, intense stresses are present where membrane joints to the side of the groove near the top surface of the workpiece.
4. The membrane continues to be pushed outward and bend over, which pulls material at the sides of the groove outward, resulting in side exit burr formation. Notably, material near the top workpiece surface is pulled further outward than material near the bottom of the cut, as shown in Fig. 8.21D. The continued bending also contributes to bottom exit burr formation. At this point the intense stresses at the side of the membrane are also causing material at its sides to start to fail, as shown in Fig. 8.21D and Fig. 8.24D.
5. Material fails through the thickness of the thinning membrane at the two points where it joins to the groove sidewalls near the top surface of the workpiece, as shown in Fig. 8.21E.

6. The failure points on the membrane expand downward, which separates the sides of the membrane from the workpiece, as shown in Fig. 8.21F. At this point the material at the sides of the groove is no longer being pulled on by the membrane, and hence the majority of side exit burr formation ceases. However, the chip, which contains what is left of the membrane, is still attached to the workpiece on its bottom, as shown in Fig. 8.22D. Both high stresses and high plastic strains are present at this remaining connection point, as shown in Fig. 8.22D and Fig. 8.23D.
7. The chip continues bending over and form a bottom exit burr until finally separating from the workpiece and leaving behind the bottom exit burr, as shown in Fig. 8.22F and two side exit burrs, as shown in Fig. 8.24H.
8. Some material remains attached to the side of the groove ahead of the tool, which is not removed with the chip, as shown in Fig. 8.24H. This material is pushed outwards at the tool passes, which results in some additional side exit burr formation until the tool clears the workpiece. The end result is two side exiting burrs and one smaller bottom exit burr.

The way in which a membrane forms in front of the tool and then pulls on material at the sides of the groove to form side exit burr is an effect that can only be seen when considering the full 3D tool exit process. This process explains both the presence and shape of experimentally observed side exit burrs shown in Fig. 8.19B. This process is also affected by the rake angle of the tool, which can be seen in Table 8.3 that lists the lengths of the side exit burrs and bottom exit burrs that occur when cutting a 500 nm deep groove using tool with a 0° and a tool with a 10° rake angle. As can be seen in the table,

increasing the rake angle from 0° to 10° slightly decreases side exit burr and causes a larger decrease in bottom exit burr.

Table 8.3: Effect of rake angle on exit burr formation

| | | |
|---|---|---|
| Depth of Cut (nm) | 500 | 500 |
| Rake Angle (deg) | 0 | 10 |
| Side Exit Burr Length (nm) | 430 | 412 |
| Bottom Exit Burr Length (nm) | 232 | 182 |

## 8.4.3 Implications of Model Predictions during Ridge Intersection

It exit burr formation process described in the previous subsection may also explain deformation that occurs when cutting groove through thin ridges of material. Recall that during Experiment 6 in Chapter 6 an experiment was described where a groove was cut through a thin ridge of material at a 45° angle. Hence, one side edge of the rake face exited from the cut before the other side edge. In this situation, it was experimentally observed that the ridge material was highly deformed on the side of the groove corresponding to the side edge that exited the cut first, and was not as deformed on the other side of the groove, as shown in Fig. 8.26.

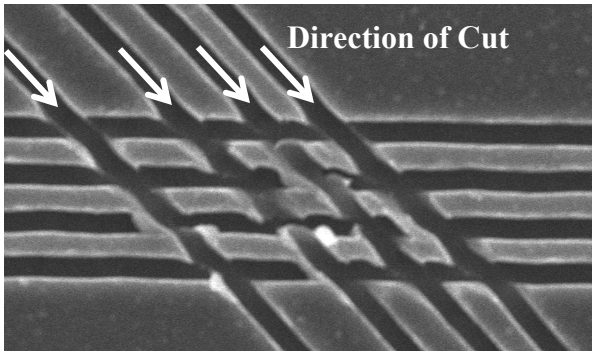


Figure 8.26: Ridges intersected at a 45° angle that are deformed on one side

In light of the simulation results, it can be inferred that when the leading side edge of the rake face exited from the workpiece a membrane formed that pulled on the

material on the side of the groove nearest the leading side edge and deformed it. This membrane then ruptured prior to the trailing side edge of the rake face exiting the workpiece. Hence, when the trailing side edge of the rake face exited from the workpiece, the membrane had lost most of its ability to carry a load and nearby material was not pulled on nearly as strongly, which resulted in less deformation. A similar effect should occur when using an oblique cutter to intersect a thin ridge at a 90° angle.

### 8.4.4 Strategies for Exit Burr Reduction

During manufacturing, exit burr reduction is often desirable. As just described, burrs are formed by the process of a membrane formed in front of a tool pulling on material at the sides of the groove and through bending over of the material in this membrane. Side exit burr formation primarily stops with the membrane ruptures and spits into the two side exit burrs and the chip. Bottom exit burr formation stops when the chip separates from the workpiece. Therefore, exit burr formation can be reduced by constraining the membrane from being able to bulge or bend over as much, by constraining the material under the membrane from being able to fold over as much, and by encouraging the membrane to rupture earlier.

At the macro-scale, constraining of the workpiece material at the end of a cut to reduce exit burr formation is sometimes accomplished by the use of a backing material clamped against the surface the tool exits, which may or may not be cut through by the exiting tool [115]. However, such an approach would be difficult to implement at the size scale of the micro-groove cutting process. What can be easily done is to plan the sequence of cuts used when manufacturing a part to reduce incidences of grooves being cut that intersect other grooves that are much deeper than the intersecting groove. By

doing this, material at the bottom of the face that the tool exits from is better constrained and hence bottom exit burr formation can be reduced. A more positive rake angle tool can also be used to slightly reduce bottom exit burr.

However, side exit burrs are larger than bottom exit burrs, and hence a strategy for reducing their size is required. One strategy is to use of tool with a more positive rake angle. However, as shown in Table 8.3, this only causes a small improvement. Another, strategy is suggested by the presence of the intense localized stresses seen in Fig. 8.24C and Fig. 8.24D, which induces the membrane to start failing. These stresses are likely caused by the sharp edges of the tool where rake face meets the side clearance faces and by the sharp edges where the sides of the chips meets the sides of the groove, both of which act as stress concentrators. Therefore, if a higher stress concentration factor could be achieved the stresses might be even higher and cause the membrane to fail while the tool was further from exiting the workpiece, which would halt much of the side exit burr formation. This might be accomplished through the use of sharper edge radii. Alternatively, structures such as ridges protruding from the side edges of the tools might be used.

## 8.5 Film Delamination Potential

Until this point, only the stresses and strains at depths within the workpiece in close proximity to the cutting zone have been considered. However, another concern is the stress-strain state of the interface between the aluminum film into which a groove is cut and the silicon substrate, which is well below the cutting zone. This is because certain stress states could cause the film to delaminate. This would be highly undesirable if grooves with various well controlled geometries are to be present in an intact metal

film. However, if the goal is to remove some of a film in order to expose a part of the underlying substrate, then delamination would be desirable. An example of such an application would be removal of a reflective film on top of a matte substrate or an opaque film on top of a transparent substrate in order to produce a photolithography mask.

Delamination can occur by subjecting the interface between the film and substrate to sufficient tensile stresses, i.e., pulling the film off the substrate. Also, 2D finite element studies have shown that shear stresses developed at the interface between film and substrate can result in delamination [153]. Hence both these stresses at the interface and at distance away from the interface are considered.

In the coordinate system defined in Fig. 8.1, tensile stress at the interface is simply the $\sigma_{22}$ component of the stress tensor. Calculation of shear stress at the interface is slightly more complicated because no one shear stress component from the stress tensor is sufficient. Rather an equivalent shear stress, $\tau_{equiv}$, developed due to stress that would cause the film to slide along the substrate is calculated as shown in Equation (8.1) where $\tau_{12}$ and $\tau_{23}$ are stress tensor components. The component of the shear stress that would tend to twist the film relative to the substrate is neglected here for simplicity.

$$\tau_{equiv} = \sqrt{\tau_{12}^{\,2} + \tau_{23}^{\,2}} \tag{8.1}$$

In the model, aluminum material properties are used for the top 3 μm of the workpiece and silicon material properties are used for the bottom 2 μm. Hence, the interface is 3 μm below the workpiece surface. Figure 8.27 shows the tensile stresses in a plane parallel with the workpiece surface 1 μm, 2 μm, and 3 μm below the surface of a 500 nm deep groove being cut using a tool with a 0° rake angle. Similarly, Fig. 8.28

shows the corresponding equivalent shear stresses. Note that the line of symmetry is on the bottom of each image and the vertical bar show midway along the bottom represents the location of the cutting edge of the tool, which is moving from right to left.

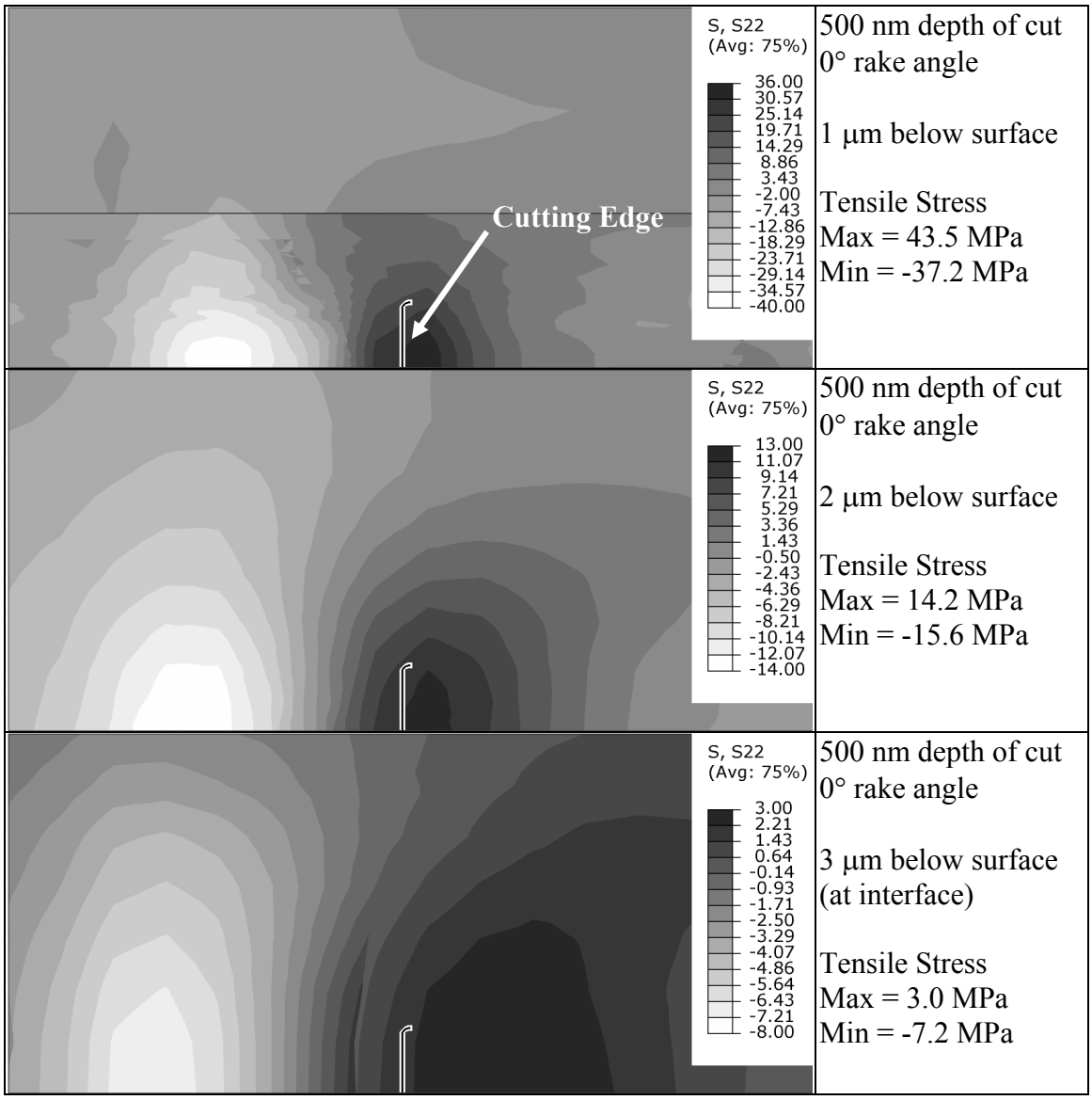


Figure 8.27: Subsurface tensile stress normal to film when cutting with a 0° rake angle

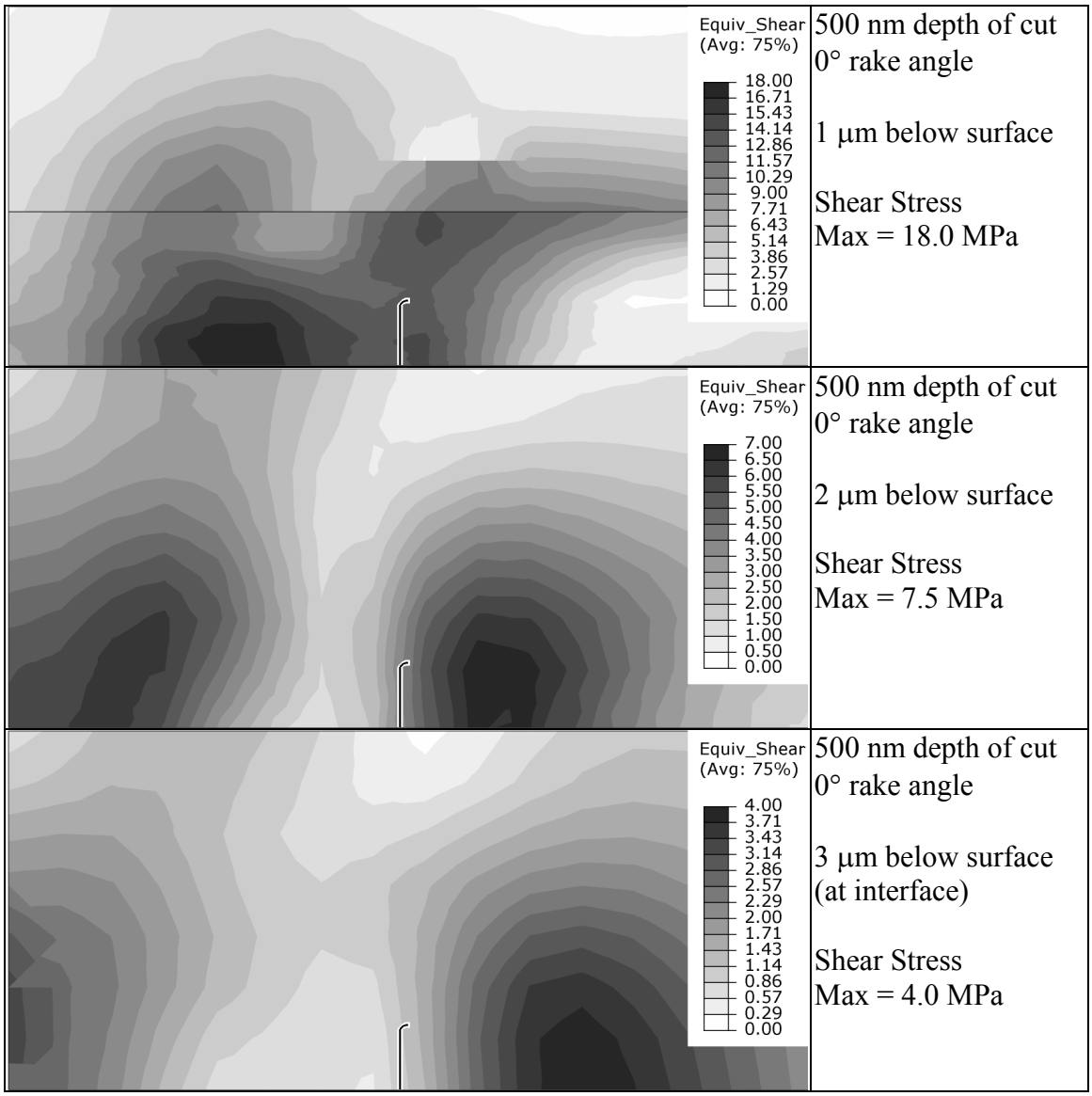


Figure 8.28: Subsurface effective shear stress when cutting with a 0° rake angle

In order to evaluate the effect of using a more positive rake angle, the shear and tensile stresses were found at the same locations as in the previous figures for the case when the depth of cut is 500 nm and the rake angle is 10°. This tensile stresses in a plane parallel with a workpiece surface 1 μm, 2 μm, and 3 μm below the workpiece surface are shown in Fig. 8.29. Similarly, Fig. 8.30 shows the corresponding equivalent shear

stresses. One again, the location of the cutting edge is indicated by a nearly vertical line near the middle of the bottom half of each image.

A summary of the max tensile stress, max compressive stress, and max shear stress in each image in Fig. 8.27 – Fig. 8.30 is provided in Table 8.4. Note that the compressive stresses listed correspond to negative tensile stresses in the figures.

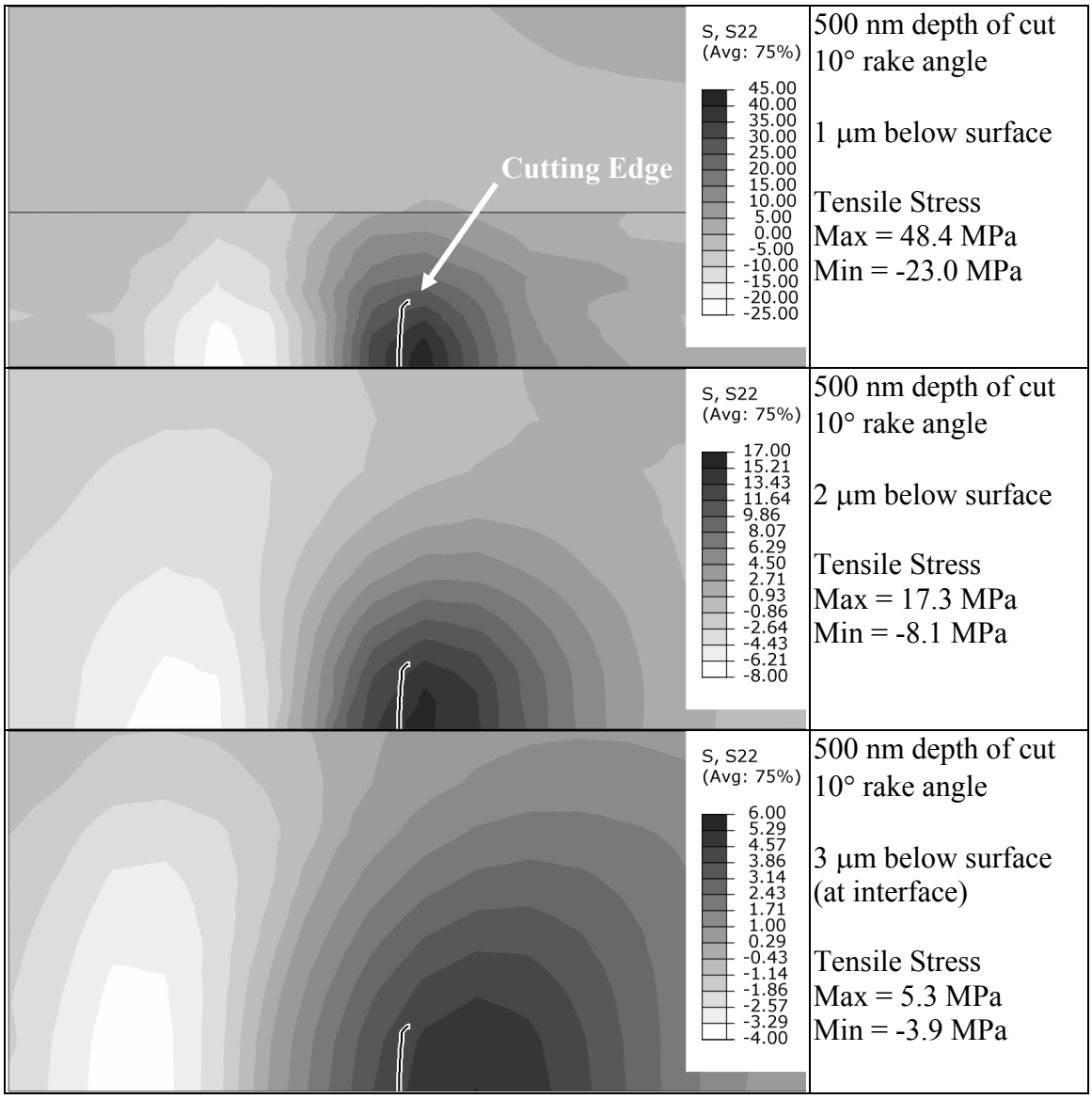


Figure 8.29: Subsurface tensile stress normal to film when cutting with a 10° rake angle

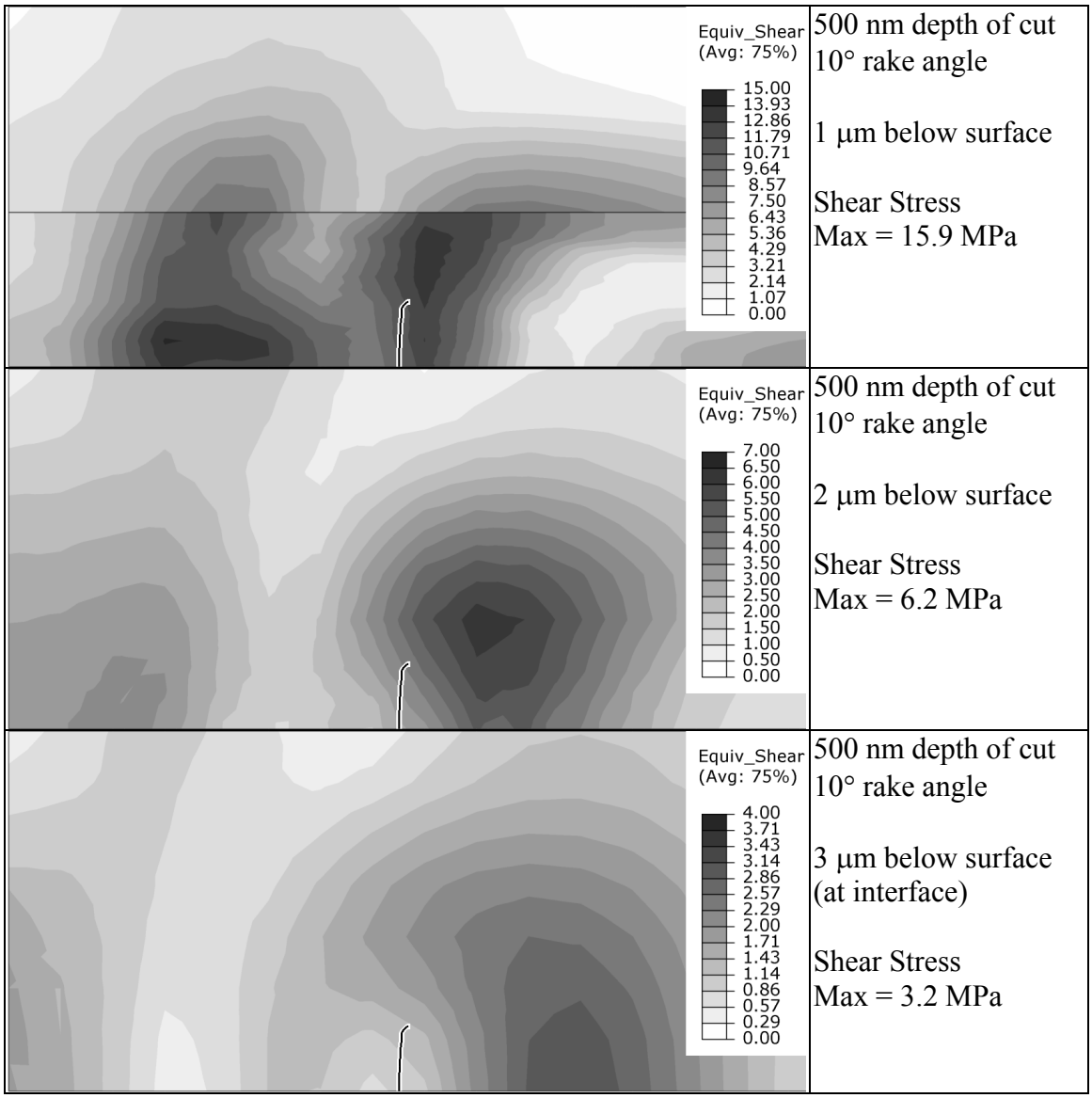


Figure 8.30: Subsurface effective shear stress when cutting with a 10° rake angle

Table 8.4: Subsurface stresses that could cause film delamination

| Depth of Cut (nm) | Rake Angle (deg) | Depth Below Surface (μm) | Max Tensile Stress (MPa) | Max Compressive Stress (MPa) | Max Shear Stress (MPa) | Max Von Mises Stress (MPa) |
|---|---|---|---|---|---|---|
| 500 | 0 | 1 | 43.5 | 37.2 | 18.0 | 34.0 |
| 500 | 0 | 2 | 14.2 | 15.6 | 7.5 | 17.9 |
| 500 | 0 | 3 | 3.0 | 7.2 | 4.0 | 7.6 |
| 500 | 10 | 1 | 48.4 | 23.0 | 15.9 | 30.9 |
| 500 | 10 | 2 | 17.3 | 8.1 | 6.2 | 19.3 |
| 500 | 10 | 3 | 5.3 | 3.9 | 3.2 | 5.8 |

It can be seen in the Fig 8.27 and Fig. 8.29 that during cutting a compressive stress is developed ahead of the tool that would tend to push the film into the substrate. Such a stress is unlikely to cause film delamination and may actual help prevent it. However, tensile stresses are developed near and behind the cutting edge that would cause film delamination if sufficiently high. As shown in Table 8.4, the magnitude of these tensile stresses is strongly dependent on the depth below the workpiece surface. For example, in the 0° rake angle case, a tensile stress of 43.5 MPa exists 1 μm below the workpiece surface, which is in excess of the quasi-static yield strength of the material. By contrast, 3 μm below the workpiece surface, the max tensile stress is only 3.0 MPa

Figure 8.28 and Fig. 8.30 show that the effective shear stresses below the workpiece surface exist both ahead of and behind the cutting edge. The shear stresses ahead of the cutting edge tend to be lower in magnitude than those behind the cutting edge. Furthermore, material ahead of the cutting edge is also subjected to compressive stresses and would tend to discourage delamination. Hence, delamination is most likely to occur behind the cutting edge of the tool due to a combination of both shear and tension. Also, the magnitude of the effective shear stress is strongly dependent on the depth below the workpiece surface. For example, in the 0° rake angle case, an effective shear stress of 18.0 MPa exists 1 μm below the workpiece surface, and 3 μm below the workpiece surface, the max effective shear stress is only 4.0 MPa

Both the effective shear stresses and the tensile stresses are also affected by the rake angle. Tensile stress increases when the rake angle in increased. However, effective shear stress decreases when the rake angle is increased, which make sense in light of the decreased cutting forces when the rake angle is increased.

Currently, the amount of tensile and / or shear stress required to cause film delamination is not known. However, since delamination did not occur in experiments using a 3 μm thick film and a tool with a 0° rake angle, it can be inferred that the combination of a 3.0 MPa tensile stress and a 4.0 MPa effective shear stress is not sufficient to cause delamination. By contrast, at a depth of 1 μm below the workpiece surface the tensile stress is in excess of the quasi-static yield strength of the workpiece material, but the material is not strained enough to experiment much work hardening. Hence, it is likely that a film that is only 1 μm thick would delaminate if a 500 nm deep groove was cut into it. Hence, delamination will occur when using some combinations of groove depth and film thickness and will not occur with others. Furthermore, it is likely that the depth of cut need not be the entire film thickness for delamination to occur.

## 8.6 Chapter Summary

In this chapter, simulation results from the finite element model of the micro-groove cutting process were evaluated and used to draw conclusions about the process. This involved evaluation of chip formation, side burr formation, the potential for film delamination, and exit burr formation through examination of deformed model geometry, stresses, and strains as they evolve over time.

At the beginning of the chapter, the 3D workpiece geometry present during steady-state cutting was presented. Next cutting forces were examined in the direction of cut, and it was noted that the profile of these forces clearly indicates that onset of steady-state cutting during the course of each simulation. It was also noted that the magnitudes of the predicted steady-state cutting forces change with depth of cut and rake angle in a manner consistent with conventional cutting.

Steady-state chip formation was examined via study of the behavior of material at the symmetry plane of the model. It was shown that a primary and secondary shear zone exist, as expected. It was also noted that the highest stresses were present at the cutting edge and the highest strains were present in the second shear zone. Also, the depth of cut and rake angle had strong effects on chip thickness, chip curl radius, the amount of plastic strain in a chip, and the distribution of plastic strain in a chip. Hence, it was concluded that these effects must be accounted for when designing and using a chip breaker geometry or when tailoring the characteristics of chips to produce micro-wires.

Out-of-cutting plane deformation, stresses, and strains were also examined by considering slices of the workpiece material at different depths below its surface. It was shown that material that is not part of the chip, but is still near the cutting zone, is pushed sideways in order to flow around the tool, which results in significant out-of-plain strains. Additionally, it was shown that regions of high stress extend from the side edges of the tool and the chip. This is concluded to be due to a stress concentrator effect, and plays an important role in chip separation from the workpiece. It was also shown that an increase in rake angle reduced the stresses present.

Side burr formation was examined by considering a slice of material, in the path of the cutting tool, oriented normal to the direction of cut. It was shown that side burr formation and chip separation involves complex 3D effects, and a sequence of events was described that occurs during side burr and chip formation. It was shown that the chip does not separate simultaneously on all sides, but rather the side of the chip first starts to separate and the bottom of chip separates later. Also, of particular interest was that side

burr formation appears to be largely due to upwards expansion of material compressed sidewalls when it flows around the tool rather than becoming part of the chip.

The model was used to examine exit burr formation. It was shown that, once again, complex 3D effects are involved. Because of these, rather than the single exit burr predicted to be attached to the bottom of the cut by 2D machining theory, there are three exit burrs: a burr attached to the bottom of the cut groove and a burr attached to each sidewall. Furthermore, it was shown that this is the result of the formation and rupture of a membrane of material formed around that tool that initially bulges out of the workpiece prior to exit of the tool. This concept of a rupturing membrane was used to explain previously seen experimental results. It was also shown that increasing the rake angle slightly decreases the predicted side exit burr and causes a larger decrease in the smaller bottom exit burr.

Lastly, in cases where the workpiece consists of a soft film on a hard substrate, the potential for film delamination during cutting was examined. It was shown that stresses can develop below a cut that can result in delamination if there is not enough film material between the bottom of the cut and the interface between the film and substrate. Hence, delamination may occur even if the depth of cut is not the same as the film thickness. However it is also shown that the intensity of the stresses below the cut falls off sharply as depth increases. Hence, if a film is thick enough relative to the depth of cut, film delamination will not occur.

The next chapter provides a summary of all the work previous presented herein. The chapter goes on to present several conclusions about the micro-groove cutting

process that has been developed. Finally, future work that can be used for further improve the micro-groove cutting process is suggested.

# Chapter 9

# Conclusions and Recommendations

## 9.1 Summary of Work

The objective of this research was to develop a versatile, cost-effective micro-manufacturing process capable of cutting micro-scale grooves, which meets process requirements imposed by potential applications. In particular, the process was to be capable of cutting programmable patterns of curvilinear grooves with nearly arbitrary cross-sections in metals that are between a few hundred nanometers and a few microns wide, up to a few microns deep, and between tens of microns to several millimeters long. The process was to accommodate both flat workpieces and workpieces with curved surface geometries. The process was to have a good material removal rate, avoid significant burr formation / material distortion, and be capable of achieving relative tolerances of approximately $10^{-2}$ or better.

In order to achieve this goal, existing micro-manufacturing processes capable of producing micro-scale grooves were considered, but found incapable of satisfying the process requirements at a reasonable cost. Therefore, a new process was developed that is similar to micro-scale shaping / planing, but which makes use of a flexible cutting tool. Rather than control the position of the cutting edge of the tool to achieve a depth of cut, controlled bending of the flexible tool is used to achieve a desired cutting load. The load, combined with tool shape and workpiece material, determines the depth of cut. The process was implemented by retrofitting an existing 5-axis micro-scale machine tool with

a specially constructed micro-groove cutting assembly. The assembly included a means of holding the flexible cutting tool and measuring the amount of tool bending, which was used as an input to a feedback loop that regulated tool bending through a cut.

Initial experiments were conducted using commercially available diamond-coated silicon AFM probes as flexible cutting tools. These experiments explored how using different cutting load, cutting speed, numbers of tool passes, and tool orientation affected groove geometry and tool wear when cutting pure aluminum. The ability of cutting long curved grooves was also evaluated. It was shown that the process is viable, but improved tool geometries are required.

Improved cutting geometries were designed that were more suitable for micro-groove cutting. An FIB machining procedure was developed that enabled these geometries to be produced on the ends of flexible tool blanks. Experiments were conducted to evaluate the performance of the improved tools in terms of tool wear and the ability to control the cutting groove cross-sectional shape. The ability to cut complex patterns of closely spaced and intersecting groove was also evaluated.

A model of the micro-groove cutting process was developed in order to gain a more thorough understanding of the process. The model made use of an Explicit Lagrangian finite element formulation, represented the workpiece in three dimensions, and handled separation of a chip from the workpiece via element failure based on the Johnson-Cook criteria. The model addressed the 3D stress / strain fields present during micro-groove cutting, chip separation on the bottom and sides of a chip, rounded tool geometry, side burr formation, and exit burr formation. Material properties were found in

the literature where possible and all other inputs were found via calibration. Model predictions were compared to experiments to evaluate model accuracy.

The model was used to simulate cutting of micro-grooves, with depths of 265, 500, and 720 nm, in a workpiece consisting of a 3 μm thick aluminum film on a silicon substrate where the rake angles considered were 0° and 10°. The results were used to analyze steady-state chip formation and the associated stress / strain fields. Side burr formation and exit burr formation were examined. The potential of delamination of the film was also considered. Several conclusions regarding potential process improvements were presented.

## 9.2 Conclusions

The following conclusions can be drawn from the research presented in this work.

### 9.2.1 Developed Micro-Groove Cutting Process

1. A micro-groove cutting process has been developed that makes use of a flexible single-point cutting tool. The tool is configured much like an AFM probe and consists of a cutting geometry mounted on the end of a flexible cantilever. In order to cut a micro-groove, the end of the flexible tool opposite the cutting geometry is first advanced towards a workpiece until the cutting edge of the tool contacts the workpiece. Advancing the held end of the tool even closer to the workpiece causes the cantilever to bend and applies a load onto the cutting edge, which in turn causes it to sink into the workpiece. The amount of cantilever deflection, and hence the amount of applied load, is maintained at some target value via feedback in order to control the load on the cutting edge. While this occurs, the workpiece is traversed underneath the tool along a desired cutting path and a chip is formed from the action

of the cutting geometry passing through the workpiece. The resultant depth of cut is determined by the workpiece material, tool geometry, and cutting conditions.

2. Using the developed cutting process, cantilever deflections required to develop a cutting load that results in a set depth of cut can be several times larger than the depth of cut. This effectively amplifies the resolution of a machine tool used to implement the process with regards to depth of cut. Also, the cutting edge is spring loaded against the workpiece. Hence, as long as constant cutting conditions are maintained, the cutting edge of the tool will always pass through the workpiece at a constant depth. Hence, the process is much more tolerant to uncertainties in tool position relative to the workpiece surface due to linear guide misalignments, insufficiently accurate tool-workpiece registration, or undesired motions due to inertial effects on insufficiently stiff components. These advantages enable the process to be implemented on machine tools that cost about a tenth of what would be required using conventional ultra-precision machining.
3. When cutting with the developed process, cantilever deflection rather than depth of cut is directly controlled. Depth of cut is dependent on tool geometry, workpiece material, and applied cutting load. For any given tool and workpiece, the relationship between cutting load and depth of cut must be found empirically. The relationship between cutting load and cantilever deflection can be calculated using an Euler-Bernoulli beam-based model of a given tool configuration.
4. As a flexible tool bends in order to generate a cutting load, the orientation of its cutting geometry, and hence its rake face, will change. Therefore, the rake angle is not set by tool geometry alone, but rather it is dependent on cutting forces, the tool

geometry, and the tool orientation. To set a cutting load without having to tolerate changes in rake angle whenever the load is adjusted, both the angle the tool is held at and the amount of cantilever deflection must be set appropriately. The combination of deflection and tool orientation required to achieve any given cutting load and rake angle can be calculated using an Euler-Bernoulli beam-based model of the tool.

5. The developed micro-groove cutting process has been implemented by retrofitting a groove cutting assembly onto an exiting 5-axis micro-scale machine tool, which serves as a motion platform. The assembly included a means of holding a flexible cutting tool and measuring the amount of tool cantilever deflection, which was used as an input to a feedback loop that regulated cantilever deflection throughout a cut. In the constructed configuration, the machine tool is capable of dynamically adjusting workpiece position relative to the tool, adjusting the distance between the tool and workpiece, adjusting the orientation of the tool, and adjusting the amount of tool cantilever deflection. The machine tool can also be used to implement cutting of curved grooves through the use of a rotary stage on which the workpiece is mounted.

### 9.2.2 Micro-Groove Cutting Using AFM Probes as Tools

1. The performance of the developed micro-groove cutting process was initially evaluated via experiments where diamond-coated silicon AFM probes, with a stiffness of 42 N/m, were used as tools. These experiments showed that flexible tool can be used to controllably cut micro-scale groove in aluminum. Also, even at the very small size scale involved, significant chip formation will occur during groove cutting. However, considerable ploughing of workpiece material also occurs, which was largely attributed to the highly negative effective rake angles present due to the

large edge radii of the tools relative to the depth of cut. Groove geometry was shown to be highly dependent on cutting conditions. Groove depth consistency was also found to be improved by the use of multiple tool passes.

2. When using commercial diamond coated AFM probes as tools, significant wear occurs, which decreases groove quality and precision. In some cases, catastrophic fracture of an AFM tip can occur during cutting due to a lack of sufficient material supporting the cutting edge. Even when there is not catastrophic tool fracture, there is still significant wear, which consists of an initial period of fast more limited fracture-based wear followed by a long period of slow abrasive wear. This lack of wear resistance is not unreasonable since AFM probes are optimized for use in metrology and are not intended for use as cutting tools in such a demanding application. The solution to this problem is to use tools with cutting geometries that are more structurally sound and constructed of harder materials, such a monocrystalline diamond or cubic boron nitride.

### 9.2.3 Fabrication of Improved Micro-Groove Cutting Tools

1. A set of flexible micro-groove cutting tool design principles were established through consideration of experiment results cutting with AFM probes, consideration of successful tool geometries used for groove cutting at the macro-scale, and through consideration of the sorts of tool geometries that can be fabricated at the micro-scale using FIB machining. These principles are that: (1) the cutting edge radius should be as small as possible to minimize ploughing and maintain a more positive effective rake angle. (2) There should be plenty of material behind the cutting edge to support it and prevent tool fracture. (3) The tool should have suitable clearance angles to

minimize rubbing with the workpiece. (4) Sharp corners that would result in stress concentration effects in the tool should be avoided. (5) It should be possible to fabricate the tool using only through cuts because precise depth control during FIB machining is difficult. (6) It should be possible to easily cut the geometry out of a tool blank shaped like a three-sided pyramid since readily available tool blanks have this geometry. (7) The rake face should be orientated such the mounting angle required to get a desired rake angle under commonly used cutting loads is at least a few degrees in order to insure that the cutting geometry, and not any other part of the tool, contacts the workpiece.

2. Cutting tools have been fabricated by modifying commercial single-crystal diamond tipped AFM probes using a FEI Dual Beam 235 FIB machine. During fabrication, the diamond tipped AFM probes serve as tool blanks that already have much of the required tool geometry. The tool fabrication process developed is a series of four FIB machining steps that cut a tool geometry out of a blank shaped like a three-side pyramid, but could also be used with different shaped blanks. These steps are designed to produce a tool that meets the tool design requirements while minimizing the presence of undesirable features introduced by the use of FIB machining. High quality tools have been fabricated with edge radii of 50 - 64 nm is most cases.

### 9.2.4 Machining Features Using Improved Cutting Tools

1. Experiments were conduced using flexible cutting tools with improved geometries produced by FIB modification of diamond AFM probes. These tools were successfully fabricated as narrow as 411 nm and had very effective cutting geometries. The tools are also capable of readily withstanding the forces they are

subjected to during cutting. Tool wear is very small when cutting aluminum, e.g., over a distance of 122.4 mm tool wear was only 19 nm on one case.

2. An experiment was conduced using a 1 μm wide tool with a 0° rake angle at cutting speeds of 25 – 50 mm/min and at loads between 0.3 and 1.4 mN. It was shown that 1 μm wide rectangular cross-sections can be repeatably cut in aluminum and that depth of cut can be well controlled by setting the cutting load. The relationship between groove depth and both cutting load and the number of tool passes is nonlinear. Cutting speed only has a small effect on groove depth. There is a critical depth of cut per tool pass, and if this value is exceeded greatly increased burr formation occurs.
3. In a second experiment, a 411 nm wide tool with a 0° rake angle was used to successfully cut grooves as narrow as 300 nm but about 2 μm deep at speeds up to 50 mm/min. It was shown that measurable elastic recovery of the sidewalls of the grooves occurs, and therefore when such narrow grooves are cut, elastic recovery must be taken into account to achieve a prescribed groove width.
4. In a third experiment, the ability of cutting compound v-shaped grooves was demonstrated. It was shown that a desired groove shape can be readily achieved when using a tool with identical geometry to the desired geometry. Side burr formation is also smaller when using tools with v-shaped rake faces than when using tools with rectangular shaped rake faces. Also, when using a v-shaped tool, side burr height is reduced via the use of second tool pass.
5. In a fourth experiment, grooves were cut in aluminum at speeds as high as 400 mm/min with less tool wear than when cutting at lower speeds of 25 – 50 mm/min. Furthermore, groove quality and the amount of side burr formation was found to not

be strongly effected by cutting speed. Hence, higher speeds up to at least 400 mm/min are beneficial.

6. Chips can remain attached to a workpiece, via their chip roots, following micro-groove cutting operations. These chips can be easily removed by blowing compressed air across the workpiece, and if left undisturbed can also be used to examine chip morphology corresponding to a particular cut. Chip morphology is primarily affected by cutting load, and hence depth of cut, when cutting 1 μm wide rectangular grooves in aluminum. At lower loads curly washer-type helical chips are formed. At higher loads, wavy ribbon chips are formed. At sufficiently high loads buckled continuous chips can be formed.
7. In a fifth experiment it was shown that one micron wide and deep parallel grooves, cut in pure aluminum, can be spaced about one micron apart controllably. If a closer spacing was commanded, the ridge of material between the grooves became wider than commanded, which is likely due to elastic recovery. In order to get the thinnest possible ridge of material between grooves, the depth of cut per tool pass should be kept low enough to avoid large amounts of burr formation, which affect ridge geometry.
8. In a sixth experiment, it was shown that grooves can be successfully cut that intersect existing grooves without affecting the characteristics of the intersecting groove after the intersection point. The depth of the intersecting groove briefly dips before the intersection point, possibly due to collapse of the sidewall of the intersected groove. Exit burr formation also occurs during groove intersection, and results in two burrs attached to the sidewalls of the intersecting groove. If two closely spaced grooves

with a ridge of material between them are intersected the ridge of material can deform significantly during intersection if it is too thin or has too high of an aspect ratio. However, sufficiently low aspect ratio ridges do not experience significant deformation.

### 9.2.5 Modeling of the Micro-Groove Cutting Process

1. A more fundamental understanding of the micro-groove cutting process is required than can be readily gained experimentally in order to enable further process improvements such as minimization of side burr formation, minimization of exit burr formation, and chip control. A finite element model of the process has been developed to help gain such an understanding. The model, which uses a Lagrangian finite element formulation and an explicit dynamics procedure, is implemented using the Abaqus version 6.9 finite element software.
2. Micro-groove cutting cannot be approximated using a 2D finite element model because the width of cut is on the order of the depth of cut and because side burr formation is a 3D event. Therefore, the developed finite element model is fully 3D. The workpiece is modeled as a film of an elastic-plastic isotropic material with strain hardening and strain rate hardening that is perfectly bonded to a substrate modeled as an anisotropic elastic material. Separation of a chip from the workpiece is handled through the use of element failure in specified sacrificial regions below and on the side of the chip, where the Johnson-Cook failure criterion is used. The model does not treat thermal effects, because they are expected to be negligible and approximates the tool as sharp, which is reasonable given the very small edge radii on tool used in experiments. The tool is modeled as rigid and tool curvature introduced by FIB

machining is incorporated. Tool-workpiece contact was modeled using the Abaqus general contract algorithm and friction was modeled using an extended coulomb friction model. The model geometry is designed to enable prediction of both steady-state chip / burr formation and transient exit burr formation.

3. Model inputs were extracted from the literature where possible. When literature values could not be found, the model was run using different inputs values and used to simulate three different cuts performed in experiments. Model inputs that resulted in the most accurate predictions of the experimental results were selected for further use. It was also shown that when using the selected model inputs, good agreement is achieved between the model and experimental results. Specifically, chip thickness prediction errors are within 21.0 – 31.8 %, burr height prediction errors are within 0.0 – 8.5 %, and chip curl prediction error is only 4.1% in cases where simulation and experiment results could be compared.

### 9.2.6 Simulation-Based Micro-Groove Cutting Process Study

A 3D finite element model of the micro-groove cutting process was used to simulate micro-groove cutting at depths of 265, 500, and 720 nm using 1 μm wide tools with rake angles of 0° and 10°. In each simulation, the workpiece consisted of a 3 μm thick aluminum film, perfectly bonded to a silicon substrate, and the cutting speed was 300 mm/min. Steady-state cutting was achieved in each simulation.

1. Steady-state cutting forces in the direction of cut increase when the depth of cut increases and decrease when the rake angle increases, which is consistent with conventional cutting. Also, during steady-state cutting primary and secondary shear zones are clearly present, and the highest strains in each cut occur in the secondary

shear zone. Also, the depth of cut and rake angle have strong effects on steady-state chip thickness, chip curl radius, the amount of plastic strain in a chip, and the distribution of plastic strain in a chip. Such effects must be taken into account when designing tool features such as a chip breaker.

2. The simulations showed that regions of significant stresses and strains extend from the cutting zone, and that the magnitude of the stress decrease with increased rake angle. Particularly intense stresses originate from the side edges of the tool and chip, and they extend ahead of the tool in the direction of cut. These stresses are likely caused by a stress concentrator effect induced by the edges of the tool where the rake face meets the side clearance faces or by where the bottom of the chip meets the sides of the newly formed grooves. These stresses play an important role in material failure at the side of the chip, which enables chip separation from the workpiece. Material ahead of the tool that does not become part of the chip is push aside by the tool and flows around it, which induces significant out-of-cutting plane strains at the sides of each cut.
3. The sequence of events that occur during chip separation and side burr formation were studied using simulation results. It is shown that a chip does not separate simultaneously form the workpiece on all sides, but rather the side of the chip first starts to separate and the bottom of chip separates later. Side burr formation is primarily due to upwards expansion of material compressed sideways at the side of each groove after flowing around the tool rather than becoming part of the chip.
4. The model was used to examine exit burr formation. Rather than the single exit burr predicted to be attached to the bottom of the cut by 2D machining theory, there are

three exit burrs: a burr attached to the bottom of the cut groove and a burr attached to each sidewall. This is the result of the formation and rupture of a membrane of material formed around that tool that initially bulges out of the workpiece prior to exit of the tool. This concept of a rupturing membrane explains experimental results where material is only highly deformed on one side of a groove exiting from a thin ridge of material when both side edges of the tool do not break through simultaneously. It was also shown that increasing the rake angle slightly decreases the predicted side exit burr length and causes a larger decrease in the smaller bottom exit burr length.

5. In cases where a workpiece consists of a soft film on a hard substrate, the potential for film delamination during cutting exits. Stresses can develop below a cut that can result in delamination if the interface between the film and substrate is close enough to the bottom of the cut. Hence, delamination may occur even if the depth of cut is not the same as the film thickness. However, the intensity of the stresses below a cut falls off sharply as depth increases, and hence if a film is thick enough relative to the depth of cut, film delamination will not occur.

## 9.3 Recommendations for Future Work

The research described herein has resulted in the development of a micro-groove cutting process capable of filling a significant gap in current micro-manufacturing capabilities. Also, through experiments and finite element modeling, a useful understanding of the process mechanics has been acquired. However, several improvements to both the process and the finite model are possible. The understanding of the process can still be expanded experimentally, and the model can still be used to

acquire more information about how the process can be improved. Hence, recommended areas of future research are as follows.

### 9.3.1 Machining of Stronger More Complex Materials

1. In the presented work, workpiece material was limited to pure aluminum that was thermally evaporated onto a silicon substrate. This provided a soft homogenous workpiece material with a fine grain structure, which simplified experiments and process modeling. However, for many engineering applications, such a die making, it is desirable to cut grooves in much harder materials with more complex heterogeneous grain structures, such as steel. Therefore, a series of experiments should be conducted to evaluate the machinability of harder materials and identify any issues that need to be addressed.
2. When cutting material with heterogeneous grain structures, the phase structure varies from grain to grain, and hence material properties differ from grain to grain. This is not an issue in macro-scale cutting because the tool is much larger than the grains. However, when cutting micro-grooves, a grain may be significantly larger than a tool. Hence, a tool will transition between materials with different properties throughout a cut. This in turn will results in changes in depth of cut since, in a load-based cutting process, the depth of cut is partially determined by workpiece material properties. To understand this effect, experiments should be conducted where the grains that the tool is cutting through are identified and characterized, and the events that occur when the tool transitions from one grain to another are carefully observed. Such experiments should enable strategies for mitigating changes in depth of cut due to grain properties.

### 9.3.2 Improvements in Tooling

1. All tools that offered good performance in this work had cutting geometry consisting of single-crystal diamond. However, while diamond is very suitable for cutting materials such as copper and aluminum alloys, it is not suitable for cutting materials such as steel because the carbon in the tool will diffuse into the workpiece and cause unacceptable tool wear. Therefore, the fabrication and use of tools with cutting geometries made of materials that are more inert than diamond, but still hard enough for use in cutting tools, such as single-crystal cubic boron nitride, should be explored.
2. Only single-point cutting tools have been used in experiments. This is not because of any limitation in the tool fabrication process. Rather, single-point tools were used in order to not unnecessarily complicate experimental results. However, from a productivity standpoint, multi-point tools are appealing because they offer the ability to cut multiple-grooves simultaneously. Hence, the use of such tools should be experimentally evaluated.

### 9.3.3 Improvements in Process Implementation

1. Currently, flexible tool bending is measured using a laser displacement sensor. Such a system is functional. However, the laser must sensor be capable of seeing the tool at all times, which can be problematic is a chip snarls around the tool and occludes the laser. Also, when a tool is first mounted, it can drift in position relative to laser displacement sensor for up to an hour, which introduces a delay between tool loading and cutting. A potential solution is to construct tools with integrated strain gages and use those to measure deflection. The output from an integrated strain gage would be insensitive to the presence of chips or debris on the tool and would not drift if tool

position shifts slightly. Hence, fabrication and use of such tools is a suggested area of future development.

### 9.3.4 Additional Simulation-Based Process Studies

1. The developed finite element model has been used to explore side burr formation and exit burr formation using a tools of similar design with a 0° and 10° rake angle. However, there is evidence that other tool shapes may enable significant reduction in exit burr size. Reduction in side burr size may also be possible. Therefore, a series of simulations should be conducted in which a wide range of tool designs are explored. Of particular interest are designs aimed at increasing the stress concentration that occurs ahead of the side edges of a tool where the rake face meets the clearance faces.
2. All simulations have made use of half symmetry in order to reduce the amount of computer time required for a simulation. This is of value since, even when making use of half symmetry, simulations can require over a week of computer time. However, this limits tool to orthogonal cutters. Since there may be advantages in oblique cutting, simulations should be run that do not make use of symmetry to study this effect. It may be necessary to acquire more computer resources in order to perform a significant number of such simulations.

### 9.3.5 Process Finite Element Model Improvements

1. The plastically deformable workpiece material in the current model is treated as isotropic and homogenous. This is suitable because the workpiece material consists of fine-grained pure aluminum. However, many other desirable workpiece materials are heterogeneous and have grain sizes large enough for the tool to only be cutting through one grain at a time. Additionally, the crystalline orientation of materials that

makes up individual grains can vary, which can result in different flow stress values depending on the direction of material deformation. Therefore, useful additions to the model would be explicit handing of grain structure, implementation of different material properties for different gains, and the ability to implement anisotropic yielding within a grain when necessary.

2. In this work, thermal effects were neglected for simplicity after it was argued that such effects are not significant when cutting materials such as aluminum at the size scale involved. However, in order to handle materials with very low thermal conductivities, such as titanium, a more careful approach may be necessary. In such a case, an adiabatic heat generation model appears to be the only computationally feasible option at the size scale involved when using the current finite element software. This would render correct selection of the fraction of plastic work converted to heat extremely critical, which would likely require significant empirical model calibration.
3. A chip breaker tool geometry may be beneficial in micro-groove cutting. However, the use of such a geometry was not handled in any simulations. This is because a long chip would have to be generated over the course of a simulation in order to see the chip breaker in action, which would render the simulation length computationally impractical when using the developed model. However, a separate chip breaking model, making use of the adaptive Lagrangian Eulerian finite element formulation, might be constructed that accepts the state of the chip as it separates form the rake face as a boundary condition. Therefore, research into the creation of such an add-on model is suggested in order to expand current predictive capabilities.

# List of References


[1] Melninkaitis, A., Balciunas, T., Sirutkaitis, V., Juzumas, V., Janusonis, J., and Slekys, G., 2008, "Formation of grooves in SiO2 coated silicon using femtosecond ytterbium DPSS laser", Proceedings of the SPIE, **7005**, pp. 70050L-1-70050L-12.

[2] Maeda, J., Sawada, H. Yoshida, M., and Fujita, M., 2004, "Micro-machining using 1.55m band fiber pulse laser with 10kW peak power", Proceedings of the SPIE, **5662**, pp. 501-506.

[3] Yeo, S.H., and Yap, G.G., 2001, "A feasibility study on the micro electro-discharge machining process for photomask fabrication", International Journal of Advanced Manufacturing Technology, **18**(1), pp. 7-11.

[4] Ehrfeld, W., Lehr, H., Michel, F., Wolf, A., Gruber, H.-P., and Bertholds, A., 1996, "Micro electro discharge machining as a technology in micromachining", Proceedings of the SPIE, **2879**, pp. 332-337.

[5] Yeo, S.H., and Murali, M., 2003, "A new technique using foil electrodes for the electro-discharge machining of micro grooves", Journal of Micromechanics and Microengineering, **13**(1), pp. N1-N5.

[6] Kuo, J.S., Chiu KT, Hsu, S.W., Chen, P.H., and Liao, V.S., 2006, "A novel technique for the fabrication of herringbone grooves in a dynamic thrust bearing combining UV-LIGA with electro-discharge machining", Microsystem Technologies, **12**(6), pp. 529-536.

[7] Shin, H.S., Kim, B.H., and Chu, C.N., 2008, "Analysis of the side gap resulting from micro electrochemical machining with a tungsten wire and ultrashort voltage pulses", Journal of Micromechanics and Microengineering, **18**(7).

[8] Kim, B.H., Park, B.J., and Chu, C.N., 2006, "Fabrication of multiple electrodes by reverse EDM and their application in micro ECM", Journal of Micromechanics and Microengineering, **16**(4), pp. 843-850.

[9] Performance Micro Tool, 2009, "Performance Micro Tool Product Catalog".

[10] Ohnishi, O., Onikura, H., Min, S.-K., Aziz, M., and Tsuruoka, S., 2008, "Effect of ultrasonic vibration on micro grooving", Memoirs of the Faculty of Engineering, Kyushu University, **68**(1), pp. 1-9.

[11] Yan, J., Uchida, K., Yoshihara, N., and Kuriyagawa, T., 2009, "Fabrication of micro end mills by wire EDM and some micro cutting tests", Journal of Micromechanics and Microengineering, **19**(2).

[12] Ali, M.Y., and Ong, A.S., 2006, "Fabricating micromilling tool using wire electrodischarge grinding and focused ion beam sputtering", International Journal of Advanced Manufacturing Technology, **31**(5-6), pp. 501-508.

[13] Morgan, C.J., Vallance, R.R., and Marsh, E.R., 2004, "Micro machining glass with polycrystalline diamond tools shaped by micro electro discharge machining", Journal of Micromechanics and Microengineering, **14**(12), pp. 1687-1692.

[14] Kawai, T., Sawada, K., and Takeuchi, Y., 2001, "Ultra-precision micro structuring by means of mechanical machining", Proceedings of the IEEE Micro Electro Mechanical Systems, pp. 22-25.

[15] Sawada, K., Odaka, S., Kawai, T., Hirai, T., Takeuchi, Y., and Sata, T., 1999, "Manufacture of diffraction grating on tiny parts by means of ultraprecision milling", Microsystem Technologies, **5**(4), pp. 157-160.

[16] Takacs, M., Vero, B., and Meszaros, I., 2003, "Micromilling of metallic materials", Journal of Materials Processing Technology, **138**, pp. 152-155.

[17] Fang, F.Z., and Liu, Y.C., 2004, "On minimum exit-burr in micro cutting", Journal of Micromechanics and Microengineering, **14**(7), pp. 984-988.

[18] Fang, F.Z., Wu, H., Liu, X.D., Lim, G.C., Liu, Y.C., and Ng, S.T., 2003, "Fabrication of micro grooves ", ASPE Annual Meeting (Portland).

[19] Lee, J.H., Park, S.R., Yang, S.H., and Kim, Y.S., 2004, "Fabrication of a v-groove on the optical fiber connector using a miniaturized machine tool", Journal of Materials Processing Technology, **155-156**, pp. 1716-1722.

[20] Adams, D.P., Vasile, M.J., and Krishnan, A.S.M., 2000, "Microgrooving and microthreading tools for fabricating curvilinear features", Precision Engineering, **24**(4), pp. 347-356.

[21] Yan, J., Oowada, T., Zhou, T., and Kuriyagawa, T., 2009, "Precision machining of microstructures on electroless-plated NiP surface for molding glass components", Journal of Materials Processing Technology, **209**(10), pp. 4802-4808.

[22] Picard, Y.N., Adams, D.P., Vasile, M.J., and Ritchey M.B., 2003, "Focused ion beam-shaped microtools for ultra-precision machining of cylindrical components", Precision Engineering, **27**(1), pp. 59-69.

[23] Ding, X., Butler, D.L., Lim, G.C., Cheng, C.K., Shaw, K.C., Liu, K.; Fong, W.S., and Zheng, H.Y., 2009, "Machining with micro-size single crystalline diamond

tools fabricated by a focused ion beam", Journal Micromechanics and Microengineering, **19**(2), pp. 1-11.

[24] Fang, T.H., Weng, C.-I., and Chang, J.G., 2000, "Machining characterization of the nano-lithography process using atomic force microscopy", Nanotechnology, **11**(3), pp. 181-187.

[25] Zhao, X., and Bhushan, B., 1998, "Material removal mechanisms of single-crystal silicon on nanoscale and at ultralow loads", Wear, **223**(1-2), pp. 66-78.

[26] Iwata, F., Kawaguchi, M., Aoyama, H., and Sasaki, A., 1997, "Ultrasonic micromachining on Al thin film using atomic force microscopy combined quartz crystal resonator", Thin Solid Films, **302**(1-2), pp. 122-126.

[27] Iwata, F., Kawaguchi, M., Aoyama, H., and Sasaki, A., 1997, "Nanometer-scale layer removal of aluminum and polystyrene surfaces by ultrasonic scratching", Japanese Journal of Applied Physics, Part 1, **36**(6B), pp. 3834-3838.

[28] Furutani, K., Suzuki, M., and Kudoh, R., 2004, "Nanometre-cutting machine using a stewart-platform parallel mechanism", Measurement Science & Technology, **15**(2), pp. 467-474.

[29] Luo, X., Cheng, K., Guo, X., and Holt, R., 2003, "An investigation on the mechanics of nanometric cutting and the development of its test-bed", International Journal of Production Research, **41**(7), pp. 1449-1465.

[30] Adams, D.P., Vasile, M.J., Benavides, G., and Campbell, A.N., 2001, "Micromilling of metal alloys with focused ion beam fabricated tools", Precision Engineering, **25**(2), pp. 107-113.

[31] Youn, S.W., and Kang, C.G., 2005, "Maskless Pattern Fabrication on Pyrex 7740 Glass surface by using nano-scratch with HF wet etching", Scripta Materialia, **52**(2), pp. 117-122.

[32] Sumomogi, T., Endo, T., Kuwahara, K., and Kaneko, R., 1995, "Nanoscale layer removal of metal surfaces by scanning probe microscope scratching", Journal of Vacuum Science & Technology B, **13**(3), pp. 1257-1260.

[33] Schultz, P.L., Hsu, H.K., Fang, N.X., and Ferreira, P.M., 2007, "Solid-state electrochemical nanoimprinting of copper", Journal of Vacuum Science and Technology B., **25**(6), pp. 2419-2424.

[34] Vogler, M.P., DeVor, R.E., and Kapoor, S.G., 2004, "On the modeling and analysis of machining performance in micro-endmilling, Part I, Surface Generation", Journal of Manufacturing Science and Engineering, **126**, pp. 685-694.

[35] Subbiah, S., and Melkote, S.N., 2007, "Evidence of ductile tearing ahead of the cutting tool and modeling the energy consumed in material separation in micro-cutting", Journal of Engineering Materials and Technology, **129**, pp. 321-331.

[36] Standa Ltd., 2010, "Translation and rotation stages", www.standa.lt/products/catalog/translation_rotation.

[37] Keyence Corporation, 2010, "LT-900 series laser displacement sensor", http://www.keyence.com/products/measure/laser/lt9000/lt9000.php.

[38] Phillip A. G., Kapoor S. G., and DeVor R. E., 2006, "A new acceleration-based methodology for micro/meso-scale machine tool performance evaluation", International Journal of Machine Tools & Manufacture, **46**, pp. 1435-1444.

[39] Matweb Material Property Data, 2009, http://www.matweb.com.

[40] Sharklet Technologies, 2010, http://www.sharklet.com.

[41] Yan, Z., Qinghua, L., Mei, L, and Xin, L., 2007, “Anisotropic wetting characteristics on submicronmeter-scale periodic grooved surface” Langmuir, **23**(11), pp. 6212-6217.

[42] Hsu, H.K., Schultz, P.L., Ferreira, P.M., and Fang, N.X., 2007, “Electrochemical nanoimprinting with solid-state superionic stamps”, Nano Letters, **7**(2), pp. 446-451.

[43] Goss, S.H., Grazulis, L., Tomich, D.H., Eyink, K.G., Walck, S.D., Haas, T.W., Thomas, D.R., and Lampert W.V., 1998, "Mechanical lithography using a single point diamond machining", Journal of Vacuum Science & Technology B, **16**(3), pp. 1439-1445.

[44] Kato, Z., Sakairi, M., and Takahashi, H., 2001, "Fabrication of grooves on aluminum surface with atomic force microscope probe processing", Journal of The Electrochemical Society, **148**(12), pp. C790-C798.

[45] Santinacci, L., Djenizian, T., and Schmuki, P., 2001, "Atomic force microscopy-induced nanopatterning of Si(100) surfaces", Journal of The Electrochemical Society, **148**(9), pp. C640-C646.

[46] McGeough, J., 2002, “Micromachining of Engineering Materials”, Marcel Dekker, Inc., pp. 203-237.

[47] Nikumb, S., Chen, Q., Li, C., Reshef, H., Zheng, H.Y., Qiu, H., and Low, D., 2005, "Precision glass machining, drilling and profile cutting by short pulse lasers", Thin Solid Films, **477**(1-2), pp. 216-221.

[48] Takahashi, S., Suzuki, Y., and Yoshida, Y., 2003, "Fabrication of micro-channels by UV laser ablation", Proceedings of the SPIE, **4830**, pp. 173-176.

[49] Binder, A., Ashkenasi, D., Muller, N., Riesbeck, T., and Eichler H.J., 2003, "Microdrilling, -scribing and cutting with high-quality and high-power ns-Nd:YAG-systems", Proceedings of the SPIE, **5063**(1), pp. 401-406.

[50] Binder, A., Jaber, H., Ashkenasi, D., Riesbeck, T., and Eichler, H.-J., 2004, "High-power and high-brightness solid state laser systems for precise and fast micromachining", Proceedings of the SPIE, **5339**(1), pp. 500-509.

[51] Compaan, A.D., Matulionis, I., and Nakade, S., 2000, "Laser scribing of polycrystalline thin films", Optics and Lasers in Engineering, **34**(1), pp. 15-45.

[52] Dhupal, D., Doloi, B., and Bhattacharyya, B., 2008, "Pulsed Nd:YAG laser turning of micro-groove on aluminum oxide ceramic (Al2O3)", Journal of Machine Tools and Manufacture, **48**(2), pp. 236-248.

[53] Dhupal, D., Doloi, B., and Bhattacharyya, B., 2008, "Parametric analysis and optimization of Nd:YAG laser micro-grooving of aluminum titanate (Al2TiO5) ceramics", Journal of Advanced Manufacturing Technology, **36**(9-10), pp. 883-893.

[54] McGeough, J., 2002, “Micromachining of Engineering Materials”, Marcel Dekker, Inc., pp.179-201.

[55] Murali, M., and Yeo, S.H., 2004, "A novel spark erosion technique for the fabrication of high aspect ratio micro-grooves", Microsystem Technologies, **10**(8-9), pp. 628-632.

[56] Soni, J.S., and Chakraverti, G., 1994, "Machining characteristics of titanium with rotary electro-discharge machining", Wear, **171**(1-2), pp. 51-58.

[57] Her, M.-G., and Weng, F.-T. , 2001, "Micro-hole machining of copper using the electro-discharge machining process with a Tungsten carbide electrode compared with a copper electrode", Journal of Advanced Manufacturing Technology, **17**(10), pp. 715-719.

[58] Chow, H.M., Yan, B.H., and Huang, F.Y., 1999, "Micro slit machining using electro-discharge machining with a modified rotary disk electrode (RDE)", Journal of Materials Processing Technology, **91**(1), pp. 161-166.

[59] Yeo, S.H., Murali, M., and Balakrishnan, S., 2006, "Effect of tool electrode material on the spark erosion of micro grooves", Materials Science Forum, **526**, pp. 79-84.

[60] McGeough, J., 2002, “Micromachining of Engineering Materials”, Marcel Dekker, Inc., pp. 239-276.

[61] Kozak, J., Rajurkar, K.P., and Makkar, Y., 2004, "Selected problems of micro-electrochemical machining", Journal of Materials Processing Technology, **149**(1-3), pp. 426-431.

[62] Zhang, Z., and Zhu, D., 2008, “Experimental research on the localized electrochemical micro-machining”, Russian Journal of Electrochemistry”, **44**(8), pp. 926-930.

[63] Forster, R., Schoth, A., and Menz, W., 2003, “Micro-ECM for production of Microsystems with a high aspect ratio”, Microsystem Technologies, **11**, pp. 246-249.

[64] Schaller, T., Bohn, L., Mayer, J., and Schubert, K., 1999, "Microstructure grooves with a width of less than 50 mm cut with ground hard metal micro end mills", Precision Engineering, **23**(4), pp. 229-235.

[65] Wada, T., Masaki, T., and Davis, D.W., 2002, "Development of micro grinding process using micro EDM trued diamond tools", Proceedings Ann. Meeting of the American Society for Precision Engineering, pp. 16–9.

[66] Chern, G.-L., Wu, Y.-J.E., Cheng, J.-C., and Yao, J.-C., 2007, "Study on burr formation in micro-machining using micro-tools fabricated by micro-EDM", Precision Engineering, **31**(2), pp. 122-129.

[67] Vogler, M.P, Liu, X., Kapoor, S.G., DeVor, R.E., and Ehmann, K.F., 2002, "Development of meso-scale machine tool (mMT) systems", Transactions of NAMRI/SME, pp. 653-661.

[68] Honegger A., 2005, "Micro/meso-scale machine tool development and calibration, master's thesis, University of Illinois, Urbana IL".

[69] Microlution Inc., 2007, http://microlution-inc.com.

[70] Friedrich, C.R., and Vasile, M.J., 1996, "The micromilling process for high aspect ratio microstructures", Microsystem Technologies, **2**(3), pp. 144-148.

[71] Vasile, M.J., Friedrich, C.R., Kikkeri, B., and McElhannon, R., 1996, "Micrometer-scale machining: tool fabrication and initial results", Precision Engineering, **19**(2-3), pp. 180-186.

[72] Friedrich, C.R., Coane, P.J., and Vasile, M.J., 1997, "Micromilling development and applications for microfabrication", Microelectronic Engineering, **35**(1-4), pp. 367-372.

[73] Vasile, M.J., Nassar, R., and Jushan X., 1998, "Focused ion beam technology applied to microstructure fabrication", Journal of Vacuum Science & Technology B, **16**(4), pp. 2499-2505.

[74] Jun, Martin B.G., DeVor, R.E., and Kapoor, S.G., 2006, "Investigation of the dynamics of microend milling - Part II: Model validation and interpretation", Journal of Manufacturing Science and Engineering, **128**(4), pp. 901-912.

[75] Sawyer, L.C., Grubb, D.T., and Meyers G.F., 2008, "Polymer Microscopy, Third Edition", Springer.

[76] Jin, X., and Unertl, W.N., 1992, "Submicrometer modification of polymer surfaces with a surface force microscope", Applied Physics Letters, **61**(6), pp. 657-659.

[77] Asylum Research, 2009, "MicroAngelo™ - Built-in Nanolithography and Nanomanipulation", http://www.asylumresearch.com/Applications/MicroAngelo/MicroAngelo.shtml.

[78] Schumacher, H.W., Kracke, B., and Damaschke, B., 1995, "Modification of thin gold film with a scanning force microscope", Thin Solid Films, **264**(2), pp. 268-272.

[79] Tseng, AA, Notargiacomo, A., and Chen, T. P., 2005, "Nanofabrication by scanning probe microscope lithography: A review", Journal of Vacuum Science & Technology B, **23**(3), pp. 877-894.

[80] Teixeira, F.S., Mansano, R.D., Salvadori, M.C., Cattani, M., and Brown, I.G., 2007, "Atomic force microscope nanolithography of polymethylmethacrylate polymer", Review of Scientific Instruments, **78**(5), pp. 53702/1-53702/3.

[81] Zhao, Q., Sun, T., Liang, Y., Dong, S., and Chen, M., 2001, "Atomic force microscope using a diamond tip: A tool for micro/nano-machining on single crystal silicon surface", Proceedings of SPIE, **4601**, pp. 73-78.

[82] Micro Star Technologies, 2009, http://www.microstartech.com/.

[83] Iwata, F., Matsumoto, T., Ogawa, R., and Sasaki, A., 1999, "Scratching on polystyrene thin film without bumps using atomic force microscopy", Journal of Vacuum Science & Technology B, **17**(6), pp. 2452-2456.

[84] Mao, Y.-T., Kuo, K.-C., Tseng, C.-E., Huang, J.-Y., Lai, Y.-C., Yen, J.-Y., Lee, C.-K., and Chuang, W.-L., 2009, "Research on three dimensional machining effects using atomic force microscope", Review of Scientific Instruments, **80**(6).

[85] Shaw, M.C., 1984, “Metal Cutting Principle”, Oxford University Press Inc., New York.

[86] Kalpakjian, S., and Schmid, S.R., 2003, “Manufacturing Processes for Engineering Materials, Fourth Edition”, Pearson Education, Inc., Upper Saddle River, New Jersey.

[87] Grzesik, W., 2008, “Advanced Machining Processes of Metallic Materials”, Elsevier, Oxford, UK.

[88] Nakayama, K., and Tamura, K., 1968, “Size effect in metal-cutting force” ASME Journal of Engineering for Industry, **90**, pp. 119-126.

[89] Vogler, M. P., 2003, “On the modeling and analysis of machining performance in micro-endmilling”, PhD. Thesis, University of Illinois, Urbana IL.

[90] Manjunathaiah, J., and Endres, W. J, 2000, "A study of apparent negative rake angle and its effects on shear angle during orthogonal cutting with edge-radiused tools", Transactions of the NAMRI/SME XXVIII, pp. 197-202.

[91] Liu, X., 2006, "Cutting mechanisms in micro-endmilling and their influence on surface generation, Ph.D. Thesis, University of Illinois, Urbana IL".

[92] Shimada, S., Ikawa, N., Tanaka, H., Ohmuri, G., Uchikoshi, J., and Yoshinaga, H., 1993, "Feasibility study on ultimate accuracy in microcutting using molecular dynamics simulation", CIRP Anneals, **42**, pp. 91-94.

[93] Liu, X., DeVor, R.E., and Kapoor, S.G., 2006, "An analytical model for the prediction of minimum chip thickness in micromachining", Journal of Manufacturing Science and Engineering, **128**(2), pp. 474-491.

[94] Kota, N., and Ozdoganlar, B., 2010, "Machining force and surface finish variation across grains during orthogonal micromachining of aluminum", 5th International Conference on MicroManufacturing, pp. 133-137.

[95] Chuzhoy, L., DeVor, R.E., Kapoor, S.G., and Bammann, D.J., 2002, "Microstructure-level modeling of ductile iron machining", Journal of Manufacturing Science and Engineering, **124**, pp. 162-169.

[96] Chuzhoy, L, DeVor, R.E., Kapoor, S.G., Beaudoin, A.J., and Dammann, D.J., 2003, "Machining simulations of ductile iron and its constituents, Part I: estimation of material model parameters and their validation", Journal of Manufacturing Science and Engineering, **125**, pp. 181-191.

[97] Chuzhoy, L, DeVor, R.E., and Kapoor, S.G., 2003, "Machining simulations of ductile iron and its constituents, Part 2: numerical simulation and experimental

validation of machining", Journal of Manufacturing Science and Engineering, **125**, pp. 192-201.

[98] Vogler, M.P., DeVor, R.E., and Kapoor, S.G., 2003, "Microstructure-level force prediction model for micro-milling of multi-phase materials", Journal of Manufacturing Science and Engineering, **125**, pp. 202-209.

[99] Waldorf, D.J., DeVor, R.E., and Kapoor, S.G., 1998, "A slip-line field for ploughing during orthogonal cutting", Journal of Manufacturing Science and Engineering, **120**, pp. 693-699.

[100] Zhang, Z.G., Fang, F.Z., Hu, X.T., and Sun, C.K., 2009, "Molecular dynamics study on various nanometric cutting boundary conditions", Journal of Vacuum Science and Technology B, **27**(3), pp. 1355-1360.

[101] Zhu, P., Hu, Y., Ma, T., and Wang, H., 2010, "Study of AFM-based nanometric cutting process using molecular dynamics" Applied Surface Science, **256**, pp. 7160-7165.

[102] Komanduri, R., Chandrasekaran, N., and Raff, L.M., 2000, "M.D. simulation of nanometric cutting of single crystal aluminum – effect of crystal orientation and direction of cutting", **240**(1-2), pp. 113-143.

[103] Shi, G., Deng, X., and Shet, C., 2002, "A finite element study of the effect of friction in orthogonal metal cutting", Finite Elements in Analysis and Design, **38**, pp. 863-883.

[104] Shih, A.J., 1996, "Finite element analysis of the rake angle effects in orthogonal metal cutting", International Journal of Mechanical Sciences, **38**(1), pp. 1-17.

[105] Marusich, T.D., 2001, “Effects of friction and cutting speed on cutting force”, Proceedings of IMECE (ASME), MED-23313, pp. 1 – 9.

[106] Yen, Y.-C., Sohner, J., Weule, H., Schmidt, J., and Altan, T., 2002, "Estimation of tool wear of carbide tool in orthogonal cutting using FEM simulation" Proceeding of the 5th CIRP International Workshop on Modeling of Machining Operations, pp. 149 - 160.

[107] Liu, K., Shreyes, N., and Melkote, N., 2007, “Finite element analysis of the influence of tool edge radius on size effect in orthogonal micro-cutting processes”, International Journal of Mechanical Sciences, **49**, pp. 650-660.

[108] Subbiah, S., and Melkote, S.N., 2008, “Effect of finite edge radius on ductile fracture ahead of the cutting tool edge in micro-cutting of Al 2024-T3”, Material Science and Engineering A, **474**, pp. 283 – 300.

[109] Liu, K., and Melkote, S.N., 2006, “Material strengthening mechanisms and their contribution of size effect in micro-cutting”, Journal of Manufacturing Science and Engineering”, **128**, pp. 730-738.

[110] Marusich, T.D., and Ortiz, M., 1995, “Modelling and simulation of high-speed machining”, International Journal for Numerical Methods in Engineering, **38**(21), pp. 3675-3694.

[111] Ng, E., El-Wardany, T.I., Dumitrescu, M., and Elbestawi, M.A., 2002, "Physics based simulation of high speed machining" Proceedings of the 5th CIRP International Workshop on Modeling of Machining Operations, pp. 1 - 19.

[112] Marusich, T.D., Brand, C.D., and Thiele, J.D., 2002, “A methodology for simulaton of chip breakage in turning processes using an orthogonal finite element model”,

Proceedings of the 5th CIRP International Workshop on Modeling of Machining Operations, pp. 139-148.

[113] Marusich, T.D., and Askari, E., 2001, "modeling residual stress and workpiece quality in machined surface", Third Wave Systems, Inc., http://www.thirdwavesys.com/news/published_papers.htm, pp. 1-5.

[114] Park, I.W., and Dornfeld D.A., 2000, "A study of burr formation processes using the finite element method: Part I", Journal of Mechanical Engineering Materials and Technology, **122**, pp. 221-228.

[115] Park, I.W., and Dornfeld D.A., 2000, "A study of burr formation processes using the finite element method: Part II – the influences of exit angle, rake angle, and backup material on burr formation processes", Journal of Engineering Materials and Technology, **122**, pp. 229-237.

[116] Guo, Y.B., and Dornfeld, D.A., 2000, "Finite element modeling of burr formation process in drilling 304 stainless steel", Journal of Manufacturing Science and Engineering, **122**, pp. 612-619.

[117] Min, S., Dornfeld, D.A, Kim, J., and Shyu B., 2001, "Finite element modeling of burr formation in metal cutting", Machining Science and Technology, **5**(3), pp. 307-322.

[118] Sartkulvanich, P., Sahlan, H., and Altan, T., 2007, "A finite element analysis of burr formation in face milling of a cast aluminum alloy", Machining Science and Technology, **11**, pp. 157-181.

[119] Marusich, T.D., Usui, S., Ma, J., and Stephenson, D.A., 2008, "Finite element modeling of drilling processes with solid and indexable tooling in metals and stack-

ups", Third Wave Systems, Inc., http://www.thirdwavesys.com/news/published_papers.htm, pp. 1-7.

[120] Third Wave Systems, Inc., 2010, http://www.thirdwavesys.com.

[121] Scientific Forming Technologies Corporation, 2010, "DEFORM", http://www.deform.com/.

[122] Dassault Systèmes Simulia Corp., 2009, "Abaqus 6.9 Analysis User's Manual".

[123] Strenhowski, J.S., and Carroll III, J.T., 1985, "A finite element model of orthogonal metal cutting", Journal of Engineering for Industry, **107**, pp. 349-354.

[124] Barge, M., Hamdi, H., Rech, J., and Bergheau, J.-M., 2005, "Numerical modeling of orthogonal cutting: influence of numerical parameters", Journal of Materials Possessing Technology, **164-165**, pp. 1148-1153.

[125] Alkbar, F., Mativenga, P.T., and Sheikh, M.A., 2010, "An experimental and coupled thermo-mechanical finite element study of heat partition effects in machining", International Journal of Advanced Manufacturing Technology, **46**, pp. 491-507.

[126] Bacaria, J-L., Dalverny, O., and Caperaa, S., 2001, "A three-dimensional transient mumerical model of milling", Proceedings of the Institution of Mechanical Engineering, Part B: Journal of Engineering Manufacture, **215**, pp. 2041-2975.

[127] Llanos, I., Villar, J.A., Urresti, I., and Arrazola, P.J., 2009. "Finite element modeling of oblique machining using an arbitrary Lagrangian Eulerian formulation", Machining Science and Technology, **13**, pp. 385-406.

[128] Akarca, S.S., Song, X., Altenhof, W.J., and Alpas, A.T., 2008, "Deformation behavior of aluminum during machining: modeling by Eulerian and smoothed-

particle hydrodynamics methods", Part L: Journal of Design and Applications, **222**, pp. 209-221.

[129] MicroE Systems, 2010, http://www.microesys.com.

[130] Delta Tau Data Systems Incorporated, 2009, www.deltatau.com.

[131] Bourne, K.A., DeVor, R.E., and Kapoor, S.G., 2010, "Study of a high performance AFM probe based micro-scribing process," Journal of Manufacturing Science and Engineering, **132**(3), pp. 030906-1 – 030906-10.

[132] ISO3685-1977(E), "Tool-life testing with single-point turning tools"

[133] Gillespie, L.K., 1999, "Deburring and Edge Finishing Handbook", ASME Press, New York.

[134] Kopalinsky, E.M., and Oxley P.L.B., 1984, "Size effects in metal removal processes", Proceedings of the 3rd Conference on Mechanical Properties of Materials at High Rates of Strain, pp. 389-396.

[135] Ng, C.K., Melkote, S.N., Rahman, M., and Kumar, A.S., 2006, "Experimental study of micro- and nano-scale cutting of aluminum 7075-T6", International Journal of Machine Tools and Manufacture", **46**, pp. 929-936.

[136] Oxley, P.L.B., 1989, "Mechanics of machining: an analytical approach to assessing machinability", Ellis Horwood Ltd., Chichester.

[137] Brantley, W.A., 1973, "Calculated elastic constants for stress problems associated with semiconductor devices", Journal of Applied Physics, **44**(1), pp. 534-535.

[138] Petersen, K.E., 1982, "Silicon as a mechanical material", Proceedings of the IEEE, vol. **70**(5), pp. 420 – 457.

[139] Efunda, 2009, “Properties of aluminum alloy AA 1100”, http://www.efunda.com/materials/alloys/aluminum.

[140] Frick, C.P., Clark, B.G., Orso, S., Schneider, A.S., and Arzt, E., 2008, “Size effect on strength and strain hardening of small-scale [1 1 1] nickel compression pillars” Materials Science and Engineering A., **489**, pp. 319-329.

[141] Lindholm, U.S., 1964, “Some experiments with the split hopkinson pressure bar”, Journal of Phys. Solids, **12**, pp. 317 – 335.

[142] Robertson K.D., Chou S.-C., and Rainey J.H., 1971, “Design and operating characteristics of a split Hopkinson pressure bar apparatus”, Army Materials and Mechanics Research Center.

[143] Khan, A.S., and Huang, S., 1992, “Experimental and theoretical study of mechanical behavior of 1100 aluminum in the strain rate range $10^{-5}$ – $10^{4}$ $sec^{-1}$”, International Journal of Plasticity, **8**, pp. 397-424.

[144] Frantz, R.A., and Duffy, J., 1972, "The dynamic stress-strain behavior in torsion of Al 1100-O aluminum subjected to sharp increase in strain rate", Journal of Applied Mechanics, **39**, pp. 939-945.

[145] Kloop, R.W, Clifton, R.J., and Shawki, T.G., 1985, “Pressure-shear impact and the dynamic viscoplastic response of metals”, Mechanics of Materials, **4**, pp. 375-385.

[146] Johnson, G.R., and Cook, W.H., 1983, “A constitutive model and data for metals subjected to large strains, high strain rates and high temperatures”, Proceedings of the 7th International Symposium on Ballistics, pp. 541-547.

[147] Johnson, G.R., 1985, “Fracture characteristics of three metals subjected to various strains, strain rate, temperatures and pressures”, Engineering Fracture Mechanics, **21**(1), pp. 31-48.

[148] Gupta, N.K., Iqbal, M.A., and Sekhon G.S., 2006, “Experimental and numerical studies on the behavior of thin aluminum plates subjected to impact by blunt- and hemispherical-nosed projectiles, “International Journal of Impact Engineering, **32**, pp. 1921-1944.

[149] Kay, G., 2003, “Failure modeling of titanium 6Al-4V and aluminum 2024-T3 with the Johnson-Cook material model”, U.S. Department of Transportation Federal Aviation Administration, DOT/FAA/AE-03/57.

[150] Zorev, N.N. 1963, “Interrelationship between shear processes occurring along tool face and on shear plane in metal cutting”, International Production Engineering Research Conference, pp. 42-49.

[151] Shi, B., and Attia, H, 2009, “Modeling the thermal and tribological processes at the tool-chip interface in machining”, Machining Science and Technology, **13**, pp. 210-226.

[152] Liu X., DeVor R. E., and Kapoor S. G., 2006, “An analytical model for the prediction of minimum chip thickness in micromachining”, ASME Journal of Manufacturing Science and Engineering, **128**(2), pp. 474-481.

[153] Miyashita, Y., Sasaki, Y., Kuroishi, T., Watanabe, T., Xu, J.-Q. Mutoh, Y., and Yasuoka M., 2003, “An evaluation of the adhesive strength of the interface between a coating and substrate”, JSME International Journal, Series A: Solid Mechanics and Material Engineering, **46**(3), pp. 335-340.

# Author's Biography

Keith Allen Bourne was born in Sewickley Pennsylvania on May 3, 1981 to Terry Allen Bourne and Susan Bourne. He grew up in Aliquippa Pennsylvania and graduated from Hopewell Senior High School in 1999. He attended The Pennsylvania State University where he completed an undergraduate thesis titled "Design, Construction, and Testing of an Instrumented Multi-jointed Arm and Software for Measurement and Visualization of 3D Coordinates on Large Objects". He received his Bachelor's degree in Mechanical Engineering from The Pennsylvania State University in 2004.

In the fall of 2004 Keith enrolled in The University of Illinois at Urbana-Champaign to pursue a direct Ph.D. in mechanical engineering. Under the guidance of Professor Shiv G. Kapoor and Professor Richard E. DeVor, he has studied micro/meso-scale machining systems, process monitoring, and process modeling. After initially working in the area of process monitoring and control of micro-endmilling, he began his research into the development of a new micro-groove cutting process and modeling of chip formation during micro-groove cutting. His graduate study has led to three journal papers, six conference papers, and two patent applications.